

**AD-A273 846**



2

**S** **DTIC**  
ELECTE  
DEC 17 1993  
**A**

**Hydrodynamics, Acoustics and Scaling  
of Traveling Bubble Cavitation**

Thesis by  
**Yan P. Kuhn de Chizelle**  
Division of Engineering and Applied Science

This document has been approved  
for public release and sale; its  
distribution is unlimited.

Report No. ENG 200.30  
on contracts  
N00014-91-J-1295  
N00014-91-J-1426

**93 12 16 024**

**93-30533**



Unclassified

SECURITY CLASSIFICATION OF THIS PAGE

## REPORT DOCUMENTATION PAGE

Form Approved  
OMB No. 0704-0188

1. REPORT SECURITY CLASSIFICATION <b>Unclassified</b>			1b. RESTRICTIVE MARKINGS		
2. SECURITY CLASSIFICATION AUTHORITY			3. DISTRIBUTION / AVAILABILITY OF REPORT <b>Unlimited</b>		
b. DECLASSIFICATION / DOWNGRADING SCHEDULE					
PERFORMING ORGANIZATION REPORT NUMBER(S) <b>E200.30</b>			5. MONITORING ORGANIZATION REPORT NUMBER(S) <b>N00014-91-J-1295</b> <b>N00014-91-J-1426</b>		
a. NAME OF PERFORMING ORGANIZATION <b>California Institute of Technology</b>		6b. OFFICE SYMBOL (If applicable)	7a. NAME OF MONITORING ORGANIZATION <b>Office of Naval Research</b>		
c. ADDRESS (City, State, and ZIP Code) <b>1201 E. California</b> <b>Pasadena, CA 91125</b>			7b. ADDRESS (City, State, and ZIP Code) <b>565 S. Wilson</b> <b>Pasadena, CA 91106-3212</b>		
1a. NAME OF FUNDING / SPONSORING ORGANIZATION <b>Dept. of the Navy</b>		8b. OFFICE SYMBOL (If applicable)	9. PROCUREMENT INSTRUMENT IDENTIFICATION NUMBER		
3c. ADDRESS (City, State, and ZIP Code) <b>800 N. Quincy</b> <b>Arlington, VA 22217-5000</b>			10. SOURCE OF FUNDING NUMBERS		
			PROGRAM ELEMENT NO.	PROJECT NO.	TASK NO.
			WORK UNIT ACCESSION NO.		
11. TITLE (Include Security Classification) <b>Hydrodynamics, Acoustics and Scaling of Traveling Bubble Cavitation</b>					
12. PERSONAL AUTHOR(S) <b>Yan Kuhn de Chizelle</b>					
13a. TYPE OF REPORT <b>technical</b>		13b. TIME COVERED FROM _____ TO _____		14. DATE OF REPORT (Year, Month, Day) <b>93/9/24</b>	
15. PAGE COUNT <b>178</b>					
16. SUPPLEMENTARY NOTATION					
17. COSATI CODES			18. SUBJECT TERMS (Continue on reverse if necessary and identify by block number)		
FIELD	GROUP	SUB-GROUP	cavitation bubble dynamics bubble acoustics		
			cavitation nuclei scaling effects numerical modeling		
19. ABSTRACT (Continue on reverse if necessary and identify by block number) Recent observations of the geometries of growing and collapsing bubbles over axisymmetric headforms have revealed the complexity of the "microfluidmechanics" associated with these flows (Hamilton et.al., 1982, Briancon Marjollet and Franc, 1990, Ceccio and Brennen, 1991). Among the complex features observed were bubble to bubble interaction, cavitation noise generation and bubble interaction with the boundary layer which leads to the shearing of the underside of the bubble and alters the collapsing process. All of these previous tests were performed on small headform sizes. The focus of this research is to determine the dynamics governing the growth and collapse of traveling bubbles and to analyze the scaling effects due to variations in geometry size, Reynolds number and cavitation number. For this effect, cavitating flows over Schiebe headforms of different sizes (5.08 cm, 25.4 cm and 50.8 cm in diameter) were studied in the David Taylor Large CAvitation Channel (LCC). This thesis presents the scaling effects captured on high-speed film and electrode sensors as well as the noise signals generated (continued on reverse side)					
20. DISTRIBUTION / AVAILABILITY OF ABSTRACT <input checked="" type="checkbox"/> UNCLASSIFIED/UNLIMITED <input type="checkbox"/> SAME AS RPT. <input type="checkbox"/> DTIC USERS			21. ABSTRACT SECURITY CLASSIFICATION <b>Unclassified</b>		
22a. NAME OF RESPONSIBLE INDIVIDUAL			22b. TELEPHONE (Include Area Code)		22c. OFFICE SYMBOL

19. during the collapse of the cavities. The influence of each of these parameters on the dynamics involved in the growth and collapse phases of the traveling bubble are presented, along with the acoustical impulse produced during the collapse of the bubble.

In order to model and analyze the dynamics of the three-dimensional bubble deformation in the presence of the pressure field around the Schiebe headform, an unsteady numerical code using traveling sources has been developed. This thesis presents calculations of the interaction between the irrotational flow outside the boundary layer of the headform and individual traveling bubbles. An error estimation of the method and comparisons with the LCC experiments are presented. This method is shown to predict some of the features of three-dimensional bubble growth and collapse dynamics remarkable well. Furthermore, analysis of these computations allow a better understanding of bubble interaction and event rate prediction.

Accession For		
NTIS	CRA&I	<input checked="" type="checkbox"/>
DTIC	TAB	<input type="checkbox"/>
Unannounced		<input type="checkbox"/>
Justification		
By		
Distribution/		
Availability Codes		
Dist	Avail and/or Special	
A-1		

DTIC QUALITY INSPECTED 1

# **Hydrodynamics, Acoustics and Scaling of Traveling Bubble Cavitation**

Thesis by

**Yan P. Kuhn de Chizelle**

Division of Engineering and Applied Science

In Partial Fulfillment of the Requirements

for the Degree of

Doctor of Philosophy

**California Institute of Technology**

**Pasadena, California 91125**

**1994**

(Submitted September 22, 1993)



## ACKNOWLEDGMENTS

*"Experience is not what happens to you; it  
is what you do with what happens to you."  
Aldous Huxley*

First I would like to thank all of those who encouraged me to pursue my research work at Caltech. In chronological order these are my girlfriend (and now wife) Anh-Ngoc, my parents, Dr. François Avellan at EPFL who initiated me to the excitement of research and Dr. Allan Acosta who made my coming here possible. I cannot enumerate here the long list of fantastic friends and coworkers who made my stay in sunny California so pleasant and unforgettable along with those who helped me throughout my thesis work and I thank them from the bottom of my heart. Among them I would especially like to mention Petr Pich, Garrett Reisman, Carl Wassgren, Douglas Hart, Elizabeth McKenney and Zhenhuan Liu.

I wish to express my deepest gratitude to my advisors Dr. Christopher Brennen and Dr. Allan Acosta for their continuing help and professional guidance. The experiments performed in the LCC required help of many people and I am very grateful to all those who were involved in this enterprise, particularly to Dr. Steve Ceccio and Po-Wen Yu from the University of Michigan and to Dr. Young Shen, Scott Gowing, Jim Blanton and Bob Etter from the David Taylor Research Center. I also thank the Office of Naval Research for funding this work under contract N00014-91-J-1295.

Finally I dedicate this thesis to my loving wife, Anh-Ngoc and to the small island, *Ile d'Arz*, off the coast of Brittany (France) where we got married.

## ABSTRACT

Recent observations of the geometries of growing and collapsing bubbles over axisymmetric headforms have revealed the complexity of the "microfluidmechanics" associated with these flows (Hamilton *et al.*, 1982, Briançon Marjollet and Franc, 1990, Ceccio and Brennen, 1991). Among the complex features observed were bubble to bubble interaction, cavitation noise generation and bubble interaction with the boundary layer which leads to the shearing of the underside of the bubble and alters the collapsing process. All of these previous tests were performed on small headform sizes. The focus of this research is to determine the dynamics governing the growth and collapse of traveling bubbles and to analyze the scaling effects due to variations in geometry size, Reynolds number and cavitation number. For this effect, cavitating flows over Schiebe headforms of different sizes (5.08cm, 25.4cm and 50.8cm in diameter) were studied in the David Taylor Large Cavitation Channel (LCC). This thesis presents the scaling effects captured on high-speed film and electrode sensors as well as the noise signals generated during the collapse of the cavities. The influence of each of these parameters on the dynamics involved in the growth and collapse phases of the traveling bubble are presented, along with the acoustical impulse produced during the collapse of the bubble.

In order to model and analyze the dynamics of the three-dimensional bubble deformation in the presence of the pressure field around the Schiebe headform, an unsteady numerical code using traveling sources has been developed. This thesis presents calculations of the interaction between the irrotational flow outside the boundary layer of the headform and individual traveling bubbles. An error estimation of the method and comparisons with the LCC experiments are presented. This method is shown to predict some of the features of three-dimensional bubble growth and collapse dynamics

remarkably well. Furthermore, analysis of these computations allow a better understanding of bubble interaction and event rate prediction.

## TABLE OF CONTENTS

ACKNOWLEDGMENTS .....	ii
ABSTRACT .....	iii
TABLE OF CONTENTS .....	v
LIST OF FIGURES.....	viii
NOMENCLATURE .....	xi
A. GENERAL CONSIDERATIONS	1
A.1 Introduction	1
A.2 Schiebe headforms	2
B. SPHERICAL BUBBLE DYNAMICS	5
B.1 Rayleigh-Plesset model	5
B.2 Nucleus stability criteria over headforms	8
B.3 Pressure impulse during collapse	12
C. SCALING EXPERIMENTS IN THE LCC	17
C.1 Introduction	17
C.2 Experimental setup	19
C.2.1 Large Cavitation Channel	19
C.2.2 Headforms	21
C.2.3 Electrode bubble detection	21
C.2.4 High speed photography and flash	24
C.2.5 Hydrophones	24
C.2.6 Water nuclei measurement	25
C.2.6.a Susceptibility meter	25
C.2.6.b Particle Dynamics Analyzer	26
C.2.6.c Dissolved air content	26

C.3 Hydrophone calibration	26
C.4 Experimental analysis	34
C.4.1 Test conditions	34
C.4.2 Cavitation inception data	34
C.4.3 Event rate observations	39
C.4.4 Cavitation appearance	49
C.4.4.a Bubble shape	49
C.4.4.b Bubble tail and patches	53
C.4.4.c Bubble-patch interactions	54
C.4.5 Bubble dimensions	56
C.4.6 Cavitation noise	64
C.4.6.a Spectral analysis	65
C.4.6.b Acoustic pressure pulses	68
C.4.6.c Electrode signal analysis	72
D. UNSTEADY 3-D BUBBLE DYNAMICS MODEL	81
D.1 Introduction	81
D.2 Description of numerical method	82
D.2.1 Potential flow over axisymmetric headform	82
D.2.1.a Potential ring panel method	82
D.2.1.b Establishment of a linear system	87
D.2.1.c Resolution of the linear system	88
D.2.2 Unsteady three dimensional source	90
D.2.3 Bubble growth and collapse algorithm	92
D.2.3.a Source strength, $Q(t)$ , and position computation	93
D.2.3.b Bubble displacement and time step incrementation	98
D.3 Pressure perturbation analysis	103
D.4 Error estimation and code validation	104
D.4.1 Normal velocity leakage into the headform	104
D.4.1.a Small normal velocity perturbation assumption	105
D.4.1.b Superposition of an axisymmetric and a three-dimensional flow	107

D.4.2 Pressure distribution on the surface of the bubble	107
D.4.3 Corrective displacement of the bubble surface nodes	112
D.5 Results	115
D.5.1 Comparison of computed bubble shapes with experiments	115
D.5.2 Typical bubble growth and collapse	118
D.5.3 Pressure distribution over headform	146
D.5.4 Program main parameters as a function of time	156
D.5.5 Comparison with the LCC experiments	162
E. CONCLUSIONS	164
REFERENCES.....	169
APPENDIX.....	174

## LIST OF FIGURES

Figure A.1 Pressure distribution around the Schiebe headform	4
Figure B.1 Rayleigh-Plesset bubble radius as a function of time	7
Figure B.2 Initial streamtube radius versus critical equilibrium nucleus radius	11
Figure B.3 Dimensionless impulse, $i_{center}$ , as a function of the cavitation number	16
Figure C.1 Schematic diagram of an attached traveling bubble	18
Figure C.2 Schematic diagram of the Large Cavitation Channel	20
Figure C.3 Schematic diagram of the headform	22
Figure C.4 Schematic diagram of the three headform setup	23
Figure C.5 Hydrophone calibration results	28
Figure C.6 Voltage gain, $G$ , between hydrophones	30
Figure C.7 Reciprocity test between the hydrophones	31
Figure C.8 Medium acoustic impedance, $M(f)$	32
Figure C.9 Cavitation inception numbers, $\sigma_i$	35
Figure C.10 Cavitation photographs over all three headforms	37
Figure C.11 Average number of observable events on the headform	38
Figure C.12 Cavitation event rate as a function of the cavitation number	40
Figure C.13 Number of excited nuclei per unit liquid volume	41
Figure C.14 Number of events in the susceptibility meter	44
Figure C.15 Water susceptibility cavitation number	45
Figure C.16 Calculated event rates for the Schiebe headform	48
Figure C.17.a-i High-speed photography of cavitation events	50
Figure C.17 High-speed photography of cavitation events	51
Figure C.18 Bubble maximum radius as a function of the cavitation number	57
Figure C.19 Bubble sphericity at the maximum size of the bubble	59

Figure C.20 Dimensionless bubble collapse location, $x_c$	61
Figure C.21 Attachment point coordinate along the x axis	62
Figure C.22 Average void fraction area over the nose of the headform	63
Figure C.23 Averaged dimensionless power spectral density signals	66
Figure C.24 Average power spectral density slope decay [dB/dec]	67
Figure C.25 Average acoustic impulse, $i_{\text{cluster}}$ , and impulse duration	69
Figure C.26 Average acoustic impulse, $i_{\text{unit}}$	70
Figure C.27 Electrode and the corresponding acoustic noise signals	73
Figure C.28 Dimensionless electrode signal duration	75
Figure C.29 Travel time between the two first electrodes	77
Figure C.30 Unit acoustic impulse, $i_{\text{unit}}$ , as a function of $\gamma$	79
Figure D.1 Distribution of ring panels on the surface of the Schiebe headform	83
Figure D.2 Schematic of the ring panel induced velocity at the control point C	85
Figure D.3 Schematic illustrating the zero normal velocity condition	89
Figure D.4 Bubble discretization scheme	96
Figure D.5 Program flow chart	102
Figure D.6 Normal velocity [%] in the axial direction on the surface of the headform	106
Figure D.7 Normal velocity [%] in the circumferential direction on the surface of the headform	108
Figure D.8 Error in the pressure coefficient distribution on the surface of the bubble	110
Figure D.9 Fractional differences between the source strengths $Q_i$ and $Q$	111
Figure D.10 Estimated volumetric rate of change of the bubble	114
Figure D.11 Comparison between computed bubbles and photographs	117
Figure D.12.1-20 Pressure field in the vicinity of the bubble	119
Figure D.13 Pressure distribution, $C_p$ , close to the bubble	139
Figure D.14.1-3 Pressure coefficient, $C_p$ , in the direction parallel to the headform	147
Figure D.15.1-3 Pressure perturbation, $\Delta C_p$ , in the direction parallel to the headform	150



Figure D.16.1-3 Pressure perturbation, $\Delta C_p$ , in the direction normal to the headform	153
Figure D.17 Average source strength, $Q$ , as a function of time	157
Figure D.18 Computed bubble base radius as a function of time	158
Figure D.19 Bubble sphericity as a function of time	159
Figure D.20 Bubble dimensions as a function of time	160

## NOMENCLATURE

$a_{qi}$	Distance from the point $i$ to the source $Q$ .....	[-]
$C_p$	Pressure coefficient, $C_p = \frac{2(P - P_\infty)}{\rho U_\infty^2}$ .....	[-]
$D$	Headform diameter .....	[m]
$i_{center}$	Dimensionless acoustic impulse referred to the center of the headform .....	[-]
$i_{unit}$	Acoustic impulse referred to a distance of one meter from the cavitation .....	[m]
$k$	Gas polytropic constant ( $k=1.4$ for isentropic air).....	[-]
$N(R)$	Nuclei number distribution .....	[m <sup>-4</sup> ]
$N_p$	Number of ring panels for potential flow calculation.....	[-]
$N_b$	Number of discretization points on the surface of the bubble .....	[-]
$P$	Static local pressure .....	[Pa]
$P_\infty$	Static free-stream pressure .....	[Pa]
$P_{air}$	Dissolved air content relative to saturation conditions .....	[%]
$P_v$	Water vapor pressure ( $P_v=3250$ at ambient temperature).....	[Pa]
$Q_i$	Local required source strength .....	[-]
$Q$	Averaged traveling source strength .....	[-]
$R$	Radius at the base of the hemispherical cap of the bubble .....	[m]
$R_{max}$	Bubble maximum radius at the base of the hemispherical cap.....	[m]
$r$	Dimensionless bubble radius $r = \frac{R}{D}$ .....	[-]
$Re$	Reynolds number $Re = \frac{U_\infty D}{\nu}$ .....	[-]
$t$	Time .....	[s]
$S$	Surface tension $S=0.0717$ .....	[kg/s <sup>2</sup> ]
$U_\infty$	Free-stream velocity.....	[m/s]
$v$	Dimensionless velocity $v = \frac{V}{U_\infty}$ .....	[-]

$v$	Dimensionless bubble volume $\frac{V}{V_0}$ .....	[-]
$We$	Weber number $We = \frac{\rho U_{\infty}^2 D}{S}$ .....	[-]
$X_a$	Attachment coordinate along the axis of revolution .....	[m]
$X_c$	Collapse coordinate along the axis of revolution.....	[m]
$\delta$	Bubble thickness in the direction normal to the headform surface .....	[m]
$\delta_i$	Normal distance to the headform of the bubble surface point i.....	[-]
$\varepsilon$	Bubble sphericity, $\varepsilon = \delta/R$ .....	[-]
$\varepsilon_i$	Displacement of the bubble surface node i.....	[-]
$\gamma$	Global coverage parameter .....	[-]
$\gamma_i$	Dimensionless electrode duration parameter for electrode i .....	[-]
$\mu_i$	Dimensionless panel strength per unit surface for $i^{th}$ ring panel .....	[-]
$\nu$	Kinematic viscosity ( $\nu = 8.5337 \cdot 10^{-7}$ at ambient temperature).....	[m <sup>2</sup> /s]
$\rho$	Water density ( $\rho = 996.3$ at ambient temperature).....	[kg/m <sup>3</sup> ]
$\sigma$	Cavitation number, $\sigma = \frac{2(P_{\infty} - P_v)}{\rho U_{\infty}^2}$ .....	[-]
$\sigma_i$	Inception cavitation number .....	[-]
$\tau$	Dimensionless time $\tau = \frac{t U_{\infty}}{D}$ .....	[-]
$\Delta\tau$	Dimensionless bubble travel time between electrodes 1 and 2 .....	[-]
$\tau_w$	Acoustic impulse duration.....	[-]

As a general rule the parameters written in lower case are dimensionless unless otherwise stated.

## **A. GENERAL CONSIDERATIONS**

### **A.1 INTRODUCTION**

Recently Ceccio and Brennen (1989, 1991) and Kumar and Brennen (1991) have performed a number of experiments to determine the interactions between the boundary layer and traveling cavitation bubbles. It appeared quite obvious that the headform and boundary layer shape significantly affected the dynamics involved in the growth and collapse phases of individual bubbles. The experiments were performed on a 5.08cm diameter axisymmetric headform and revealed a surprising complexity in the flow around single cavitation bubbles. Among the phenomena observed during those experiments were the fact that the bubbles have an approximately hemispherical shape and are separated from the solid surface by a thin film of liquid. This general conformation persists during the growth phase, though especially with the larger bubbles the thin film appears to become unstable and may begin to shear off the underside of the bubble leaving a cloud of smaller bubbles behind. On the other hand, the collapse phase is quite complex and consists of at least three processes occurring simultaneously, namely collapse, shearing due to the velocity gradient near the surface and the rolling up of the bubbles into vortices as a natural consequence of the first two processes. These processes tend to produce small transverse vortices with vapor/gas filled cores. It was noted that the collapse phase was dependent on the shape of the headform and the details differed between the ITTC headform (Lindgren and Johnson, 1966) which possesses a laminar separation and the Schiebe body (Schiebe, 1972; Meyer, Billet and Holl, 1989) which does not.

All of these previous experiments were, however, conducted in the same facility with the same headform size (5.08cm in diameter) and over a fairly narrow range of flow velocities (around 9m/s). Clearly this raises the issue of how the phenomena identified change with speed, scale and facility. There are very real questions as to how the

observed phenomena might scale with both headform size and with tunnel velocity. The experiments described here represent one effort to answer some of these questions for the case of cavitation occurring on simple axisymmetric headforms. This thesis will focus on traveling bubble cavitation, and the interaction between the flow and the dynamics and acoustics of individual bubbles. The current investigation employed Schiebe headforms with a minimum pressure coefficient on the surface of  $C_{p_{min}} = -0.78$ . We note that such scaling experiments are difficult to undertake since they require the testing of several geometries. Billet and Holl (1979) have performed such experiments on a series of NACA and Joukowski hydrofoils. They mostly observed data for the desinent cavitation number,  $\sigma_d$ , and observed an increase of this quantity as the Reynolds number was increased.

In chapter B of this thesis we will investigate the spherical bubble dynamic model developed by Plesset (1949) and apply it to the case of the flow over the Schiebe headform, in order to gain some insight as to what dynamics govern the growth and collapse of a cavitation bubble. Presented in chapter C are the scaling experiments performed in the Large Cavitation Channel (LCC) over three Schiebe headforms of different sizes. In light of the complexity of the dynamics of the traveling bubbles and the important bubble-to-bubble interactions seen (particularly over the larger headforms) it becomes clear that the spherical Rayleigh-Plesset model cannot reproduce many of the phenomenon observed. For understanding this effect a novel unsteady three-dimensional numerical code has been developed and is presented in chapter D. This model attempts to reproduce the three-dimensional bubble-flow interactions in the presence of the pressure gradient field induced by the headform. An error estimation of the method is then presented along with some computational results. These results are also compared with the experimental data taken in the LCC.

## A.2 SCHIEBE HEADFORMS

The cavitating flow around Schiebe headforms (Schiebe, 1972) has been widely studied for small headform sizes (Meyer *et al.*, 1985, Ceccio, 1989, Kumar, 1991) and has therefore become a useful geometry to compare cavitation data taken from various research laboratories. The shape of this headform is the solution of the geometry induced by a potential disc-source placed perpendicular to a uniform flow. This headform presents relatively smooth but strong adverse pressure gradients and the boundary layer has therefore the property of being relatively robust to laminar detachment, unlike the ITTC body (Lindgren and Johnson, 1966). As a guide to interpretation of the flow over this headform, a panel method was developed to solve the axisymmetric potential flow in the absence of cavitation. Some results from these calculations are presented in figure A.1, which shows the isobars in the low pressure region on the surface of the headform. The minimum pressure coefficient on this headform has a value  $C_{p_{min}} = -0.78$ . Note the large pressure gradient normal to the surface of the headform in the vicinity of the minimum pressure point and the elongated shape of the isobars as the pressure decays. This pressure gradient distribution will be shown in later sections of this thesis to be a determinant factor for the bubble deformation.

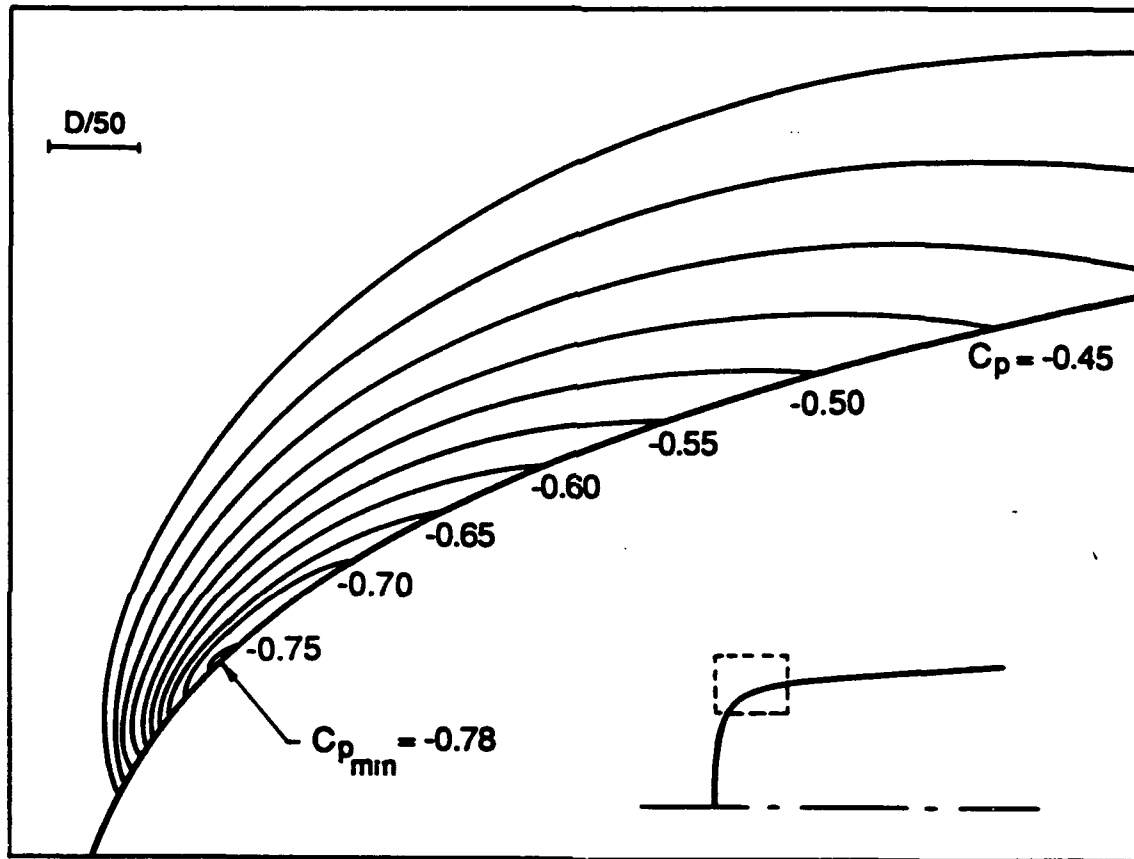


**Figure A.1 Pressure distribution around the Schiebe headform**

*This figure shows the solution of the flow around the headform using an axisymmetric potential flow calculation. The low pressure region near the nose of the headform is shown with lines of constant  $C_p$ . The minimum calculated pressure is shown as  $C_{p_{min}} = -0.78$ .*

## B. SPHERICAL BUBBLE DYNAMICS

A simple approach to understand the dynamics of growing and collapsing cavitation bubbles is made by considering the case of an expanding bubble in an infinite incompressible fluid (Plesset, 1949). The driving pressure perturbations causing the growth or collapse of the cavity are applied through changes in the medium pressure at infinity,  $P_\infty$ . The nuclei from which the bubble grows is assumed to be typically a micron-size gas bubble and is initially in equilibrium with the surrounding medium. Such a model has been widely used to predict some features of bubble cavitation in various flows (Plesset and Prosperetti 1977, Hamilton *et al.* 1982, Kumar and Brennen 1992), and remains an extremely useful tool to understand the underlying dynamics of complex three-dimensional viscous cavitating flows. In this chapter we will attempt to use this model to predict some features of the cavitation bubbles traveling over Schiebe headforms.

### B.1 RAYLEIGH-PLESSET MODEL

By writing the force balance on the surface of the spherical bubble and integrating the momentum equation from the bubble surface to an infinite radius, we can derive the Rayleigh-Plesset equations for spherical bubble dynamics (Plesset, 1949).

$$\frac{P_v - P_\infty(t)}{\rho} + \frac{P_{g0}}{\rho} \left( \frac{R_0}{R} \right)^{3k} = R \frac{d^2 R}{dt^2} + \frac{3}{2} \left( \frac{dR}{dt} \right)^2 + \frac{4\nu}{R} \frac{dR}{dt} + \frac{2S}{\rho R} \quad (B.1)$$

Where  $R_0$  is the initial radius of the nucleus in its equilibrium state,  $R$  is the current bubble radius,  $P_v$  is the water vapor pressure at ambient temperature and  $P_\infty$  is the pressure at infinity. This equation includes the partial pressure of the gas inside the bubble which is assumed to follow a polytropic law (power  $k$  term), the surface tension effects ( $S$  term), the viscous growth effects ( $\nu$  term) and the fluid inertia terms. The gas in the initial nucleus has been assumed to be air which behaves isentropically, so that the gas polytropic



constant  $k=1.4$ . The compressibility, gas diffusion and thermal effects have been omitted in this analysis.

Using the length (diameter,  $D$ ) and time scale (free-stream velocity,  $U_\infty$ ) of the flow over an axisymmetric headform, it is possible to write the Rayleigh-Plesset equation in the following dimensionless form

$$Cp_\infty + \sigma = -2r \frac{d^2 r}{d\tau^2} - 3 \left( \frac{dr}{d\tau} \right)^2 - \frac{8}{r Re} \left( \frac{dr}{d\tau} \right) - \frac{4}{r We} + \left( \sigma + \frac{4}{r_0 We} \right) \left( \frac{r_0}{r} \right)^{3k} \quad (B.2)$$

where  $Cp_\infty$  is the pressure coefficient,  $We$  the Weber number,  $Re$  the Reynolds number,  $\tau$  the dimensionless time, and  $r$  the dimensionless radius and are defined as

$$Cp_\infty = \frac{P - P_\infty}{1/2 \rho U_\infty^2}; \quad We = \frac{\rho U_\infty^2 D}{S}; \quad Re = \frac{U_\infty D}{\nu}; \quad \tau = \frac{t U_\infty}{D}; \quad r = \frac{R}{D}. \quad (B.3)$$

Knowing the pressure distribution over the Schiebe headform (see figure A.1), we can follow a streamline close to the surface of the headform and obtain the pressure coefficient time history  $Cp(\tau)$  that a traveling nucleus would encounter. If we crudely approximate that the pressure field in the vicinity of the bubble is isotropic and that the local pressure the nucleus experiences may be considered as an infinite reference pressure, we can then substitute the term  $Cp_\infty(\tau)$  by  $Cp(\tau)$  in equation B.2. It then becomes possible to numerically solve the dimensionless Rayleigh-Plesset equation B.2 using a standard adaptive finite difference method with a fourth-order Runge-Kutta algorithm to find the radius of the bubble as a function of time  $r(\tau)$ . The results of such computations are presented as a function of time,  $\tau$ , in figure B.1 for various cavitation numbers and the following cavitation conditions:  $R_0=100\mu\text{m}$ ,  $D=50.8\text{cm}$ ,  $U_\infty=11.5\text{m/s}$ , with an initial nucleus position at  $x_0=-1$ .

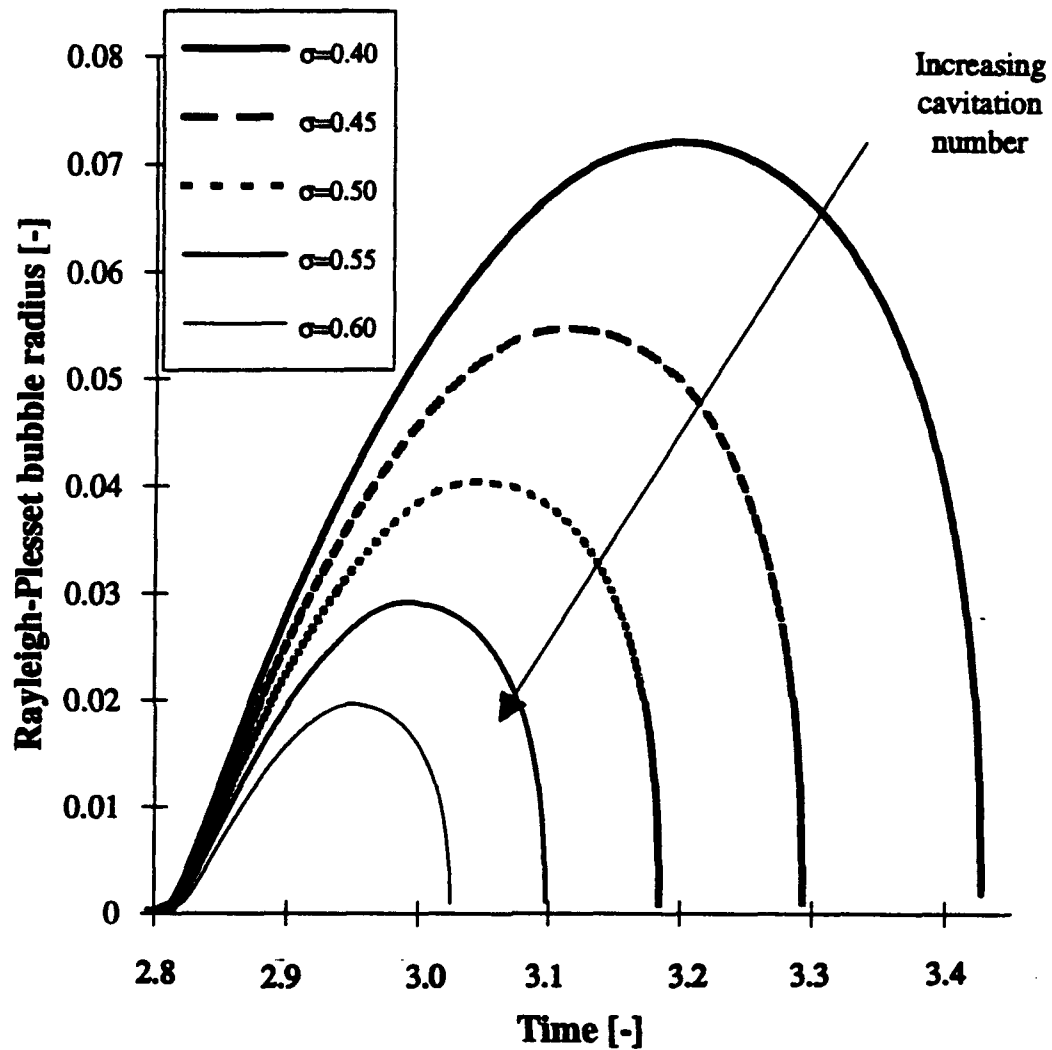


**Figure B.1 Rayleigh-Plesset bubble radius as a function of time**

The computed bubble base radius from the Rayleigh-Plesset spherical bubble model is shown as a function of time. The calculation uses the pressure distribution on the surface of the headform. Conditions shown are for  $We = 93 \times 10^4$ ,  $Re = 6.8 \times 10^6$  and for cavitation numbers ranging from  $\sigma = 0.40$  to  $\sigma = 0.60$ . The time origin  $\tau = 0$  corresponds to a nucleus position upstream of the headform at  $x_0 = -1$ .

## B.2 NUCLEUS STABILITY CRITERIA OVER HEADFORMS

A stable equilibrium state of the nucleus may be found by setting all the first and second time derivatives of the bubble radius to zero in the Rayleigh-Plesset equation B.2. The equilibrium radius  $r_e$  is thus given by

$$Cp_{\infty} + \sigma = -\frac{4}{r_e We} + \left( \sigma + \frac{4}{r_o We} \right) \left( \frac{r_o}{r_e} \right)^{3k}. \quad (B.4)$$

Solutions for this equation do not exist when the critical pressure coefficient drops below the value for which  $dr_e/dCp_{\infty} = \infty$ . Therefore, for pressures less than this critical value both the first and second time derivative of the bubble radius have to be of the same positive sign in equation B.2, indicating a bubble explosion. The limit of stability is thus given by the critical pressure

$$Cp_{\infty crit} = \frac{4}{3k} \frac{1-3k}{r_{e\_crit} We} - \sigma \quad (B.5)$$

with

$$r_{e\_crit} = r_o^{3k-1} \sqrt{\frac{3}{4} k (\sigma r_o We + 4)}. \quad (B.6)$$

The critical bubble equilibrium radius,  $r_{e\_crit}$ , was first identified by Blake (1949) and Neppiras and Noltingk (1951). The critical pressure coefficient,  $Cp_{\infty crit}$ , is often referred to as Blake's threshold pressure. If the minimum pressure coefficient along a streamline is below the Blake's critical pressure coefficient  $Cp_{min} \leq Cp_{\infty crit}$  the nucleus is bound to become unstable.

This criteria is useful to define a critical nucleus radius above which all nuclei will become unstable and explode. Using equations B.6 and B.4, the critical initial radius,  $r_{o\_crit}$ , is found as the solution of the following equation

$$r_{o\_crit}^{3k-1} (\sigma r_{o\_crit} We + 4) = \frac{4}{3k} \left( \frac{4}{3k} \frac{1-3k}{(Cp_{min} + \sigma) We} \right)^{3k-1}. \quad (B.7)$$

We note that Ceccio and Brennen (1991) observed that for the isothermal case ( $k=1$ ), a solution of this equation for the critical radius adheres fairly closely to the following expression

$$r_{o\_crit} \approx \frac{-\kappa}{We(Cp_{min} + \sigma)} \quad (B.8)$$

where the factor  $\kappa$  is close to unity. This expression can be easily derived if we assume that  $\sigma r_{o\_crit} We < 4$  which is the case for the smallest headform ( $D=5.08\text{cm}$ ) at most cavitation numbers, but becomes erroneous for the larger headforms.

In the case of the Schiebe headform, potential flow calculations (Z. Liu *et al.*, 1993) have shown that the minimum pressure decays as a function of the normal distance,  $\delta$ , to the headform as  $Cp_{min}(\delta) = Cp_{min} - 10\delta(Cp_{min} - 1)$ . Thus, using equation B.11 we find that

$$Cp_{min}(r_i) = Cp_{min} + 5r_i^2 \sqrt{1 - Cp_{min}} \quad (B.9)$$

Using Ceccio and Brennen's approximation (equation B.8) then yields

$$r_{i\_crit} \approx \sqrt{\frac{1}{5\sqrt{1 - Cp_{min}}} \left( \frac{-\kappa}{r_{o\_crit} We} - (Cp_{min} + \sigma) \right)} \quad (B.10)$$

This equation gives the critical initial streamtube radius within which a nucleus of minimum radius  $r_o$  will encounter low enough pressures to cause it to become unstable. In figure B.2 are presented solutions of this equation and are referred to as "Critical nucleus stability criteria" curves, for various cavitation numbers for the 5.08cm headform and  $U_\infty=11.5\text{m/s}$  ( $We = 93 \cdot 10^3$ ). Note that all these curves attain an asymptotic value as  $r_o$  becomes large. This value is independent of the Weber number and is given by  $r_{i\_crit\_max} = 0.4\sqrt{-(Cp_{min} + \sigma)}$ .

A great limitation of this critical radius theory comes from that fact that it assumes that the nucleus remains spherical until it becomes unstable and explodes. We will show that, in fact, for many nucleus initial upstream positions and initial radius values,  $r_o$ , the value of the critical radius,  $r_{e\_crit}$ , is larger than the distance of the nucleus pathline from

the headform. Consequently the nucleus is not allowed to grow spherically to the critical radius and the previous assumption is erroneous. Examine a streamline starting far upstream from the headform with an initial off-axis dimensionless radius  $r_i$ . From the continuity and Bernoulli equations, the dimensionless distance,  $\delta$ , between the streamline and the headform surface around the minimum pressure coefficient point is

$$\delta \approx \frac{r_i^2}{2\sqrt{1-Cp_{\min}}}. \quad (B.11)$$

Obviously the nucleus cannot remain spherical when its radius becomes larger than a fraction of its distance,  $\delta$ , to the headform. The maximum limiting case occurs when the nucleus would touch the surface of the headform, i.e., when  $\delta=r_{e\_crit}$ . Inserting this condition in equation B.11 yields critical values of initial streamline radii of

$$r_{i\_intersect}^2 = 2r_o\sqrt{1-Cp_{\min}}^{3k-1}\sqrt{\frac{3}{4}k(r_o\sigma We + 4)}. \quad (B.12)$$

For the case when  $r_i < r_{i\_intersect}$ , the nucleus stability theory becomes invalid because the nucleus would intersect the surface of the headform before it becomes unstable. We note that, for a given headform shape, this critical radius is only a function of the initial nucleus radius  $r_o$  and the product  $\sigma We$ . In figure B.2 are also presented the values of the critical initial off-axis radius,  $r_{i\_intersect}$ , as a function of the nucleus radius,  $r_o$ , for various values of  $\sigma We$ . These curves are referred to as the "Interaction with headform criteria" curves. The region under each one of these curves represents conditions for which a spherical nucleus would overlap the headform surface before it reaches its critical unstable radius.

Comparing the two sets of curves in figure B.2, we can see that the initial streamtube radius region within which the instability criteria does not apply can be substantial for certain conditions, especially for the low  $\sigma We$  values. We may consider, for example, the 5.08cm headform under the following conditions:  $\sigma=0.45$  and  $U_\infty=11.5\text{m/s}$  ( $\sigma We = 42 \cdot 10^3$ ). If we look at all the nuclei in the upstream flow field of

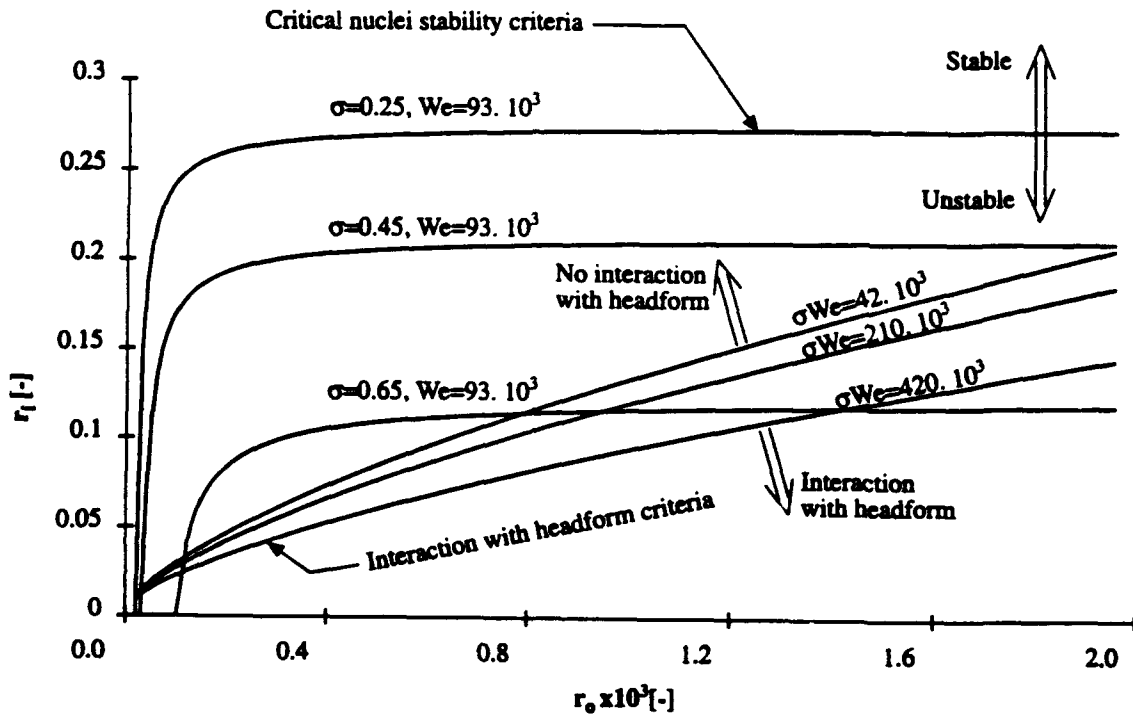


**Figure B.2 Initial streamtube radius versus critical equilibrium nucleus radius**

*The first set of curves represents the standard equilibrium solution to the critical unstable nucleus radius. The figure represents this nucleus radius versus the initial upstream radial distance it came from, thus indicating the minimum pressure it will encounter. The second set of curves indicates the limit of validity of this criteria due to interaction of the nucleus with the headform.*

size approximately  $R_0=25 \mu\text{m}$  that could become unstable and cavitate according to the spherical stability criteria (considering the flow rate in the streamtube to follow  $U_\infty \pi r_i^2$ ), 25% may not since they intersect the headform before becoming unstable. This value rises to 40% for nuclei of size  $R_0=50 \mu\text{m}$  and 100% of the nuclei larger than  $R_0=100 \mu\text{m}$  will intersect the headform. This headform interaction effect can therefore be significant in estimating event rates, particularly for the smaller headforms. Further study of the stability of deformed nucleus therefore needs to be done in order to take this effect into account.

### B.3 PRESSURE IMPULSE DURING COLLAPSE

The acoustic noise produced at a distance  $R$  by a spherical bubble of varying radius  $R(t)$ , may be modeled by the pressure induced by a monopole source of varying strength,  $Q(t)$ . The potential induced at a distance  $R$  by such a source is

$$\phi(t, R) = \frac{-Q}{4\pi R} = \frac{-\dot{R}R^2}{R}. \quad (\text{B.13})$$

From the unsteady Bernoulli equation, the solution for the pressure perturbation induced by the source is

$$P(t, R) - P_\infty = \frac{\rho}{R} (2R\dot{R}^2 + R^2\ddot{R}) - \frac{1}{2}\rho \left( \frac{\dot{R}R^2}{R^2} \right)^2. \quad (\text{B.14})$$

In a manner similar to equation B.2, using the length and time scale of the flow over the headform, it is possible to write this equation in the following dimensionless form

$$C_p(\tau, r) = - \left( \frac{r' r^2}{r^2} \right)^2 + \frac{2}{r} (2r\tau'^2 + r^2 r'') = \left( \frac{4r}{r} - \frac{r^4}{r^4} \right) r'^2 + \frac{2r^2 r''}{r}. \quad (\text{B.15})$$

Examining the pressure far from the bubble (neglecting the fourth order term in  $r/r$ ) we find that

$$C_p(\tau, r) = \frac{1}{2\pi r} \frac{d^2 v}{d\tau^2} = \frac{1}{2\pi r} \frac{dQ}{d\tau} \quad (\text{B.16})$$

where  $\nu$  is the dimensionless volume of the bubble and  $Q$  the dimensionless source strength ( $Q=Q/D^2U_\infty$ ).

The amplitudes of the acoustic pressure pulses generated from a collapsing bubble at a distance  $R$  can be quantified by defining the impulse,  $I(R)$ , as the integral of the instantaneous pressure perturbation, from the beginning of the collapse pulse to the moment when the pressure returns to its mean value. Thus

$$I(R) = \int_{\text{begin at } p=p_\infty}^{\text{end at } p=p_\infty} (P(t, R) - P_\infty) dt. \quad (B.17)$$

Consider the pressure seen at the center of the headform (thus roughly at a distance  $D/2$  from the collapsing bubble). The pressure at this location will be referred to as  $P_{\text{center}}$ . The importance of defining this pressure we become clear later since it is the one that is recorded by the hydrophone located in the center of the headform. We know from equation B.16 that the pressure perturbation decays inversely with the distance,  $r$ , to the bubble source. The pressure induced by the collapsing bubble at any point in the flow is thus related to the pressure in the center of the headform as

$$P(t, R) - P_\infty = \frac{D}{2R} (P_{\text{center}} - P_\infty). \quad (B.18)$$

The impulse at the center of the headform is then

$$I_{\text{center}} = \int_{\text{begin at } p=p_\infty}^{\text{end at } p=p_\infty} (P_{\text{center}}(t) - P_\infty) dt = \frac{2R}{D} I(R). \quad (B.19)$$

If we define the dimensionless pressure impulse,  $i(r)$ , as

$$i(r) = \int_{\text{begin at } Cp=0}^{\text{end at } Cp=0} Cp(\tau, r) d\tau \quad (B.20)$$

then we find that it relates to the dimensional impulse as

$$i(r) = \frac{2}{\rho U_\infty D} I(R) = \frac{1}{\rho U_\infty R} I_{\text{center}}. \quad (B.21)$$



To compare the noise signals from cavitation bubbles over different headform sizes, we may refer all the impulses to that which we would record at the center of the headform,  $R=D/2$ . This impulse will be referred to as the dimensionless center impulse, where

$$i_{\text{center}} = i(r = 0.5) = \frac{2}{\rho U_{\infty} D} I_{\text{center}}. \quad (\text{B.22})$$

Another way to compare signals over different headform sizes is to refer the recorded impulses to that which we would record at a unit radius  $R=1\text{m}$  from the cavitation noise source. This impulse will be referred to as the unit impulse, where

$$i_{\text{unit}} = i(r = 1/D) = \frac{1}{\rho U_{\infty}} I_{\text{center}}. \quad (\text{B.23})$$

This impulse has the unit of length, [m]. In the next section both of these impulses shall be used to analyze the noise signals recorded by the inner hydrophone.

In order to estimate theoretical values of these impulses, numerical calculations of the growth and collapse of bubbles were carried out using the same method as presented in section B.1. For these calculations, the time steps were chosen particularly small, such that the maximum radius change of the bubble per time step does not exceed  $1/10000^{\text{th}}$  of its current radius. For these calculations, variations of the Weber number, Reynolds number or initial nucleus radius,  $r_0$ , have shown little effect on the computation of the dimensionless center impulse. Numerical results for  $i_{\text{center}}$  are thus shown in figure B.3 for  $We = 93 \times 10^4$ ,  $Re = 6.8 \times 10^6$ ,  $r_0 = 1.9 \times 10^{-4}$ , and different cavitation numbers,  $\sigma$ .

As expected, the impulse increases with decreasing cavitation number. The reason for the small influence of  $We$ ,  $Re$  or  $r_0$  on the impulse can be explained as follows. From equation B.16, the impulse may be rewritten as

$$i_{\text{center}} = \int_{\text{begin at } Cp=0}^{\text{end at } Cp=0} Cp(\tau, r = 0.5) d\tau = \frac{1}{\pi} \frac{dv}{d\tau} \Big|_{\text{begin at } Cp=0}^{\text{end at } Cp=0} = 4r^2 \frac{dr}{d\tau} \Big|_{\text{begin at } Cp=0}^{\text{end at } Cp=0}. \quad (\text{B.24})$$

We observe from numerical calculations that the bubble growth velocity just after rebound has roughly the same magnitude as the collapse velocity (within 20%). Indeed, as the

radius of the bubble tends to zero during collapse ( $r \rightarrow 0$ ), the partial pressure of the gas term dominates all the other terms in the Rayleigh-Plesset equation B.2. Thus

$$\frac{d^2 r}{d\tau^2} \approx \frac{1}{2r} \left( \sigma + \frac{4}{r_0 We} \right) \left( \frac{r_0}{r} \right)^{3\gamma}. \quad (B.25)$$

It follows from equation B.25, that during rebound the second derivative of the bubble radius with time is mostly dependent on the radius of the bubble itself, thus yielding almost identical bubble collapse and growth rates. We note that in effect, the rebound velocity is slightly smaller than the collapse velocity by about 20% due to viscous dissipative effects.

Thus we have roughly

$$\begin{aligned} r|_{C_p=0 \text{ at rebound}} &\approx r|_{C_p=0 \text{ at collapse}} \\ \left. \frac{dr}{d\tau} \right|_{C_p=0 \text{ at rebound}} &\approx - \left. \frac{dr}{d\tau} \right|_{C_p=0 \text{ at collapse}} \end{aligned} \quad (B.26)$$

and therefore the impulse is mostly dependent on the collapse radius rate of change

$$i_{\text{center}} \approx 8r^2 \left. \frac{dr}{d\tau} \right|_{C_p=0 \text{ at collapse}}. \quad (B.27)$$

We also notice that the Weber number, Reynolds number and relative nucleus size  $r_0$  terms become quickly negligible in the Rayleigh-Plesset equation B.2 as the bubble explodes and grows beyond a few times its initial nucleus size. The radius rate of change of the bubble is thus fairly insensitive to these parameters during the growth and collapse phases. Therefore the theoretical dimensionless impulse  $i_{\text{center}}$  is mostly a function of the cavitation number and remains about the same for all headform sizes,  $D$ , or nucleus radius,  $R_0$ .

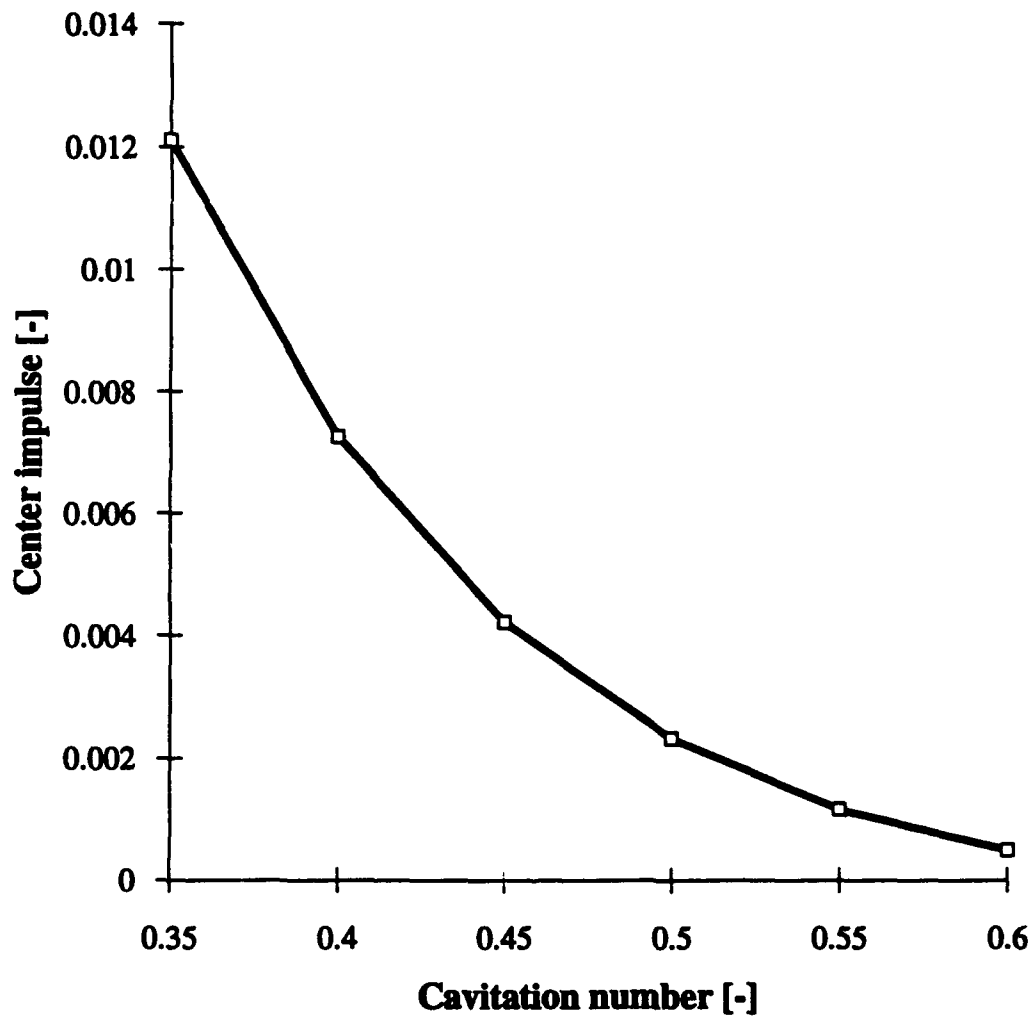


**Figure B.3** Dimensionless impulse,  $i_{center}$ , as a function of the cavitation number

*Calculated dimensionless center impulse,  $i_{center}$ , based on the Rayleigh-Plesset spherical bubble model.*

## **C. SCALING EXPERIMENTS IN THE LCC**

### **C.1 INTRODUCTION**

The experiments performed by Ceccio and Brennen (1989, 1991) and Kumar and Brennen (1991) over various headforms showed a great complexity in the fluid mechanics associated with traveling cavitation bubbles and need to be mentioned here. On the ITTC headform, when some of the larger bubbles pass the point of laminar separation they induce an attached "streak" of cavitation at the lateral extremes of the bubble as represented in figure C.1. These streaks stretch out as the bubble proceeds downstream, being anchored at one end to a point on the body surface along the laminar separation line and at the other end to the "wing-tips" of the bubble. The main bubble then collapses, leaving the two streaks it induced to persist longer.

The directional terminology used in describing the traveling bubble is as follows. The exterior surface of the bubble corresponds to the bubble side furthest from the headform surface. The interior of the bubble corresponds to the bubble surface exposed to the headform. The upstream side of the bubble is located in the upstream direction with respect to the uniform flow. This side is the side on which the streaks appear and is also referred to as the wake side or the trailing surface of the bubble. The downstream side is also referred to as the leading surface of the bubble.

One of the important consequences of these variations in the details of the collapse processes is the effect on the noise produced by a single cavitation event (Ceccio and Brennen, 1992; Kumar and Brennen, 1992). Bubble fission can produce several bubble collapses and therefore several acoustic pulses. Presumably this would also effect the cavitation damage potential of the flow. Kumar and Brennen (1991-1992) have further

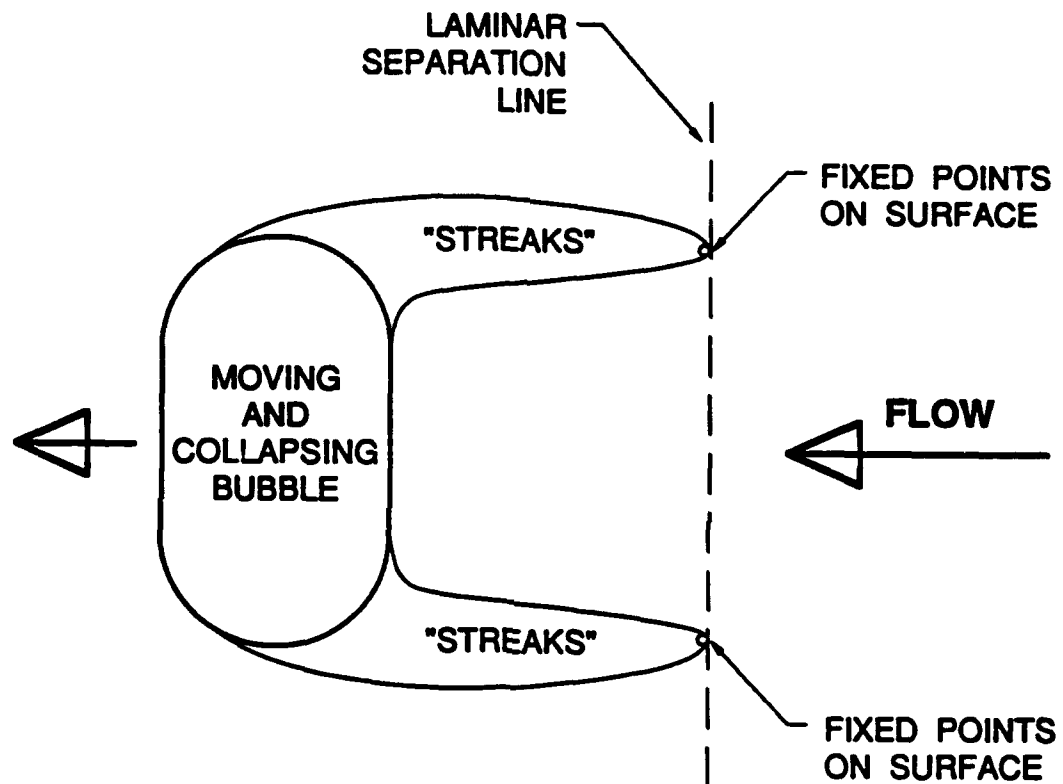


**Figure C.1 Schematic diagram of an attached traveling bubble**  
*This schematic shows the development of attached separation streaks shed in the wake of the traveling bubble.*

examined the statistical properties of the acoustical signals from individual cavitation bubbles on two different headforms in order to learn more about the bubble/flow interactions. They were also able to demonstrate a relationship between the number of cavitation events and the nuclei number distribution measured by holographic methods in the upstream flow.

We note that questions on the scaling of cavitation have been asked for many years but particularly in the aftermath of the ITTC comparative tests conducted by Lindgren and Johnsson (1966) who showed how disparate the appearance of cavitation was at different speeds, in different facilities and at different water "qualities". This characterization refers to the number of cavitation nuclei present in the water, where most of these nuclei usually consist of very small air bubbles in the range of 5 to 300 $\mu$ m. As O'Hern *et al.* (1985, 1988) have shown, the nuclei are similar in size distribution in most deaerated water tunnels and in the ocean. This causes one set of scaling questions since the ratio of body size to the nucleus size will change with the body size. The other set of scaling issues derives from the complex interactions between the bubbles and the flow close to the headform, where the flow is Reynolds number dependent. Scaling effects will thus be caused by the changes in both body size and tunnel velocity. In order to address this problem, the present experiments were conducted in the Large Cavitation Channel of the David Taylor Research Center in Memphis Tennessee, on geometrically similar Schiebe headforms which are 5.08, 25.4 and 50.8cm in diameter for speeds ranging up to 15m/s and for a range of cavitation numbers.

## **C.2 EXPERIMENTAL SETUP**

### **C.2.1 Large Cavitation Channel**

We were fortunate to have the opportunity to examine some cavitation scaling effects by conducting experiments in a new facility called the Large Cavitation Channel,

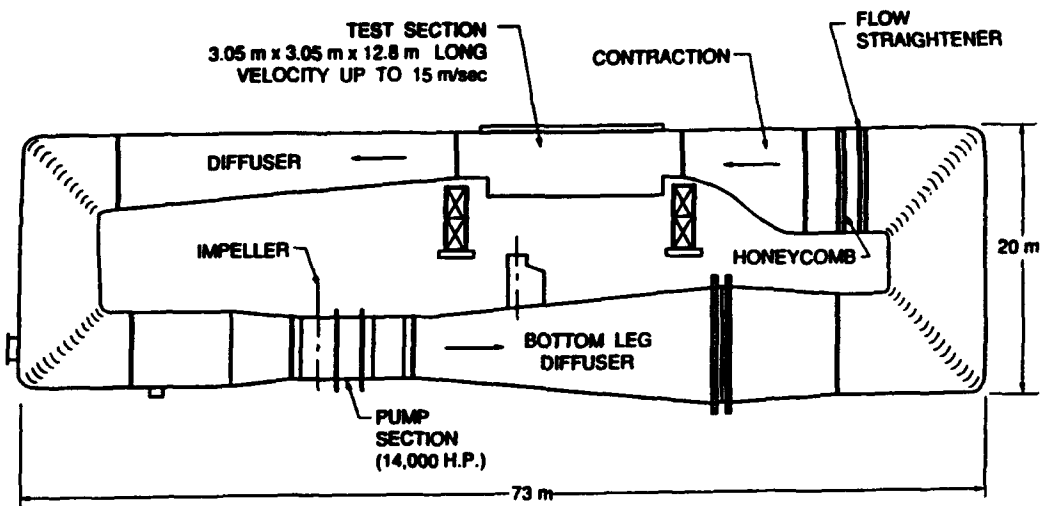
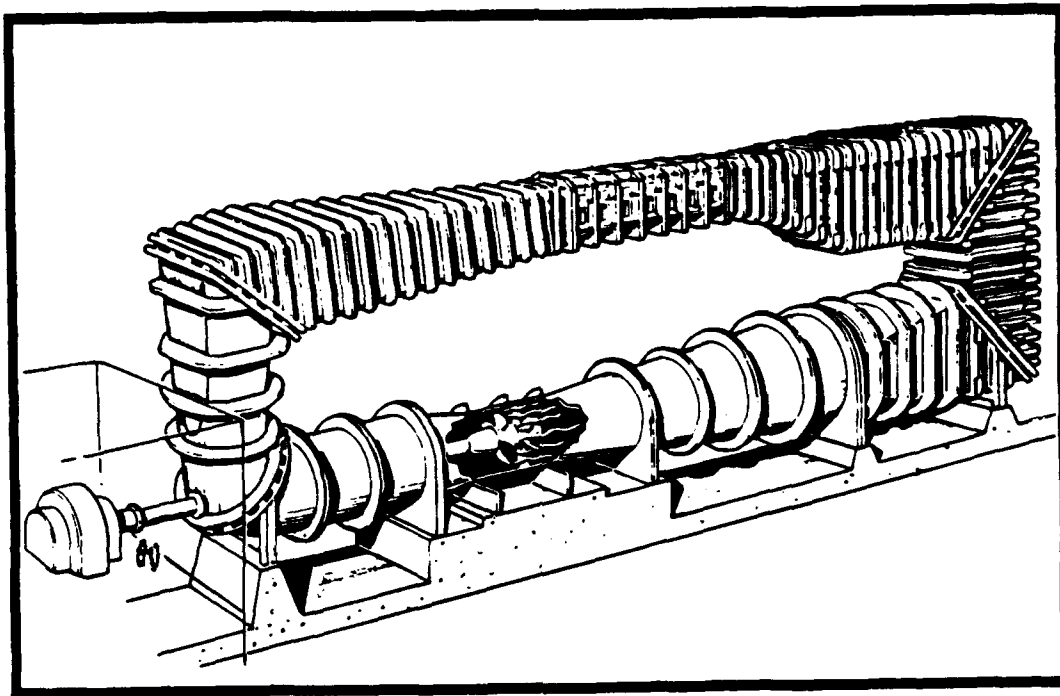


**Figure C.2 Schematic diagram of the Large Cavitation Channel**

*This figure shows the overall dimensions and setup of the LCC. Notice flat top and the asymmetric contraction upstream of the test section. The entire bottom half of the tunnel may be immersed in a pool for acoustical isolation.*

which has just been constructed for the David Taylor Research Center (Morgan, 1990). Briefly this facility is a very large water tunnel with a working section which is 3.05m x 3.05m in cross-section. It is capable of tunnel speeds above 15m/s and the pressure control allows operation at sufficiently low pressures in the working section to permit cavitation investigations. Polished lucite windows are located along the side walls of the test section and in the corners at the top and bottom. Figure C.2 shows a schematic of the water tunnel indicating the overall dimensions.

### **C.2.2 Headforms**

Three Schiebe headforms of diameter 5.08cm, 25.4cm and 50.8cm were machined out of solid blocks of clear lucite. The instrumentation used is identical for all three headforms and consists of a series of electrodes and an inner hydrophone. A second hydrophone was also placed in the 25.4cm headform. The interiors of the headforms were hollowed out in order to place the hydrophones in the center and as close as possible to the cavitation. The insides were then filled with water at atmospheric pressure. Lucite was chosen for its good acoustical match with water in addition to its electrically insulating properties required for the electrodes. Figure C.3 shows a schematic of the headform with its instrumentation. The dimensionless quantities represented are identical for all headforms. These headforms were mounted in the center of the working section using after-bodies and a supporting strut as shown in figure C.4.

### **C.2.3 Electrode bubble detection**

Silver epoxy electrodes were machined flush in the lucite headform as presented in figure C.3 and can be seen on the photographs of figure C.17. A pattern of alternating voltages is applied to the electrode pairs, and the electric current from each electrode is monitored. When a bubble passes over one of the electrodes, the impedance of the flow is altered, causing a drop in current (Ceccio 1989). Thirteen of these electrodes take the



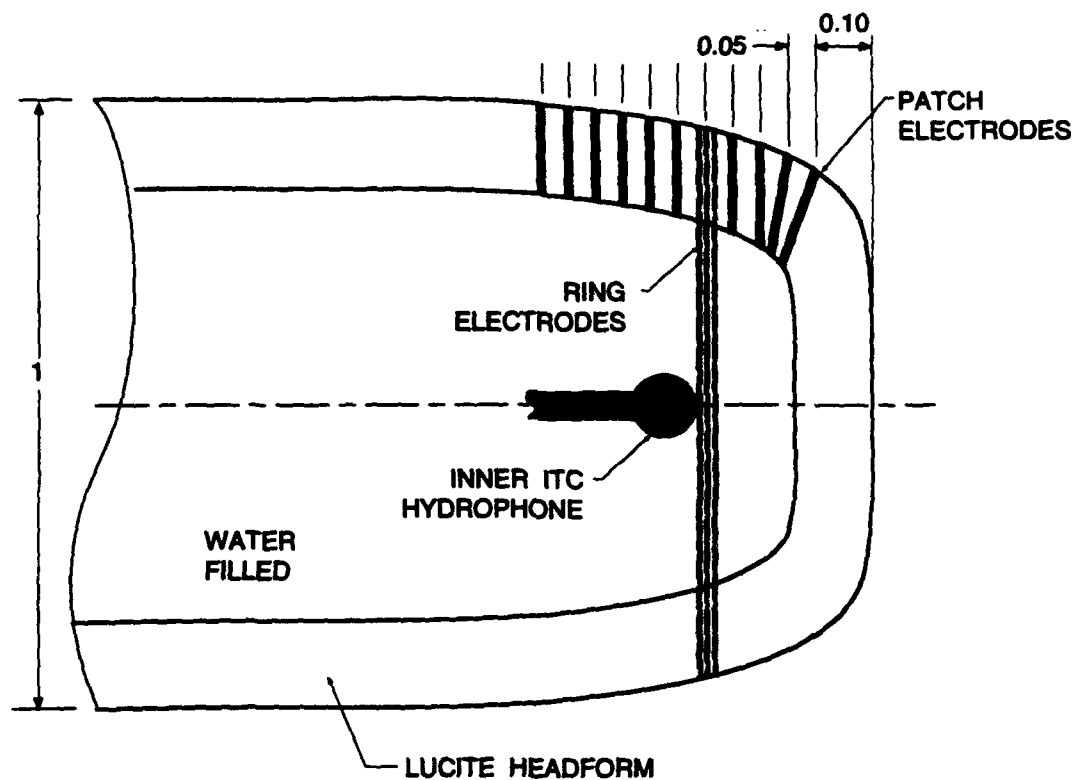


**Figure C.3 Schematic diagram of the headform**

*Presented here are the dimensionless locations of the electrodes and hydrophone. The same locations were used for all three headforms.*

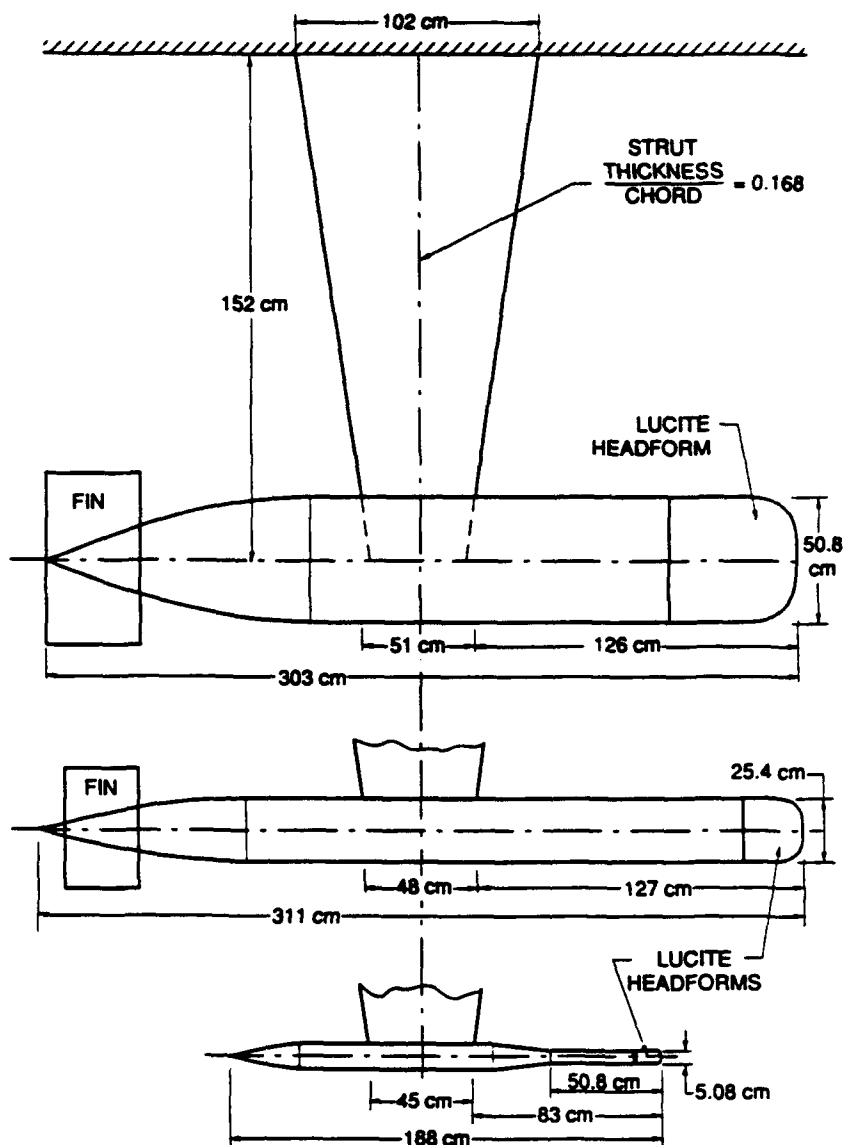


**Figure C.4 Schematic diagram of the three headform setup**

*Also shown are the after-bodies with stabilizing fins and supporting strut. The same strut was used for all three headforms, placing them in the tunnel centerline.*

form of small circular patches (about 1mm in diameter) at different axial locations. In addition, three ring electrodes covering the entire circumference of the body are installed at particular axial locations in order to measure the cavitation event rate over the entire headform. An electronic Schmitt trigger peak detector box connected to one of the electrodes allows us to detect the presence of a traveling bubble. The trigger pulse is then fed to both the digital recorders and to the photographic setup.

#### **C.2.4 High speed photography and flash**

Two cameras, triggered simultaneously, were set up in order to take flash pictures of individual cavitation bubbles at different angles and different enlargements. Four powerful EG&G model SS166 flash heads with SS162-165 energy storage racks were used. The film exposure time was of the flash duration and was measured to be about 30 $\mu$ s. Triggering can be done either manually or through a computer controlled lock-out system connected to the electrode peak detector signal. A variable delay unit was employed in order to take photographs of bubbles at various times after passing an electrode. The delay time can be adjusted by increments of 10 $\mu$ s and up to 10ms. In addition, a CCD video camera was focused on the top surface of the headform. The EG&G flash heads were used in strobing mode, synchronized with the video camera framing rate in order to make a video recording for each operating condition.

#### **C.2.5 Hydrophones**

An International Transducer Corporation hydrophone model ITC-1042 with a flat isotropic gain response of  $\pm 2$ dB out to 80kHz was installed inside each of the headforms. The center of the hydrophone was placed on the axisymmetric axis, one headform radius from the front stagnation point. In addition a Bruel & Kjaer 8103 hydrophone with similar performances was placed sideways inside the 25.4cm headform in order to record local noise signals. The 64 kbyte digital pressure signal acquisitions of the collapsing bubbles were made at a sampling rate of 1MHz with a 16 bit resolution. By filling the interior of

the headform with water, the intention was to provide a fairly reflection and reverberation free acoustic path between the cavitation and the hydrophone. Ceccio (1989) successfully checked this technique earlier by comparing the signals from a single cavitation event using hydrophones installed inside and outside the headform. In the present tests, a similar check was performed by comparing the internal hydrophone signals with those from two Sonatech STI-01-02 hydrophones (with a flat frequency response up to 100kHz). These STI hydrophones were mounted in a water-filled polyurethane encapsulation, flush in a recess in the side wall of the test section, one upstream and the other downstream from the headform. In addition, using each of the ITC and STI hydrophones in turn as a transmitter and a receiver over a range of frequency from 1kHz to 100kHz, it was possible to accomplish reciprocity type calibrations. Results of these calibrations are presented later in the thesis.

## **C.2.6 Water nuclei measurement**

### **C.2.6.a Susceptibility meter**

The David Taylor cavitation susceptibility meter (Shen and Gowing, 1984) was installed in the lower upstream part of the test section. Such devices cause the water to cavitate by pumping it through a venturi where it undergoes sufficiently low pressures. The cavitation number in the venturi can be adjusted by varying the flow rate through the venturi. Susceptibility measurements are made by counting the number of bubble cavitation events per volume of water passing through the venturi, over a range of cavitation numbers. In the present experiments the inlet tube is connected to a 5.08cm diameter hole in the test section tunnel wall. The flow then passes through the venturi, a variable speed pump, a flow-meter and is then exhausted back through another port hole to the LCC. The diameter of the venturi at the throat is 2mm. The flow rate through the venturi is regulated by varying the pump speed. The cavitation number in the venturi is calculated by measuring the flow velocity with the flow-meter and by monitoring the

pressure just upstream of the venturi nozzle using a Sensotec 430 pressure transducer. Individual cavitation events are counted by the means of a high frequency hydrophone (band-passed between 10 and 100kHz) located next to the venturi.

#### **C.2.6.b Particle Dynamics Analyzer**

A Dantec Particle Dynamics Analyzer was set up to measure the nuclei distribution about 3 meters upstream from the headform. This device is similar to a Laser Doppler Velocimeter but in addition uses measurements of the spatial distribution of light scattered by particles crossing the control volume. Phase information of light scattered at different angles by bubbles passing through the control volume is collected via three photomultipliers. The Bragg theory of light scattering through spherical micro-bubbles of different radii allows, in principle, to correlate this phase information with the actual size of the bubble. In our case the PDA optics had a focal length of 150cm which allowed the control volume to be located close to the tunnel centerline.

#### **C.2.6.c Dissolved air content**

Two bypass water lines connected to two Orbisphere type probes monitored the dissolved oxygen content. This value is then referred to percentages of dissolved air contents relative to atmospheric conditions at ambient temperatures,  $P_{air}$ . The dissolved oxygen content of the tunnel water was being varied by pumping the water through vertical deaeration tanks. Water temperature was also constantly monitored and recorded for each condition.

### **C.3 HYDROPHONE CALIBRATION**

Acoustic calibration was performed for both the internal hydrophone (ITC), mounted in the center of the Schiebe headforms and the outer hydrophone (STI-02), mounted on the upper side wall of the test section, just ahead of the headforms. In order to achieve consistent data comparisons, the same ITC hydrophone model was installed in

all three headforms. For the purpose of these calibrations, both hydrophones have no signal pre-amplification and are fed directly into the digital recorders. A spectrum analyzer has been used to measure the transfer function gain between the hydrophones at frequencies ranging from 3kHz to 100kHz. Both hydrophones were used as a receiver and as a transmitter, allowing us to perform reciprocity calibrations. Furthermore the specification curves supplied by the hydrophone manufacturers allow us to verify the voltage-to-pressure transfer gain between the hydrophones, in the following manner.

Using one of the hydrophones (hydrophone A) as a transmitter and the other (hydrophone B) as a receiver we may write the overall transfer function between the transmitted input voltage signal through A,  $V_{in}^A$ , and the received output voltage signal through B,  $V_{out}^B$ , as

$$V_{out}^B(f) = H_{trans}^A(f) \cdot M(f) \cdot H_{rec}^B(f) \cdot V_{in}^A(f) \quad (C.1)$$

where  $H_{rec}^B(f)$  is the transfer function of hydrophone B in the receiving mode which includes the pressure to voltage signal conversion [dB re 1Volt/ $\mu$ Pa]. The transfer function of hydrophone A in the transmitting mode is given by  $H_{trans}^A(f)$  which includes the voltage to pressure signal conversion [dB re 1m- $\mu$ Pa/Volt]. Finally  $M(f)$  is the medium transfer function between hydrophones A and B. This term includes the influence of the water between both hydrophones and the influence of the tunnel setup including the headform and its supporting structure. The transmitted voltage signals were obtained for frequencies between 3kHz to 100KHz by frequency increments of one third octave. All the input and output voltage measurements are given in dB relative to 1 Volt. Reciprocity test in the STI to ITC direction and in the ITC to STI direction were performed for all three headforms. The table in figure C.5 presents the data from these calibration tests.

For each headform we may write the following two reciprocal transfer function equations

$$\begin{aligned} V_{out}^{ITC}(f) &= H_{trans}^{STI}(f) \cdot M(f) \cdot H_{rec}^{ITC}(f) \cdot V_{in}^{STI}(f) \\ V_{out}^{STI}(f) &= H_{trans}^{ITC}(f) \cdot M(f) \cdot H_{rec}^{STI}(f) \cdot V_{in}^{ITC}(f) \end{aligned} \quad (C.2)$$

f (kHz)	Hydrophone calibrations dB re 1V/mPa				D=5.08cm dB re 1V/m				D=25.4cm dB re 1V/m				D=50.8cm dB re 1V/m			
	H <sub>rec</sub> dB	H <sub>trans</sub> dB	H <sub>rec</sub> dB	H <sub>trans</sub> dB	V <sub>in</sub> dB	V <sub>out</sub> dB	V <sub>in</sub> dB	V <sub>out</sub> dB	V <sub>in</sub> dB	V <sub>out</sub> dB	V <sub>in</sub> dB	V <sub>out</sub> dB	V <sub>in</sub> dB	V <sub>out</sub> dB	V <sub>in</sub> dB	V <sub>out</sub> dB
3.15	-199.5				10.6	-110.5			10.7	-118			10.6	-113.7		
4	-199.5				10.6	-110.5			10.7	-105.6			10.6	-112.4		
5	-199.5				10.6	-107.4			10.7	-108.8			10.5	-115		
6.3	-199.5				10.6	-102.2			10.7	-89.3	10.4	-111.6	10.4	-103.4		
8	-199.5				10.6	-100.8			10.7	-89.3	10.2	-111.6	10.3	-104.1		
10	-200	114	-200.8		10.5	-98.6			10.8	-92	10.6	-101.9	10.7	-97		
12.5	-200.5	117	-201		10.5	-91.9			10.9	-76	10.5	-97	10.7	-87.7		
14	-201	119	-201		10.4	-91.8			11	-79	10.4	-93.5	10.8	-81.5		
16	-201.5	121	-201.2		10.5	-95			11.1	-81.8	10.5	-91	10.7	-81.8		
20	-202.2	123.5	-201.5		10.7	-101.5			11.2	-74	10.6	-89.5	11.2	-75.3		
25	-203	127	-204		10.7	-88			11.6	-79.7	10.6	-82.4	11.5	-73.3		
31.5	-203.2	130.8	-208.5		10.7	-79.8			13.3	-66	10.5	-81.9	11.8	-75.5		
40	-203	135	-208		10.6	-71.5			10.2	-75.9	10.7	-84.1	10.2	-75		
50	-202.6	140	-212		10.6	-85.7			7.9	-75.5	10.6	-75.1	7.8	-66.3		
63	-202	146	-213		10.4	-78.4			4.9	-76.8	10.4	-81.4	4.9	-78.1		
80	-200.2	149	-213		9.6	-72			5	-56	9.8	-72.8	3.7	-72		
100	-202.2	145	-213		7.6	-76.3			4.9	-69.5	7.9	-69.5	5.2	-66.7		

**Figure C.5 Hydrophone calibration results**

For each headform the input and output voltage is shown in dB re 1V/m using each hydrophone as a transmitter and a receiver. The positive dB values correspond to the transmitted signal,  $V_{out}$ , and the negative dB values to the received signal,  $V_{in}$ . Also shown in the first three columns are the manufacturer hydrophone specifications.

Dividing the transmitted voltage signal (hydrophone A) by the received signal (hydrophone B) yields the overall transfer function gain,  $G^{A \rightarrow B}(f)$ . This gain includes all effects from one end of the hydrophone lead to the other, for signals transmitted in both directions. Thus

$$\begin{aligned} G^{STI \rightarrow ITC}(f) &= H_{trans}^{STI}(f) \cdot M(f) \cdot H_{rec}^{ITC}(f) \\ G^{ITC \rightarrow STI}(f) &= H_{trans}^{ITC}(f) \cdot M(f) \cdot H_{rec}^{STI}(f) \end{aligned} \quad (C.3)$$

Both of these transfer function gains are presented in figure C.6 as a function of frequency, for all three headforms.

A system is shown to be reciprocal if the overall transfer function from hydrophone A to B can be scaled with the overall transfer function from B to A, over the entire frequency range. This condition has to be met in the present experiment since the hydrophones and the medium impedance are all known to be reciprocal (Albers 1902).

Thus we should find that

$$G^{STI \rightarrow ITC}(f) / G^{ITC \rightarrow STI}(f) = C \quad (C.4)$$

where C is a constant independent of the frequency. Figure C.7 presents this theoretical constant value, C, for the frequency range between 3kHz to 100kHz. We observe from this figure the flat shape of the curves over the measured frequency range for all three headforms. This constant value C is about -9dB with a noise measurement less than  $\pm 5$ dB. Reciprocity calibration has therefore proven successful with a  $\pm 5$ dB noise level. This noise level will thus be representative for the cavitation noise data presented in a later section.

In addition to reciprocity, the hydrophones calibration transfer functions,  $H(f)$ , [ $\mu$ Pa to Volts] supplied by the hydrophone manufacturers can be verified in the following way. Among the hydrophone transfer functions supplied are the ITC transfer functions in both the transmitter and receiver mode ( $H_{trans}^{ITC}(f)$  and  $H_{rec}^{ITC}(f)$ ) and the STI transfer



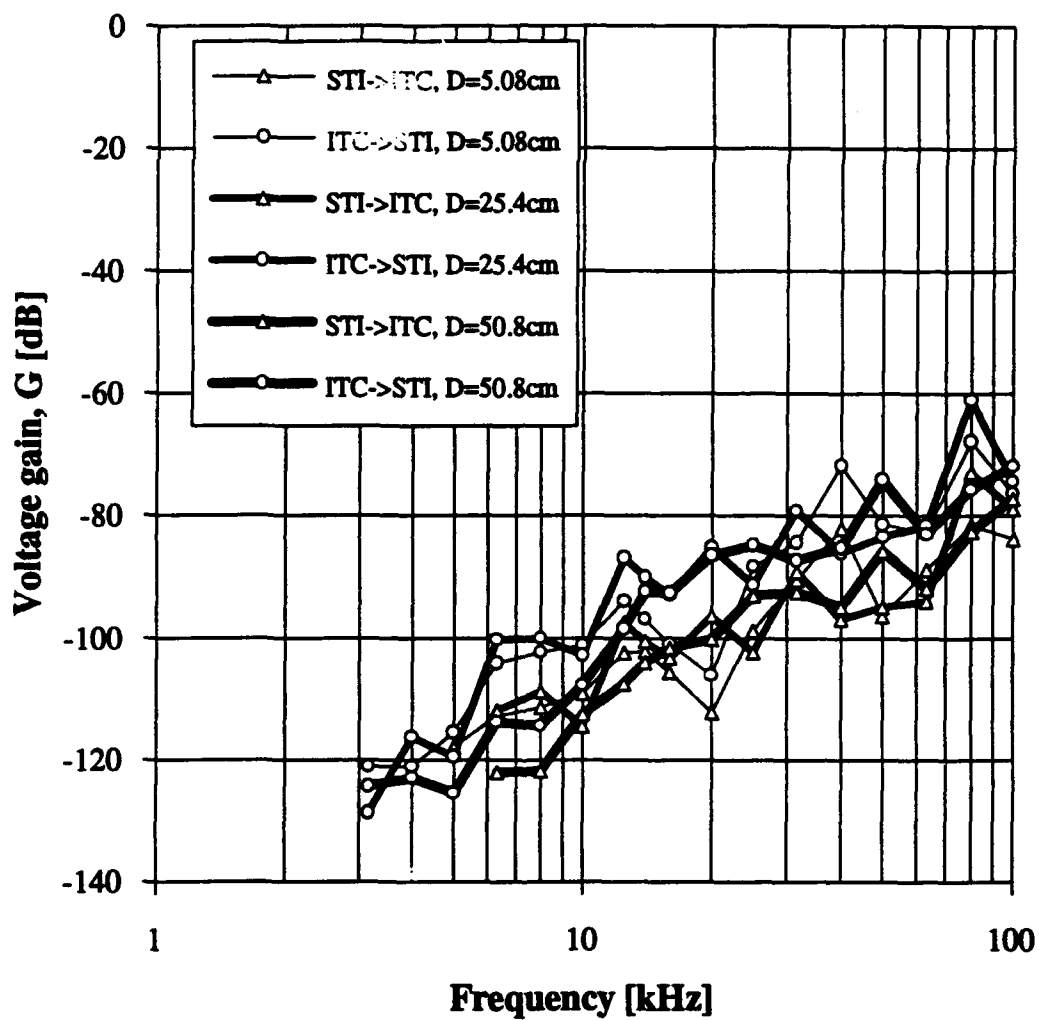


**Figure C.6 Voltage gain, G, between hydrophones**

*The gains are shown as a function of the frequencies measured. Gains are shown in dB from the ITC to the STI and from the STI to the ITC hydrophones for all three headforms.*

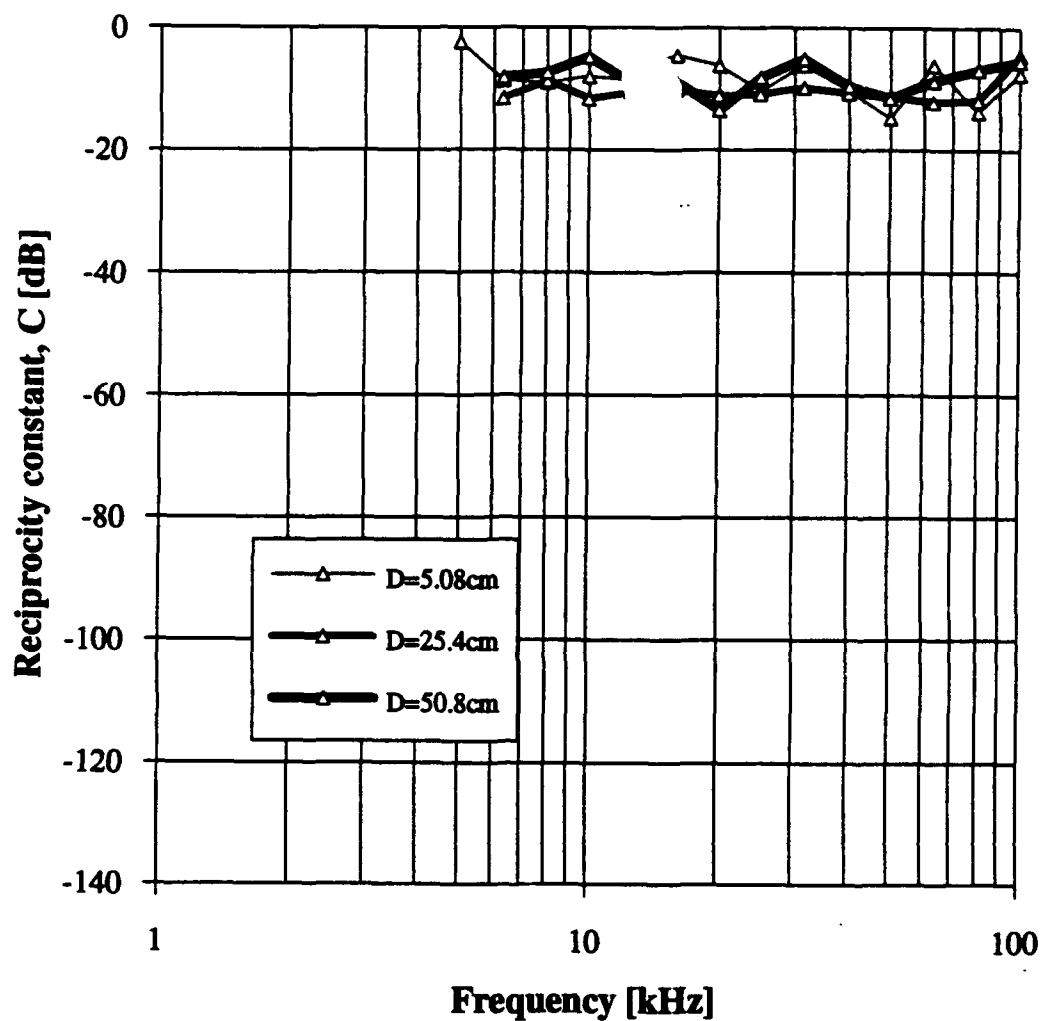


**Figure C.7 Reciprocity test between the hydrophones**

*The system is said to be reciprocal if the reciprocity constant  $C$  is independent of frequency. This figure shows a reciprocal constant value  $C \approx -9$  dB with a  $\pm 5$  dB noise level over this frequency range.*

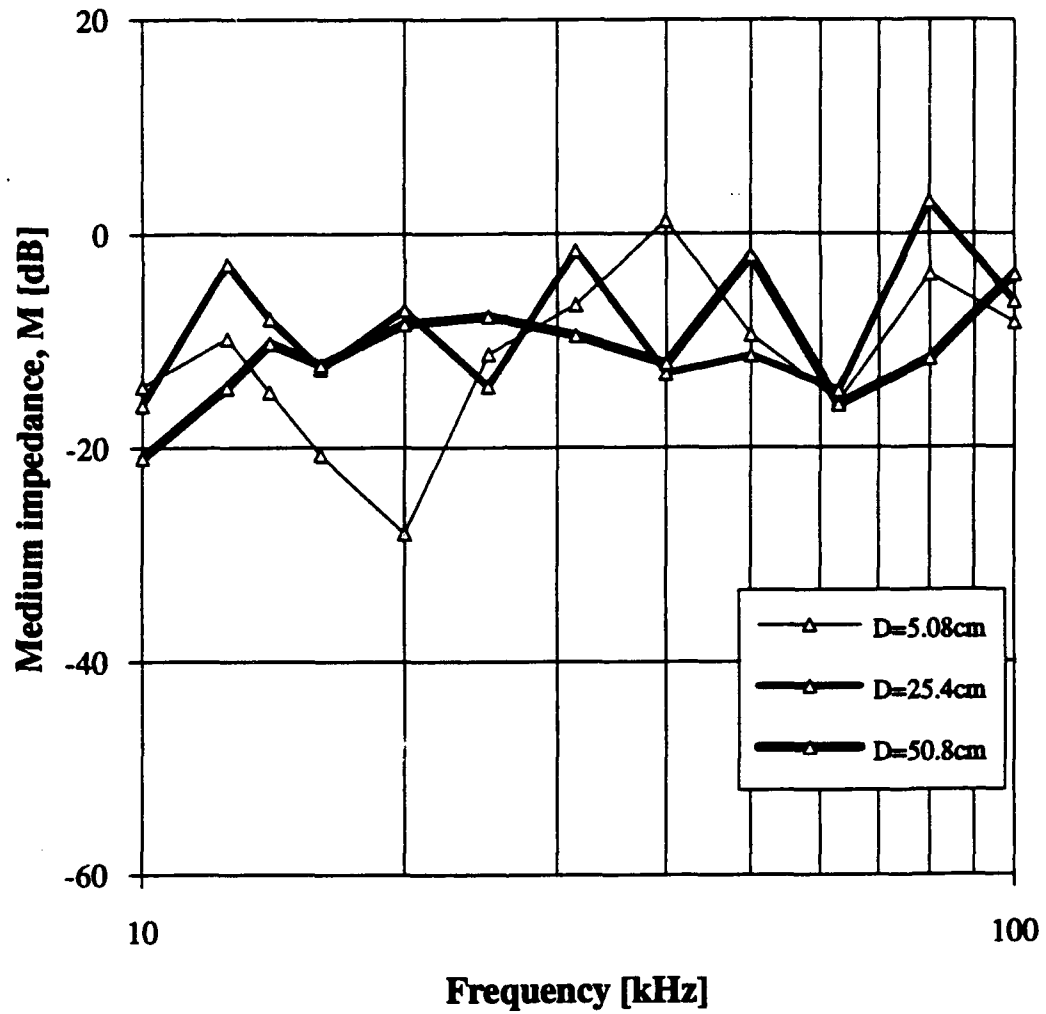


**Figure C.8 Medium acoustic impedance,  $M(f)$**   
*The medium acoustic impedance is shown as a function of frequency, for all three headforms.*

function in receiver mode ( $H_{rec}^{STI}(f)$ ). These functions are summarized in the table in figure C.5 for discrete frequencies. From equation C.2 we are able to determine the medium acoustic impedance as

$$M(f) = \frac{V_{out}^{STI}(f)}{H_{trans}^{ITC}(f) \cdot H_{rec}^{STI}(f) \cdot V_{in}^{ITC}(f)} \quad (C.5)$$

where all the hydrophone transfer functions are known. Figure C.8 shows the values of  $M(f)$  for all three headforms for frequencies up to 100kHz.

We notice that all the data points have a value of about -10dB with a noise level of about  $\pm 8$ dB. This impedance appears roughly the same for all the three headform configurations, indicating that the presence of the lucite headform and the different afterbodies do not have a significant impact on the acoustical properties of the tunnel. A theoretical value of  $M(f)$  may be estimated by assuming that the medium consists of water whose impedance is independent of frequency for this frequency range (Albers, 1902, Coates, 1989) and whose point source noise transfer gain decreases as  $1/R$ , where  $R$  is the distance between the two hydrophones (as in equation B.16). Knowing that distance for the three different headform setups, we find the following theoretical values of  $M$ .

Headform diameter	Distance between ITC and STI	Theoretical medium impedance
D=5.08cm	R=2.56m	M=-8.18dB
D=25.4cm	R=2.31m	M=-7.28dB
D=50.8cm	R=2.44m	M=-7.75dB

We observe that theoretical values of  $M$  are close to the average -10dB medium value obtained from figure C.8. This agreement therefore validates the calibration curves  $H_{trans}^{ITC}(f)$  and  $H_{rec}^{STI}(f)$  given by the manufacturers within an overall measurement noise of about  $\pm 8$ dB. We note that this  $\pm 8$ dB noise level is also that given by the frequency

response curve of the STI hydrophone and therefore probably originates mostly from that hydrophone. The inner ITC hydrophone transfer function gain given is said to be accurate to  $\pm 2\text{dB}$ . The conversion of the recorded acoustical cavitation signals from Volts to Pascals using the ITC manufacturer calibration curves should therefore be somewhat accurate (within frequencies up to  $100\text{kHz}$ )

## C.4 EXPERIMENTAL ANALYSIS

### C.4.1 Test conditions

All three headforms ( $D=50.8\text{cm}$ ,  $D=25.4\text{cm}$  and  $D=5.08\text{cm}$ ) were tested for similar conditions. The test matrix included the three dissolved air contents ( $P_{\text{air}}=80\%$ ,  $P_{\text{air}}=50\%$  and  $P_{\text{air}}=30\%$ ) and three velocities ( $U_{\infty}=9\text{m/s}$ ,  $U_{\infty}=11.5\text{m/s}$  and  $U_{\infty}=15\text{m/s}$ ). Combined effect of the headform size and flow velocity thus allowed a Reynolds number range from  $Re=0.54 \times 10^6$  to  $Re=9.41 \times 10^6$ . For each of these conditions about five cavitation numbers were investigated, ranging from bubble inception to fully attached cavitation.

### C.4.2 Cavitation inception data

Figure C.9 presents the observed cavitation inception numbers,  $\sigma_i$ , as a function of the headform diameter,  $D$ , tunnel velocity,  $U_{\infty}$ , and dissolved air content,  $P_{\text{air}}$ . Inception was based on an arbitrarily chosen event rate of about 50 cavitation events per second. The events were detected by means of the first upstream flush-mounted patch electrode, the current from which was moderated by the presence of a bubble (Ceccio and Brennen, 1989-1991).

The trends in figure C.9 are fairly clear. All the curves can be seen to have an asymptote value equal to the magnitude of the minimum pressure coefficient on the surface of the headform ( $C_{p_{\min}} = -0.78$ ). The inception number increases with increasing

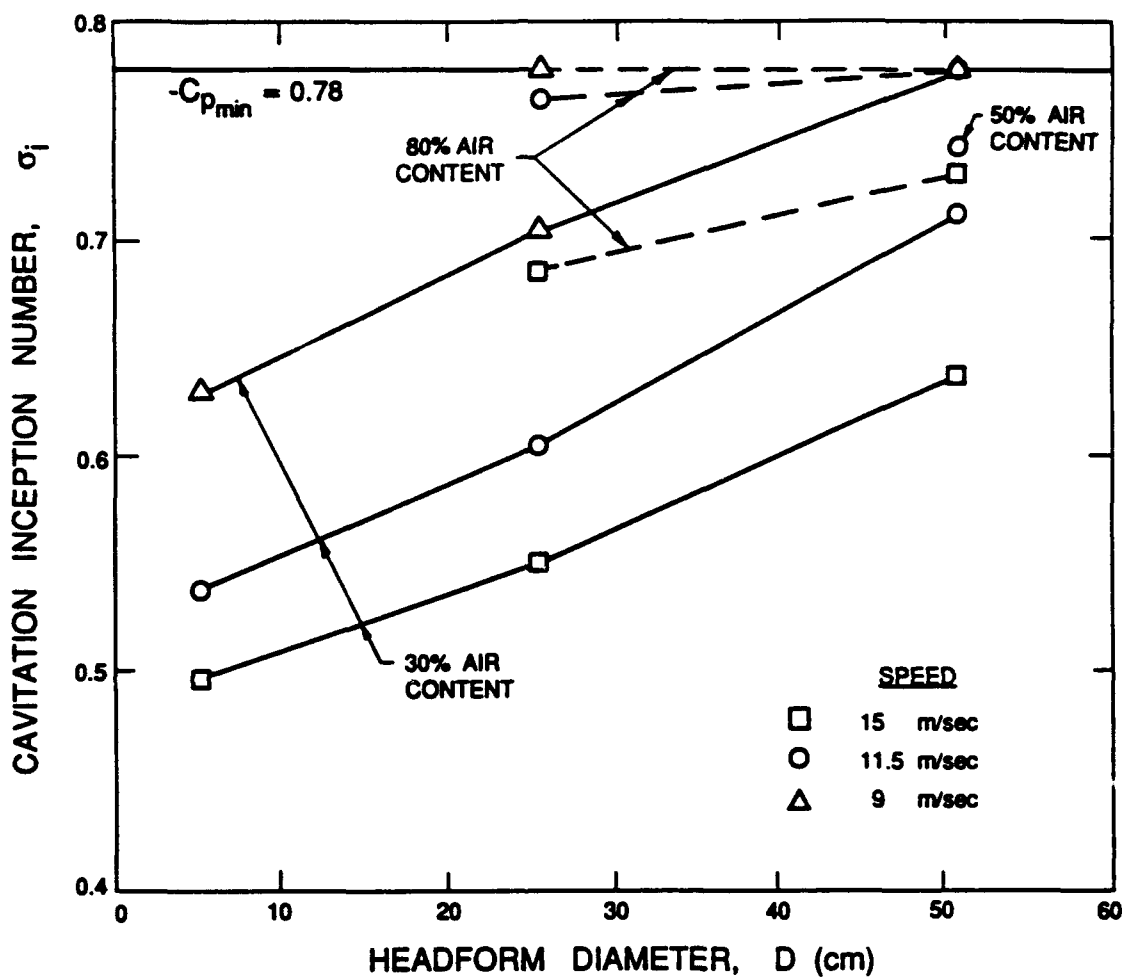


**Figure C.9 Cavitation inception numbers  $\sigma_i$**   
*Data shows measurements for all velocities, headform diameters and air contents.*

headform size. This headform size effect is a consequence of the fact that the flow rate of water passing through the low pressure region increases with larger headforms. More nuclei are thus susceptible to initiate cavitation and therefore, for a specific event rate, the value of  $\sigma_i$  is larger. The values of  $\sigma_i$  also increase with an increase in air content for a similar reason, namely more nuclei at the larger air contents. In order to illustrate the important difference in cavitation inception and event rate scaling effects with headform size, we contrast in figure C.10 the cavitation patterns over the three headforms for identical cavitation conditions. This figure shows photographs of all three headforms scaled to the same relative size, for the same cavitation number,  $\sigma=0.51$ , the same dissolved gas content,  $P_{air}=30\%$ , and the same flow velocity,  $U_\infty=11.5\text{m/s}$ .

We note from figure C.9 that these conditions correspond to inception cavitation conditions on the smallest headform, and are thus conditions where we very occasionally observe a traveling bubble. Figure C.10 shows one of these bubbles on the smallest headform. In contrast, on the 25.4cm headform we already observe the presence of bubbles and patch type cavities. Finally, on the 50.8cm headform, for the same cavitation conditions, we observe quite extensive cavitation patterns. Scaling effects with headform size are therefore very significant. Figure C.9 also demonstrates that the cavitation inception number increases with decreasing tunnel velocity. This effect is not so readily explained. However it is clear that in order to achieve the same cavitation number at a lower velocity one requires a lower tunnel pressure. It may therefore be that the nuclei concentration in the tunnel increases considerably with decreasing operating pressure. Hamilton *et al.* (1982) had also observed similar trends over 5.08cm headforms with increasing free stream flow velocities and had also attributed this effect to the decrease in tunnel velocity. They also found incipient cavitation numbers which were substantially higher than the ones presented here ( $\sigma_i \approx 1.1$ ). Billet and Holl (1979) had observed

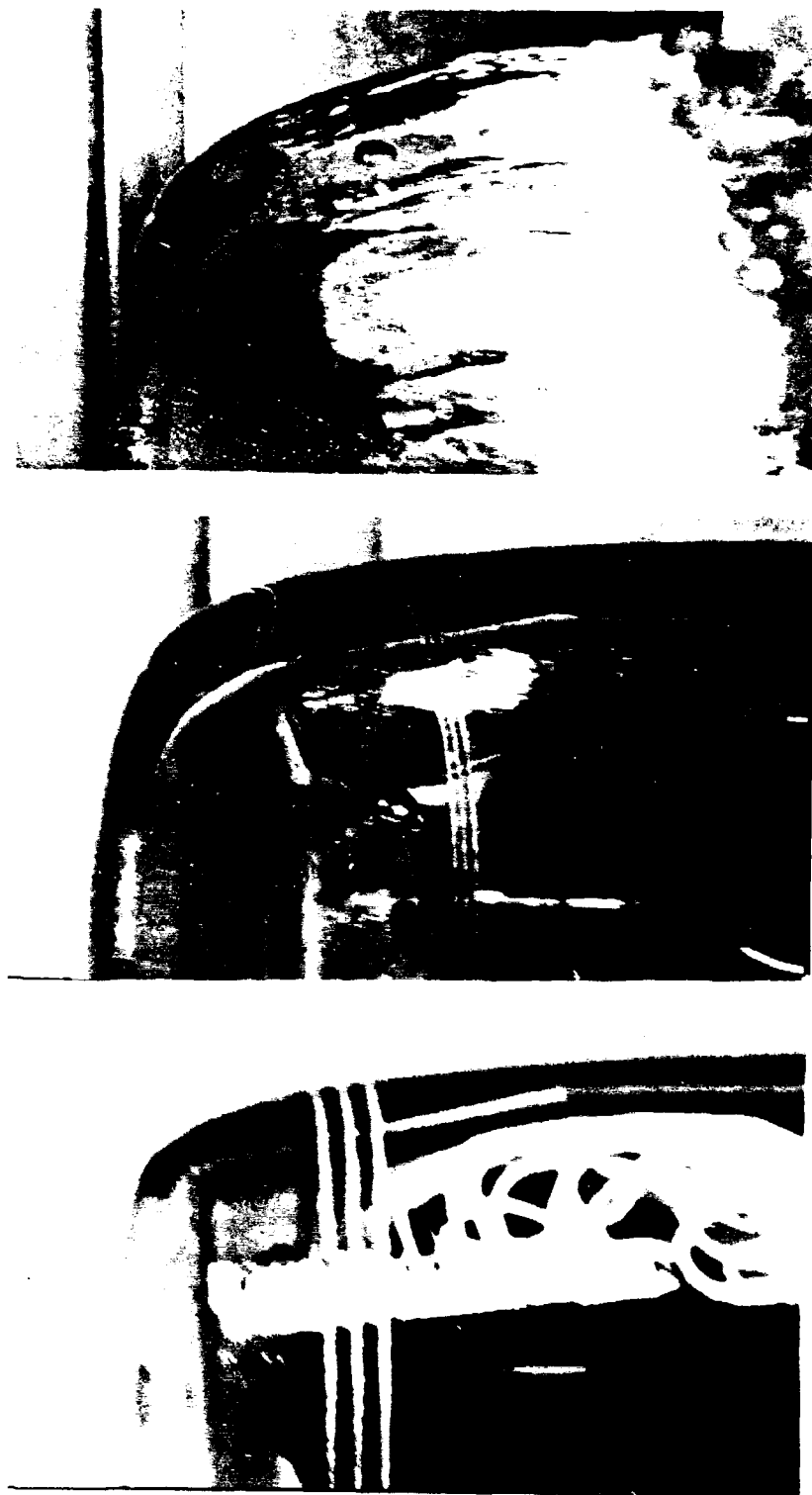


**Figure C.10 Cavitation photographs over all three headforms**  
*All three headforms are presented for identical cavitation conditions:  $P_{air}=30\%$ ,  $\sigma=0.51$ ,  $U_{\infty}=11.5\text{m/s}$ . Scaled to the same relative size are presented, from top to bottom,  $D=50.8\text{cm}$ ,  $D=25.4\text{cm}$ ,  $D=5.08\text{cm}$ .*



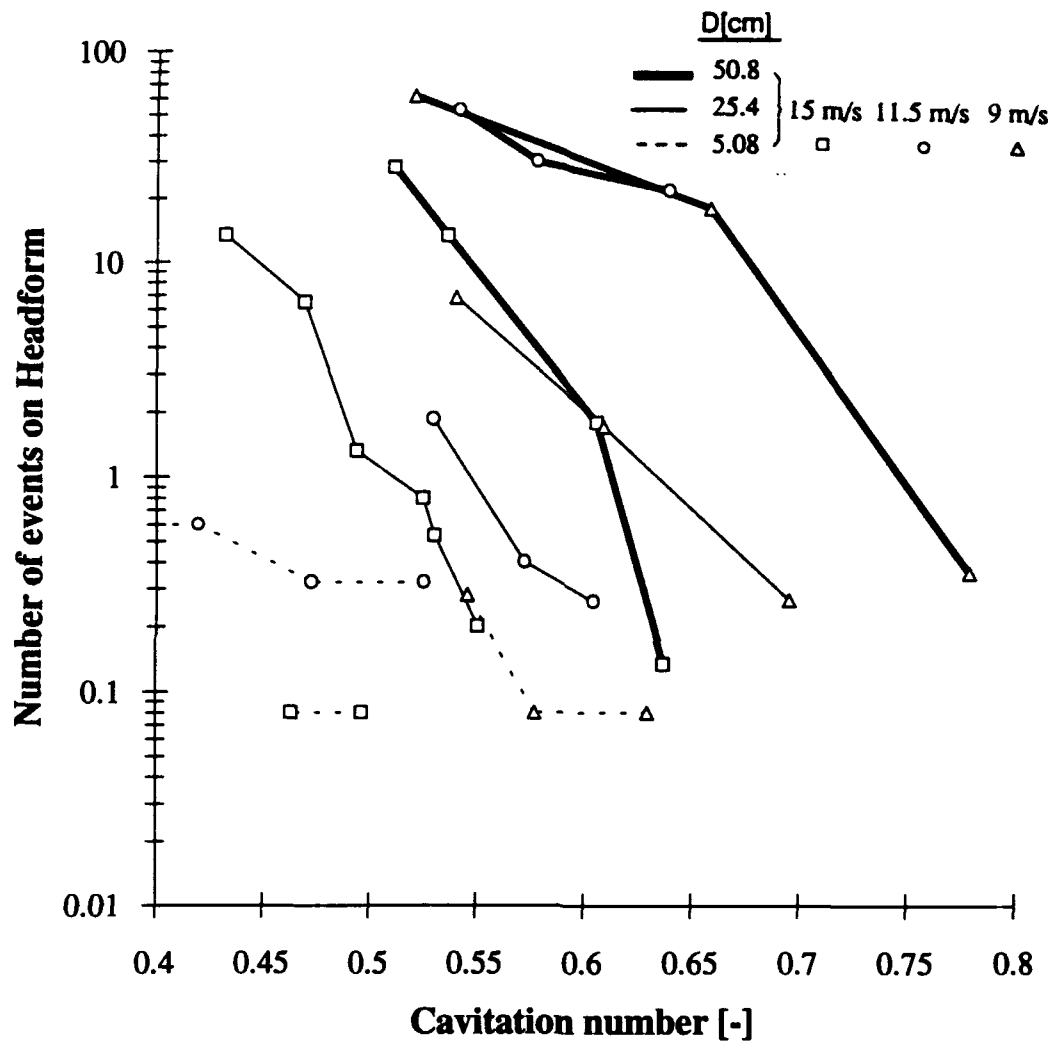


**Figure C.11 Average number of observable events on the headform**  
*Data shows measurements for all velocities and headform diameters as a function of the cavitation number.*

desinent cavitation numbers that were very close to the ones presented here (around 0.6) for different air contents of 3ppm and 9ppm. Higher air contents also yielded higher desinent cavitation numbers.

#### **C.4.3 Event rate observations**

Both the photographs and the video tapes were analyzed in order to explore the variations in the cavitation event rates with headform size and tunnel velocity. The event rates were evaluated by counting the number of individual bubbles (or events) observable in a single frame and averaging this number over many frames. This allowed construction of figure C.11 in which the average number of observable events is plotted against the cavitation number,  $\sigma$ , for each of three velocities (9, 11.5 and 15m/s) for the three headforms (this data is for 30% dissolved air content).

Not surprisingly, the number of events increases with decreasing cavitation number and with increasing headform size. Not so predictable is the tendency for the number of events to decrease with increasing speed. The data on the number of events may be converted to cavitation event rates using bubble lifetimes obtained from the knowledge of the local velocity of the bubble over the headform (using the panel method potential flow calculations) and the measured locations of bubble appearance and collapse (presented later in the thesis in figures C.21 and C.20 as a function of  $\sigma$ ). The resulting event rate data for 30% dissolved oxygen content is presented in figure C.12. It is clear that this is consistent with the cavitation inception data of figure C.9 given the selected criterion of 50 events/sec.

As previously stated, one of the purposes of the present investigations was to demonstrate the connection between the event rate (and the inception number) and the nuclei number distribution. It is instructive to present the event rate data of figure C.12 in the following modified form. Let us estimate that all the nuclei which pass through an

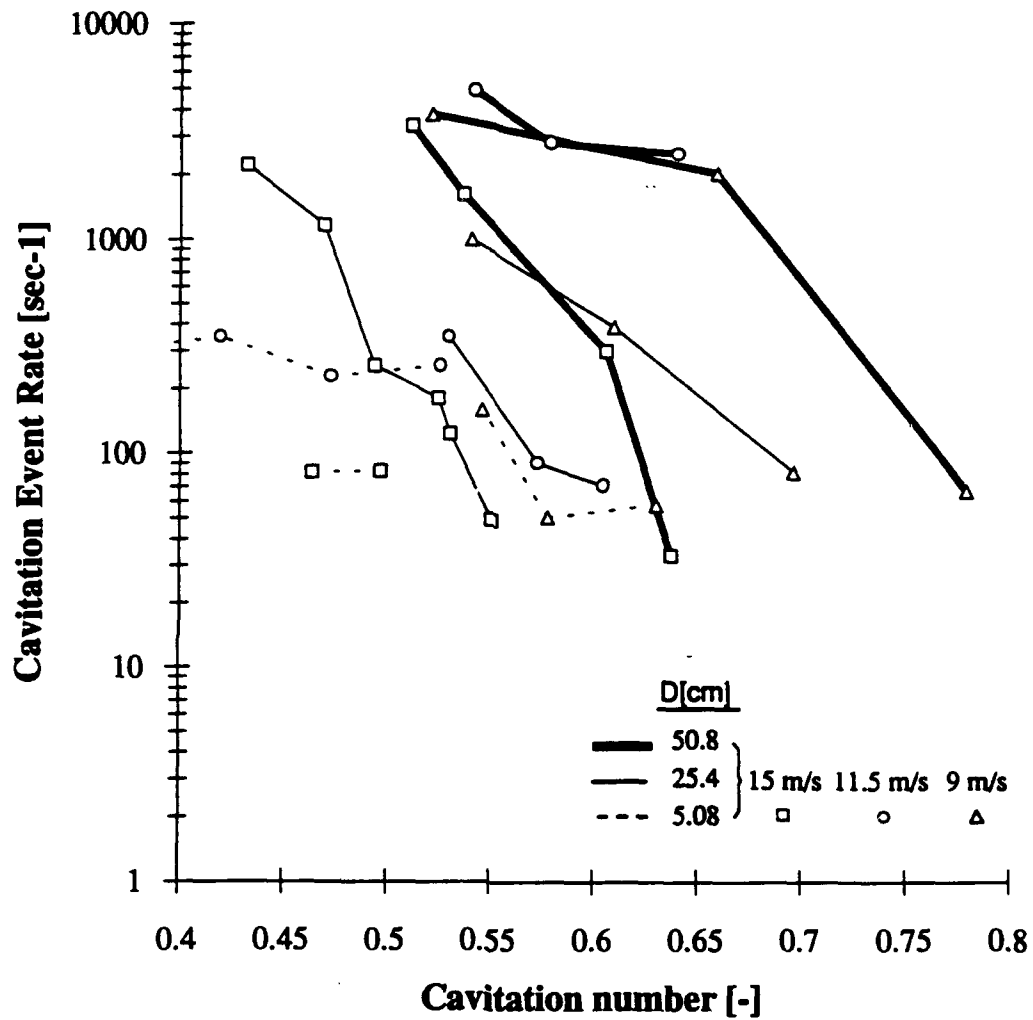


**Figure C.12 Cavitation event rate as a function of the cavitation number**  
*Data shows measurements for all velocities and headform diameters.*

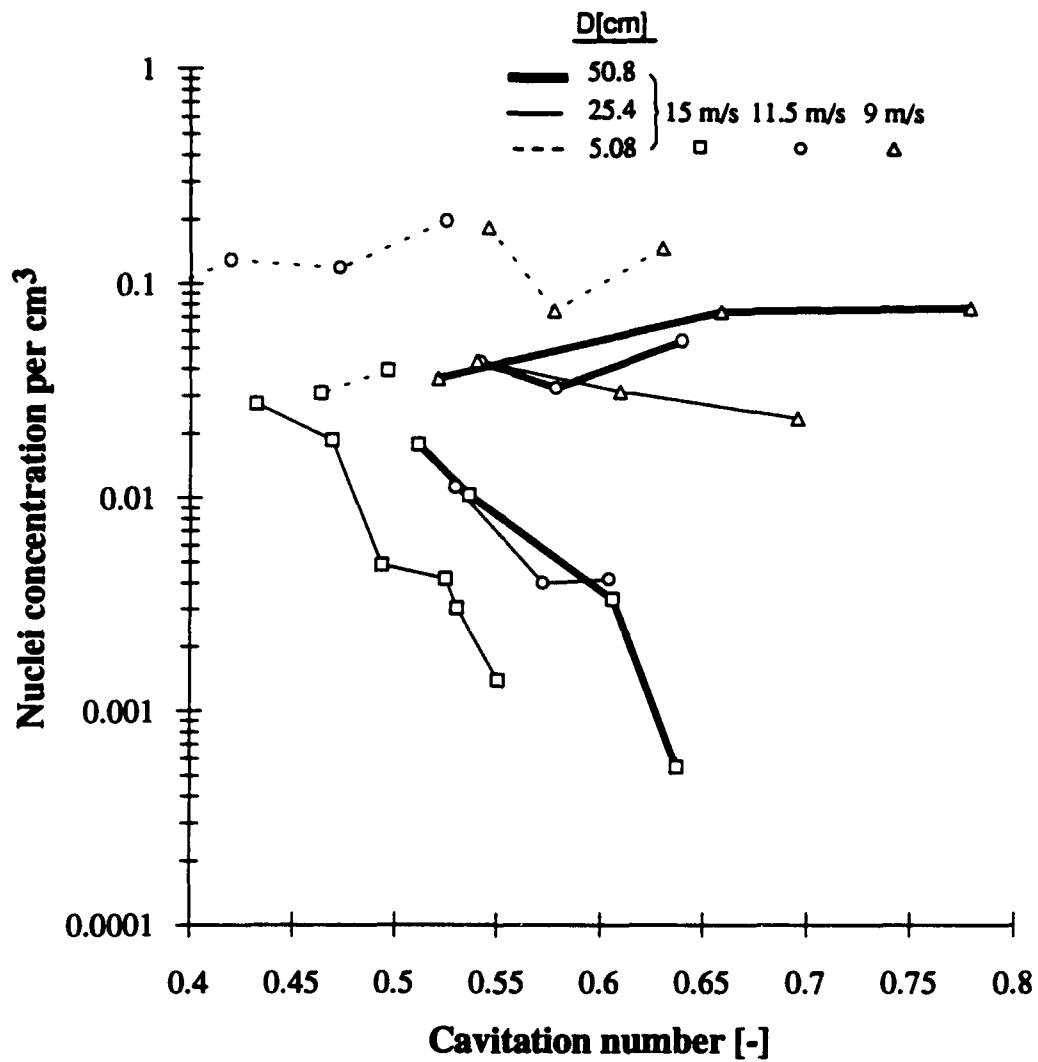


**Figure C.13** Number of excited nuclei per unit liquid volume  
*Data shows measurements for all velocities and headform diameters as a function of the cavitation number.*

annular stream-tube bounded on the inside by the headform and on the outside by the stream-surface which just touches the  $C_p = -\sigma$  isobar (see Fig. A.1) cavitate and form observable bubbles. Then, using the pressure distribution from figure A.1 and the potential flow calculations of the streamtube shapes (therefore neglecting boundary layer effects) extended in the upstream direction, we can calculate the volume flow rate of liquid in the stream-tube for each cavitation number operating condition. Dividing the data of figure C.12 by these values we obtain an estimate of the number of cavitation nuclei per unit liquid volume. This data is presented in figure C.13.

It is significant that some of the variation with cavitation number, headform size and tunnel velocity which was present in figures C.11 and C.12 has now been substantially removed. Indeed, with several exceptions a fair fraction of the data of figures C.11 and C.12 would now appear to correspond to a nuclei concentration of  $0.1 \text{ nuclei/cm}^3$ . The most noticeable deviation from this uniform value occurs at the highest speed ( $U_\infty = 15 \text{ m/s}$ ) with the two larger headforms. The fact that most of the data appears to correspond to the same nuclei concentration is simultaneously encouraging and puzzling. It is encouraging because it suggests that a more careful analysis which begins with the same nuclei number distribution and follows each nucleus along its streamline may allow synthesis of the event rates and the inception numbers. But it is also puzzling because the concentration of  $0.1 \text{ nuclei/cm}^3$  is at least an order of magnitude smaller than most of the measurements of cavitation nuclei would suggest.

Referring to Billet's (1985) useful review on the subject of nuclei concentrations and distributions, one method for counting nuclei is the cavitation susceptibility meter in which the liquid is drawn through an orifice (or other device) and is subjected to low pressures. The device is of sufficiently small size so that cavitation events occur individually. Then the concentration of actual cavitation nuclei (as opposed to potential nuclei) is obtained from the measured event rate and the known volume flow rate. Billet's review indicates that the typical concentrations measured by susceptibility meters is

usually of the order of one nuclei per  $\text{cm}^3$ , significantly smaller than the concentrations obtained by holographic methods. While this may suggest that only a fraction of the potential nuclei actually cavitate, the data is, as yet, inadequate to support any firm conclusion. The other principal and most reliable method for observation of nuclei (micro-bubbles and particles) is obtained by systematically surveying the reconstructed holograms of volumes of tunnel water, taken while the tunnel is in operation (for example Gates *et al.*, 1979). For de-aerated tunnel water, such inspections typically reveal concentrations of the order of  $20 \text{ nuclei/cm}^3$  with sizes ranging from about  $5\mu\text{m}$  to about  $200\mu\text{m}$ . However the next question to ask is what fraction of these potential nuclei do, in fact, cavitate when subjected to sub-critical pressures. Here the answer is quite unclear.

In the present experiments a number of measurements have been made using the David Taylor susceptibility meter simultaneously with the cavitation measurements performed on the headform. The cavitation number in the venturi is defined as

$$\sigma_v = \frac{P_o - P_v}{1/2 \rho V_T^2} \quad (\text{C.6})$$

where  $P_o$  is the stagnation pressure upstream of the venturi and  $V_T$  is the average throat velocity in the venturi. For a given flow condition in the LCC test section the cavitation number in the venturi of the susceptibility meter was being varied by varying the flow rate. For different venturi cavitation numbers,  $\sigma_v$ , the number of cavitation events per minute was counted. By decreasing  $\sigma_v$ , the event rate in the nozzle was varied from none to about 50/min. Knowing the flow rate we can thus calculate the number of events per liquid volume. Figure C.14 shows the measurements taken for different tunnel conditions and different headforms.

A number of trends may be observed from this figure. For each condition, as the cavitation number is increased, we notice a decrease in the number of cavitation events, which is to be expected. The conditions from this figure seem to be split in two

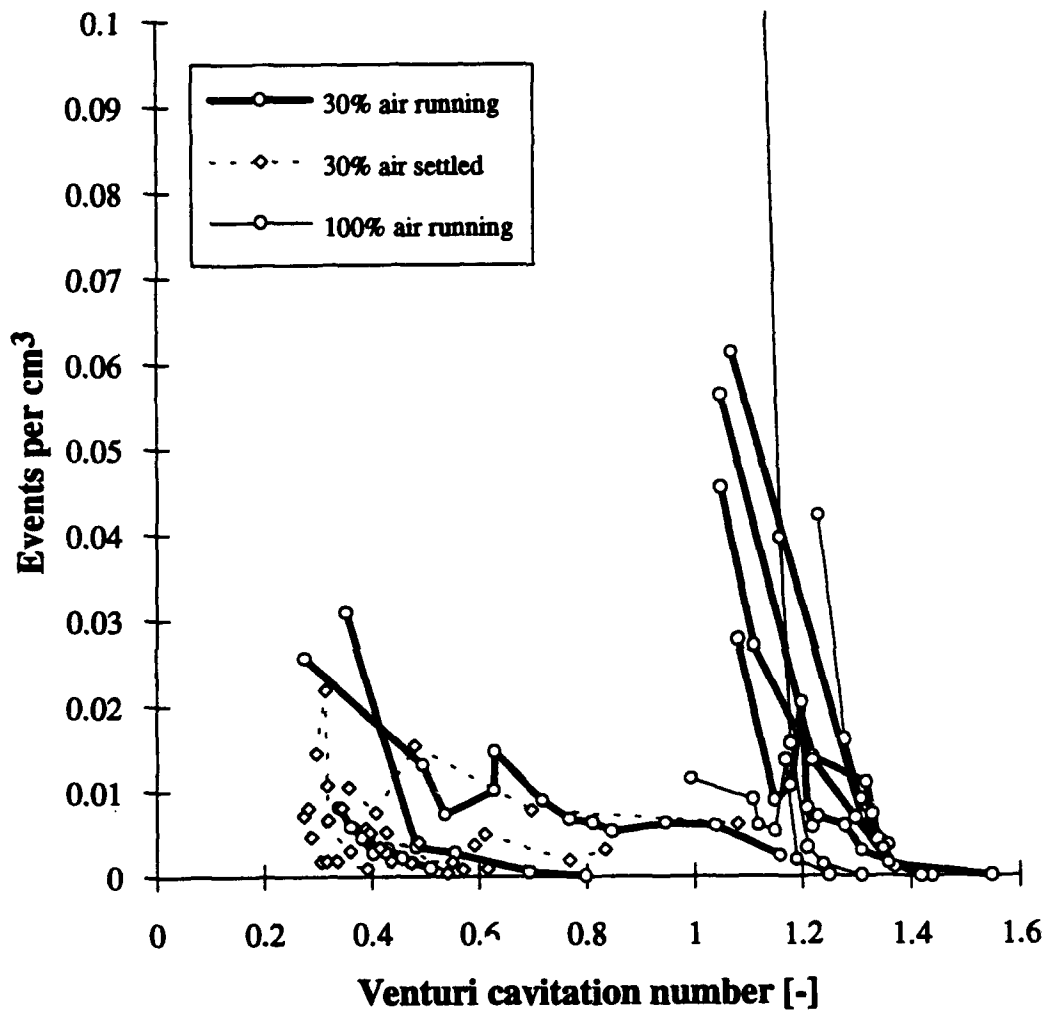


**Figure C.14 Number of events in the susceptibility meter**

*This figure shows the number of cavitation events occurring in the venturi nozzle per volume of water pumped. The cavitation number in the nozzle is reduced for each tunnel condition, increasing the event rate. Shown here are measurements for various tunnel operating conditions.*

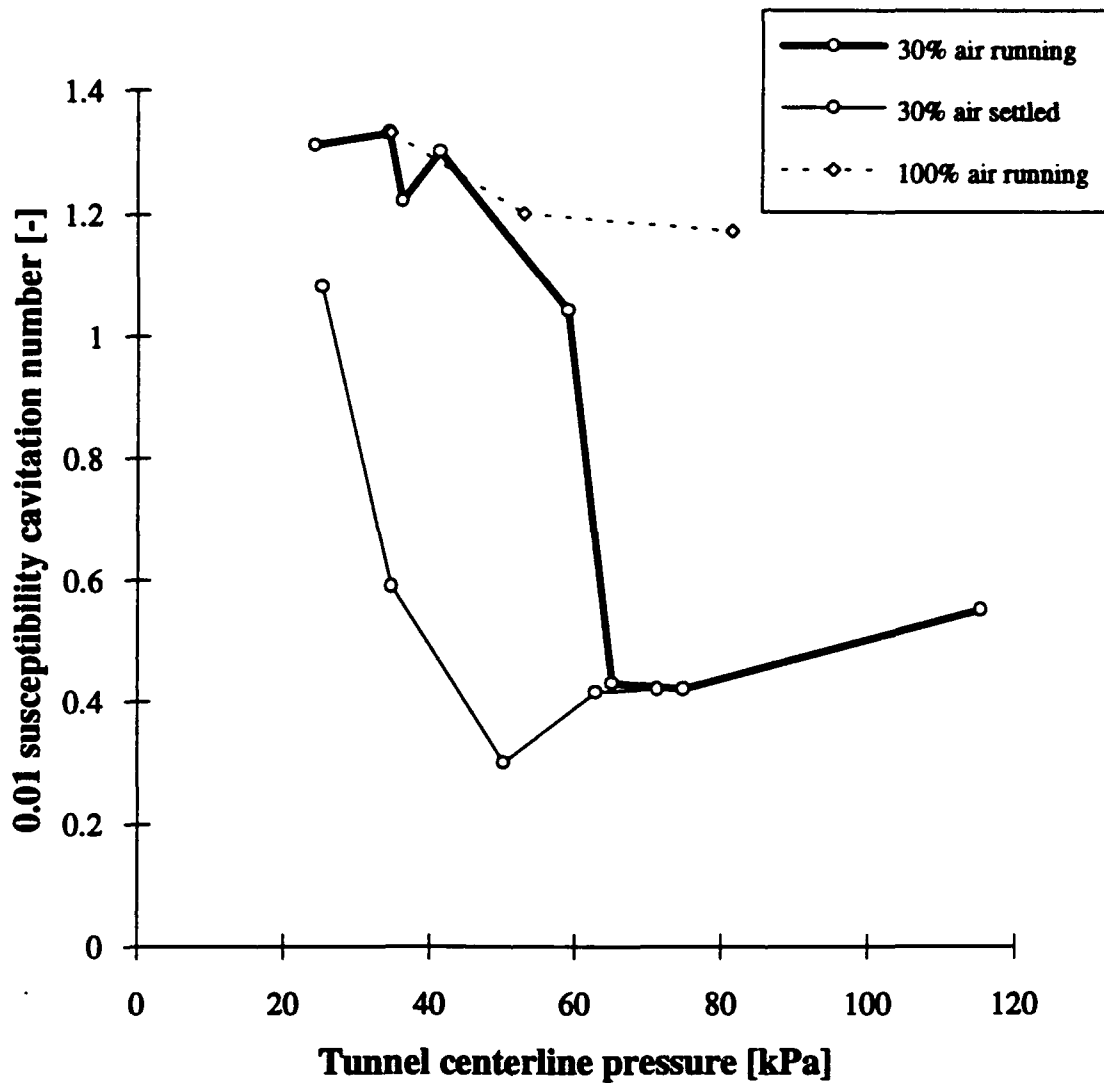


**Figure C.15 Water susceptibility cavitation number**

*This figure shows the susceptibility cavitation number  $\sigma_{v,0.01}$  as a function of the LCC test section centerline pressure. Presented here are data for different headform sizes and different dissolved air contents.*



categories. The first category of data already shows a high number of events per  $\text{cm}^3$  for high cavitation numbers (around  $\sigma_v \approx 1.2$ ), indicating that the water has a tendency to "cavitate easily." The other category requires cavitation numbers around 0.5 to cavitate. We note that observing events for cavitation numbers above unity is surprising since it indicates that we already observe events for venturi throat pressures which are above vapor pressure. This would indicate that this device is also capable of measuring large air bubbles passing through the venturi. In order to summarize these curves and to quantify the water susceptibility for a given tunnel condition we define the susceptibility cavitation number,  $\sigma_{v0.01}$ , as the venturi cavitation number for which we measure 0.01 events per  $\text{cm}^3$ . Figure C.15 presents this cavitation number versus the tunnel test section centerline pressure, for the same tunnel conditions as presented in figure C.14.

It appears clearly from this figure that the conditions at higher dissolved air content (100%) are much more susceptible to cavitate than the 30% air content conditions. For the conditions at 30% air content, a sudden increase of susceptibility is observed as the tunnel pressure is lowered below 60kPa. It suggests that the nuclei population is substantially larger when the facility is operated at the lower pressures. These observations correlate well with the headform event rates shown in figure C.13 where we observed an increase in cavitation events with higher dissolved air contents. We also observed in figure C.13 an increase in the event rates with a decrease in tunnel velocity and thus with a decrease in tunnel pressure needed to achieve the same cavitation numbers at a lower velocity. Visual observation of the tunnel at those lower pressures also indicated a substantial increase in the larger free stream bubbles. We do observe though, a few data points at 30% air content which indicate low water susceptibility even for relatively low pressures (represented on the figure as "30% air settled"). Careful analysis of these points indicate that these measurements were taken at times when the tunnel has been just started after a few days settling time, or when the tunnel has just been emptied and refilled again. Therefore, it appears as though running the tunnel for long periods of

time at low pressures will tend to increase the water susceptibility. However decisive conclusions would require more tests in the tunnel, and the understanding of the evolution of the dissolved nuclei population in time remains a difficult problem to address.

In the present experiments a Dantec Particle Dynamics Analyzer was also set up to measure the nuclei distribution about 3 meters upstream from the headform, but provided no reliable data. Due to the extreme sensitivity of this instrument to various settings we were unable to produce sufficiently reproducible signals. Part of the problem came from the fact that the LCC lucite windows were subjected to deformations at different pressures as the cavitation number was varied, which forced us to constantly realign the laser beams. Results of these measurements are therefore not presented here.

Ceccio (1991) described a model to calculate the cavitation event rate which is based on a known nuclei number distribution function and follows all the possible sizes of nuclei along the streamlines on which cavitation might occur. This model may be corrected and improved by including other effects which may be important such as the effect of the boundary layer and the screening effect which occurs in the stagnation point flow and was first described by Johnson and Hsieh (1966), or by taking into account the intersection with the headform criteria described earlier in chapter B. A brief preview of these results is given here. If one assumes a typical nuclei number distribution function,  $N(R)$  of the form  $N(R) = 10^{-5} / R^{3.5}$  for  $R < 200\mu\text{m}$ , then typical event rates for the Schiebe headform are shown in figure C.16.

Qualitative comparison of figure C.16 with figure C.12 reveals significant areas of both agreement and disagreement. Note first that the trends in event rate with headform size and with cavitation number are quite similar. However the trend with tunnel velocity predicted by the model is contrary to the trend in most of the experiments. This discrepancy appears to be caused by assuming a common nuclei distribution for all operating conditions when, in fact, the nuclei population may be much higher at the low

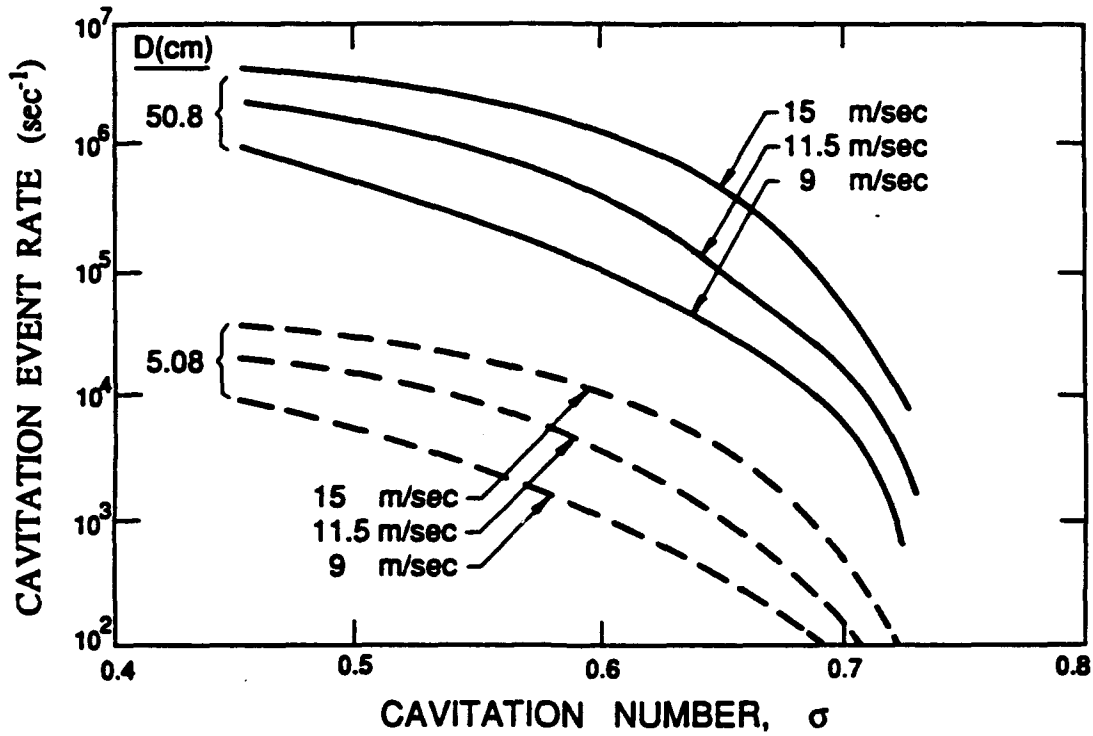


**Figure C.16 Calculated event rates for the Schiebe headform**  
*Data shows measurements for all velocities and headform diameters. The bubble screening effects are not included here. They are known to reduce these values by a factor of about 2 to 5.*

tunnel velocities than at the high as stated earlier. The other area of disagreement to which reference was made earlier is that the event rates in the model are much higher than in the experiments.

#### **C.4.4 Cavitation appearance**

A typical bubble cavitation event consists of the growth and collapse of a bubble as it travels through the low pressure region close to the headform surface. The shape and size the bubble will assume are dependent on the cavitation number and the pressure coefficient history it experiences along its trajectory. In this section we shall describe in more detail the observations made during a study of the photographs and video recordings. The following observations were made at dissolved air contents of 30%.

##### **C.4.4.a Bubble shape**

For cavitation numbers close to the minimum pressure coefficient  $\sigma=0.78$ , the bubble life-time is very short. In figure C.9 we noted that the highest inception cavitation numbers occur for the largest bodies at the lowest velocities. Figure C.17.a shows a cavitation bubble for such conditions ( $\sigma_i=0.77$ ;  $D=50.8\text{cm}$ ;  $9\text{m/s}$ ; 30% dissolved air content). All the bubbles assume a very thin disc-like geometry. For such cavitation numbers there is little or no growth normal to the headform surface. The bubble grows almost entirely in the plane parallel to the headform. At the end of its lifetime the center of the bubble does not collapse first. Instead we observe the evanescence of the bubble's leading edge. There seems to be a fixed location on the headform at which the cavity collapses, creating a fairly straight leading edge on the bubble. At these cavitation numbers we can see from figure A.1, that the critical isobar  $C_p=-\sigma$  is very elongated and close to the body surface. The region below vapor pressure is quite similar to the shape the bubbles assume. It appears that the bubbles are prevented from growing in the direction perpendicular to the body surface by the high normal pressure gradients normal

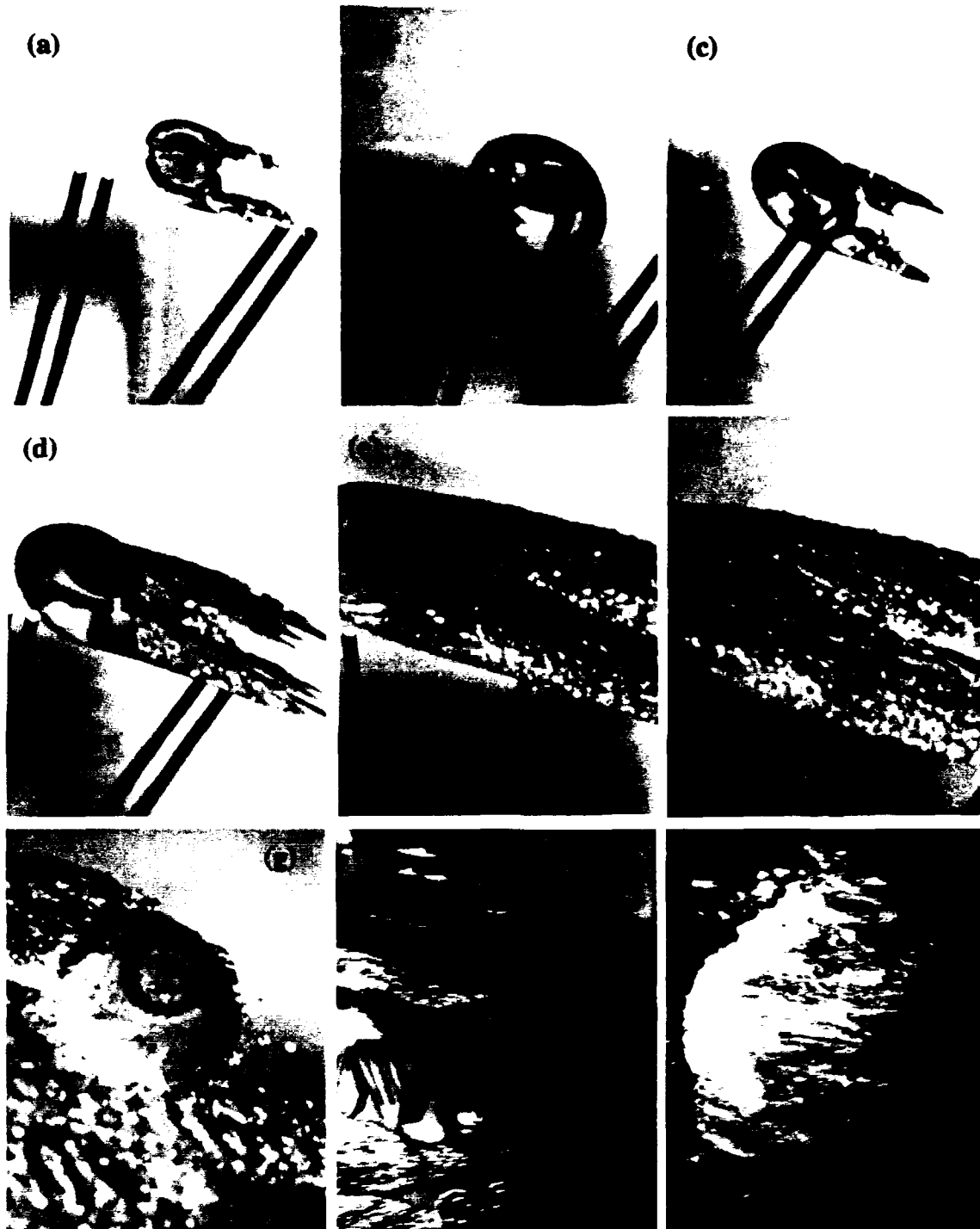


**Figure C.17 High speed photography of cavitation events**

• 50.8cm diameter headform (distance between two patch electrodes: 2.54cm) :  
Figure a:  $U_{\infty} = 9\text{m/s}$ ,  $\sigma = 0.77$ ; Figures b-c-d-e-f:  $U_{\infty} = 15\text{m/s}$ ,  $\sigma = 0.60$ ;  
Figures g-h:  $U_{\infty} = 15\text{m/s}$ ,  $\sigma = 0.54$ ; Figure i:  $U_{\infty} = 15\text{m/s}$ ,  $\sigma = 0.51$

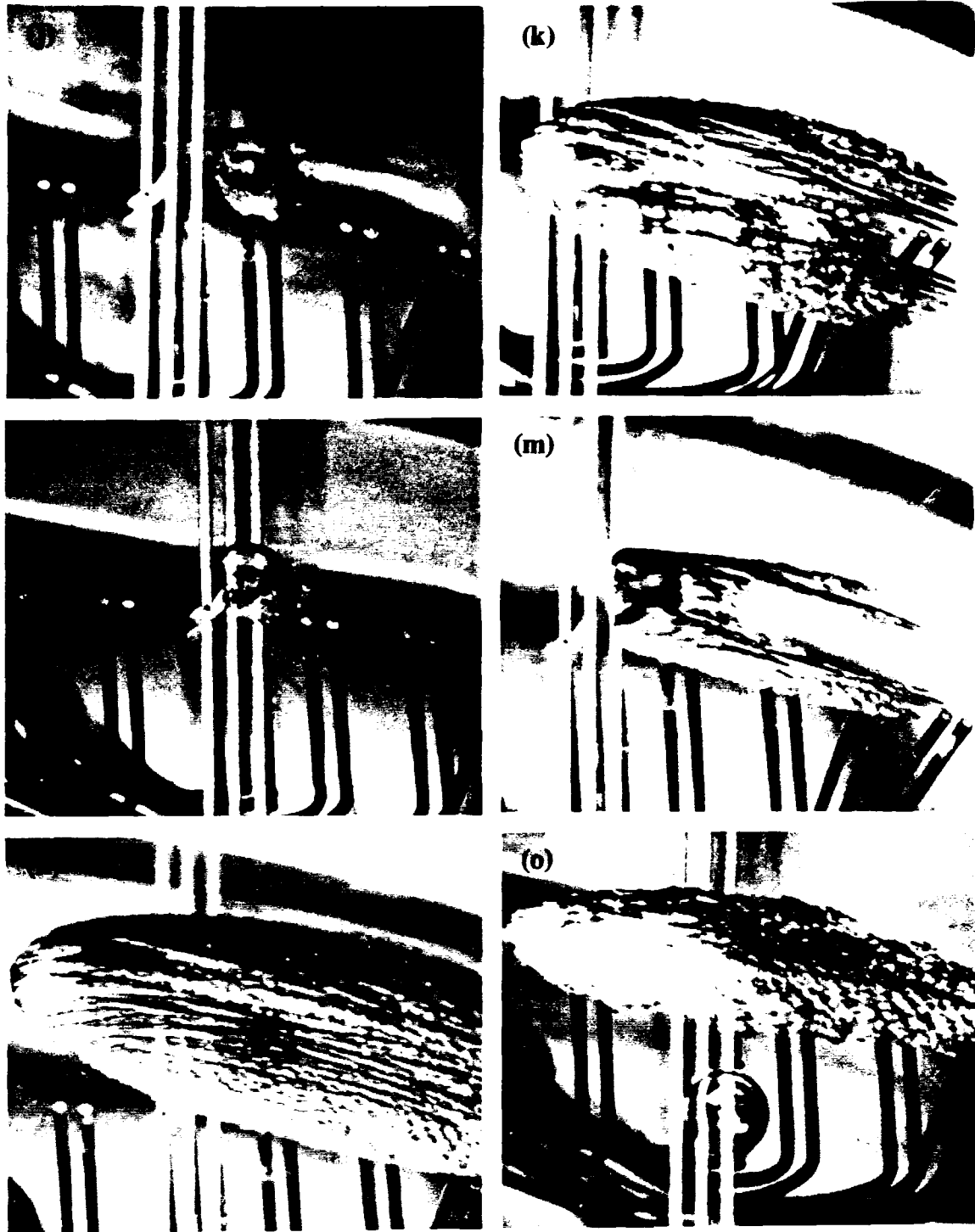


**Figure C.17 High speed photography of cavitation events**

• 25.4cm diameter headform (distance between two patch electrodes: 1.27cm) :

Figures j-k:  $U_{\infty} = 15\text{m/s}$ ,  $\sigma = 0.55$ ; Figures l-m-n:  $U_{\infty} = 15\text{m/s}$ ,  $\sigma = 0.53$ ;

Figure o:  $U_{\infty} = 15\text{m/s}$ ,  $\sigma = 0.49$

to the surface. On the other hand, since the smallest headform has much smaller cavitation inception numbers (significantly less than 0.78), the bubbles observed on this headform do not assume such a flattened shape, even under inception conditions.

As the cavitation number is decreased below  $\sigma_i$ , the bubbles grow in volume (in diameter and in height) and assume the roughly hemispherical shape typified by figure C.17.b. The maximum volume is mostly cavitation number dependent. As the bubbles approach their collapse phase their thickness,  $\delta$ , normal to the headform surface decreases faster than their base radius,  $R$ , and the leading edge collapses most rapidly along a fairly straight front (figures C.17.j, C.17.l). At this stage they appear thin and close to the headform surface (see also Ceccio, 1989) and look similar to the bubbles observed under inception conditions.

One unique feature of the present experiments was the appearance of wave-like circular dimples on the exterior of the hemispherical cap (figures C.17.b, C.17.e, C.17.f, C.17.g, C.17.j, C.17.l, C.17.m). The dimples seem to become more pronounced as the volume of the bubble increases. They are absent during the growth phase as seen in figure C.17.c, and appear early in the collapse phase. Their ring shape could be interpreted as a precursor of a collapsing reentrant jet, but we note that the center of the dimple retains a concave curvature at all times. The dimple seems quite stable, and remains on the bubble until the very last stage of collapse. The reason for its presence is unclear, although they might be due to a local over-pressure that forms early during the growth phase on the exterior of the bubble, as will be discussed later in chapter D. On the 50.8cm headform the dimples sometimes also appear in pairs on the largest bubbles. On the smallest headform they are not as pronounced and thus were never observed in the past experiments performed by Ceccio and Brennen (1989) and by Kumar and Brennen (1990).

Measurements of the bubbles on all three headforms show that the radius at the base of the hemispherical cap  $R$ , scales linearly with the headform diameter  $D$ , thus, at the same cavitation number, the ratio  $R/D$  appears to be the same for all three headforms. We

do not observe any variation of  $R/D$  with the velocity  $U_\infty$  either. Furthermore the dimensionless collapse location is approximately the same for all headforms. This appears to be true as long as the interactions between bubbles, or between bubbles and patch cavities remains limited. Therefore simple size scaling of the base diameter of the bubble cap with the headform size seems to be possible. This simple scaling applies only to the bubble's base radius though, since the shape of the bubble, its thickness  $\delta$ , the amount of shear on its base and the cavitation event rate vary greatly from one headform to the other.

#### **C.4.4.b Bubble tail and patches**

Figure C.17.a shows the presence of streaks of vapor or "tails" extending behind both sides of the bubble. It appears as though the bubble is sheared in the region extremely close to the headform surface leaving the tails behind in its wake. The undersides of some bubbles appear roughened towards the trailing and leading edges. The structure of the tails is always extremely wavy and turbulent, and they seem to be attached to the headform surface (fig. C.17.c). They always appear early in the growth phase of the bubble. As the bubble is convected downstream it continues to "feed vapor" into the tails, allowing them to extend in length and height (figures C.17.c, C.17.d, C.17.e, C.17.f). Ultimately the larger bubbles will collapse leaving behind patch-like cavities. It seems clear that whether a bubble will be sheared or not is determined early in the growth phase. If a bubble does not exhibit the trailing edge streaks early in its passage as seen in figure C.17.c, it will grow and collapse with a smooth cap shape (fig C.17.b, C.17.j, C.17.l). For this reason, at fixed cavitation conditions, the leading edge of the streaks are always located around the same position on the headform (fig. C.17.c, C.17.d, C.17.e, C.17.f). The same statement can thus be made for the leading edge of the patches. If the thickness of those streaks is small, the dynamic of the final collapse of the bubble appears unaffected by them and appears similar to the process described in the previous paragraph and seen in figure C.17.m. However, for small enough cavitation numbers the patch can



out-grow the bubble and swallow it leaving behind a patch-like cavity (fig. C.17.k, C.17.n). At this point it is not clear if all the patch cavitation structures are generated by traveling bubbles. Some of them evidently are, and can be recognized by a planform shape, similar to a "V" with its vertex pointing downstream. The final length and thickness of the patch cavity are dependent on the bubble that generated it, and therefore vary with the headform diameter and cavitation number. For cavitation numbers close to the minimum pressure coefficient  $\sigma = 0.78$ , no patches and very few bubble tails are observed as in figure C.17.a. For these conditions the tails seem unable to grow sufficiently to form a patch-like cavity. Figures C.17.k and C.17.n show two typical patches at lower cavitation numbers. We notice that the patch on figure C.17.k (higher cavitation number) is thinner and does not extend as far downstream as that of figure C.17.n. The collapse mechanism of the patch itself is quite unclear. In the video recordings they vanish entirely between two frames (1/30 seconds). Is the entire patch swept downstream once the bubble head has vanished, or does it entirely collapse on the headform? The current investigation has not, as of yet, been able to answer these questions.

The number of sheared bubbles seems to increase with the cavitation number, headform diameter and flow velocity. Since the ratio of the laminar boundary layer thickness to headform size will scale with  $Re^{-1/2}$ , we would expect that the shearing of the cavitation bubbles would increase as the relative boundary layer thickness decreases. However, at the highest Reynolds number of  $10^7$ , we note that the theoretical laminar to turbulent transition comes close to the low pressure region and might cause further disruptive effects.

#### **C.4.4.c Bubble-patch interactions**

When the cavitation number is sufficiently reduced, the transient patches become fairly stable and remain on the headform, thus creating attached cavities for periods of up

to a few seconds. As their number increases the patches will merge to create larger attached structures. Favre and Avellan (1987) have shown that those attached cavities disturb the initial pressure distribution in such a way that they actually extend downstream beyond the original  $C_p = -\sigma_i$  isobar. Those attached cavitation pockets have been seen to shed large structures downstream without "disrupting" the upstream original attachment point to the headform. The cavitation number at which this phenomenon happens varies considerably from one headform to the other. It can be seen in figure C.17.i at a cavitation number of about 0.5 for the 50.8cm headform. By contrast, at the same cavitation number, the 25.4cm headform produces just a few bubbles and patches (figure C.17.o) and the 5.08cm headform shows no cavitation. At this point we note that the transient cavitation patch phenomenon was never observed on the smallest headform. That headform seems to exhibit an abrupt switch from traveling bubble cavitation (some of which have long trailing tails) to persistent attached cavities. The attachment location of these cavities on the smallest headform is fixed for all conditions, and usually corresponds to a roughness element. This has not been observed on the larger headforms, even though the polished finish was identical to that of the 5.08cm body. Roughness scaling appears to be a very critical parameter for the attached cavitation scaling of these bodies.

For all test conditions on the larger headforms at cavitation number below 0.7 we noticed the coexistence of the two different kinds of cavitation patterns: traveling bubbles and transient patches. Quite remarkably, even for the conditions at which we observe many patch-type cavities, some very smooth hemispherical traveling bubbles are still present (figure C.17.b, C.17.h). We can see in figures C.17.g, C.17.h, C.17.i bubble type cavitation riding above fully attached cavities.

Comparing the shape of the bubbles encountering patch cavities with those which do not, it is clear that the shapes differ because the former are not subjected to the boundary layer shear which the latter experience. Bubbles which do encounter patches or attached cavities will eventually collapse and merge completely with the larger structure

upstream of its closure region. By doing so they appear to perturb the attached cavity shape, as has been observed by Briançon-Marjollet *et al.* (1990).

#### C.4.5 Bubble dimensions

In order to examine the relative size of the bubbles on the three headforms and at different cavitation numbers, various bubble dimensions were measured from the still photographs and the video tape recordings. The base of an individual bubble (surface next to the headform) at the point of maximum bubble growth, being close to circular, was characterized by its radius  $R_{\max}$ . The height,  $\delta$ , of the bubble in a direction normal to the headform surface was also estimated, as was the location of bubble collapse at an axial distance,  $X_c$ , from the front stagnation point. First we present in figure C.18 the ratio of maximum base radius to headform diameter,  $r_{\max} = R_{\max}/D$  as a function of the cavitation number. We can see that the velocity has very little influence on the non-dimensional bubble size. Furthermore, for all three headforms, this non-dimensional bubble size parameter remains roughly the same for a fixed cavitation number. This result can be explained by analysis of the Rayleigh-Plesset equation for spherical bubble growth. Once the nucleus has begun to grow, viscous (Reynolds number) and surface tension (Weber number) effects soon become negligible and the dimensionless bubble growth rate,  $(dR/dt)/U_{\infty}$  (where  $R$  is the spherical bubble radius, and  $U_{\infty}$  is the reference free stream velocity) depends only on the cavitation number,  $\sigma$ , and the pressure coefficient history,  $C_p(t)$ . Moreover the bubble's travel time " $t$ " available for growth in the low pressure region scales like  $D/U_{\infty}$  and so the equations yield values for  $R_{\max}/D$  which depend only on the headform shape (as manifest in  $C_p$ ) and  $\sigma$ . To obtain the necessary input to this calculation, namely  $C_p$  along a streamline, the potential flow around the Schiebe headform was obtained using a panel method. Substitution of the pressure coefficient history on a streamline close to the headform surface into the Rayleigh-Plesset equation produced the

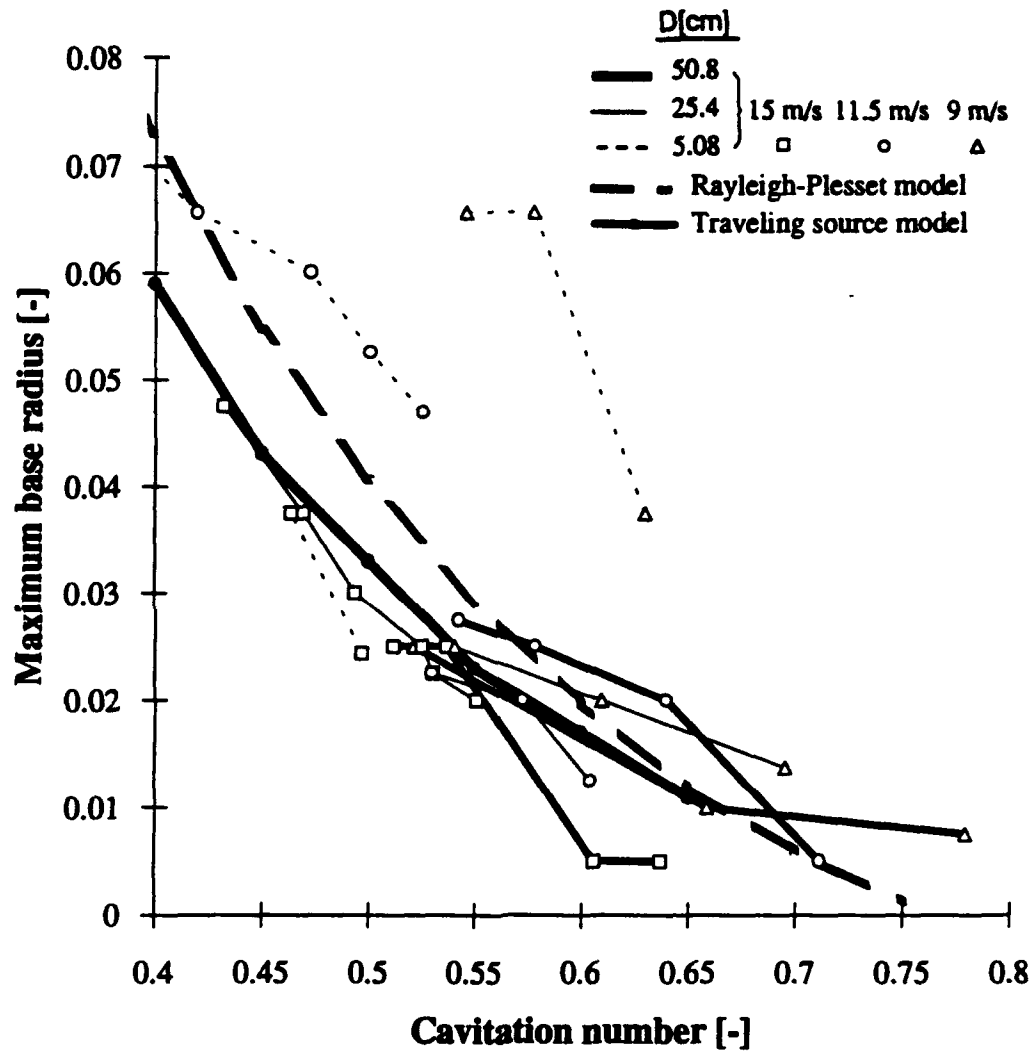


**Figure C.18 Bubble maximum radius as a function of the cavitation number**

*This figure shows measurements for all velocities and headform diameters. Also included is the theoretical radius calculations based on the Rayleigh-Plesset and on the traveling source model.*

theoretical maximum bubble radius result included in figure C.18. It is remarkable that, despite the very non-spherical shape of the actual cavitation bubbles, the Rayleigh-Plesset equation yields values which are close to the base radius of the actual bubbles. It is as if the headform surface acts as a plane of symmetry for the growth of the bubble and the pressure distribution parallel to the surface are the sole driving terms in that plane. For the low cavitation numbers though the Rayleigh-Plesset model departs from the experimental data and yields larger bubble sizes. Also presented on this figure is the result of the bubble radius calculated using the single source model and will be discussed in the next chapter.

The only experimental data in figure C.18 which differs substantially from the rest are that for the  $D=5.08\text{cm}$  headform at  $U_\infty=9\text{m/sec}$ . This might be due to measurement errors since the gas coming out of solution at these low pressures make an accurate reading of the small bubble radius difficult. Finally we note that for inception conditions the bubbles on the smaller headform appear larger relative to the size of the headform because the inception cavitation number  $\sigma_i$  is lower for that smaller headform.

The bubble sphericity, as measured by  $\epsilon=\delta/R$  at the point of maximum growth of the bubble, also changes substantially with cavitation number as seen in figure C.19. The difference in sphericity between the two larger headforms at the same cavitation number is not clear. On the larger diameter headforms, we observed that bubbles appeared extremely thin for cavitation numbers close to inception. The  $C_p$  distribution curves above the headform in figure A.1, show that the isobars near the minimum pressure region  $C_p=-0.78$  are extremely elongated and close to the surface. Hence there exists a high normal pressure gradient close to the headform surface. Rayleigh-Plesset calculations for a nucleus experiencing pressures along a streamline extremely close to the headform show that for cavitation numbers higher than 0.6, a hemispherical bubble would grow to a radius that exceeds at all times the height of the critical isobar  $C_p=-\sigma$ . This over-pressure on the exterior of the bubble forces it to be flattened. The three-dimensionality of the bubble for

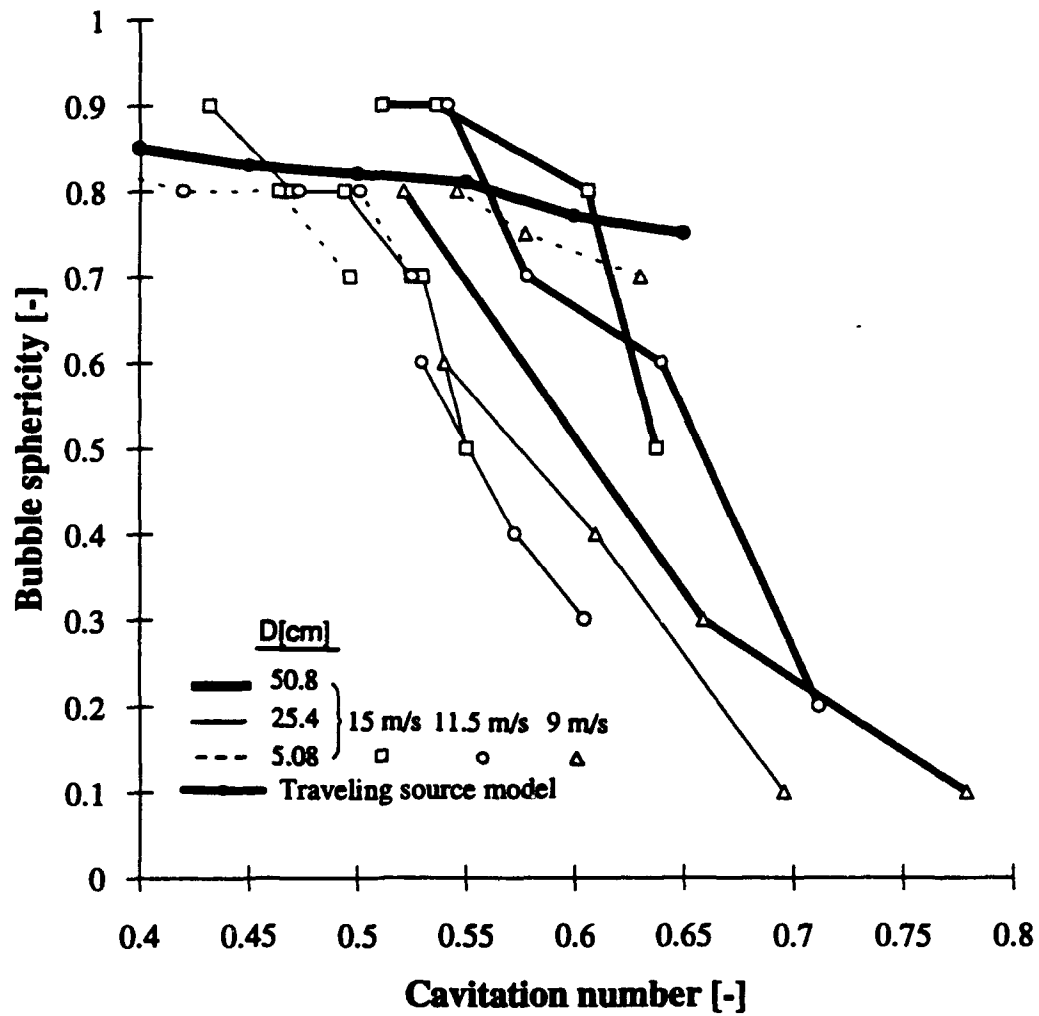


**Figure C.19 Bubble sphericity at the maximum size of the bubble**  
*This figure shows measurements for all velocities and headform diameters as a function of the cavitation number.*

those conditions therefore has to be very important. For smaller cavitation numbers, the critical isobar is considerably further from the headform surface and it transpires that even the exterior of the bubble experiences pressures below the vapor pressure for some time, allowing it to grow in the direction normal to the headform surface. The cavitation inception number for the 5.08cm headform is around 0.55 . Therefore all the bubbles we have observed on this headform are quite hemispherical since the  $C_p = -\sigma$  isobar is far from the surface at this cavitation number. We note that even in this case the pressure gradient normal to the surface remains much larger than that parallel to the surface (figure A.1) and the bubble height  $\delta$ , in the direction normal to the headform surface, will decay faster than its base radius  $R$  in the collapse phase. Therefore, for any cavitating condition, the sphericity of a bubble will always decrease towards the collapse phase. Also presented on this figure is the result of the bubble radius calculated using the single source model.

Measurements of the non-dimensional location of bubble collapse as represented by  $x_c = X_c/D$  are presented in figure C.20 and exhibit a clear dependence on cavitation number with little dependence on the body diameter or the free-stream velocity. The Rayleigh-Plesset calculations provided similar results and the location of collapse is in fair agreement with the observations for high cavitation numbers. We note that as soon as the attached cavities appear for low cavitation numbers, the pressure distribution is modified and the bubbles tend to merge into these cavities at locations further upstream making these measurements more difficult.

The influence of the Reynolds number on the non-dimensional attachment location of cavitation  $x_a = X_a/D$  is shown in figure C.21. The data in that figure include measurements made on all three headforms and all cavitation numbers.

The attachment position appears to be the same for both trailing tails on traveling bubbles, for the leading edge of transient patches or for the separation of attached cavities. We note that this location is mostly Reynolds number dependent, and is affected very little by the cavitation number.

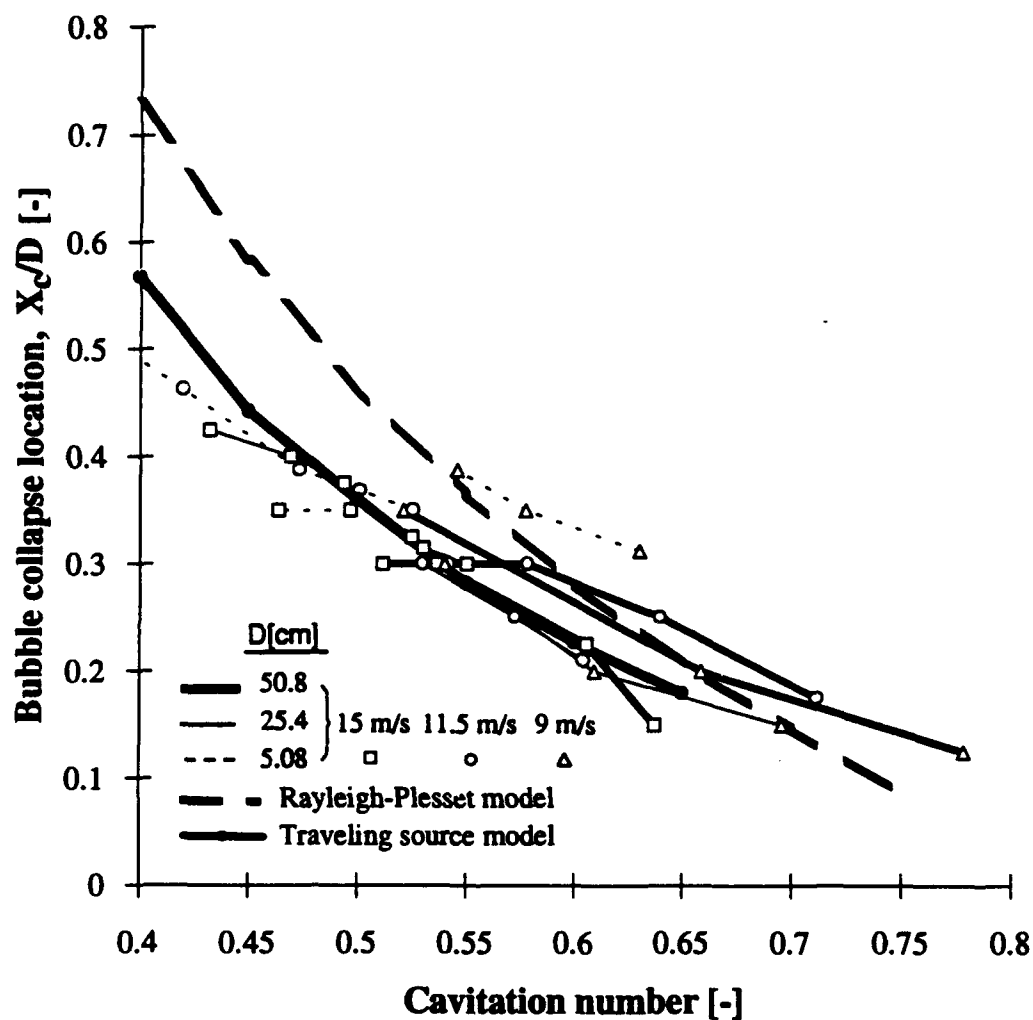


**Figure C.20** Dimensionless bubble collapse location,  $x_c$   
 The data are shown for all velocities and headform diameters as a function of the cavitation number. Also included are the theoretical radius calculations based on the Rayleigh-Plesset theory.



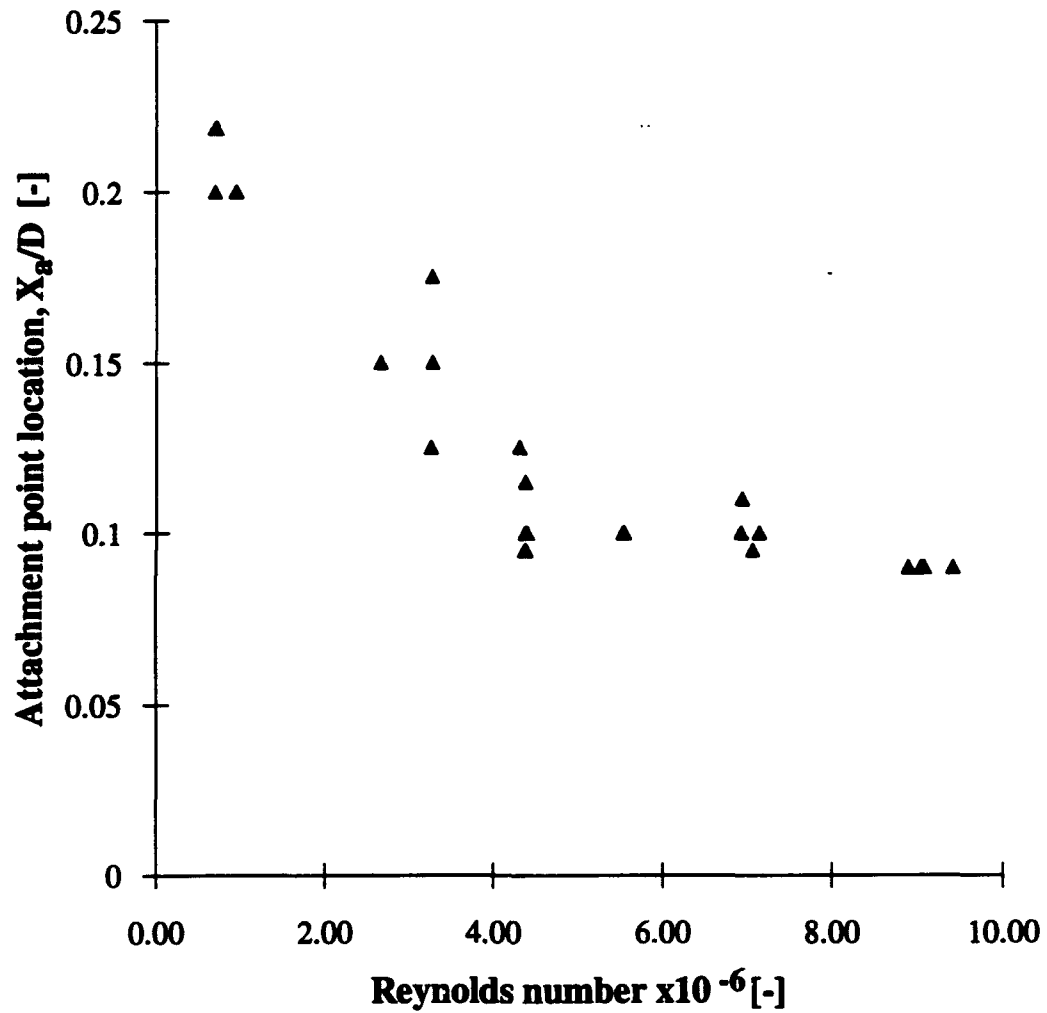


**Figure C.21 Attachment point coordinate along the x axis**  
*Data show measurements for all cavitation numbers and headform diameters as a function of the Reynolds number.*

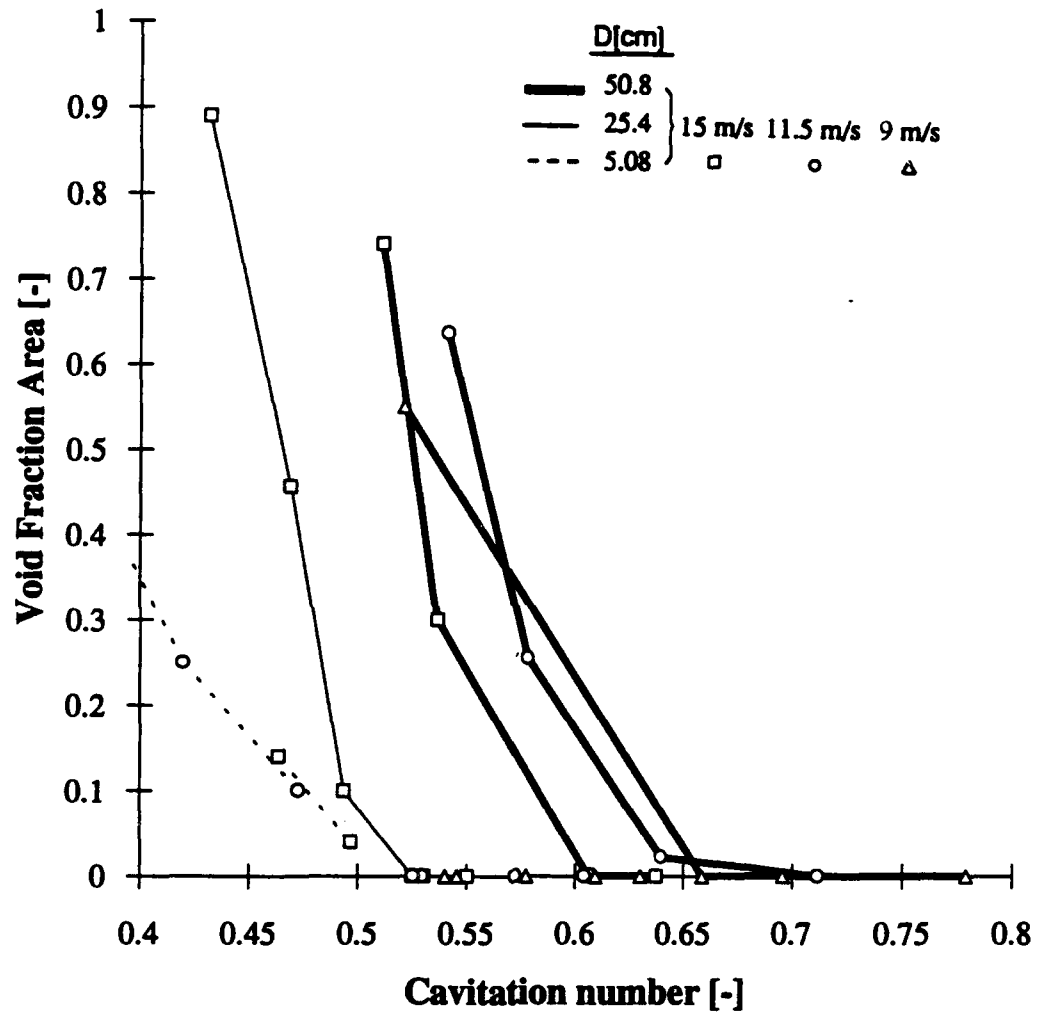


**Figure C.22 Average void fraction area over the nose of the headform**  
*Data show measurements for all velocities and headform diameters as a function of the cavitation number.*

As the cavitation number is reduced, the number of cavitating bubbles appearing on the surface in a still photograph increases. The fraction of the surface in the low pressure region which is covered by bubbles was estimated from the pictures and plotted against  $\sigma$  in figure C.22. Note that the increase in the void fraction at lower  $\sigma$  is mostly due to the presence of patches and attached cavities; bubbles do not contribute significantly to this void fraction. Examining this graph, we see that the void fraction increases with headform diameter. Clearly this void fraction depends on the cavitation nuclei number distribution in the incoming stream. We should address the possible reasons for the trend toward an increasing number of patches or extent of attached cavitation for larger headforms and lower velocities. While the explanation is not at all conclusive, it seems reasonable to suggest that this trend is related to the boundary layer thickness in the region in which cavity attachment may occur. If attachment were related to the ratio of the boundary layer thickness (proportional to  $(D/U)^{1/2}$ ) to the size of a typical roughness (about the same for all headforms) then this might explain the observed trends.

#### C.4.6 Cavitation noise

For a range of cavitation numbers between inception and a value at which the cavitation patches persisted, it was possible to identify within the hydrophone output the signal produced by each individual bubble collapse. In order to isolate individual bubble signals it was found necessary to digitally high-pass filter the signals using a cut-off frequency of 5kHz in order to reduce the effect of vibration and noise caused by cavitation at the top of the supporting strut. This filtering did not, however, substantially effect the results. The processing amplifier gain response was calibrated and applied to the results. The noise from the cavitation was analyzed in several ways. We present first a spectral analysis which is the traditional approach normally taken toward cavitation noise.

However more fundamental information can be gained from an analysis of the pressure pulses produced by individual cavitation events as will be described later.

#### C.4.6.a Spectral analysis

FFT analyses of the signals from individual events were performed for different cavitation conditions for Nyquist frequencies up to 500kHz. In order to compare the shape of the Power Spectral Density for different cavitating conditions the values have been non-dimensionalized by the number of sampled points,  $N$ , multiplied by the mean squared power amplitude,  $\overline{PSD}$ , where

$$\overline{PSD} = \frac{1}{N^2} \left[ C^2(f_0) + C^2(f_{N/2}) + 2 \sum_{i=1}^{i=N/2-1} C^2(f_i) \right]. \quad (C.7)$$

The dimensionless PSD curves are presented in figure C.23 and consist of data averaged over several cavitation events.

First we notice that, for all headforms and tests conditions, the measured spectral shape varies little with the operating condition and cavitation number as was reported by Arakeri and Shanmuganathan (1985). Most of the data represented here was taken close to inception. The influence of the hydrophone cutoff frequency above 80kHz can be observed in all signals. The measured decay between 1kHz and 80kHz in the present data appears roughly constant, with a value of about -22dB/dec for all conditions. This value is similar to the value of -24dB/dec (or  $f^{-6/5}$ ) obtained earlier by Kumar and Brennen (1992) and by Ceccio and Brennen (1991,1992) in the Caltech Low Turbulence Water Tunnel. By way of comparison we note that the spectra obtained by Blake *et al.* (1977) for cavitation on a hydrofoil show a comparable frequency dependence of -20dB/dec (or  $f^{-1}$ ), though there is also a consistent dip in their spectra at 10kHz. Arakeri and Shanmuganathan (1985) have presented data with a similar frequency dependence though the slope also increases from about -12dB/dec (or  $f^{-3/5}$ ) to -30dB/dec (or  $f^{-3/2}$ ) as the bubble interactions increase. None of this data is very close to the value of -8dB/dec

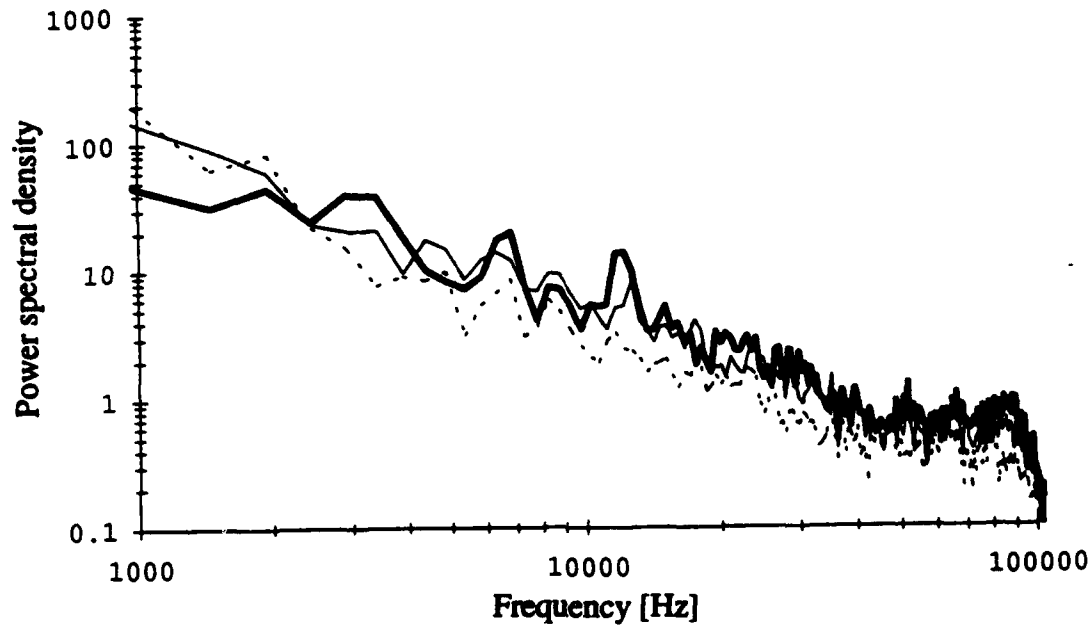


**Figure C.23 Averaged dimensionless power spectral density signals**  
*Data presented for the 50.8cm headform diameter and 30% dissolved air.*  
——  $U_{\infty} = 9\text{ m/s}$ ,  $\sigma = 0.66$ ;      ———  $U_{\infty} = 11.5\text{ m/s}$ ,  $\sigma = 0.64$ ;  
.....  $U_{\infty} = 15\text{ m/s}$ ,  $\sigma = 0.61$ .

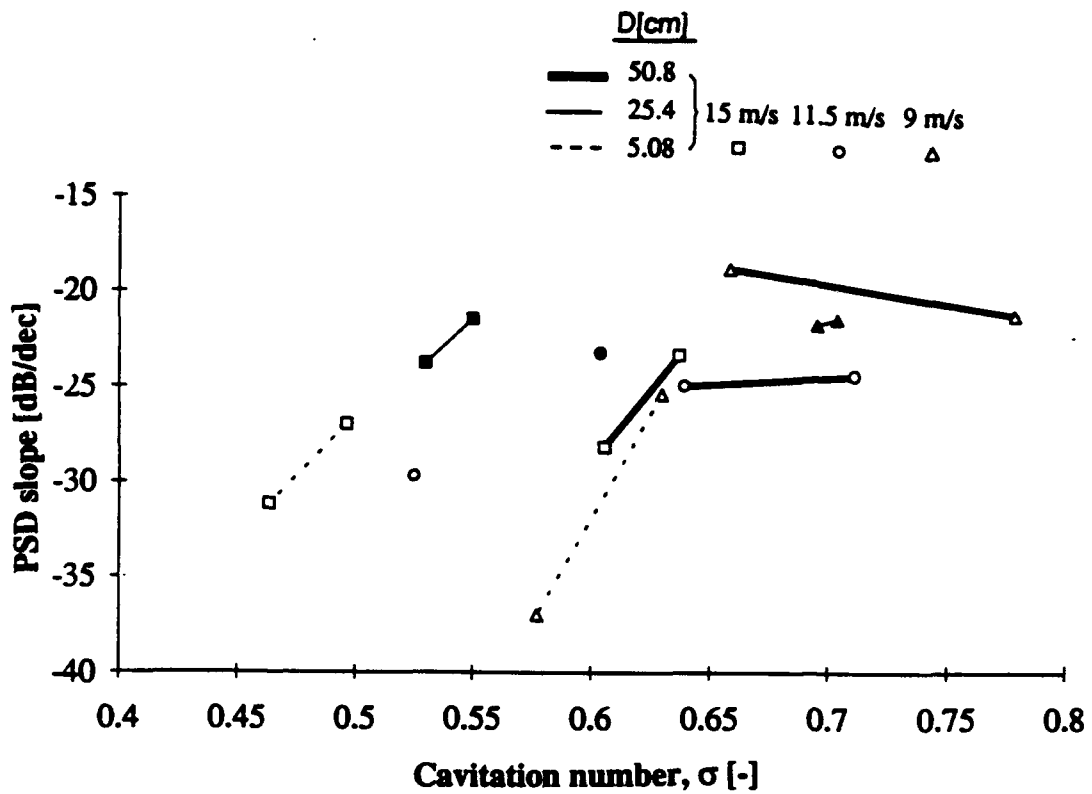


**Figure C.24 Average power spectral density slope decay [dB/dec]**  
*The decay has been measured between 1kHz and 80kHz. Measurements for different headform diameters and velocities as a function of the cavitation number.*

which Fitzpatrick and Strasberg (1956) predicted for the range 10 to 100kHz based on a Rayleigh-Plesset analysis. Taking fluid compressibility into account yields decays as low as -40dB/dec ( $f^{-2}$ ) for the very high frequencies (around 100kHz and up), but these frequencies are beyond the capability of the hydrophone used in the present experiments.

Measurement of the frequency decay as a function of the cavitation number for different cavitating conditions is shown in figure C.24. We observe that this slope seems to decrease as the cavitation number value is reduced below 0.6. For some cavitation conditions the slope can be as low as -35dB/dec. This change is consistent with the effects of bubble interactions observed by Arakeri and Shanmuganathan (1985). It appears as though increasing bubble interactions destroy the coherent structure of the pressure fronts, thus reducing their high frequency content.

#### C.4.6.b Acoustic pressure pulses

As described in chapter B in equation B.17, the amplitudes of the acoustic pressure pulses were measured by defining the impulse,  $I$ , as the integral of the pressure time history from the beginning of the collapse pulse to the moment when the pressure returns to its mean value. Since the impulse varies inversely with the distance of the hydrophone from the noise source, we formed a dimensionless impulse,  $i_{center}$ , in equation B.22 by dividing the impulse recorded by the inner hydrophone by the headform radius, the free-stream velocity and the fluid density as indicated by the Rayleigh-Plesset analysis. We also defined a unit impulse in equation B.23 as the impulse one would measure at a unit distance from the cavitation noise source. The hydrophone output for each of the experimental conditions was examined in order to identify at least 40 of the larger pulses associated with a bubble collapse. The average values of the impulses obtained in this way are plotted against cavitation number in figure C.25 and C.26. All these points were taken for a 30% dissolved air content.

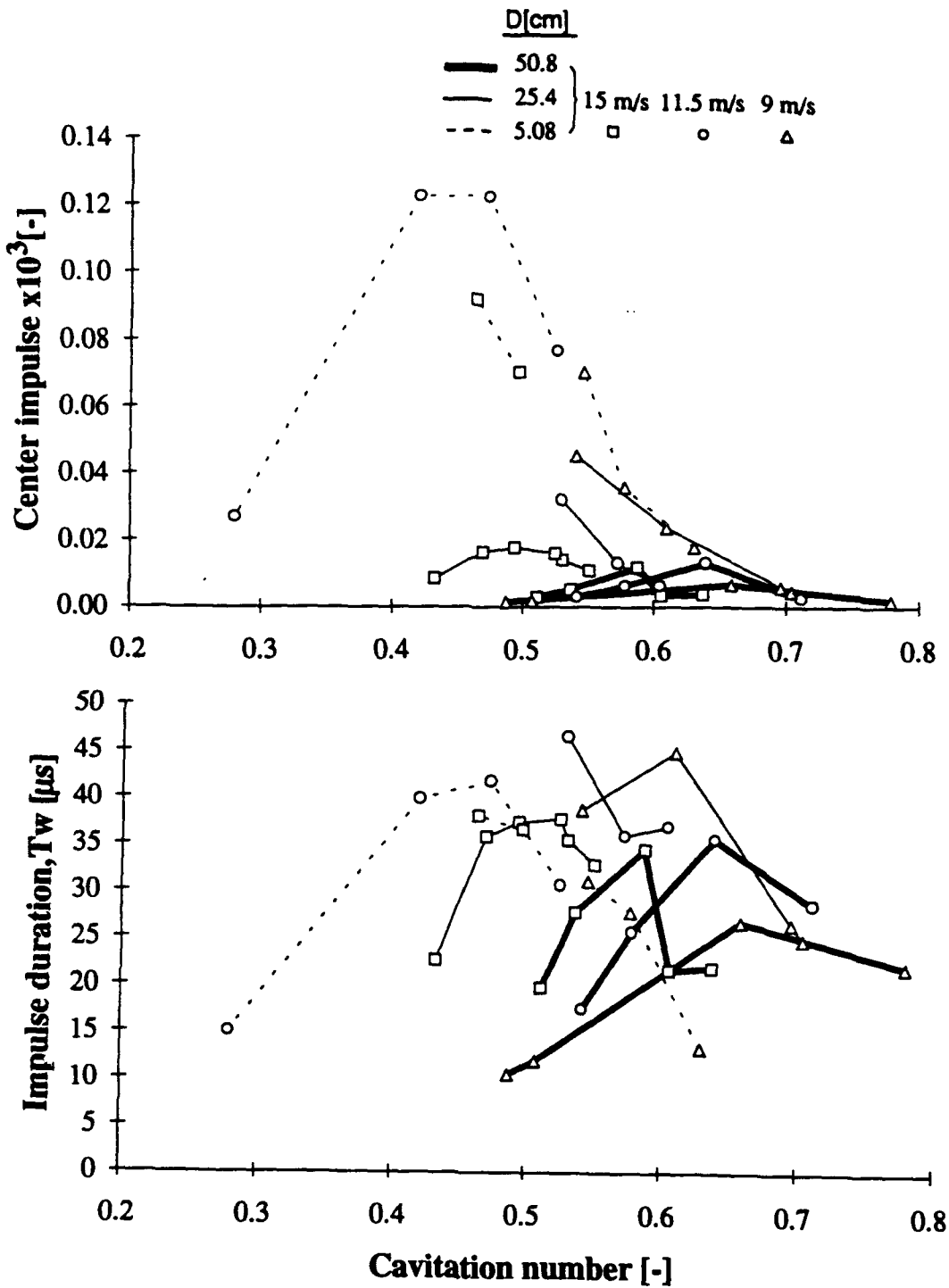


**Figure C.25 Average acoustic impulse,  $i_{center}$ , and impulse duration**  
 The average dimensionless maximum center impulse,  $i_{center}$  and the impulse duration  $t_w$  [ $\mu$ s] are presented for all three headforms and all flow velocities as a function of the cavitation number.



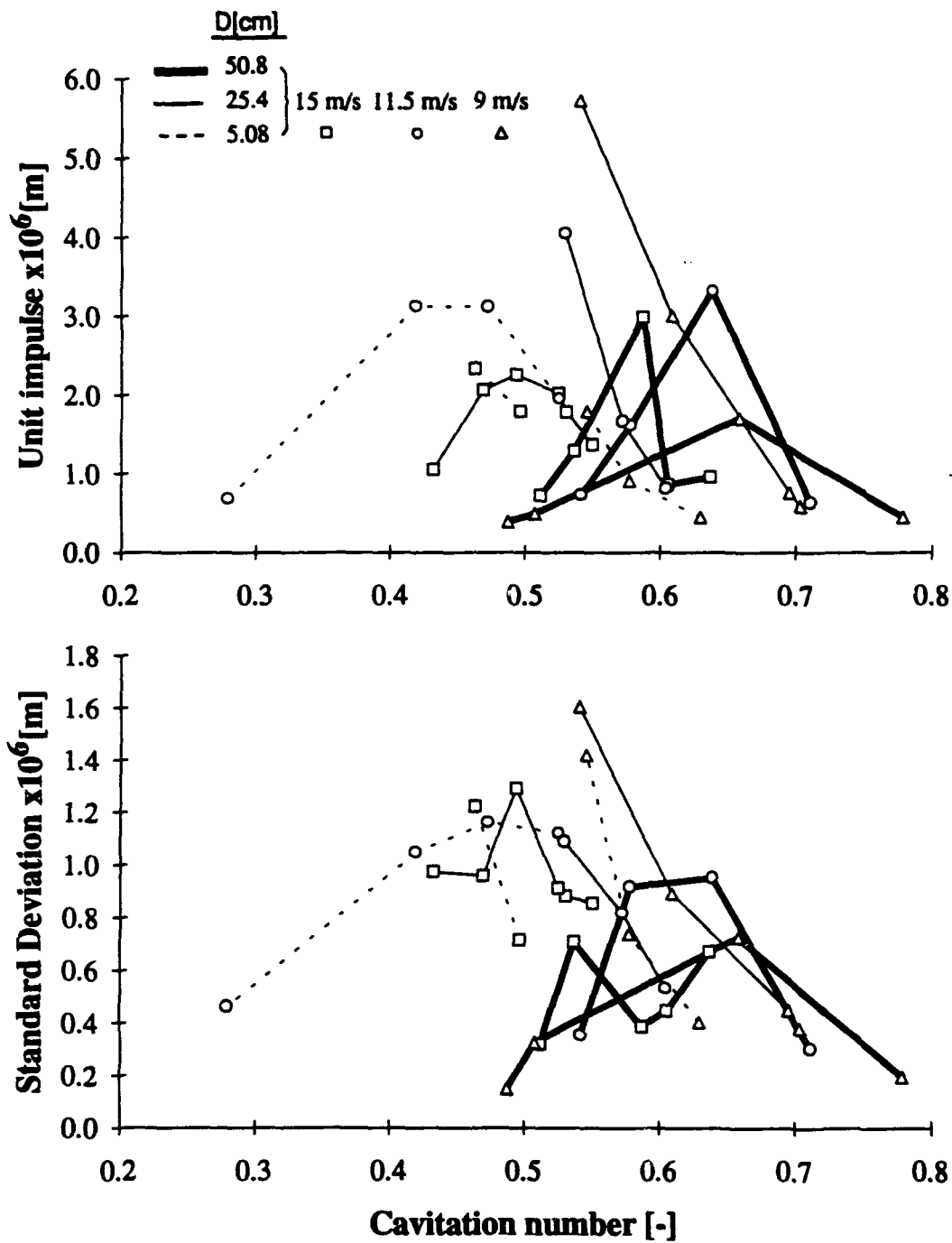


**Figure C.26** Average acoustic impulse,  $i_{\text{unit}}$   
 The average dimensionless maximum unit impulse,  $i_{\text{unit}}$  and the standard deviation of that impulse are presented for all three headforms and all flow velocities as a function of the cavitation number.

We observe that the dimensionless center impulse increases with lower cavitation numbers as is expected. Comparing the value of these impulses with the theoretical values presented in figure B.3 we notice that they are substantially lower (by almost two orders of magnitude). The complexity of the fluid dynamics involved during the collapse of real bubbles (viscous shearing, interaction with headform, interaction with other bubbles...) therefore appear to result in a smaller impulse than for the ideal spherical case. We have to note that the discrepancy also certainly comes in large part from the poor frequency response of the hydrophone above 100kHz, and from the high-pass filtering that was required to "clean" the signals. Even with these limitations, valuable information can be gained by comparing the different impulses with one another.

If we compare the unit impulse for all three headforms we observe that it is the same order of magnitude. This impulse calculation might therefore be more suitable to model the scaling effects. We observe that it initially increases as the cavitation number is decreased below inception. However most of the data also indicates that the unit impulse ceases to increase and, in fact, decreases when  $\sigma$  is decreased below a certain value ( $\sigma_{\text{peak}} = 0.43, 0.50$  and  $0.62$  for the 5.08cm, 25.4cm and 50.8cm diameter headform). The decrease at low cavitation numbers might be caused by the increasing presence of attached cavitation patches, damping the bubble collapse mechanism. The conditions at which the impulses are maximum seem to correspond well to circumstances in which the cavities cover about 20% of the surface area of the headform in the neighborhood of the minimum pressure point. Higher void fractions increase the interactions between the bubbles and the patches and considerably reduce the acoustic impulse. Such an effect was previously reported by Arakeri and Shanmuganathan (1985) who noticed strong interaction effects for void fraction values larger than 25%. The location of the peaks appears to be somewhat shifted towards higher cavitation numbers for lower velocities. This trend is consistent with the previous observations from figure C.22 of the average

void fraction over the headform at constant cavitation numbers, which exhibited an increase with a decrease in velocity.

The unit impulse standard deviation also shown in figure C.25 is substantial, around 40% of the average value. Therefore for identical cavitation conditions the cavitation noise may vary considerably from one event to another. The dimensional duration of the impulse  $t_w$ , presented in figure C.25, reveals a cavitation number dependence similar to that observed for the impulse. It appears to be of the same order of magnitude for all velocities and diameters. Examining this data it should be recalled that the typical response time of the hydrophone is about  $3\mu s$  and is not negligible compared with the measured duration.

In summary, we find that the acoustic impulse produced by a single bubble collapse, while exhibiting considerable variability, nevertheless scales with headform size and tunnel velocity in the way which is expected on the basis of the Rayleigh-Plesset analysis. Moreover, when the bubble concentration exceeds a certain value the noise from individual events becomes attenuated. Because of this attenuation a unit impulse scaling has been shown to be more suitable for comparing the signals from different headform sizes.

#### **C.4.6.c Electrode signal analysis**

When a bubble is located over a particular electrode, denoted by the index "i", it modifies the water electrical impedance in its vicinity which eventually yields a voltage signal  $v_i(t)$ , from that electrode. Figure C.27 presents an example of the signals over the 50.8cm diameter headform from the first and second patch electrodes (located at axial distances of 5.08 and 7.62cm from the headform stagnation point). The corresponding noise signal is plotted on the same figure, time shifted by  $170\mu s$  which corresponds to the time necessary for the acoustic noise to travel from the headform surface to the

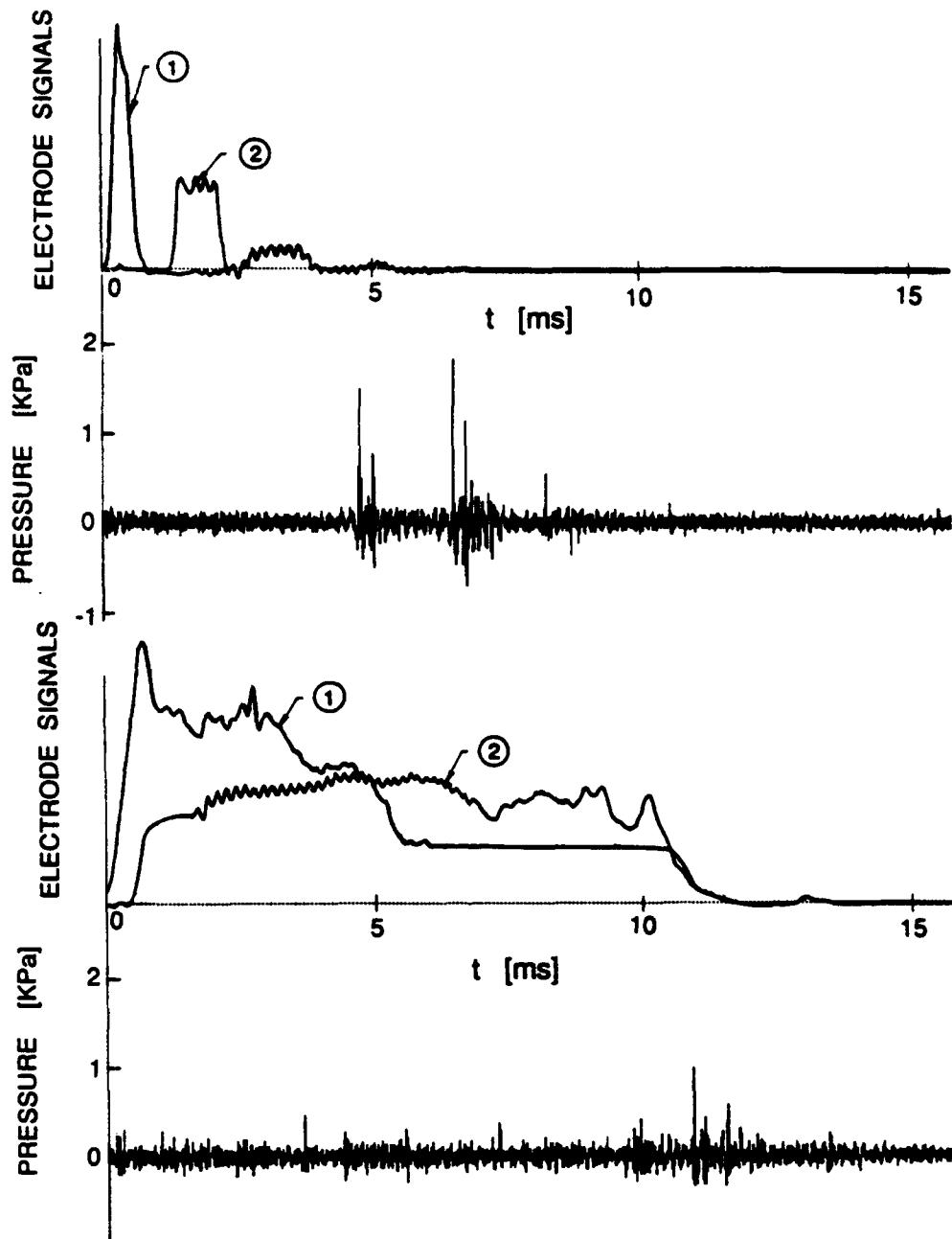


**Figure C.27 Electrode and the corresponding acoustic noise signals**  
*The electrode signals from upstream patch electrodes 1 and 2 and the corresponding acoustic noise signals are shown simultaneously. The signals plotted correspond to the bubbles presented in photographs C.17.b and C.17.d.*

hydrophone. The signals from an unsheared bubble (seen in photograph C.17.b) and from a sheared bubble developing attached streaks (seen in photograph C.17.d) are contrasted in this figure.

Analyses of these electrode signals sheds additional light on the mechanism of the bubble collapse. Sheared bubbles produce much longer electrode signals. Moreover, the trace from the first electrode will vanish before that from the second electrode, indicating that the collapse mechanism always proceeds in a downstream direction. Whether the cavity disappears by collapsing on the headform itself or detaches and is convected away by the flow is unclear. The time interval between the ends of the two electrode signals is often comparable to that measured for the case of unsheared traveling bubbles. This might suggest that the leading edge of the patch detaches first and the cavity is convected away by the flow.

The typical time during which a bubble covers an electrode is given by

$$\tau_i = \frac{\int_{t=0}^{t=\text{end of signal}} v_i(t) dt}{v_{i\max}} \quad (\text{C.8})$$

and can be written in dimensionless form by defining an electrode signal duration parameter  $\gamma_i = \tau_i U_\infty / D$ . Clearly a bubble with attached streaks or patches will yield substantially larger  $\gamma_i$  values than single unattached bubbles. Therefore  $\gamma_i$  provides a valuable indicator of the type of event which has occurred. The global coverage parameter  $\gamma$  groups the electrode duration parameters of the first two upstream patch electrodes and is defined as

$$\gamma = \sqrt{\gamma_1 \gamma_2} \quad (\text{C.9})$$

Non-sheared bubbles have all been observed to have coverage parameters typically less than 0.01.

For single traveling bubbles, the duration parameters over the first and the second upstream patch electrode are strongly correlated. Figure C.28 represents a plot of  $\gamma$

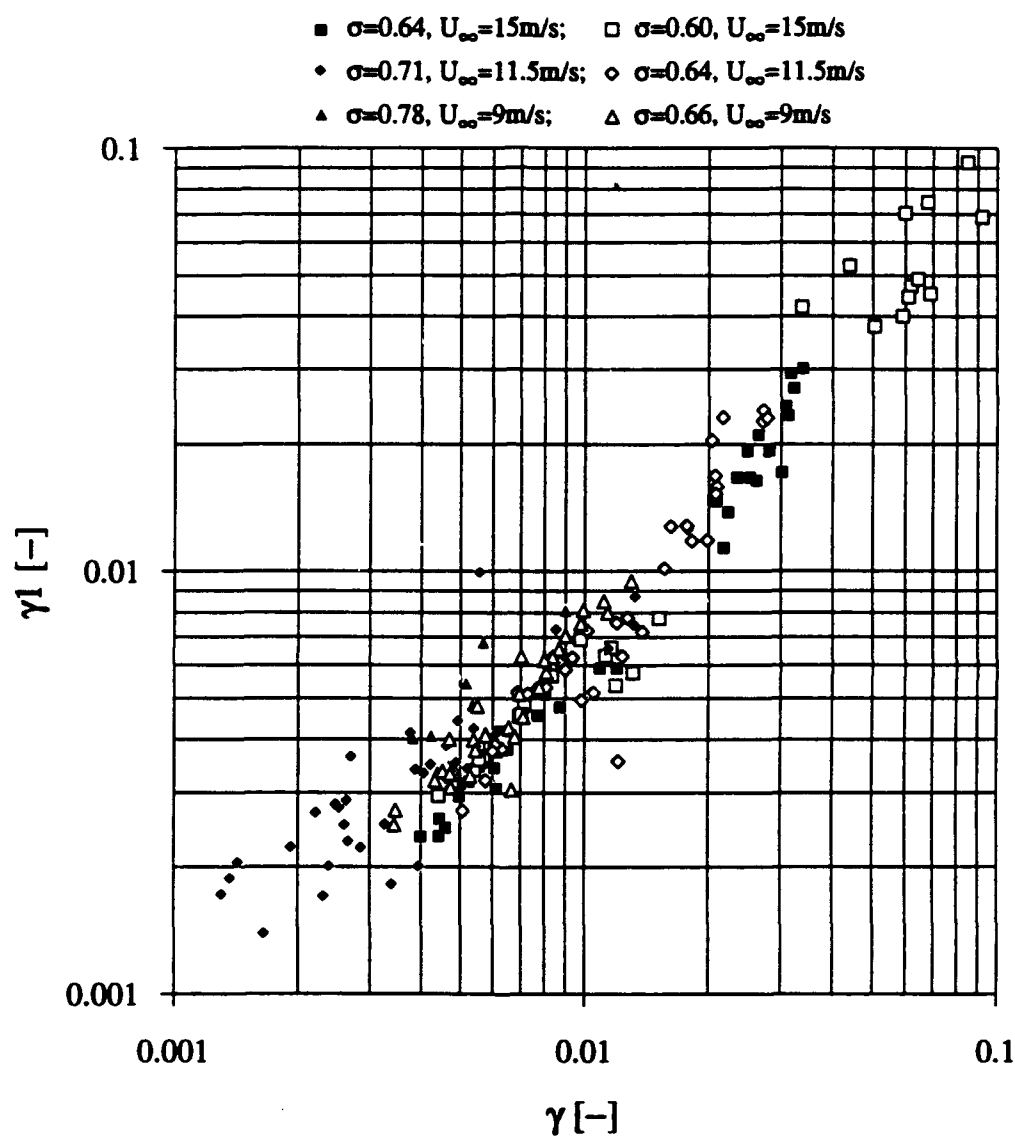


**Figure C.28 Dimensionless electrode signal duration**

*Presented here are the durations on the first and second upstream electrodes (located at axial coordinates  $x_1=0.1$  and  $x_2=0.15$ ). Data show measurements for various flow velocities and cavitation numbers.*

versus the dimensionless electrode duration for the first electrode,  $\gamma_1$ , for a wide range of cavitation numbers and velocities. Clearly there exists a strong correlation between both electrode durations  $\gamma_1$  and  $\gamma_2$ . It follows that a long (or short) duration at the first electrode leads to a long (or short) duration at the second electrode. Therefore we may conclude from figure C.28 that trailing streaks or tails (which cause larger duration) only appear very early in the bubble evolution and that, if they do not appear, the bubble will continue without a tail for the rest of its lifetime. This conclusion was also reached from studies of photographs and video observations. Note that the above implies that the leading edges of the attached patches are always upstream of the first electrode.

The instant at which a bubble passes over the electrode "i" is denoted by  $t_i$  and may be defined by the quantity

$$t_i = \frac{\int_{t=0}^{t=\text{end of signal}} v_i(t) dt}{\int_{t=0}^{t=\text{end of signal}} v_i(t) dt}. \quad (\text{C.10})$$

Then the non-dimensional interval (or bubble travel time) between the signals from electrodes 1 and 2 can be thus defined as

$$\Delta\tau = \frac{(t_1 - t_2)U_\infty}{D}. \quad (\text{C.11})$$

Data about this quantity are presented in figure C.29. For all conditions we see that the non-dimensional interval is concentrated around a value of  $\Delta\tau=0.043$ . Panel method calculations of the non-dimensional travel time along a streamline between electrode 1 and electrode 2 yield an exactly identical value of  $\Delta\tau=0.043$  for the streamline closest to the headform. This travel time increases only slightly as the streamline is located further from the headform. From the photographs we estimated that a typical non-dimensional bubble thickness for cavitation numbers around 0.65 is about  $\delta=0.01$  and the potential flow travel time for streamlines located at that distance above the headform surface is  $\Delta\tau=0.044$ . The agreement between the measured travel time for non-sheared bubbles (represented by  $\gamma$

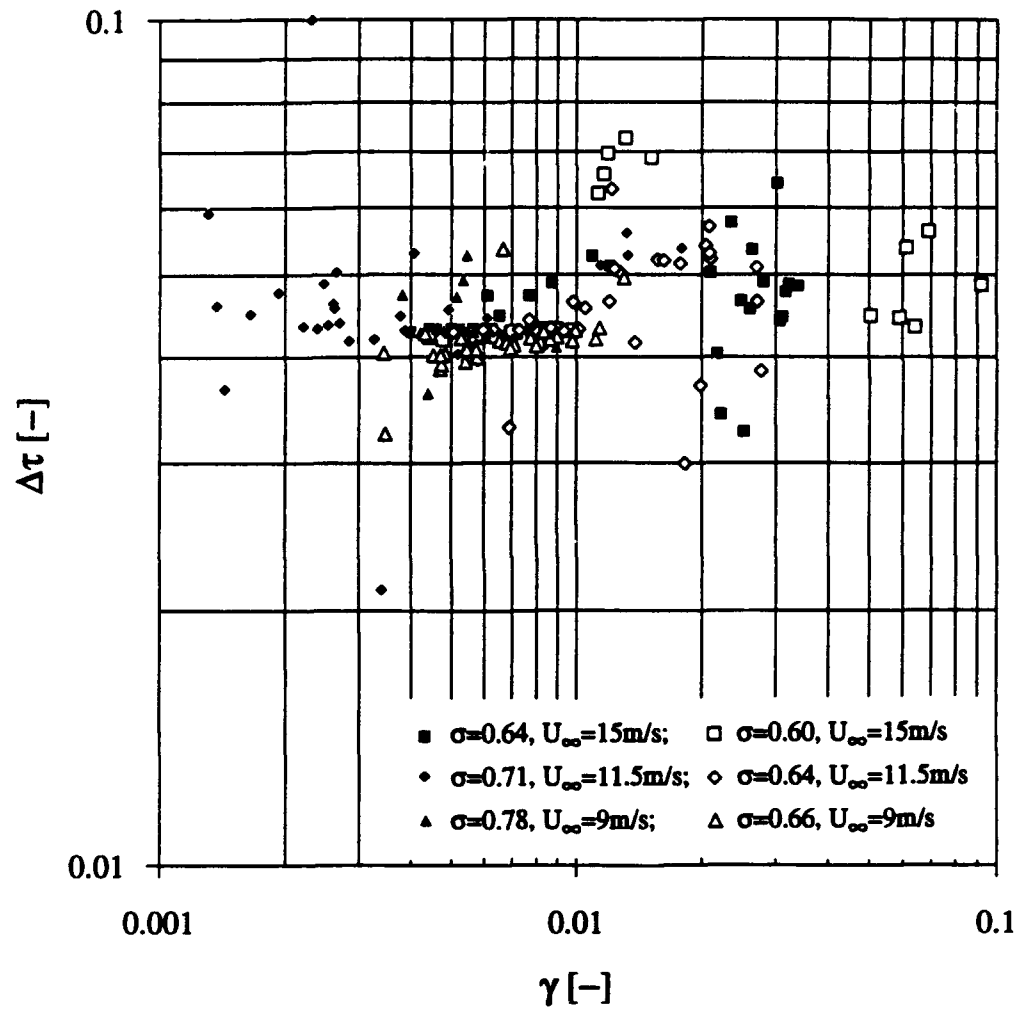


**Figure C.29** Travel time between the two first electrodes  
*Non-dimensional electrode peak interval,  $\Delta\tau$ , for various flow velocities and cavitation numbers.*



values less than 0.01) and the potential flow calculation thus indicates that there is no slip between the bubble and the inviscid flow outside the boundary layer. The bubbles appear to ride over the boundary layer and travel at the same velocity as the outer flow.

For  $\gamma$  coverage parameters less than 0.005 which correspond to the smallest bubbles at the highest cavitation numbers ( $\sigma \geq 0.70$ ) some scatter can be observed. For those conditions photographs indicate that many bubbles collapse before they reach the second electrode. The signals measured on the second electrode may therefore be generated by rebounded bubbles. At the other extreme the large values of  $\gamma$  ( $>0.01$ ) correspond to long sheared bubbles with tails attaching to the headform surface. Note from figure C.29 that the scatter in  $\Delta t$  increases significantly with  $\gamma$  and that there is a trend toward greater travel times indicating that the bubble velocity is slower than that of the flow outside the boundary layer. This is consistent with part of the bubble being within the boundary layer. Part of the reason also originates from the difficulty to pinpoint a precise bubble passage instant for these conditions.

Since the electrodes and the hydrophone signals were recorded simultaneously, it is possible to correlate the acoustic output of each event with the  $\gamma$  value for that event in order to explore the effect of bubble attachment on the noise. Figure C.30 presents the coverage parameter  $\gamma$  as a function of the unit acoustic impulse,  $i_{unit}$ , for the 50.8cm headform at 30% dissolved oxygen content. Most of the data is confined to cavitation numbers close to inception (low event rates) in order to ensure no overlap between events.

This figure leads to several conclusions. First we focus on the data on the left-hand side for values of  $\gamma$  less than 0.01. These correspond to unattached bubbles with the smallest bubbles having the smallest values of  $\gamma$ . In this regime the impulse increases with increasing  $\gamma$  (i.e., decreasing cavitation numbers and increasing bubble size) as previously suggested by many authors, for example Fitzpatrick and Strasberg (1956) and Hamilton *et al.* (1982). The data here clearly exhibit an upper bound or envelope on the impulse.

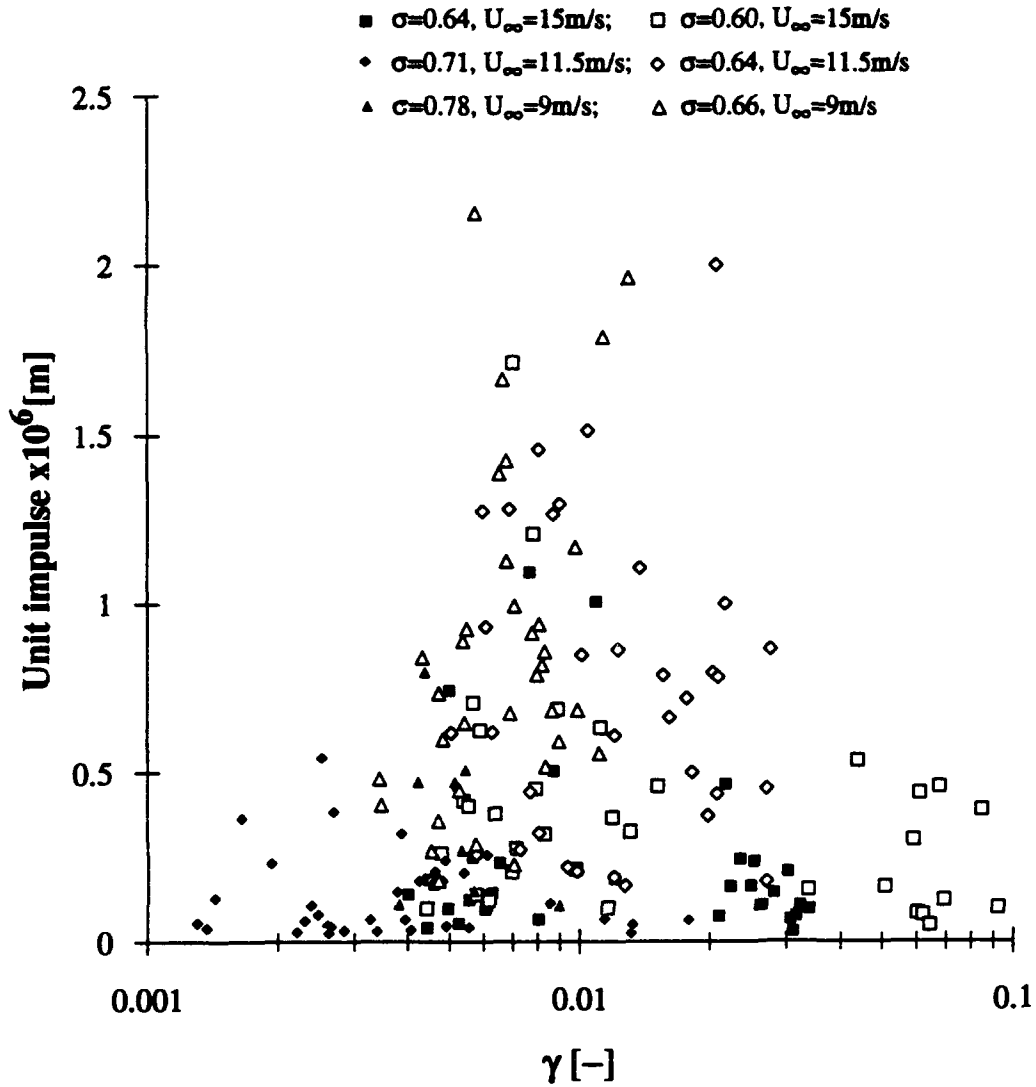


**Figure C.30** Unit acoustic impulse,  $i_{\text{unit}}$ , as a function of  $\gamma$   
*The data is presented for the 50.8cm headform diameter, for electrode signal coverage parameters,  $\gamma$ , ranging from 0.001 to 0.1. Data show measurements for various flow velocities and cavitation numbers.*

Ceccio and Brennen (1989, 1991) also demonstrated that the impulse may be much smaller than this maximum. Vogel *et al.* (1989) have also reported that the cavitation noise increases for the case of unsheared bubbles as the ratio of the maximum bubble radius to the distance to the headform increases. The present data adds to these earlier studies in that it shows a clear decline in the impulse when the value of  $\gamma$  exceeds about 0.02. These  $\gamma$  values correspond to bubbles which have attached streaks and patches and it is apparent that this results in a decrease in the impulse associated with the collapse of these events. The largest coverage parameters,  $\gamma$ , correspond to the lowest cavitation numbers and thus to the largest patch cavities. The reduction in cavitation noise for these types of events can probably be attributed to the fact that the collapse is much less coherent, producing high pressure nodes which are much smaller in magnitude.

## D. UNSTEADY 3-D BUBBLE DYNAMICS MODEL

*"For every problem there is one solution  
which is simple, neat and wrong."  
H.L. Menckel*

### D.1 INTRODUCTION

The purpose of the following method is to model the three dimensional dynamics of the growth and collapse of bubbles as they travel through the low pressure region in a nominally steady flow. Several studies have attempted to model the geometry of collapsing bubbles in simple quiescent flows such as a bubble in the vicinity of a solid wall, or a group of bubbles placed in a symmetric pattern, or a bubble placed in the vicinity of a vortex core (G. Chahine *et al.*, 1993). The method presented here takes into account the presence of a pressure gradient in the flow over an axisymmetric headform and observes the deformations that occur in the shape of the bubble. The numerical model is unsteady, three dimensional and inviscid. The shearing and vorticity resulting from the interactions with the boundary layer have been omitted. The method therefore models the type of traveling bubble that has been observed to grow outside the boundary layer and does not seem to be too affected by its presence. The attached trailing streaks seen in the wake of some of the bubbles are not modeled here.

A solution to the non-cavitating steady potential flow over the headform may be found using a classical panel method approach (Kellogg, 1953, Kuethe and Chow, 1986). The three-dimensionality of the bubbles observed in the LCC experiments indicates that a large number of three-dimensional panels meshed on the surface of the traveling bubble would be necessary to model the dynamics of the flow accurately. Such a method has been developed by Chahine (1977) in which several boundary elements are distributed on the surface of the bubble. The computational time and memory required to solve such a

complex model is very large and limits the solution to a small number of bubbles with a small number of mesh points and simple flow cases.

This present work demonstrates that it is, in fact, possible to model the dynamics of the bubble using a single traveling three-dimensional source whose intensity and position will be determined by averaged conditions on the bubble surface. The deformation of the bubble surface will be entirely determined by the axisymmetric velocity flow field over the headform on which is superimposed the traveling variable intensity source representing the bubble. An image source of identical strength is added inside the headform and travels along with the bubble source. Its position is at all times symmetrically located with respect to the headform surface. This source is added to ensure "smoother" conditions for the zero normal velocity conditions on the headform.

## **D.2 DESCRIPTION OF NUMERICAL METHOD**

### **D.2.1 Potential flow over axisymmetric headform**

#### **D.2.1.a Potential ring panel method**

For the incompressible and irrotational flow considered here, a velocity potential  $\phi$  may be defined such that

$$\nabla^2 \phi = 0. \quad (D.1)$$

Due to the linear nature of Laplace's equation we can apply the principle of superposition in order to model the flow field for complex geometries. The potential flow around an axisymmetric headform may be modeled by the superposition of a uniform free-stream velocity  $U_\infty$  and a series of ring sources distributed over the surface of the headform. The intensity of these rings is uniform over their circumference. For the present case of the flow over a Schiebe headform, the density distribution of the panel rings has been increased in the low pressure region on the surface of the headform as shown in figure D.1.

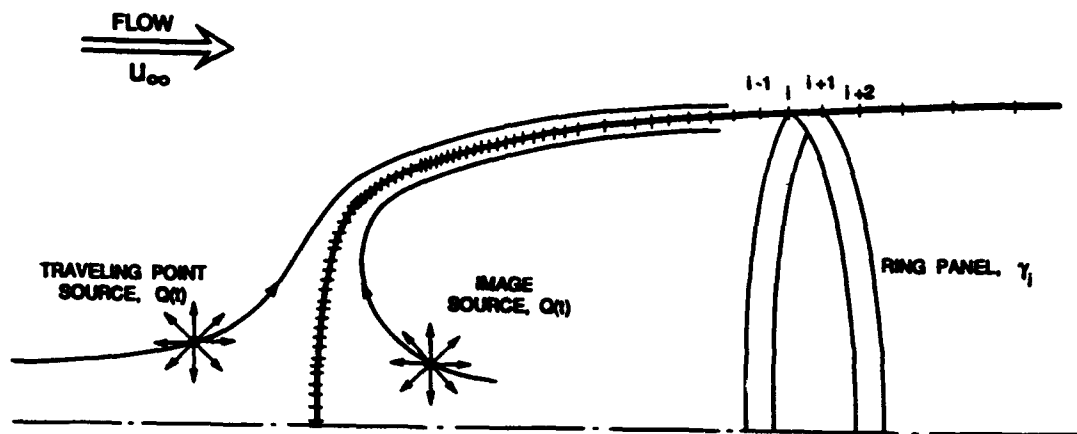


**Figure D.1 Distribution of ring panels on the surface of the Schiebe headform**

*This figure shows the location of the  $N_p$  panels on the headform surface and their increased concentration near the low pressure region. The total number of panels,  $N_p$ , has been set to 93.*

For the purpose of simplifying calculations each ring source has a uniform intensity distribution per unit surface,  $M_i$  [m/s]. A normalized panel intensity,  $\mu_i$ , may be defined using the free-stream velocity :  $\mu_i = M_i / U_\infty$ . The potential flow theory allows us to calculate the induced velocity of each ring panel at any point in the flow field. Superposition further allows us to add the contribution of each panel to determine the flow over the complete headform.

In order to find the induced velocity of the  $i^{\text{th}}$  ring panel at the point C we need to integrate the potential over both the entire width and circumference of the ring. Consider a source ring of thickness  $dx$  and radius  $R$  (which can be visualized as a circular wire) with a total intensity  $2\pi R\mu_i dx$  as shown in figure D.2. The integration of the induced potential over the entire circumference of the wire proceeds as follows. The induced potential of the wire at the point C is

$$d\phi_i = \oint \frac{\mu_i dx}{a} ds \quad (D.2)$$

where  $a$  is the distance from the control point C to the point on the ring represented by the angle  $\theta$  with respect to the vertical axis and can be written as

$$a^2 = r_c^2 + R^2 + (x_c - x)^2 - 2r_c R \cos \theta. \quad (D.3)$$

The induced axial and radial velocity components are derived from the potential  $\phi_i$  as

$$\begin{aligned} dv_{xi} &= \frac{\partial d\phi_i}{\partial x} \\ dv_{ri} &= \frac{\partial d\phi_i}{\partial r} \end{aligned} \quad (D.4)$$

Due to the symmetrical nature of the problem we need only integrate the potential equation D.2 over half of the wire so that

$$\begin{aligned} d\phi_i &= 2R\mu_i dx \int_0^\pi \frac{d\theta}{\sqrt{r_c^2 + R^2 + (x_c - x)^2 - 2r_c R \cos \theta}} \\ dv_{xi} &= -2R\mu_i dx \int_0^\pi \frac{x_c - x}{\sqrt{r_c^2 + R^2 + (x_c - x)^2 - 2r_c R \cos \theta}} d\theta. \\ dv_{ri} &= -2R\mu_i dx \int_0^\pi \frac{r_c - R \cos \theta}{\sqrt{r_c^2 + R^2 + (x_c - x)^2 - 2r_c R \cos \theta}} d\theta \end{aligned} \quad (D.5)$$

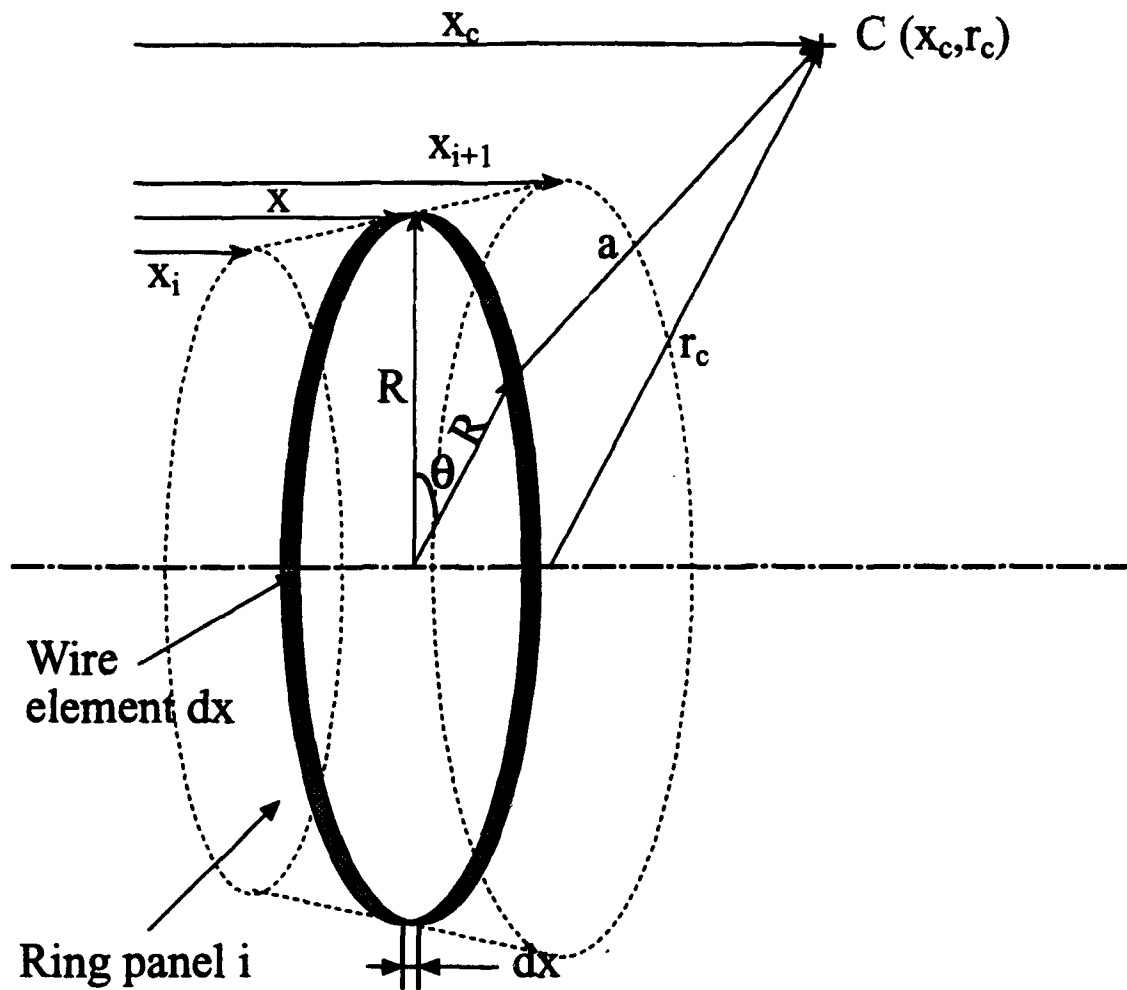


**Figure D.2 Schematic of the ring panel induced velocity at the control point C**

*This figure shows the layout of the  $i$ th ring panel and the variables used to integrate the potential and velocity field at the point C.*



The radial velocity term  $dv_{ri}$  may be rewritten as

$$dv_{ri} = \frac{R\mu_i dx}{r_c} \left[ \int_0^\pi \frac{-r_c^2 + R^2 + (x_c - x)^2}{\sqrt{r_c^2 + R^2 + (x_c - x)^2 - 2r_c R \cos \theta}} d\theta - \int_0^\pi \frac{1}{\sqrt{r_c^2 + R^2 + (x_c - x)^2 - 2r_c R \cos \theta}} d\theta \right]$$

Furthermore, Kellogg (1953) has shown that it is possible to solve these equations in terms of elliptic integrals by defining the quantities  $p^2 = (r_c + R)^2 + (x_c - x)^2$  and  $q^2 = (r_c - R)^2 + (x_c - x)^2$  and letting  $\eta^2 = 1 - \frac{q^2}{p^2}$ . We thus find that

$$\int_0^\pi \frac{d\theta}{\sqrt{r_c^2 + R^2 + (x_c - x)^2 - 2r_c R \cos \theta}} = \frac{2}{p} \int_0^{\pi/2} \frac{d\theta}{\sqrt{\cos^2 \theta + \frac{q^2}{p^2} \sin^2 \theta}} = \frac{2}{p} \int_0^{\pi/2} \frac{d\theta}{\sqrt{1 - \eta^2 \sin^2 \theta}} = \frac{2}{p} E\left(\eta, \frac{\pi}{2}\right)$$

where  $E\left(\eta, \frac{\pi}{2}\right)$  is the complete elliptic integral of the first kind. Similarly we can write that

$$\int_0^\pi \frac{d\theta}{\sqrt{r_c^2 + R^2 + (x_c - x)^2 - 2r_c R \cos \theta}} = \frac{2}{p^3} \int_0^{\pi/2} \frac{d\theta}{\sqrt{1 - \eta^2 \sin^2 \theta}} = \frac{2}{p^3(1 - \eta^2)} \int_0^{\pi/2} \sqrt{1 - \eta^2 \sin^2 \theta} d\theta = \frac{2}{q^2 p} F\left(\eta, \frac{\pi}{2}\right)$$

where  $F\left(\eta, \frac{\pi}{2}\right)$  is the complete elliptic integral of the second kind. Thus we find the

following expressions for the potential and velocity fields in terms of the complete elliptic integrals

$$\begin{aligned} d\phi_i &= \frac{4R\mu_i dx}{p} E\left(\eta, \frac{\pi}{2}\right) \\ dv_{xi} &= \frac{-4R\mu_i dx (x_c - x)}{q^2 p} F\left(\eta, \frac{\pi}{2}\right) \\ dv_{ri} &= \frac{2R\mu_i dx}{r_c p} \left( \frac{-r_c^2 + R^2 + (x_c - x)^2}{q^2} F\left(\eta, \frac{\pi}{2}\right) - E\left(\eta, \frac{\pi}{2}\right) \right) \end{aligned} \quad (D.6)$$

Expressions for the complete elliptic integrals can be found using Hastings' approximations

$$\begin{aligned} E\left(\eta, \frac{\pi}{2}\right) &= \frac{\pi}{2} \left[ 1 - \left(\frac{1}{2}\right)^2 \eta^2 - \left(\frac{3}{2 \cdot 4}\right)^2 \frac{\eta^4}{3} - \left(\frac{3 \cdot 5}{2 \cdot 4 \cdot 6}\right)^2 \frac{\eta^6}{5} - \dots \right] \\ F\left(\eta, \frac{\pi}{2}\right) &= \frac{\pi}{2} \left[ 1 + \left(\frac{1}{2}\right)^2 \eta^2 + \left(\frac{3}{2 \cdot 4}\right)^2 \eta^4 + \left(\frac{3 \cdot 5}{2 \cdot 4 \cdot 6}\right)^2 \eta^6 + \dots \right] \end{aligned} \quad (D.7)$$

In order to find the total potential and velocity vector components at the control point C due to the ring panel "i" we still need to integrate the wire over the width of the panel. Since we assume that the intensity of the source is uniform on the panel we can write

$$\begin{aligned}\varphi_i &= 4\mu_i \int_{x_i}^{x_{i+1}} \frac{R}{p} E\left(\eta, \frac{\pi}{2}\right) dx \\ v_{xi} &= -4\mu_i \int_{x_i}^{x_{i+1}} \frac{R(x_c - x)}{q^2 p} F\left(\eta, \frac{\pi}{2}\right) dx \\ v_{ri} &= \frac{2\mu_i}{r_c} \int_{x_i}^{x_{i+1}} \frac{R}{p} \left( \frac{-r_c^2 + R^2 + (x_c - x)^2}{q^2} F\left(\eta, \frac{\pi}{2}\right) - E\left(\eta, \frac{\pi}{2}\right) \right) dx\end{aligned}\quad (D.8)$$

In the present calculations, these integrals were evaluated numerically using Simpson's rule of integration.

#### D.2.1.b Establishment of a linear system

In order to find the flow at the control point C induced by the entire headform, we superimpose the influence of each of the ring panels, as well as the uniform flow,  $U_\infty$ , in the direction of the x axis. The dimensionless equations for the uniform stream can be simply written as

$$\begin{aligned}\varphi^c &= x_c \\ v_x^c &= 1 \\ v_r^c &= 0\end{aligned}\quad (D.9)$$

For simplicity we extract from equation D.8 the following potential and velocity influence coefficients for the  $i^{\text{th}}$  panel at the point C.

$$\begin{aligned}A_{\varphi i}^c &= 4 \int_{x_i}^{x_{i+1}} \frac{R}{p} E\left(\eta, \frac{\pi}{2}\right) dx \\ A_{xi}^c &= -4 \int_{x_i}^{x_{i+1}} \frac{R(x_c - x)}{q^2 p} F\left(\eta, \frac{\pi}{2}\right) dx \\ A_{ri}^c &= \frac{2}{r_c} \int_{x_i}^{x_{i+1}} \frac{R}{p} \left( \frac{-r_c^2 + R^2 + (x_c - x)^2}{q^2} F\left(\eta, \frac{\pi}{2}\right) - E\left(\eta, \frac{\pi}{2}\right) \right) dx\end{aligned}\quad (D.10)$$

These integral coefficients were numerically evaluated for each of the  $N_p$  panels. By superposition, the potential and velocities at the point C are given by

$$\begin{aligned}\varphi^c &= x_c + \sum_{i=1}^{i=N_p} A_{\phi i}^c \mu_i \\ v_x^c &= 1 + \sum_{i=1}^{i=N_p} A_{xi}^c \mu_i \\ v_r^c &= \sum_{i=1}^{i=N_p} A_{ri}^c \mu_i\end{aligned}\quad (D.11)$$

### D.2.1.c Resolution of the linear system

Our system consists of the  $N_p$  source strengths  $\mu_i$  as unknowns. These are determined so that the boundary condition of zero normal velocity on the surface of the headform is satisfied. To this effect we establish  $N_p$  linearly independent conditions to obtain a closed system. The  $N_p$  zero normal velocity boundary conditions are chosen at the center of each ring panel. Consider  $j$  to be the control point for the boundary condition located in the middle of the  $i^{\text{th}}$  panel, as shown in figure D.3.

The same set of equations is applied to calculate the velocity at the control point  $j$ . In doing so, though, we must take into account the fact that the point  $j$  is located on the panel singularity itself. Indeed we need to exclude the immediate vicinity of the point  $j$  when we use Simpson's integration to integrate over the width of the  $j^{\text{th}}$  panel in order to calculate the self-influence coefficients  $A_{\phi j}$ ,  $A_{xj}$  and  $A_{rj}$ . The boundary condition requires that

$$V_{\text{normal}}|_j = 0 \quad (D.12)$$

which can be written as

$$v_r^j \cos \alpha_j - v_x^j \sin \alpha_j = 0 \quad (D.13)$$

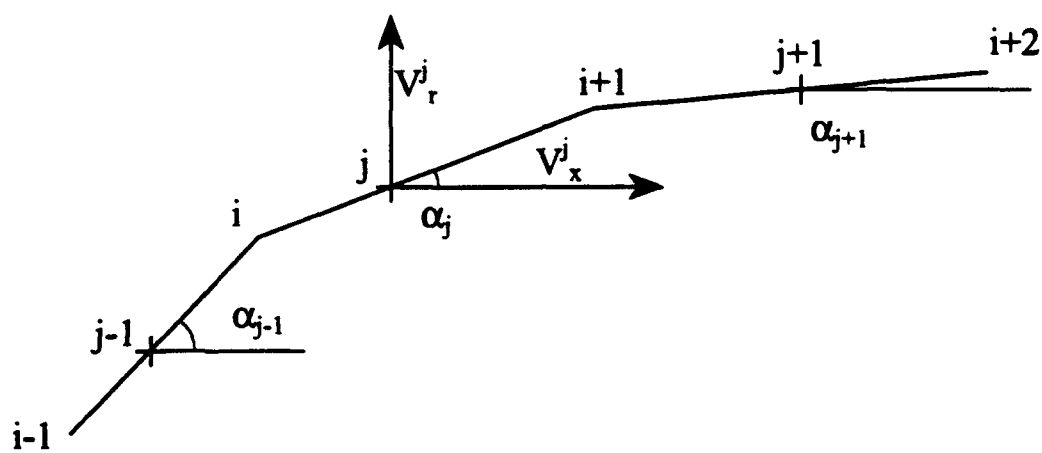


**Figure D.3** Schematic illustrating the zero normal velocity condition  
*The ring panels are represented by the indices "i". The zero normal velocity conditions are imposed at the control points denoted by the indices "j" located at the center of the panels.*

where

$$\begin{aligned} v_x^j &= 1 + \sum_{i=1}^{i=N_p} A_{xi}^j \mu_i \\ v_r^j &= \sum_{i=1}^{i=N_p} A_{ri}^j \mu_i \end{aligned} \quad (D.14)$$

Therefore

$$\sum_{i=1}^{i=N_p} A_{ri}^j \mu_i - \tan \alpha_j \cdot \sum_{i=1}^{i=N_p} A_{xi}^j \mu_i = \tan \alpha_j. \quad (D.15)$$

Therefore, the  $N_p$  linear equations which must be solved can be written in matrix form as

$$A_{ij} \mu_i = t_j \quad (D.16)$$

where  $A_{ij} = A_{ri}^j - A_{xi}^j \cdot \tan \alpha_j$  and  $t_j = \tan \alpha_j$ .

The algorithm employs a standard successive orthogonalization method to solve this set of linear equations. This has the advantage of only requiring one additional dummy vector of size  $N_p^2/4$ .

### D.2.2 Unsteady three dimensional source

In order to model the dynamics of the individual traveling bubble, a three dimensional source is placed in the oncoming uniform stream. A corresponding image source is located inside the headform, at the same distance from the headform surface as the original source. The intensity of the image source is identical to that of the original source at all times, thus ensuring that the combined effect of both sources on the velocity at the headform surface approximately cancels out. The intensity and exact position of the source as a function of time is determined by the conditions on the surface of the bubble and is discussed later.

The effect of a three dimensional source of strength  $Q$  on the potential and velocity flow field is as follows

$$\begin{aligned}\varphi_Q^c &= -\frac{Q}{4\pi a_{cq}} \\ v_{xQ}^c &= \frac{Q}{4\pi} \frac{(x_c - x_q) \cos \theta_c}{a_{cq}^3} \\ v_{rQ}^c &= \frac{Q}{4\pi} \frac{(r_c - r_q) \cos \theta_c}{a_{cq}^3}\end{aligned}\quad (D.17)$$

where  $a_{cq}$  is the distance of the control point C from the source Q and can be written as

$$a_{cq} = \sqrt{(x_c - x_q)^2 + (r_c \cos \theta_c - r_q)^2 + r_c^2 \sin^2 \theta_c}. \quad (D.18)$$

The source strength Q represents the dimensionless volumetric rate of fluid emitted by the source

$$Q = \frac{1}{U_\infty D^2} \frac{dV}{dt} = \frac{dv}{d\tau} \quad (D.19)$$

where V and v are the dimensional and dimensionless bubble volumes. Later we compare the value of the source strength Q to the sum of the strengths of the  $N_p$  ring panels distributed on the headform's surface,  $Q_{\text{headform}} = \sum_{i=1}^{i=N_p} \mu_i$ . From potential flow theory we

can show that the overall volumetric flow rate necessary to generate an infinite body of diameter D is  $\frac{dV}{dt} = \frac{\pi}{4} U_\infty D^2$ . Thus the dimensionless headform source strength is

$$Q_{\text{headform}} = \frac{\pi}{4}. \quad (D.20)$$

We will see later that the source strength required to model the traveling cavitation bubble is always substantially less than this value of  $\pi/4$ . In order to take into account the effect of the traveling bubble source and its image source on the zero normal velocity boundary condition, we need to add one term in the linear system previously defined by equation D.16. We compute the normal velocity condition only in the plane containing the source and image source (i.e., where  $\theta_c=0$ ). The consequences of this will be analyzed later in the code validation section. The linear system is now written as

$$\sum_{i=1}^{i=N_p} (A_{in}^j - \tan \alpha_j \cdot A_{xi}^j) \mu_i = (1 + v_{rQ}^j(\tau) + v_{r\bar{Q}}^j(\tau)) \tan \alpha_j - v_{xQ}^j(\tau) - v_{x\bar{Q}}^j(\tau) \quad (D.21)$$

where the subscript Q denotes bubble source terms and  $\bar{Q}$  denotes image source terms. Therefore only the right-hand side vector term needs to be changed in our  $N_p$  system of equations. The matrix equation becomes

$$A_{ij}\mu_i = t'_j \quad (D.22)$$

where, as before

$$A_{ij} = A_{ni}^j - A_{xi}^j \cdot \tan \alpha_j. \quad (D.23)$$

but the vector on the right hand side is now

$$t'_j = (1 + v_{rQ}^j(\tau) + v_{r\bar{Q}}^j(\tau)) \tan \alpha_j - v_{xQ}^j(\tau) - v_{x\bar{Q}}^j(\tau). \quad (D.24)$$

We will see later that the influence of these additional terms is small and they can therefore be neglected in the solution of the flow field. Indeed, the combined effect of the source, Q, and the image source,  $\bar{Q}$ , on the normal velocity is small over the entire headform. Neglecting these terms, we may therefore simply use equation D.16 and thus avoid having to solve this  $N_p$  system of equations for every time step, that is for every different source position and strength Q. The computational time can therefore be greatly reduced since the linear system needs to be solved just once at the beginning of the program.

### D.2.3 Bubble growth and collapse algorithm

Initially the algorithm assumes a stable spherical nucleus of radius  $R_0$  in equilibrium in the oncoming uniform flow. The initial position of the nucleus,  $x_{q0}$  and  $r_{q0}$ , may be chosen as desired. In order to reduce computational time in the early nucleus growth phase, the algorithm is effectively started only when the nucleus becomes explosively unstable. Until then the nucleus is assumed to follow a streamline and remain in a stable spherical equilibrium state, with a radius equal to the equilibrium radius  $r_e$  given by equation B.4. The unsteady bubble growth algorithm starts when the nucleus becomes neutrally stable and reaches the critical pressure condition according to equations B.5 and B.6.

After the nucleus becomes unstable, the source position  $x_q(\tau)$ ,  $r_q(\tau)$  and strength  $Q(\tau)$  need to be computed for each time step,  $\tau$ . The source displacement is also modified from the simple displacement along a streamline in a manner described below. These quantities,  $x_q(\tau)$ ,  $r_q(\tau)$  and  $Q(\tau)$ , then determine the pressure and velocity field for the time  $\tau$ . During each time step, the velocity vectors on the surface of the bubble derived from the potential flow are used to compute the new bubble shape and source location. This cycle is repeated in time. The algorithm continues to compute the bubble shape until the bubble has completely collapsed.

#### D.2.3.a Source strength, $Q(\tau)$ , and position computation

Consider the bubble shape at a particular time step  $\tau$ . As in the derivation of the Rayleigh-Plesset equation, the balance of forces acting on the surface of a growing bubble consists of the liquid pressure on the surface of the bubble (manifest by the  $Cp^*_{surf\_i}$  term), the vapor pressure (manifest by the  $\sigma$  term) and partial pressure of the gas inside the bubble (manifest by the  $(V_0/V)^k$  term), the surface tension (manifest by the  $We$  term) and the viscous normal stress (manifest by the  $Re$  term) due to the expansion of the bubble surface. In a dimensionless form, this balance yields

$$Cp^*_{surf\_i} = -\sigma + \frac{4}{Re} \left( \frac{\partial v_i}{\partial r} \right) + \left( \sigma + \frac{4}{r_0 We} \right) \left( \frac{V_0}{V} \right)^k - \frac{4}{r_{curv\_i} We} \quad (D.25)$$

where the index "i" indicates a local quantity at some point on the surface of the bubble.  $V_0$  is the initial equilibrium nucleus volume and  $V$  the current bubble volume.  $Cp^*_{surf\_i}$  is thus the local boundary pressure coefficient one expects to find on the surface of the bubble.

Note that in the case of a spherical bubble we can derive from the equation of continuity the velocity gradient normal to the bubble surface

$$\frac{\partial v_i}{\partial r} = -\frac{2}{r} \frac{\partial r}{\partial \tau} \quad (D.26)$$

and thus



$$Cp_{surf}^* = -\sigma - \frac{8}{rRe} \left( \frac{\partial r}{\partial \tau} \right) + \left( \sigma + \frac{4}{r_0 We} \right) \left( \frac{r_0}{r} \right)^{3k} - \frac{4}{rWe}. \quad (D.27)$$

Furthermore, for the spherical case the momentum equation yields

$$Cp_{surf}^* = Cp_{\infty}^* + 2r \frac{\partial^2 r}{\partial \tau^2} + 3 \left( \frac{\partial r}{\partial \tau} \right)^2 \quad (D.28)$$

where  $Cp_{\infty}^*$  is the pressure coefficient in a quiescent media at an infinite distance. One therefore obtains the dimensionless Rayleigh-Plesset equation B.2.

The unsteady Bernoulli equation for the pressure in a potential flow, when written in dimensionless form yields

$$Cp = 1 - v_x^2 - v_r^2 - 2 \frac{\partial \phi}{\partial \tau}. \quad (D.29)$$

In the present circumstances, the potential flow calculations described in section D.2.2 (including the influence of the traveling sources) provide the potential and velocity field at all points in the flow. The velocities  $v_x^c$  and  $v_r^c$  and the potential  $\phi^c$  induced at a point C in the flow are given by

$$\begin{aligned} \phi^c &= x_c + \sum_{i=1}^{i=N_p} A_{\phi i}^c \mu_i - \frac{Q}{4\pi} \left( \frac{1}{a_{cq}} + \frac{1}{a_{cq}^-} \right) \\ v_x^c &= 1 + \sum_{i=1}^{i=N_p} A_{xi}^c \mu_i + \frac{Q}{4\pi} \left( \frac{(x_c - x_q) \cos \theta_c}{a_{cq}^3} + \frac{(x_c - x_q^-) \cos \theta_c}{a_{cq}^{3-}} \right) \\ v_r^c &= \sum_{i=1}^{i=N_p} A_{ri}^c \mu_i + \frac{Q}{4\pi} \left( \frac{(r_c - r_q) \cos \theta_c}{a_{cq}^3} + \frac{(r_c - r_q^-) \cos \theta_c}{a_{cq}^{3-}} \right) \end{aligned} \quad (D.30)$$

Therefore the pressure coefficient given by the unsteady Bernoulli equation is strongly dependent on the traveling source strength, position and rate of change in time.

The evaluation of the source strength,  $Q$ , proceeds as follows. For each time step, the algorithm finds the value of the source  $Q_i$ , such that the pressure coefficient,  $Cp_i$ , calculated using equation D.29, matches the required boundary condition,  $Cp_i^*$ , given by equation D.25, so that

$$Cp_i = Cp_i^*. \quad (D.31)$$

Note that this computation is done locally at each point on the surface of the bubble (as indicated by the indices "i"). For that purpose, the surface of the bubble is discretized by defining  $N_b$  nodes which are equidistant from one another and cover the circumference of the bubble in the axial plane of symmetry ( $\theta_c=0$ ). This plane of symmetry contains the highest pressure gradient in the flow above the headform and thus captures most of the dynamics of deformation of the bubble. The method could be extended to include additional nodes not on this plane of symmetry in order to have an even better estimate of the required source strength  $Q$ . For the present calculation  $N_b=45$ , as can be seen in figure D.4. Also note the fact that the radius of curvature of the bubble at each node is estimated by measuring the radius of curvature in the symmetry plane only. This approximation can be made since the surface tension effects are influential only when the radius of curvature is very small, which is the case when the bubble has an almost spherical shape.

The computation of the condition D.31 at each node of the bubble surface yields  $N_b$  values of the source strengths  $Q_i$ . In order to compute the bubble growth over the next time step we need to determine an average source strength  $Q$  for this particular time. For this purpose we use a weighted average of the  $N_b$  values of  $Q_i$ . The weighting term is chosen to give more weight to the points furthest from the headform and is given by the normal distance,  $\delta_i$ , of the bubble surface node "i" to the headform's surface, as shown in figure D.4. Therefore the averaging expression for the source is given by

$$Q = \frac{\sum_{i=1}^{i=N_b} \delta_i Q_i}{\sum_{i=1}^{i=N_b} \delta_i} \quad (D.32)$$

This choice is justified by the fact that it leads to bubble pressures which are constant from one time step to the next. We will see later that the values of  $Q_i$  also vary little over the surface of the bubble.

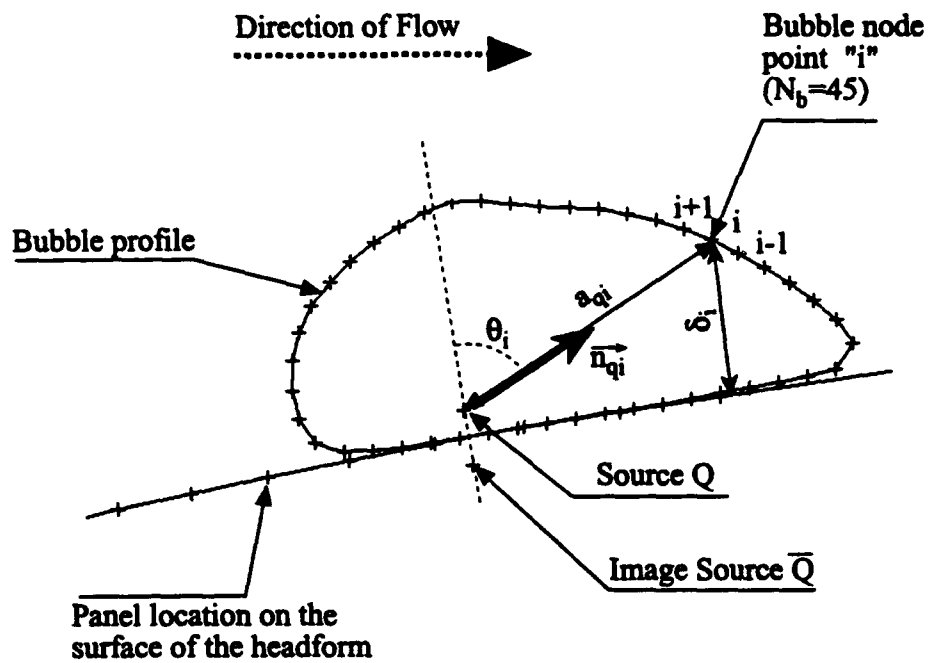


**Figure D.4 Bubble discretization scheme**

*The bubble is discretized using  $N_b=45$  equidistant nodes. All the nodes are located on the plane of symmetry of the bubble. Also presented in this figure are the variables used to compute the bubble evolution.*

The next step is to displace the source in order to minimize the variation in source strengths,  $Q_i$ , over the surface of the bubble. Indeed, experience showed that there is an optimum location for the source in the bubble such that the differences between the average source strength  $Q$  and the local ideal value  $Q_i$ , are minimized over the  $N_b$  bubble points. Naturally the image source in the headform is also displaced along with the bubble source. The displacement vector of the source,  $\bar{\epsilon}$ , is determined in the following manner. From equation D.31, we find the source strength,  $Q_i$ , necessary to satisfy the pressure boundary condition at each point  $i$ . The algorithm then calculates the displacement,  $\epsilon_i$ , of the source in the direction of the bubble surface node "i" (indicated in figure D.4 by the unit vector  $\bar{n}_{qi}$ ), such that the pressure boundary condition in equation D.31 is satisfied for the average source strength value  $Q$ . In other words we find the displacement of the source that would yield  $Q_i=Q$ . In order to compute the displacement  $\epsilon_i$ , two pressure coefficient gradients are computed. The first gradient,  $\nabla_{Qi} = \frac{\partial C_{pi}}{\partial Q}$ , represents the change in pressure coefficient on the surface of the bubble as the source strength varies. The second gradient,  $\nabla_{\epsilon i} = \frac{\partial C_{pi}}{\partial \epsilon}$ , represents the change in pressure coefficient on the surface of the bubble as the source moves in the direction  $\bar{n}_{qi}$ . A first-order approximation of the source displacement  $\epsilon_i$  can then be obtained as

$$\epsilon_i = (Q_i - Q) \frac{\nabla_{Qi}}{\nabla_{\epsilon i}}. \quad (D.33)$$

The final overall displacement vector  $\bar{\epsilon}$  applied to the source is then given by averaging all the displacements,  $\epsilon_i$ , in all the directions  $\bar{n}_{qi}$ . It is again effective to weight the displacements  $\epsilon_i$  by the distance  $\delta_i$  of the bubble node from the headform surface. Thus, the final source displacement vector used is

$$\bar{\epsilon} = \frac{\sum_{i=1}^{i=N_b} \delta_i \epsilon_i \bar{n}_{qi}}{\sum_{i=1}^{i=N_b} \delta_i}. \quad (D.34)$$

The process of averaging the source strength and repositioning the source is repeated until the values converge. Usually three iterations are necessary for convergence.

#### D.2.3.b Bubble displacement and time step incrementation

Having located the optimal source location and strength for a particular time,  $\tau$ , the computation then proceeds to the next time step. During the time increment the bubble is deformed and travels downstream in the following manner. From equation D.30 the velocity at each node on the surface of the bubble is calculated. The position and shape of the bubble at the next time step is then given by displacing each node through a distance equal to the velocity vector times the time increment,  $\Delta\tau$ . During this time increment the bubble source is also displaced along its pathline and finally the image source is moved accordingly. We note that the Bernoulli equation D.29 requires the values of the source strength and position from the previous time step in order to compute the unsteady inertial term,  $\partial\phi/\partial t$ .

The averaged value of the source strength,  $Q$ , is thus used to compute the unsteady pressure field and the deformation of the bubble surface during each time step. We note, though, that this averaging can create some instabilities on the bubble surface, particularly during the collapse phase. The use of an average source strength does not correct for local errors in the surface location. Some error instabilities are caused by the fact that the velocity vector induced by the source increases inversely with the square of the distance from the source,  $\vec{v}_{qi} \propto Q/\vec{a}_{qi}^2$ . To some extent, the bubble displacement algorithm tends to correct errors in the node location and to stabilize itself during the growth phase ( $Q>0$ ). Nodes located too close to the source will automatically generate larger outward velocities and are thus displaced further from the source. However, during the collapse phase ( $Q<0$ ), a node on the bubble surface located too close to the source will tend to generate a larger inward velocity. Thus this surface distortion will increase during each time step. These instabilities are thus prone to generate reentrant jets.

Reentrant jet instabilities on the bubble surface during collapse have been widely studied, particularly in the case of non-symmetrical flow configurations. Benjamin and Ellis (1966) first observed such jets experimentally in the case of bubbles in the presence of a nearby solid wall boundary. Later Plesset and Chapman (1971) studied the formation of these reentrant jets theoretically. Additional studies by Duncan and Zhang (1991) have shown the effect of compliant walls of different stiffness. They have shown that the direction and intensity of the jet are dependent on the stiffness of the boundary. The collapse of a bubble near a free surface has been shown to develop reentrant jets directed away from the free surface (Chahine 1977). It is important to note, though, that the present algorithm generates instabilities on some nodes of the surface that are not caused by real hydrodynamic instabilities. These reentrant jets are due to a suction of the source on these nodes located too close to the source. The pressure coefficient field does not exhibit the reentrant jet-like depression that one would expect if these jets had a physical meaning. The dynamic pressure boundary condition on the surface of these nodes (equation D.31) is therefore not satisfied and we can thus conclude that this jet formation is erroneous. In order to counter such error instabilities the calculation of the displacement of the bubble surface needs to include some corrective terms in addition to the simple velocity displacement described previously. The purpose for these corrections is to reposition the unstable bubble surface points closer to the required boundary condition of equation D.31.

The unstable bubble surface nodes requiring such corrective terms may be identified as those exhibiting "adverse conditions". For the growth case ( $Q > 0$ ) an adverse condition may be defined by a node requiring a slower growth rate than the average source strength  $Q_i < Q$ . For the collapse case ( $Q < 0$ ) adverse conditions may be defined as requiring a slower collapse rate than the average source strength  $Q_i > Q$ . We may generalize these two cases by stating that adverse conditions occur when the relative difference between the average source,  $Q$ , and the local source intensity,  $Q_i$ , is larger than

some chosen fractional value  $k$ :  $\frac{(Q - Q_i)}{Q} > k$ . For the present calculations  $k$  has been set to  $k=10^{-3}$ . The stabilizing method applied at these node points takes the form of source strength corrections. For the velocity displacement calculation at these points, a corrected source strength,  $Q_{\text{corrected}_i}$ , is used in place of the average source strength  $Q$ . A first-order approximation using the same pressure coefficient gradients as in equation D.33 is used to compute this corrected source and is expressed in the following equation

$$Q_{\text{corrected}_i} = Q + (Q_i - Q) \frac{\nabla_{Q_i} a_{qi}^2}{\nabla_{\epsilon_i} \Delta\tau} = Q + (Q_i - Q) \epsilon_i. \quad (\text{D.35})$$

We note that, without the influence of the image source, this correction would displace the surface node "i" by an additional value  $\epsilon_i$  in the direction of the unit vector  $\bar{n}_{qi}$ .

The time increment,  $\Delta\tau$ , used has to be adapted during the growth or collapse phase of the bubble. Two important factors need to be taken into account in determining its value:

1) The source displacement per time step should not exceed a fraction  $k$  of the bubble size. This is particularly important when we consider that the computation of the unsteady pressure term in the Bernoulli equation D.31,  $\frac{\partial\phi}{\partial\tau}$ , requires the computation of a finite difference using values of the source location at two successive time steps. This condition may be expressed as

$$\Delta\tau < \frac{k \cdot r_{\text{cap}}}{\sqrt{v_{qx}^2 + v_{qy}^2}} \quad (\text{D.36})$$

where  $r_{\text{cap}}$  is the average radius of the bubble and  $v_{qx}$  and  $v_{qy}$  are the velocities used for the displacement of the source.

2) The volume change of the bubble per time step should not exceed a fraction,  $k$ , of the bubble volume. This condition becomes crucial when the bubble volume is small, particularly during the final phase of the collapse. We may express this condition as

$$\Delta\tau < \frac{kQ}{\frac{4}{3}\pi r_{\text{volume}}^3}. \quad (\text{D.37})$$

Experience indicated that preferred values of both of the  $k$  factors were about 0.05. The time step used in the algorithm corresponds to the more restrictive of the two conditions.

Even though the presence of the image source inside the headform should minimize the normal velocity on the surface of the headform, it is good practice to check and see whether any of the nodes on the bubble surface have entered the headform during the time incrementation procedure. Indeed the underside of the bubble is located extremely close to the headform surface and numerical errors may cause some points to actually penetrate the headform. For the same reason it is wise to check that the source location does not come too close to the surface of the bubble (especially during the phase of the bubble growth when the source is strongly attracted to the headform). Finally, because of the deformation of the bubble, it is necessary to redefine the  $N_b$  nodes on the surface of the bubble at each time step to ensure that they are equidistant from one another. All of these steps may be summarized in the flow chart of figure D.5.



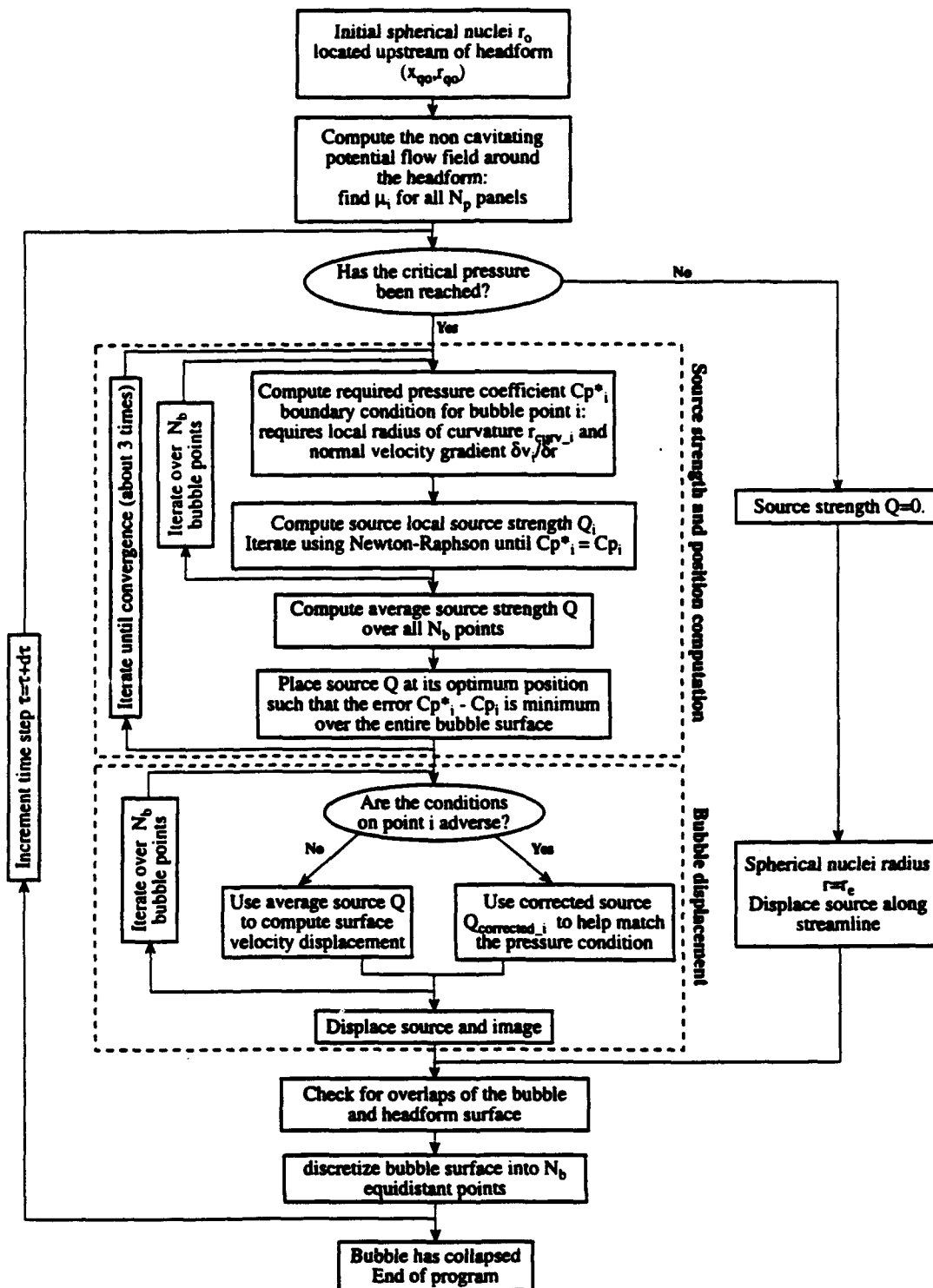


**Figure D.5 Program flow chart**

*Illustrates the algorithm used to calculate the bubble motion and deformation from an initial spherical nucleus to the end of the collapse. The major outer loop involves the increment with time and the inner one the iterations required in order to find the correct source strength and location at each time.*

### D.3 PRESSURE PERTURBATION ANALYSIS

In order to analyze the dynamics of a traveling bubble the following quantities need to be defined. The pressure coefficient perturbation,  $\Delta C_p$ , is defined as the difference between the unsteady pressure caused by the traveling bubble over the headform surface and the original pressure under non-cavitating conditions.

$$\Delta C_p = C_p|_{\text{with bubble}} - C_p|_{\text{without bubble}} \quad (D.38)$$

Using the unsteady Bernoulli equation D.29, the pressure perturbation can also be written as the combined effect of a perturbation in the velocity field,  $\Delta C_{p_v}$ , and a perturbation in the time derivative of the potential field,  $\Delta C_{p_\phi}$ , such that

$$\Delta C_p = \Delta C_{p_v} + \Delta C_{p_\phi} \quad (D.39)$$

where

$$\begin{aligned} \Delta C_{p_v} &= (v_x^2 + v_r^2)|_{\text{without bubble}} - (v_x^2 + v_r^2)|_{\text{with bubble}} \\ \Delta C_{p_\phi} &= -2 \frac{\partial \phi}{\partial \tau}|_{\text{with bubble}} \end{aligned}$$

Both of these effects are quite complex and generate three dimensional perturbations in the pressure field. We may write the cavitating velocity field as the superposition of the velocity field induced by the headform without cavitation and the velocity field induced only by the sources

$$v|_{\text{with bubble}} = v|_{\text{headform}} + v|_{\text{sources}} \quad (D.40)$$

Replacing those velocities in equation D.39 we find that

$$\Delta C_{p_v} = -2v_x|_{\text{sources}}v_x|_{\text{headform}} - 2v_y|_{\text{sources}}v_y|_{\text{headform}} \quad (D.41)$$

We see that the change in the velocity related pressure coefficient perturbation,  $\Delta C_{p_v}$ , consists of the product of the velocity induced by the sources and the velocity induced by the non-cavitating headform. As a first approximation we may consider the velocity field induced by the sources to be isotropic and to decay in a spherical manner far from the sources. The velocity field induced by the flow over the headform has a much more complex, three-dimensional structure. Therefore the product of those two velocity fields

generates a pressure coefficient perturbation field,  $\Delta C_{p_v}$ , which is not spherical. Furthermore, the pressure perturbation field due to the time derivative of the potential field,  $\Delta C_{p_\phi}$ , is also non-isotropic. Indeed the sources change position as their strength varies, thus generating a preferred direction in the pressure perturbation. The addition of these two non-spherical pressure field perturbations in equation D.39 leads to a complex pressure field perturbation,  $\Delta C_p$ . The shape of this perturbation is crucial in the present algorithm since it eventually determines the shape of the bubble. This three-dimensionality is an essential feature of the dynamic boundary condition on the surface of the bubble, and will ultimately lead to the differences we will observe between this method and the spherical Rayleigh-Plesset calculations. A more detailed analysis of the shape of the pressure perturbation field will be described later in section D.5 where we discuss some results of bubble computations.

#### **D.4 ERROR ESTIMATION AND CODE VALIDATION**

All the figures illustrating estimates of the errors in the numerical method use the following typical cavitation condition:  $R_0=100\mu\text{m}$ ,  $D=50.8\text{cm}$ ,  $U_\infty=11.5\text{m/s}$ ,  $\sigma=0.45$  with an initial nucleus position:  $x_{q0}=-1.0$ ,  $r_{q0}=0.01$ . This condition is roughly in the middle of the range of the conditions calculated and thus the errors are quite representative.

##### **D.4.1 Normal velocity leakage into the headform**

In this paragraph we will look at the normal velocity leakage into the headform due to the presence of the traveling sources. As stated in equation D.20 the overall dimensionless source strength required to model the Schiebe headform is equal to  $\pi/4$ . We can see from figure D.17 that for the range of cavitation numbers tested the bubble source strength,  $Q$ , does not exceed a value of about 0.002. The traveling source strength is therefore less than 0.2% of headform strength. This small percentage, combined with the fact that the source is coupled to an image source of equal intensity inside the headform, shows how little influence the bubble has on the overall flow over the

headform. We must note that this conclusion applies to the influence of the source on the velocity field but not to the influence of the source on the pressure field in the vicinity of the bubble, since the pressure calculation also takes into account the time derivative of the source strength, as manifest in equation D.29.

#### **D.4.1.a Small normal velocity perturbation assumption**

As mentioned previously and in paragraph D.2.2, the presence of the traveling source together with its image source has very little effect on the zero normal velocity condition on the surface of the headform. Therefore, the computation of the linear system D.22 does not appear to be necessary at every time step. In this paragraph we will attempt to quantify the error caused by not solving the zero normal velocity condition on the headform surface for each new source position and strength. For this purpose, the normal velocity on the surface of the headform has been computed in the plane of symmetry containing the bubble source and the axis of revolution. Figure D.6 shows the normal velocity divided by the tangential velocity at different times during the growth and collapse phases. We observe that the maximum normal velocity error is about 0.4%, thus validating our approximation. This small error is due to the following effects. In the region of the headform surface close to the bubble, where the influence due to the traveling source might be substantial, the normal velocity is countered by the presence of the image source inside the headform. The exact location of this image source with respect to the original source is crucial and requires careful consideration of the position, slope and radius of curvature of the panel distribution on the surface of the headform. For the headform control points further from the bubble, the source has little influence on the normal velocity condition since the velocity induced by the source decays as the inverse square of the distance from the source.

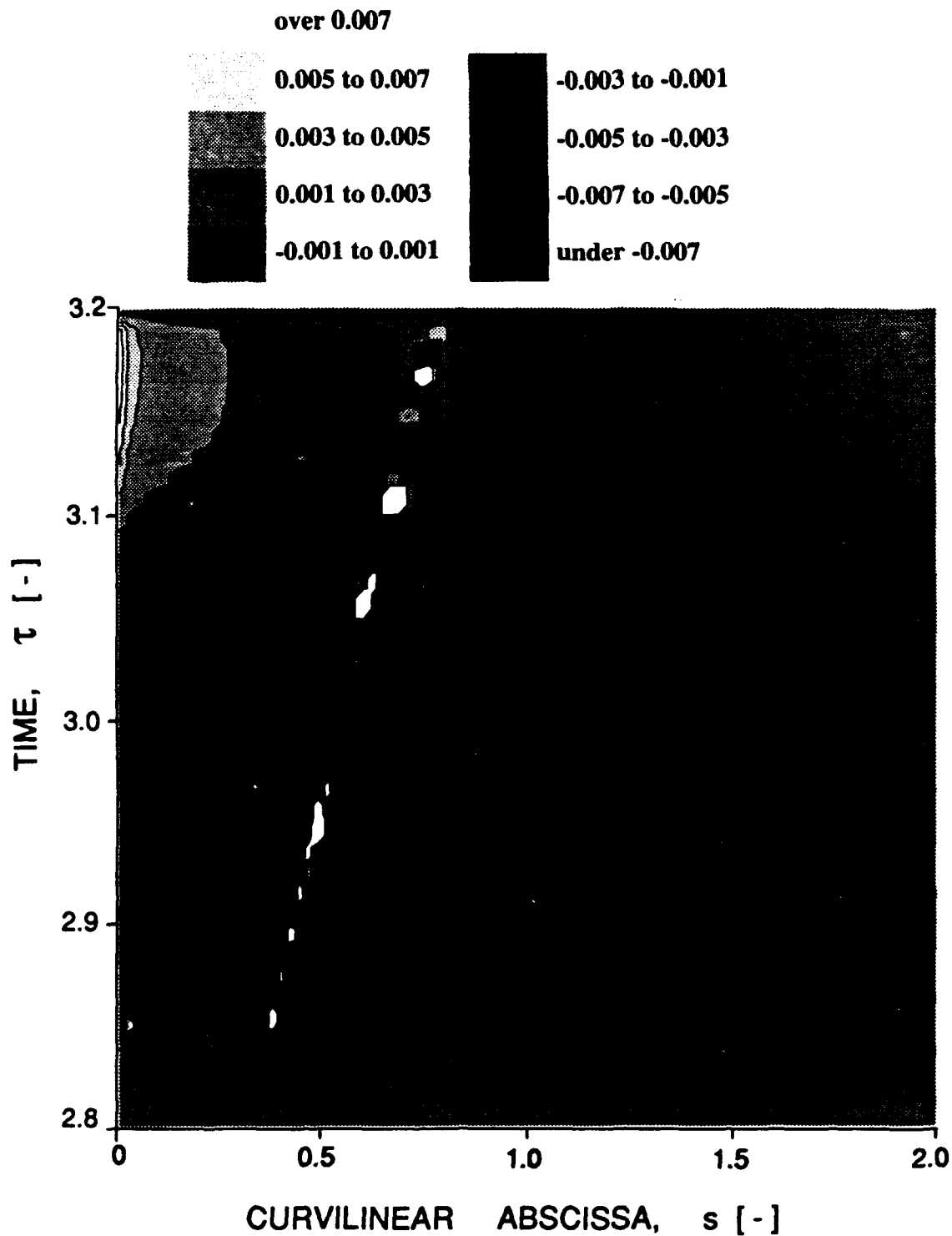


**Figure D.6 Normal velocity [%] in the axial direction on the surface of the headform**

*Calculated normal velocities divided by the tangential velocity for different locations on the surface of the headform, as indicated by the dimensionless curvilinear abscissa,  $s$ .*

#### **D.4.1.b Superposition of an axisymmetric and a three-dimensional flow**

We should also quantify the error due to the superposition of a series of axisymmetric ring panels and a three-dimensional source. A full three-dimensional flow computation would require the discretization of the ring panels in the circumferential direction. The error introduced by not performing this discretization may be estimated by looking at the normal velocity distribution over the circumference of the headform. Figure D.7 shows the distribution of the normal velocity divided by the tangential velocity over the circumference of the headform. The plot shows these values for various times, ranging from growth to collapse conditions. The axial locations,  $x$ , at which the velocities have been computed around the circumference are identical to the axial positions of the traveling source for each time step. The angle,  $\theta$ , shown is taken relative to symmetry plane containing the source (as shown in figure D.2).

We can see that the maximum error is less than 1%, thus validating our approximation. Once again, due to the decay of the velocity with the distance from the source, the influence of the source appears to be only significant for angles,  $\theta$ , under 30 degrees. We conclude that this model, combining axisymmetric ring elements with an unsteady traveling three-dimensional source, is capable of modeling the three-dimensional geometry of the bubble. Discretization of the ring panels around their circumference is therefore not necessary.

#### **D.4.2 Pressure distribution on the surface of the bubble**

In this section we estimate the error in the computation of the shape of the bubble by examining the pressure distribution on the surface of the bubble as a function of time. This error may be quantified by contrasting the pressure coefficient on the surface of the bubble,  $C_p$ , given by solving the potential flow, with the pressure coefficient,  $C_p^*$ , given by the pressure boundary condition in equation D.25. Figure D.8 shows the difference

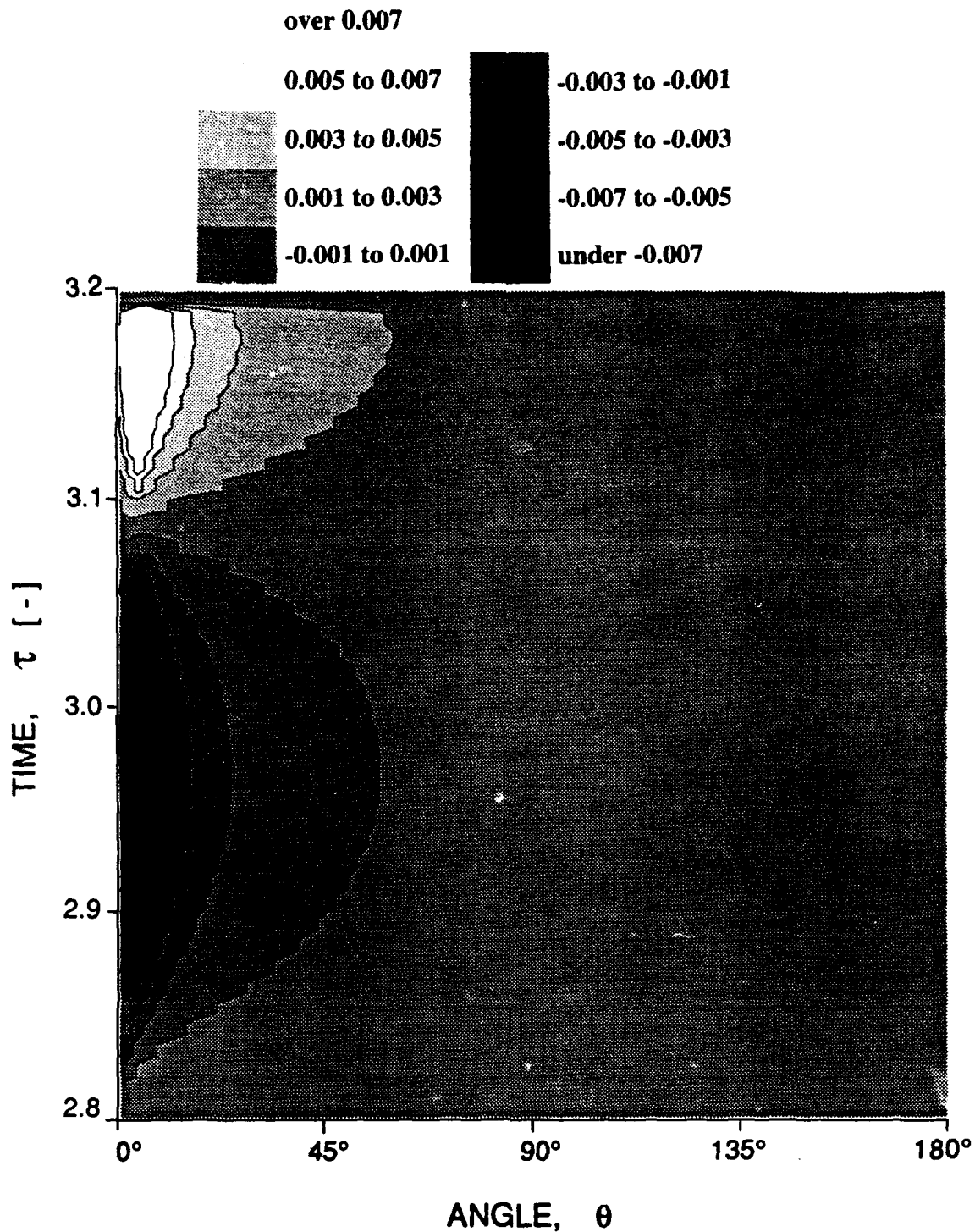


**Figure D.7 Normal velocity [%] in the circumferential direction on the surface of the headform**

*Calculated normal velocities divided by the tangent velocity for different angular positions on the surface of the headform, as indicated by the angle  $\theta$ . The axial locations for the velocity computation are the same as the axial location of the source.*

between these two pressures on the exterior surface of the bubble for various times. The angle,  $\theta$ , is defined relative to the direction normal to the headform as represented in figure D.4. Figure D.8 shows the pressure difference for angles,  $\theta$ , between  $-90^\circ$  to  $+90^\circ$  corresponding to the exterior surface of the bubble.

We observe that, for all time steps, the difference between pressure coefficients,  $C_p - C_p^*$ , over the exterior surface of the bubble is between 0.05 and -0.1. The condition on the surface pressure is thus fairly well satisfied at all times. The single source model is therefore able to appropriately modify the original pressure field induced by the headform in the vicinity of the bubble. From the computation of equation D.25 we also know that, once the bubble is larger than a few times its original nucleus size, the viscous, surface tension and non-condensable gas content terms become small compared to the cavitation number term. Thus, for almost all times  $C_p^*$  is roughly equal to  $-\sigma$  and figure D.8 simply represents the sum  $C_p + \sigma$ . The absolute pressure coefficient variations on surface of the bubble are thus less than  $\pm 0.1$ .

It is also possible to quantify the error in the shape of the surface of the bubble by examining the local source strength distribution,  $Q_i$ . Figure D.9 shows the difference between the ideal source strength,  $Q_i$ , required in order to fulfill the  $C_p = C_p^*$  condition and the averaged source strength,  $Q$ , used by the model at each time increment. The difference presented in this figure is divided by  $|Q|$  and is shown for the exterior surface versus time in a manner similar to figure D.8.

We observe that the departure from the average source value  $Q$  is small, the values of  $(Q_i - Q)/|Q|$  being less than 0.01 at all times. Thus a simple source comes very close to modeling the three dimensionality of the bubble. Naturally, the relative error becomes large when the source strength  $Q$  approaches zero around the time  $\tau \approx 3.09$ . Some important trends may be noted by comparing figures D.8 and D.9.



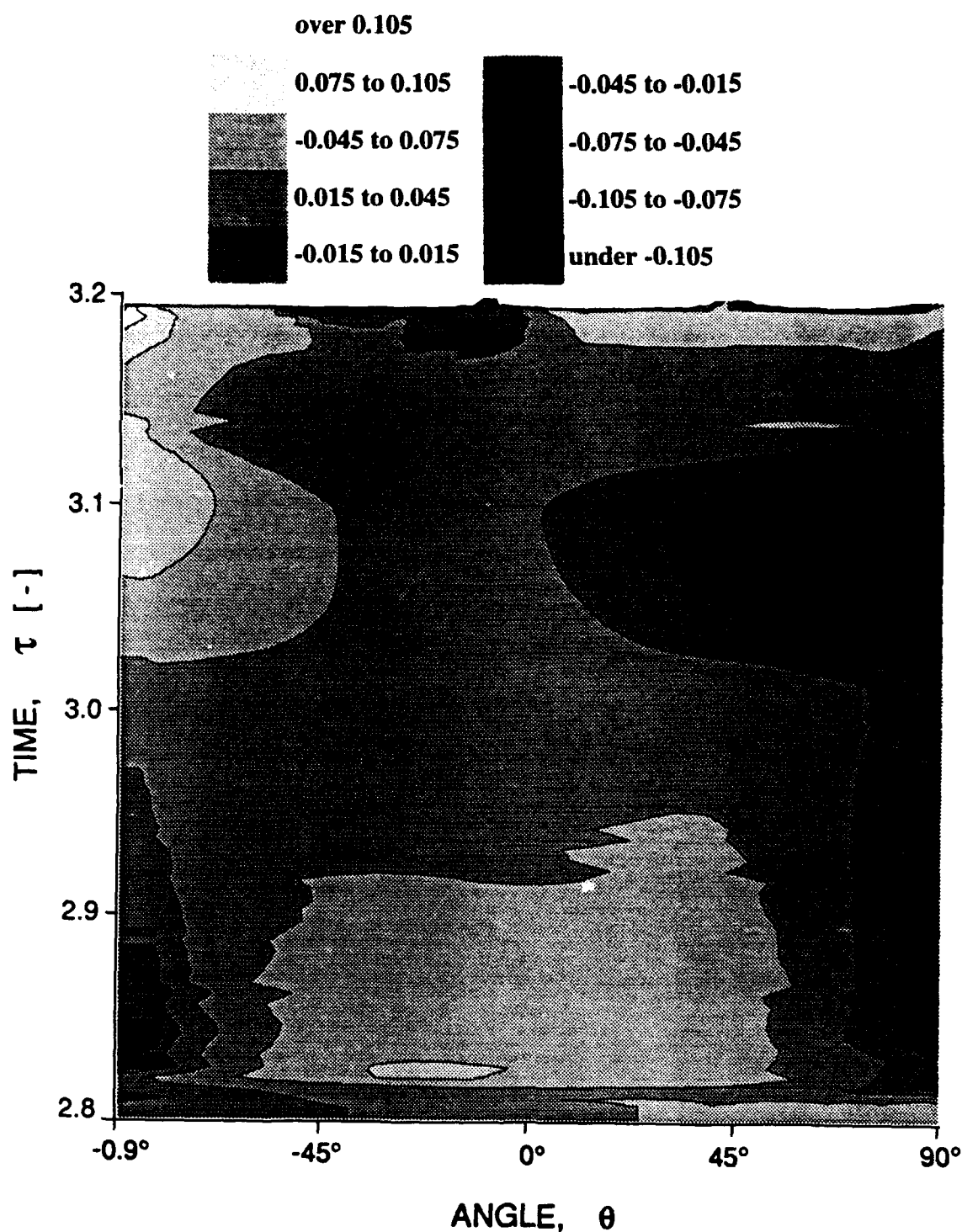


**Figure D.8 Error in the pressure coefficient distribution on the surface of the bubble**

*The plot shows the difference in pressure coefficients  $C_p - C_p^*$  for different locations on the surface of the bubble represented by the angle  $\theta$ . The range of angles shown covers the exterior surface of the bubble. These values are plotted for different dimensionless times during the growth and collapse phases.*

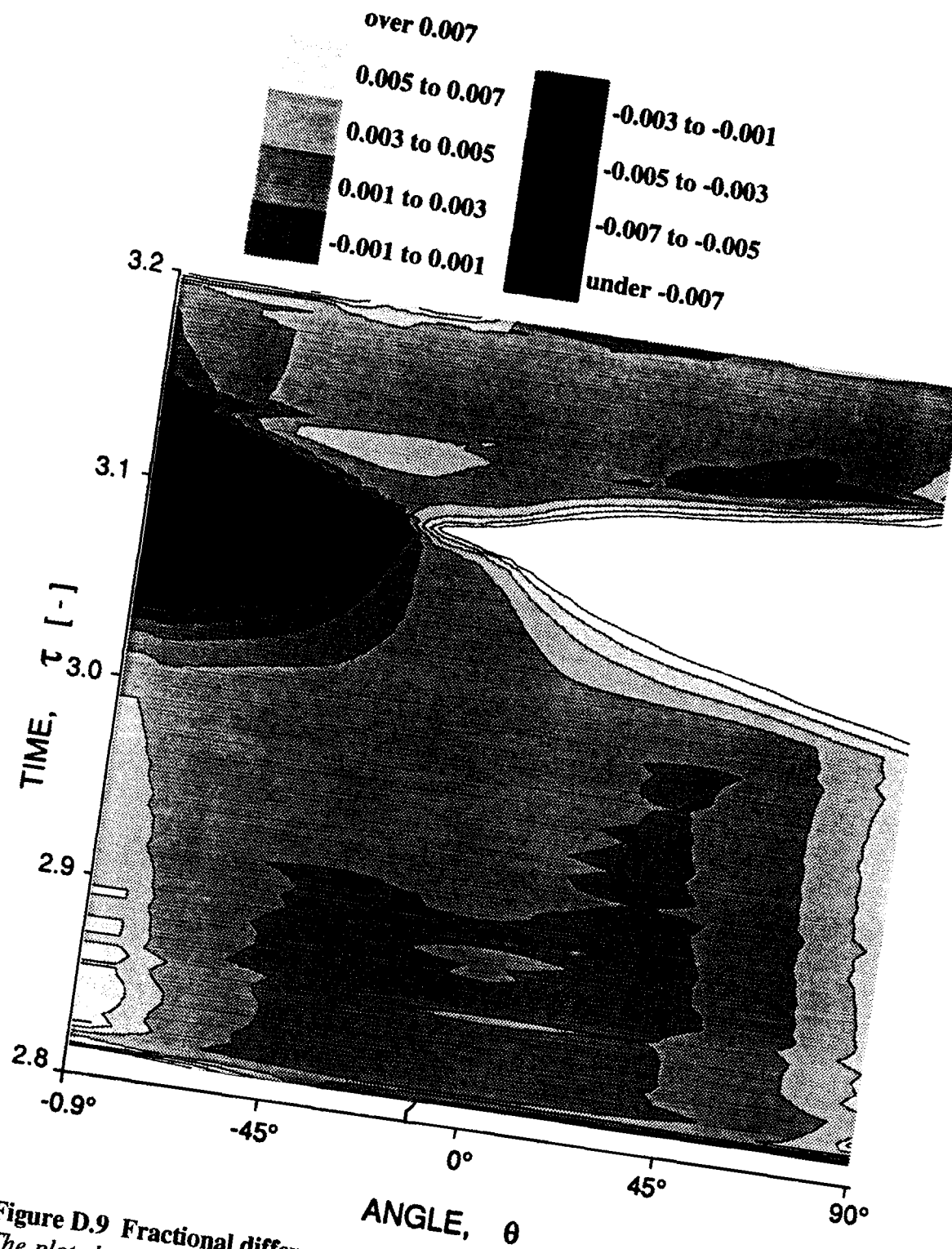


**Figure D.9 Fractional differences between the source strengths  $Q_i$  and  $Q$**   
 The plot shows the fractional difference,  $(Q_i - Q)/|Q|$ , between the ideal,  $Q_i$ , and average,  $Q$ , source strengths for different points on the surface of the bubble represented by the angle  $\theta$ . These values are plotted for different dimensionless times during the growth and collapse phases.

During the early bubble growth phase ( $2.82 < \tau < 2.95$ ), we observe an over-pressure of up to  $C_p = 0.05$  on the exterior surface of the bubble. This over-pressure first appears when the growing nucleus encounters the surface of the headform and begins to be compressed against it. One consequence of this can be seen in figure D.9 where the exterior of the bubble requires smaller source values during the growth phase ( $Q_i$  is smaller by 0.3%). This indicates the tendency for the exterior of the bubble surface to come closer to the source, i.e., for the bubble to be flattened. Also the values of  $Q_i$  are larger than the average source value  $Q$  at the leading and trailing surfaces of the bubble (angles around  $\pm 90^\circ$ ). This again indicates the tendency of the bubble to expand in a direction parallel to the headform surface (where the pressures are lower), thus producing a flattened and elongated bubble shape.

As the bubble reaches its maximum size at  $\tau = 3.09$ , we see from figure D.8 that the leading edge of the bubble ( $\theta \approx 90^\circ$ ) is subjected to a strong under-pressure ( $C_p < -0.01$ ), whereas the trailing edge ( $\theta \approx -90^\circ$ ) is subjected to an over-pressure ( $C_p > 0.005$ ). The local source strength  $Q_i$  reflects the same asymmetry (larger values at the leading edge and smaller values at the trailing edge), indicating that the bubble tends to continue to grow at the leading edge and shrink at the trailing edge. This phenomena is responsible for the wedge-like shape of the bubble that is observed during collapse. The fact that the single source model is not able to completely follow such complex three-dimensional bubble deformations and produces the errors shown in those two figures partly explains the need to add the corrective terms defined in equation D.35 and discussed in the following paragraph.

#### **D.4.3 Corrective displacement of the bubble surface nodes**

The importance of the corrective terms applied to the bubble surface nodes exhibiting adverse conditions described by equation D.35 can be estimated by comparing the actual volumetric rate of growth of the bubble with the average source strength  $Q$ .

Indeed, if the corrective source strength terms,  $Q_{\text{corrected}_i}$ , were non-existent, the volume of the bubble would simply increase by the average source strength value  $Q$ . The following equation would then hold

$$\frac{dV}{d\tau} = Q(\tau) \quad (\text{D.42})$$

where  $V$  is the volume of the bubble. Departures from this equation represent corrections to the local source strength,  $Q_{\text{corrected}_i}$ , that have been necessary for bubble surface to match the pressure boundary condition. We note that this error estimation gives us only an integral representation of the local corrective source strengths over the entire circumference of the bubble. In reality these corrective effects are applied only to a few nodes on the surface of the bubble. Furthermore the values of  $Q_{\text{corrected}_i}$  depend on the adverse condition of these nodes (as defined in paragraph D.2.3). These nodes may be identified by examining the regions where the conditions are adverse in figure D.9.

Because of the three dimensionality of the bubble shape, the actual volume of the bubble is hard to estimate. It is possible though, to compute the bubble surface area,  $S$ , in the plane of symmetry. If we assume that the bubble has roughly a hemispherical cap shape of base radius  $r_{\text{cap}}$ , the bubble volume would be  $V = 2/3 \pi r_{\text{cap}}^3$ . Furthermore the surface area of the cap in the plane of symmetry would be given by  $S = 1/2 \pi r_{\text{cap}}^2$ . Thus the volume of the bubble may be estimated as

$$V = \frac{4}{3} \sqrt{\frac{2S^3}{\pi}}. \quad (\text{D.43})$$

Figure D.10 plots the variation of the volume of the bubble based on this estimate.

Comparing figure D.10 to figure D.17 we can see that the rate of change of the bubble volume is less than we would anticipate by examining the average source strength,  $Q$ . For all the cavitation numbers shown the maximum volume deficiency is about 30%.

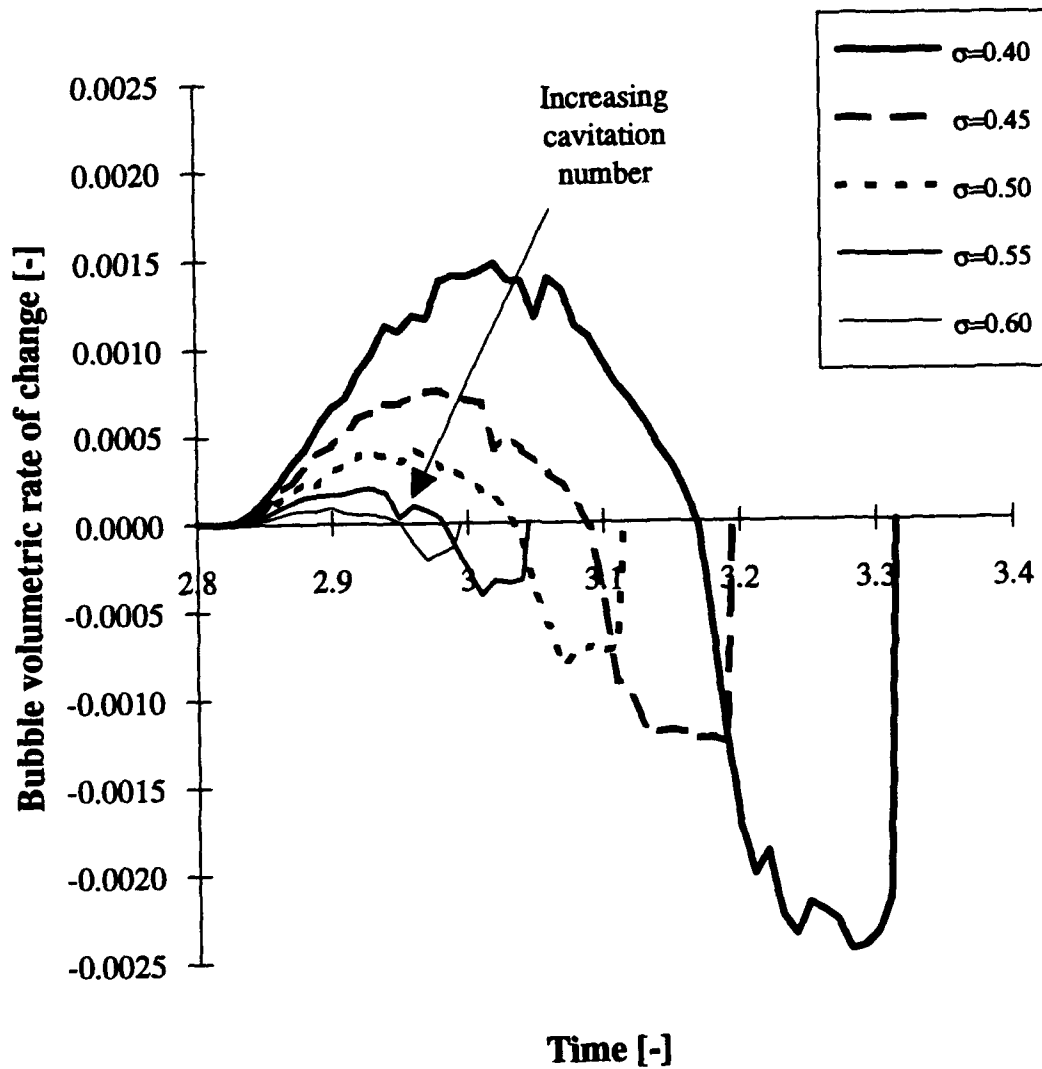


**Figure D.10 Estimated volumetric rate of change of the bubble**

*The estimated dimensionless rate of change of the bubble volume based on the surface area  $S$  in the plane of symmetry is represented as a function of time for a range of cavitation numbers. The discrepancy between these curves and those of figure D.17 gives an indication of the correction required to match the pressure boundary condition on the bubble surface.*

The local corrective source terms,  $Q_{corrected_i}$ , therefore tend to slow the growth and collapse of the bubble. This is not surprising since they are only applied when the local conditions are adverse and therefore always decrease the magnitude of the average source strength,  $Q$ , yielding an overall reduction in the bubble growth or collapse rate. The average source strength  $Q$  thus overestimates the real bubble volume rate of change. When analyzing these curves, though, we need to be alert to the fact that this calculated volume is quite crude and probably underestimates the real bubble volume, since the bubbles tend to be wider in the circumferential direction than in the plane of symmetry. The volume deficiency value of 30% therefore overestimates the magnitude of the correction applied.

## D.5 RESULTS

### D.5.1 Comparison of computed bubble shapes with experiments

A number of photographs of the profiles of traveling cavitation bubbles on a 5.08cm diameter Schiebe headform were taken by Ceccio (1990) in the Caltech Low Turbulence Water Tunnel (LTWT). A large number of photographs were also taken during the LCC experiments but these were taken from an oblique angle as seen in figures C.17.a through C.17.m. This angle makes comparisons between the computed bubble shapes and those photographs more difficult. Figure D.11 includes a comparison between the photographs of bubbles in the LTWT and the computed bubble shape at five different times. The comparison is made for the same cavitation number and roughly identical axial bubble location on the headform surface. For the purpose of this comparison, the effective cavitation number in the experiments has been calculated taking into account the blockage effects due to the small cross section area of the LTWT test section ( $A_t \approx 929\text{cm}^2$ ). The corrected cavitation number,  $\sigma_h$ , which includes the tunnel blockage effect is given by

$$\sigma_h = \left(1 - \frac{A_h}{A_t}\right)^2 (\sigma_\infty + 1) - 1 \quad (\text{D.44})$$

where  $\sigma_{\infty}$  is the cavitation number without blockage effects,  $A_h$  is the headform frontal area ( $A_h = \pi D^2/4$ ) and  $A_t$  is the tunnel cross-sectional area. The experimental cavitation number  $\sigma_{\infty} = 0.45$  presented here therefore yields a corrected cavitation number  $\sigma_h = 0.39$  with blockage effects. Presented in figure D.11 are the photographs of the bubble. Next to each photograph are superimposed at the same scale the computed bubble shape (solid line) and the outline of the bubble from the photograph (dashed line). The five photographs were taken at different times during the bubble lifetime. The first two during the growth phase, the third one when it has reached its maximum size and is just starting to collapse and the last two during collapse. The computed values for each of these times are as follows

photo number	time, $\tau$	$x_n$ coordinate	$r_n$ coordinate	Source, Q
1	2.95	0.19	0.42	$1.49 \cdot 10^{-4}$
2	3.06	0.30	0.44	$1.50 \cdot 10^{-4}$
3	3.16	0.40	0.46	$-2.80 \cdot 10^{-6}$
4	3.22	0.47	0.47	$-1.17 \cdot 10^{-4}$
5	3.30	0.56	0.48	$-1.68 \cdot 10^{-4}$

First we observe that the program simulates a spherical cap bubble shape similar to that observed in the experiments. The underside of the bubble is relatively flat and conforms to the headform surface. Then, during the growth phase the program shows a compression of the cap in the direction normal to the headform. This flattening of the bubble appears more pronounced in the experiments than in the computation. As the bubble starts to collapse it produces a wedge shape similar to the experiments, with the leading edge of the bubble thinner than the trailing edge. Furthermore the overall bubble

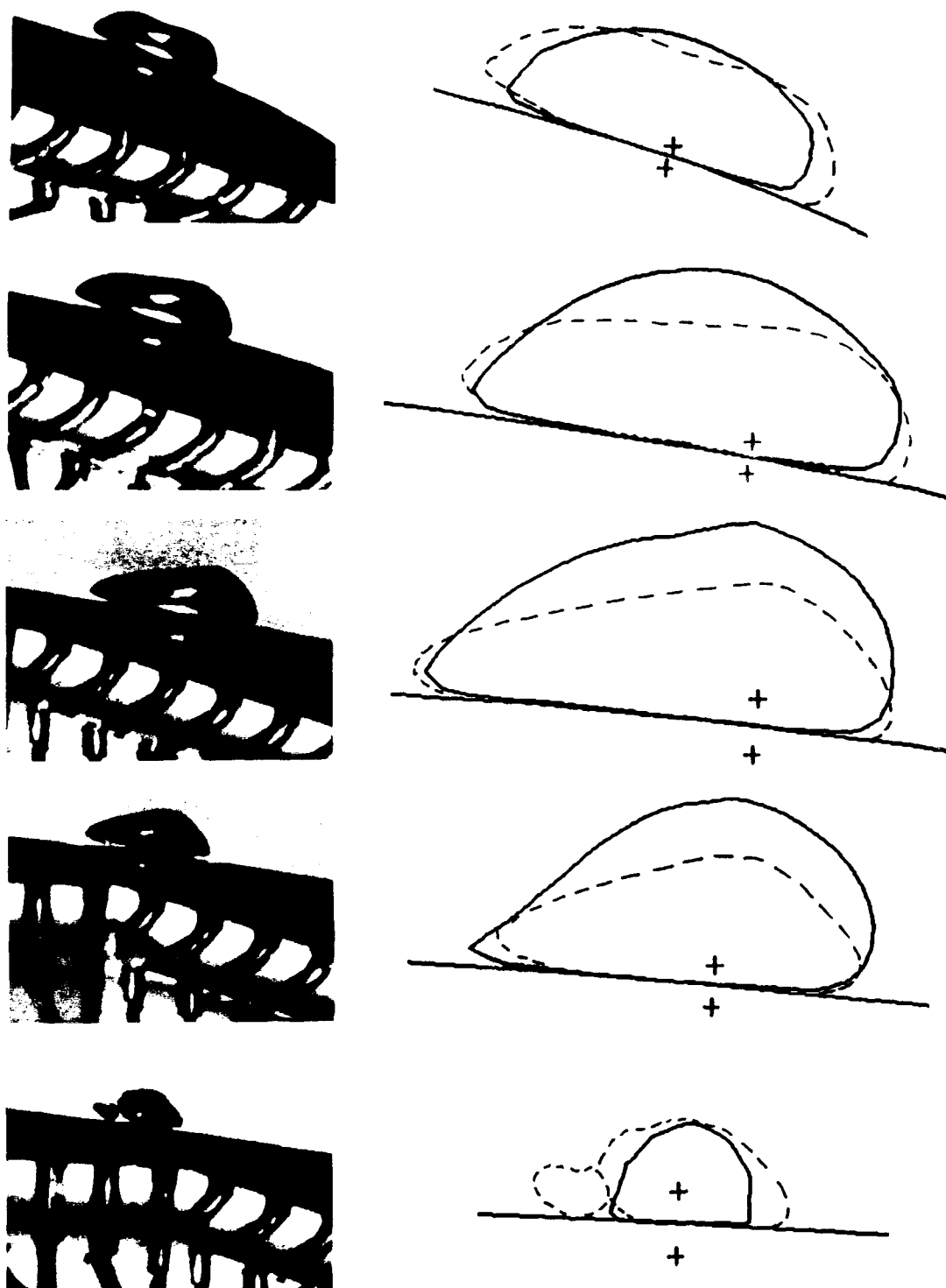


**Figure D.11 Comparison between computed bubbles and photographs**  
 Typical bubble shape over the Schiebe headform for  $\sigma=0.39$ . Next to each photograph is superimposed, at the same scale, the computed bubble shape (solid line) and the outline of the bubble from the photograph (dashed line). The crosses indicate the location of the sources.



dimensions and growth and collapse locations match the photographs remarkably well. Consequently the program captures many of the dynamics of the flow that determine the bubble shape. As previously mentioned, the largest discrepancy observed is that the computed bubbles do not appear as elongated as in the experiments, particularly for higher cavitation numbers. This limitation seems to be inherent in the single source model. Also the program does not produce the dimple that has been observed on the exterior surface of the bubble, but does point out the possible cause of its formation as will be discussed later. A more extensive analysis of the bubble shape computation in time is presented in figures D.12 for a cavitation number  $\sigma=0.45$ .

#### D.5.2 Typical bubble growth and collapse

Figures D.12.1 through D.12.20 present the time history of a typical bubble growth and collapse for the following conditions:  $R_o=100\mu\text{m}$ ,  $D=50.8\text{cm}$ ,  $U_\infty=11.5\text{m/s}$ ,  $\sigma=0.45$  with an initial nucleus position:  $x_{qo}=-1.0$ ,  $r_{qo}=0.01$ . The time increment between each figure is  $\Delta\tau=0.02$ . The first figure is for  $\tau=2.809$  and corresponds to the time the nucleus reaches its critical size and becomes unstable. The presentation of the bubble dynamics in figure D.12 includes for each time: a) (top left) the bubble shape; b) (top right) the pressure coefficient,  $C_p$ , on the surface of the headform; c) (bottom left) the pressure coefficient perturbation,  $\Delta C_p$ , due to the presence of bubble; d) (bottom right) the pressure perturbation term induced by the time derivative of the potential field,  $\Delta C_{p\phi}$ . Furthermore, by comparing the pressure distributions in figures (c) and figures (d) and using equation D.39 it is possible to estimate the influence of the velocity induced pressure perturbation,  $\Delta C_{p_v}$ . The figure captions give information on the time  $\tau$ , the average source strength  $Q$ , the source location  $x_q$  and  $r_q$ , the pressure coefficient  $C_{p_q}$  that would be experienced at the source location if no bubble were present (i.e.  $Q=0$ ), the average radius of the bubble,  $r_{\text{circ}}$ , based on the circumference of the bubble ( $r_{\text{circ}} = \text{circumference}/2\pi$ ), and the average bubble surface growth or collapse velocity,  $v_{\text{surf}}$ , defined as  $v_{\text{surf}} = Q/r_{\text{circ}}^2$ .

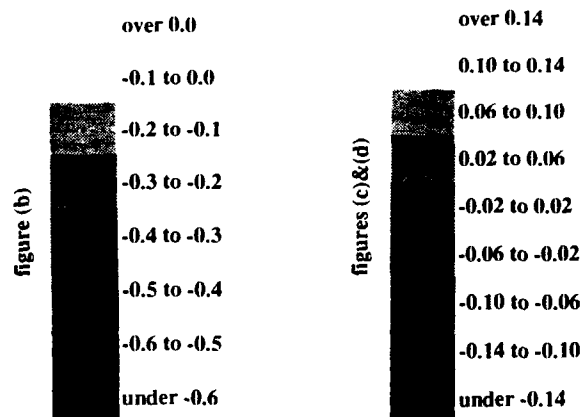
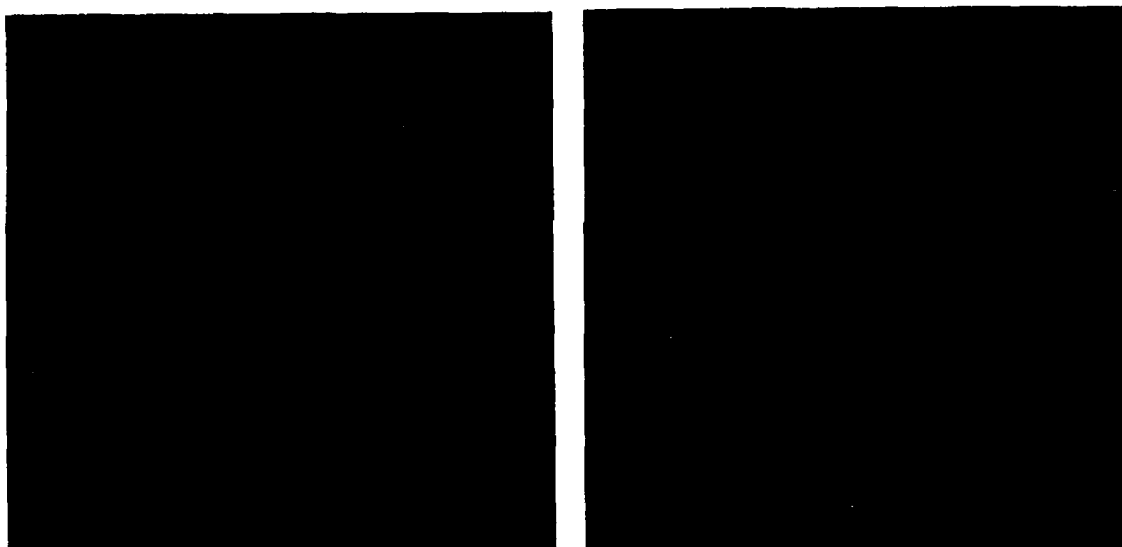
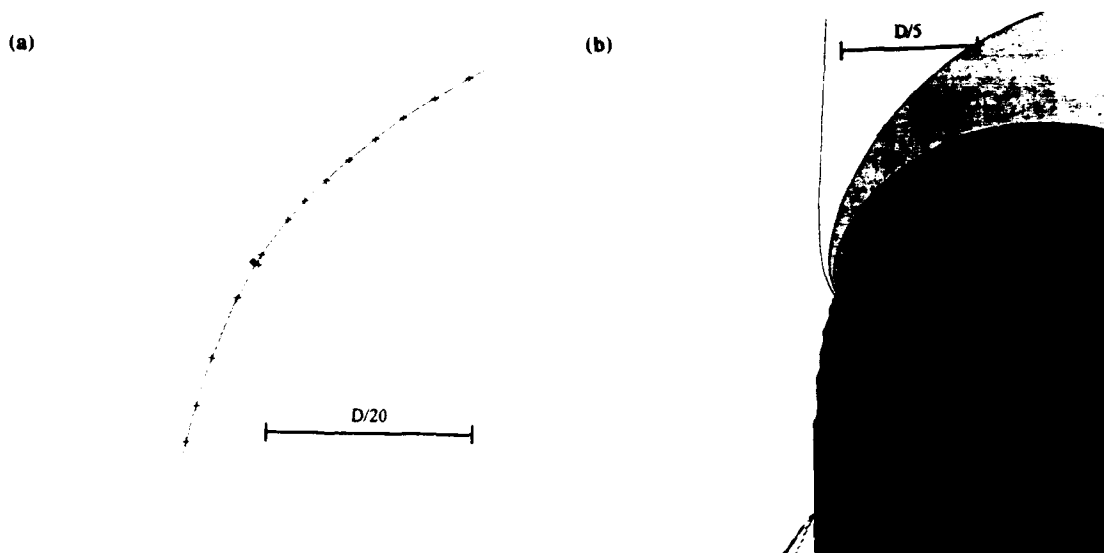


Figure D.12.1 Time,  $\tau=2.808$ . (a) bubble shape, (b)  $C_p$ , (c)  $\Delta C_p$ , (d)  $\Delta C_{p\phi}$   
 $Q=1.20 \times 10^{-10}$ ,  $x_q=0.042$ ,  $r_q=0.335$ ,  $C_{p_q}=-0.46$ ,  $r_{circ}=8.05 \times 10^{-4}$ ,  $v_{surf}=0.0002$ .

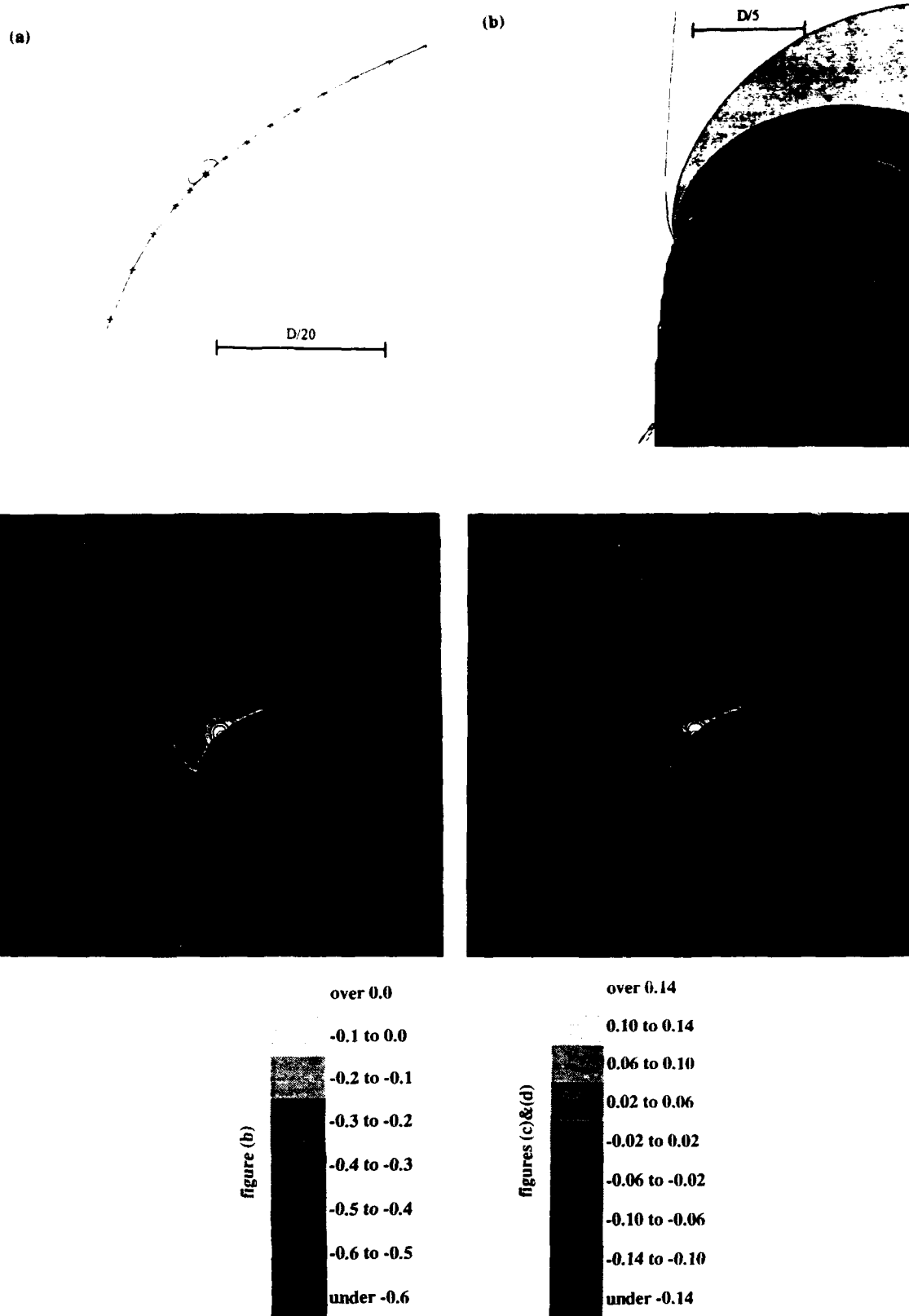


Figure D.12.2, Time,  $\tau=2.828$ . (a) bubble shape, (b)  $C_p$ , (c)  $\Delta C_p$ , (d)  $\Delta C_{p\phi}$   
 $Q=4.24 \times 10^{-6}$ ,  $x_q=0.059$ ,  $r_q=0.355$ ,  $C_{p_q}=-0.78$ ,  $r_{circ}=3.93 \times 10^{-3}$ ,  $v_{surf}=0.274$

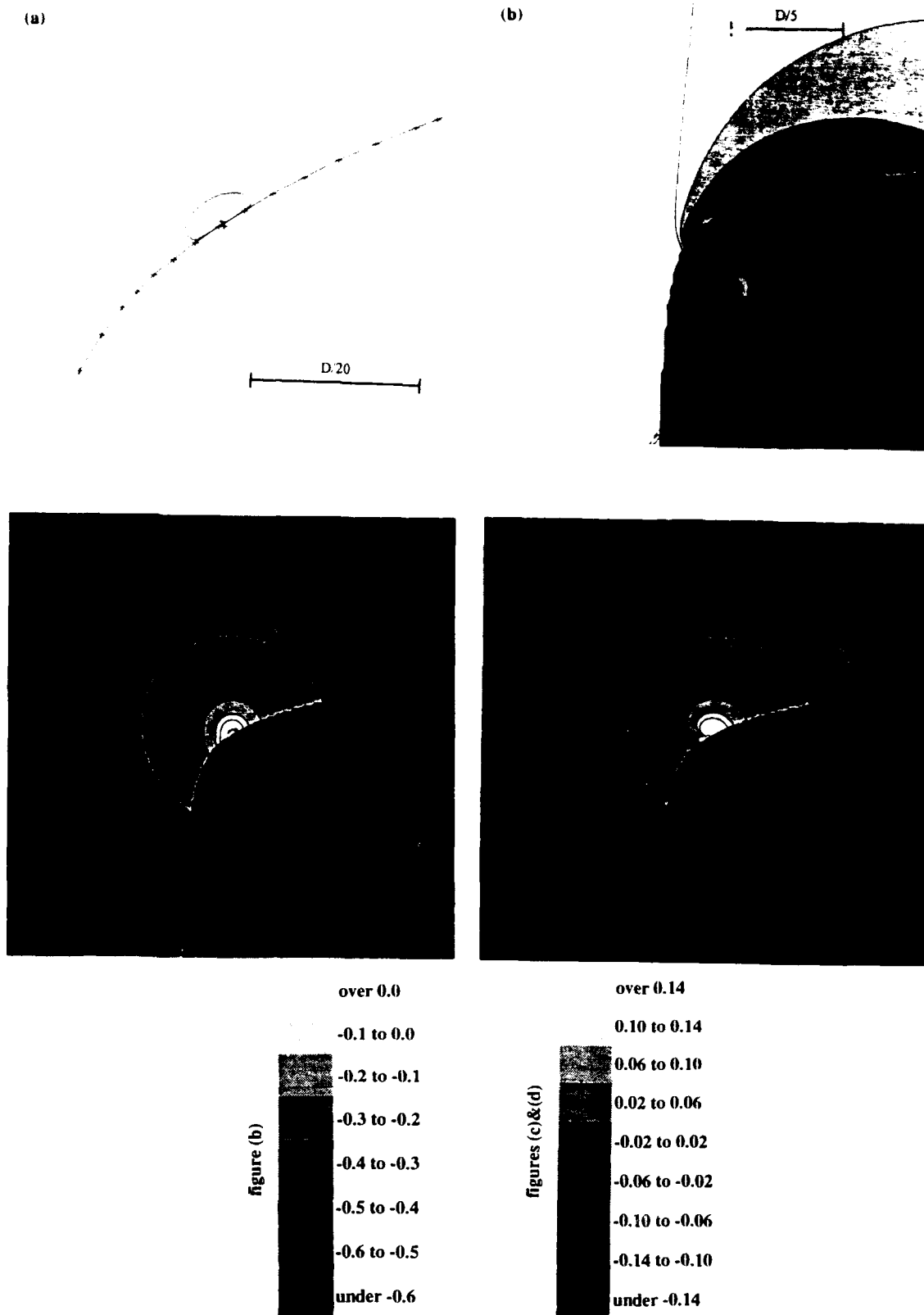


Figure D.12.3, Time,  $\tau=2.848$ . (a) bubble shape, (b)  $C_p$ , (c)  $\Delta C_p$ , (d)  $\Delta C_{p_\phi}$   
 $Q=1.81 \times 10^{-5}$ ,  $x_q=0.080$ ,  $r_q=0.371$ ,  $C_{p_q}=-0.73$ ,  $r_{circ}=8.28 \times 10^{-3}$ ,  $v_{surf}=0.263$

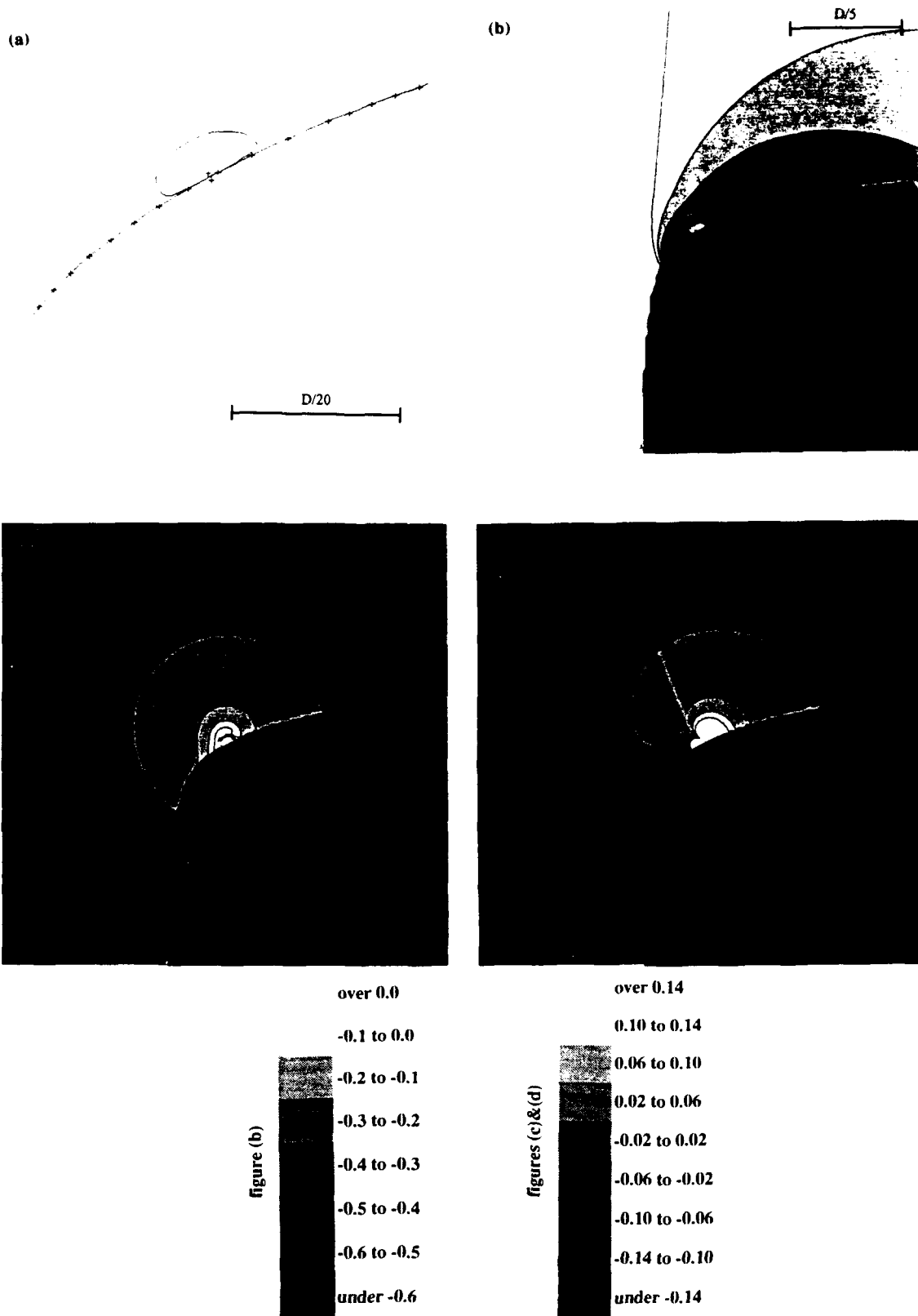
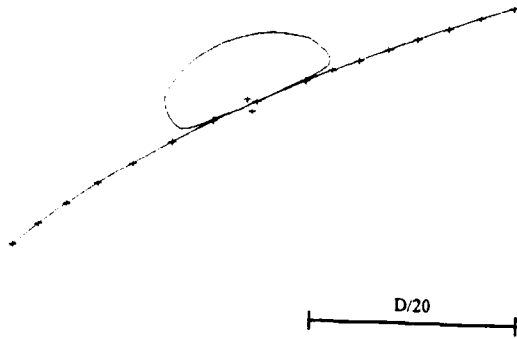


Figure D.12.4, Time,  $\tau=2.868$ . (a) bubble shape, (b)  $C_p$ , (c)  $\Delta C_p$ , (d)  $\Delta C_{p_\phi}$   
 $Q=3.65 \times 10^{-5}$ ,  $x_q=0.101$ ,  $r_q=0.384$ ,  $C_{p_q}=-0.67$ ,  $r_{circ}=1.22 \times 10^{-2}$ ,  $v_{surf}=0.243$

(a)



(b)

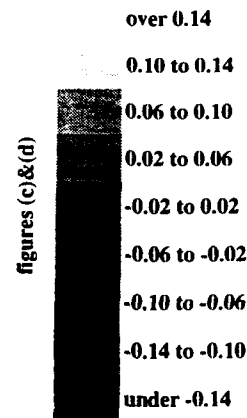
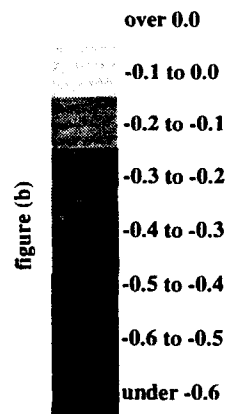
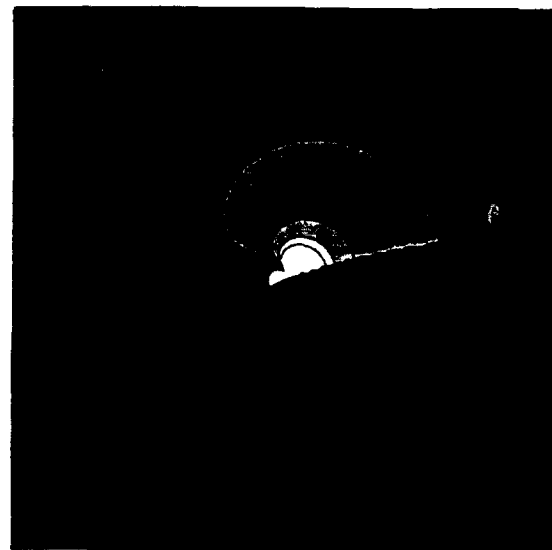
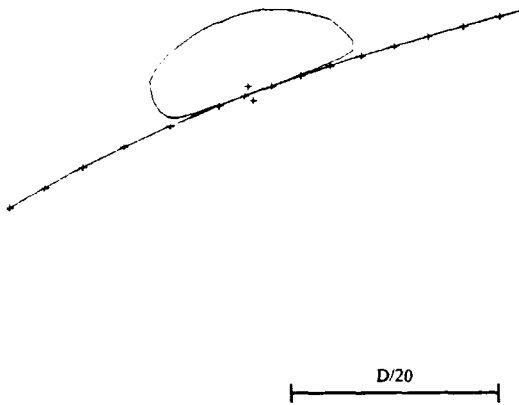


Figure D.12.5, Time,  $\tau=2.888$ . (a) bubble shape, (b)  $C_p$ , (c)  $\Delta C_p$ , (d)  $\Delta C_{p\phi}$   
 $Q=5.54 \times 10^{-5}$ ,  $x_q=0.123$ ,  $r_q=0.395$ ,  $C_{p_q}=-0.62$ ,  $r_{circ}=1.59 \times 10^{-2}$ ,  $v_{surf}=0.219$

(a)



(b)

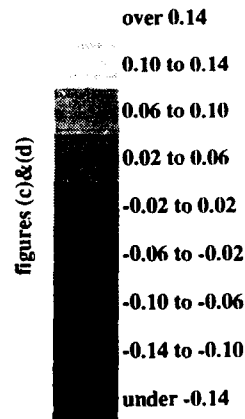
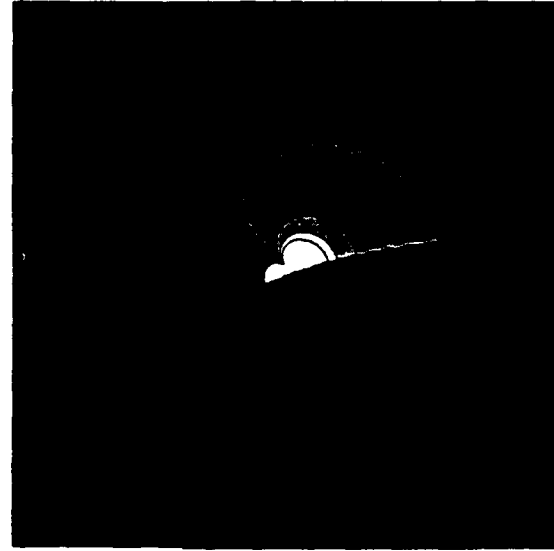
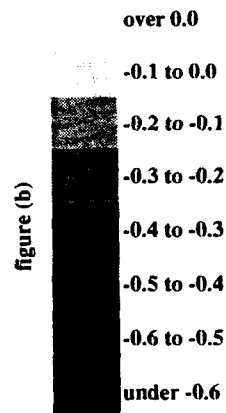
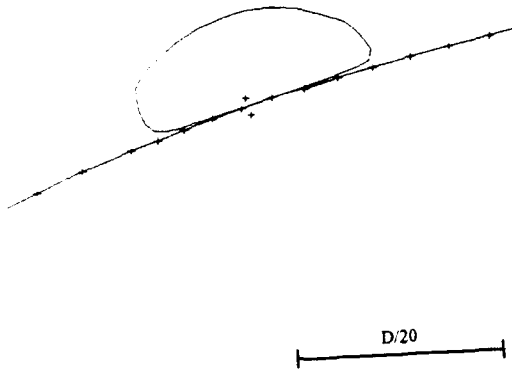


Figure D.12.6, Time,  $\tau=2.908$ . (a) bubble shape, (b)  $C_p$ , (c)  $\Delta C_p$ , (d)  $\Delta C_{p\phi}$   
 $Q=7.21 \times 10^{-5}$ ,  $x_q=0.145$ ,  $r_q=0.404$ ,  $C_{p_q}=-0.58$ ,  $r_{circ}=1.91 \times 10^{-2}$ ,  $v_{surf}=0.197$

(a)



(b)

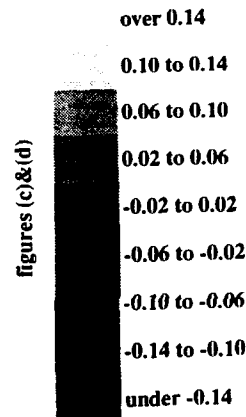
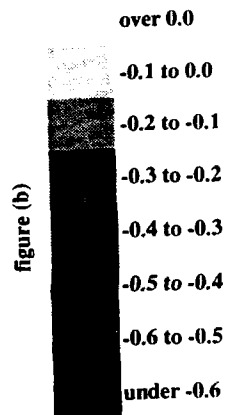


Figure D.12.7, Time,  $\tau=2.928$ . (a) bubble shape, (b)  $C_p$ , (c)  $\Delta C_p$ , (d)  $\Delta C_{p\phi}$   
 $Q=8.48 \times 10^{-5}$ ,  $x_q=0.166$ ,  $r_q=0.412$ ,  $C_{p_q}=-0.54$ ,  $r_{circ}=2.19 \times 10^{-2}$ ,  $v_{surf}=0.175$



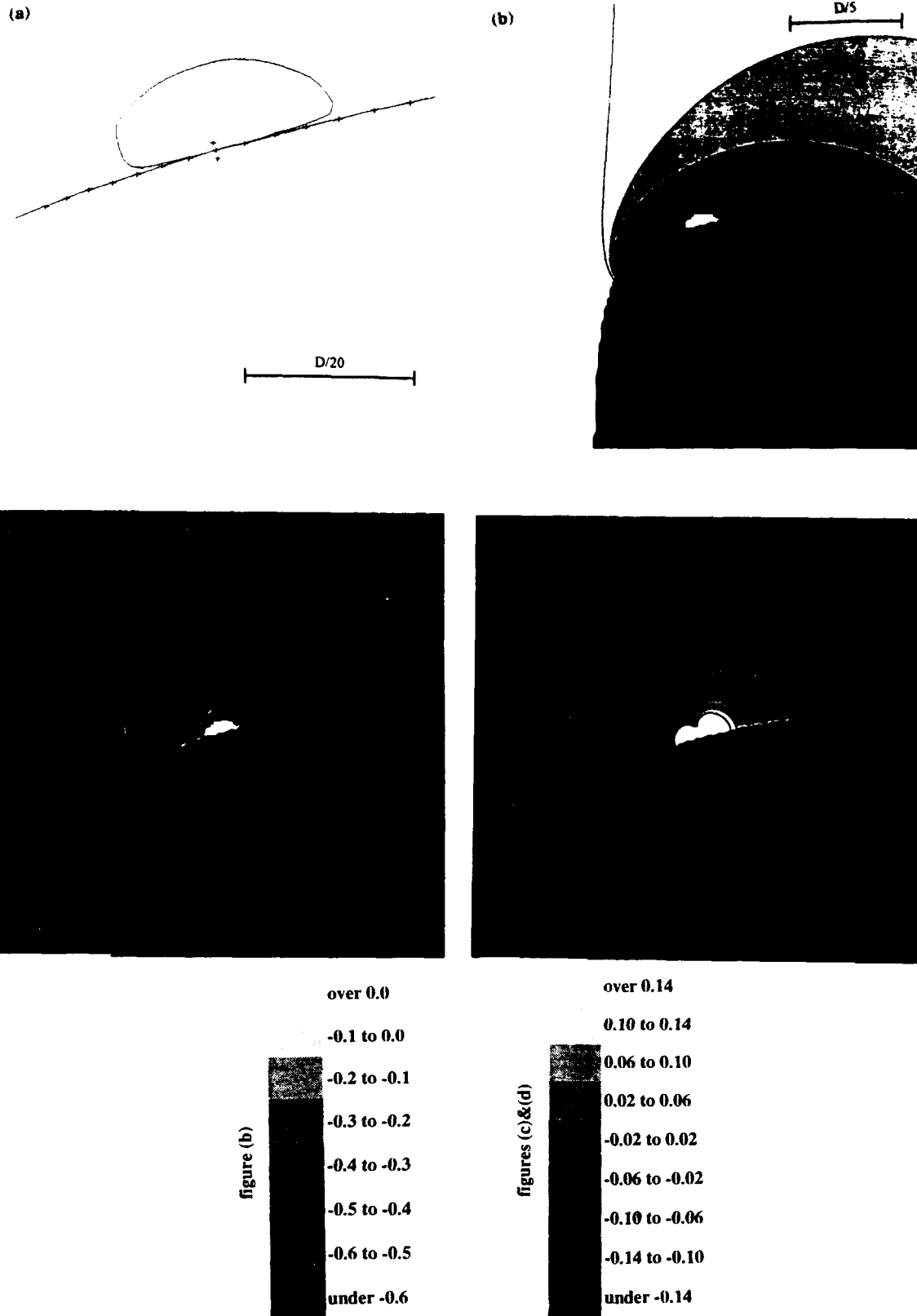


Figure D.12.8, Time,  $\tau=2.948$ . (a) bubble shape, (b)  $C_p$ , (c)  $\Delta C_p$ , (d)  $\Delta C_{p\phi}$   
 $Q=9.29 \times 10^{-5}$ ,  $x_q=0.187$ ,  $r_q=0.419$ ,  $C_{p_q}=-0.50$ ,  $r_{circ}=2.46 \times 10^{-2}$ ,  $v_{surf}=0.153$

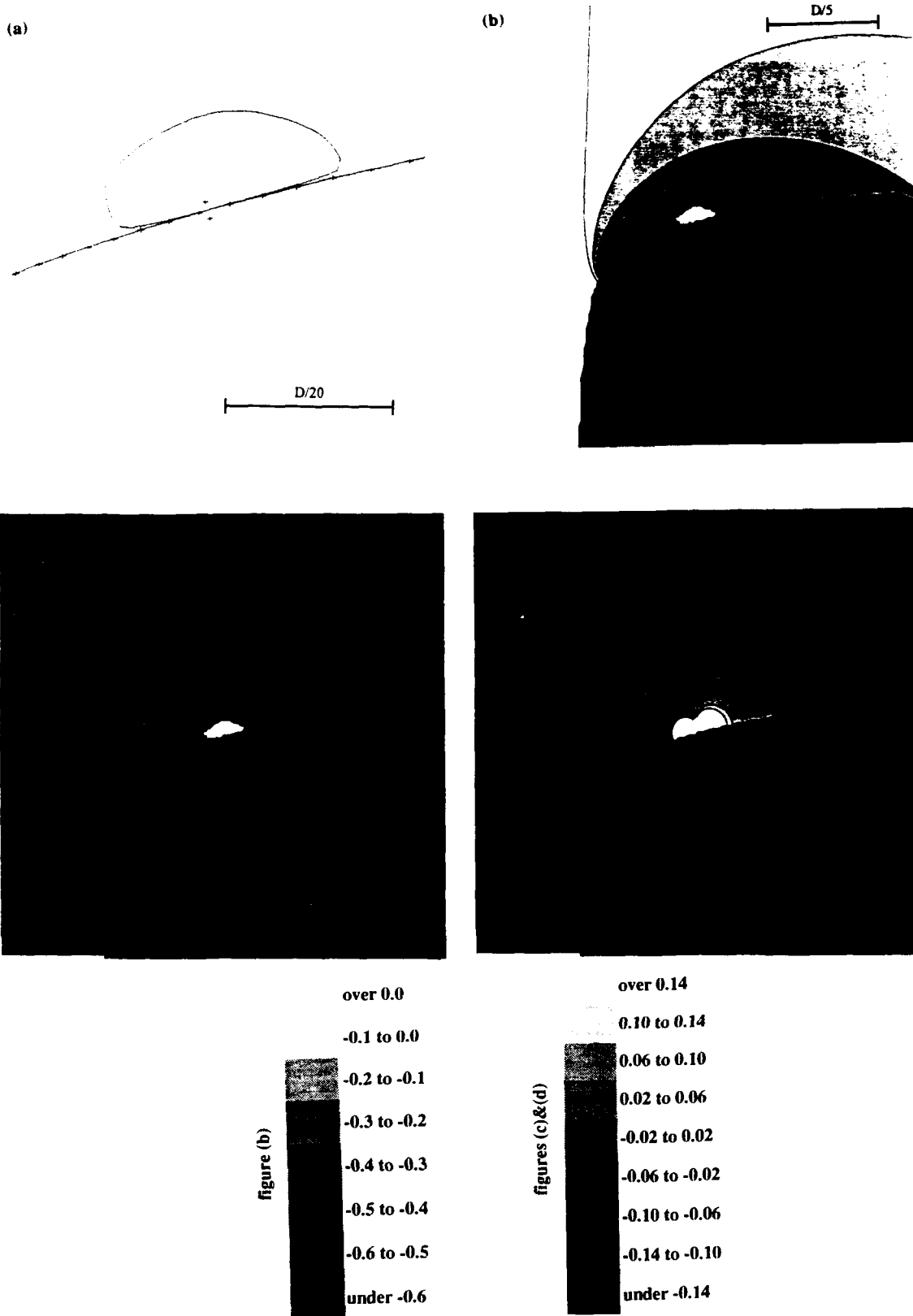


Figure D.12.9, Time,  $\tau=2.968$ . (a) bubble shape, (b)  $C_p$ , (c)  $\Delta C_p$ , (d)  $\Delta C_{p_\phi}$   
 $Q=9.52 \times 10^{-5}$ ,  $x_q=0.208$ ,  $r_q=0.426$ ,  $C_{p_q}=-0.47$ ,  $r_{circ}=2.68 \times 10^{-2}$ ,  $v_{surf}=0.132$

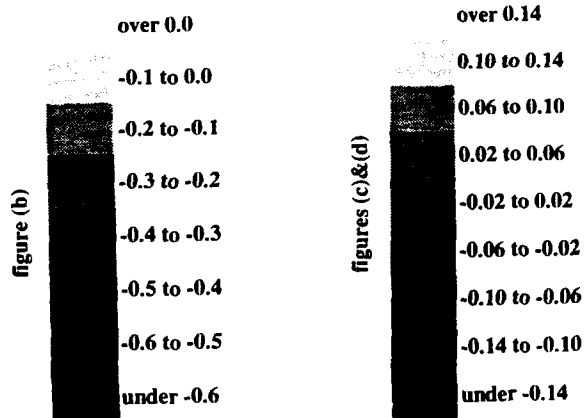
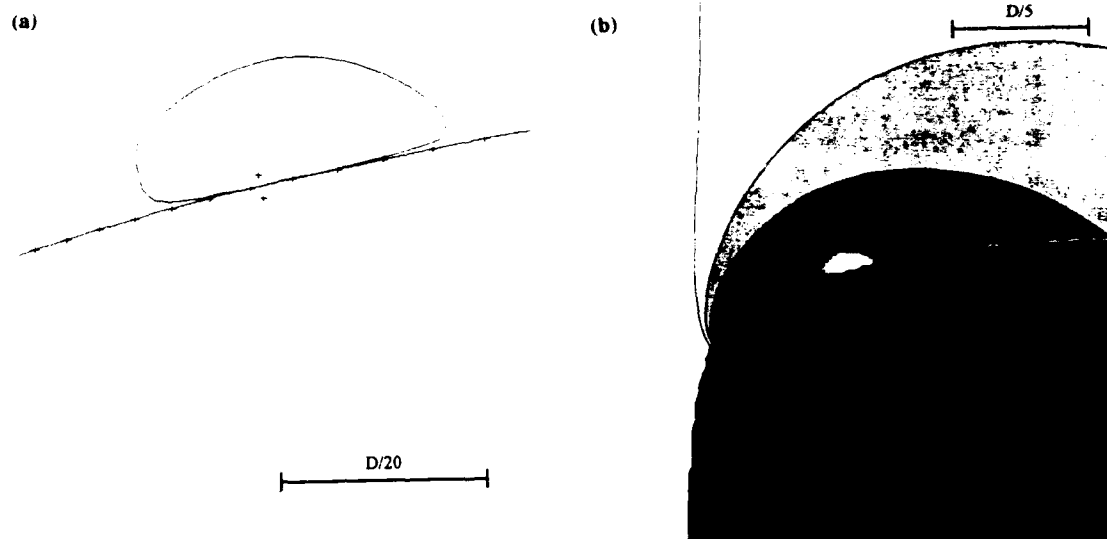


Figure D.12.10, Time,  $\tau=2.988$ . (a) bubble shape, (b)  $C_p$ , (c)  $\Delta C_p$ , (d)  $\Delta C_{p\phi}$   
 $Q=9.23 \times 10^{-5}$ ,  $x_q=0.227$ ,  $r_q=0.431$ ,  $C_{p_q}=-0.45$ ,  $r_{circ}=2.86 \times 10^{-2}$ ,  $v_{surf}=0.112$

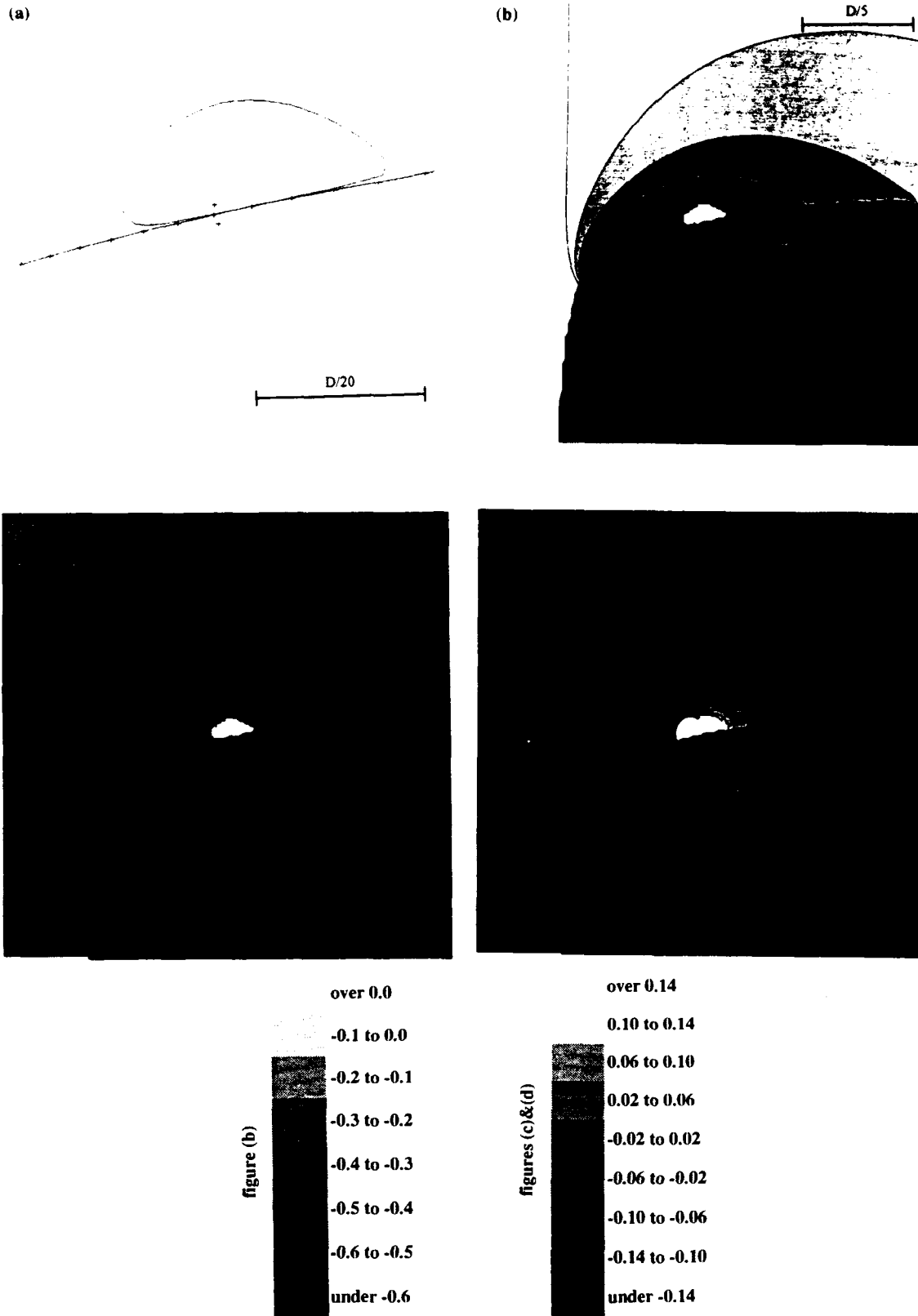


Figure D.12.11, Time,  $\tau=3.008$ . (a) bubble shape, (b)  $C_p$ , (c)  $\Delta C_p$ , (d)  $\Delta C_{p\phi}$   
 $Q=8.35 \times 10^{-5}$ ,  $x_q=0.245$ ,  $r_q=0.435$ ,  $Cp_q=-0.43$ ,  $r_{circ}=3.02 \times 10^{-2}$ ,  $v_{surf}=0.0915$

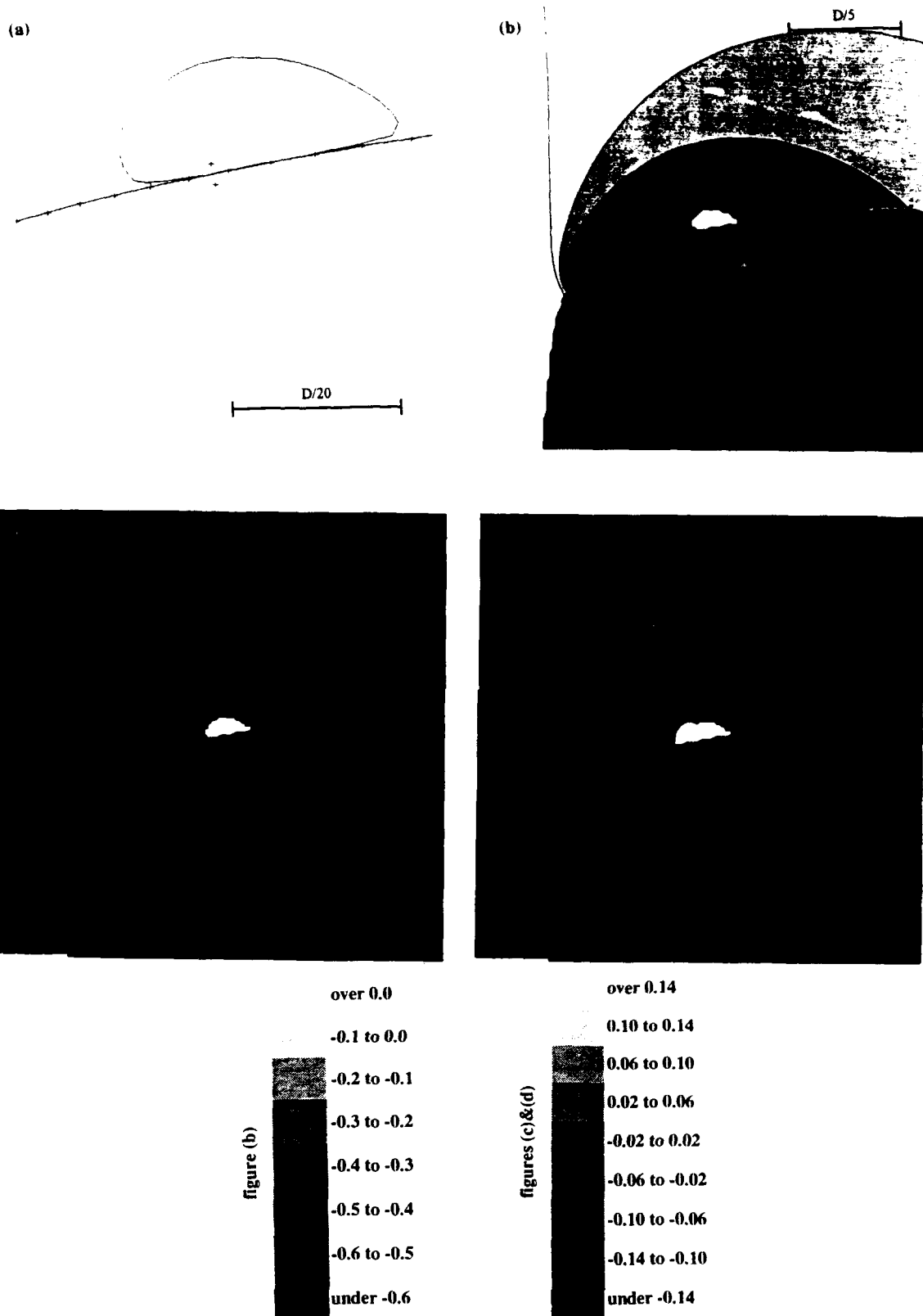


Figure D.12.12, Time,  $\tau=3.028$ . (a) bubble shape, (b)  $C_p$ , (c)  $\Delta C_p$ , (d)  $\Delta C_{p_\phi}$   
 $Q=6.98 \times 10^{-5}$ ,  $x_q=0.264$ ,  $r_q=0.439$ ,  $C_{p_q}=-0.41$ ,  $r_{circ}=3.13 \times 10^{-2}$ ,  $v_{surf}=0.0710$

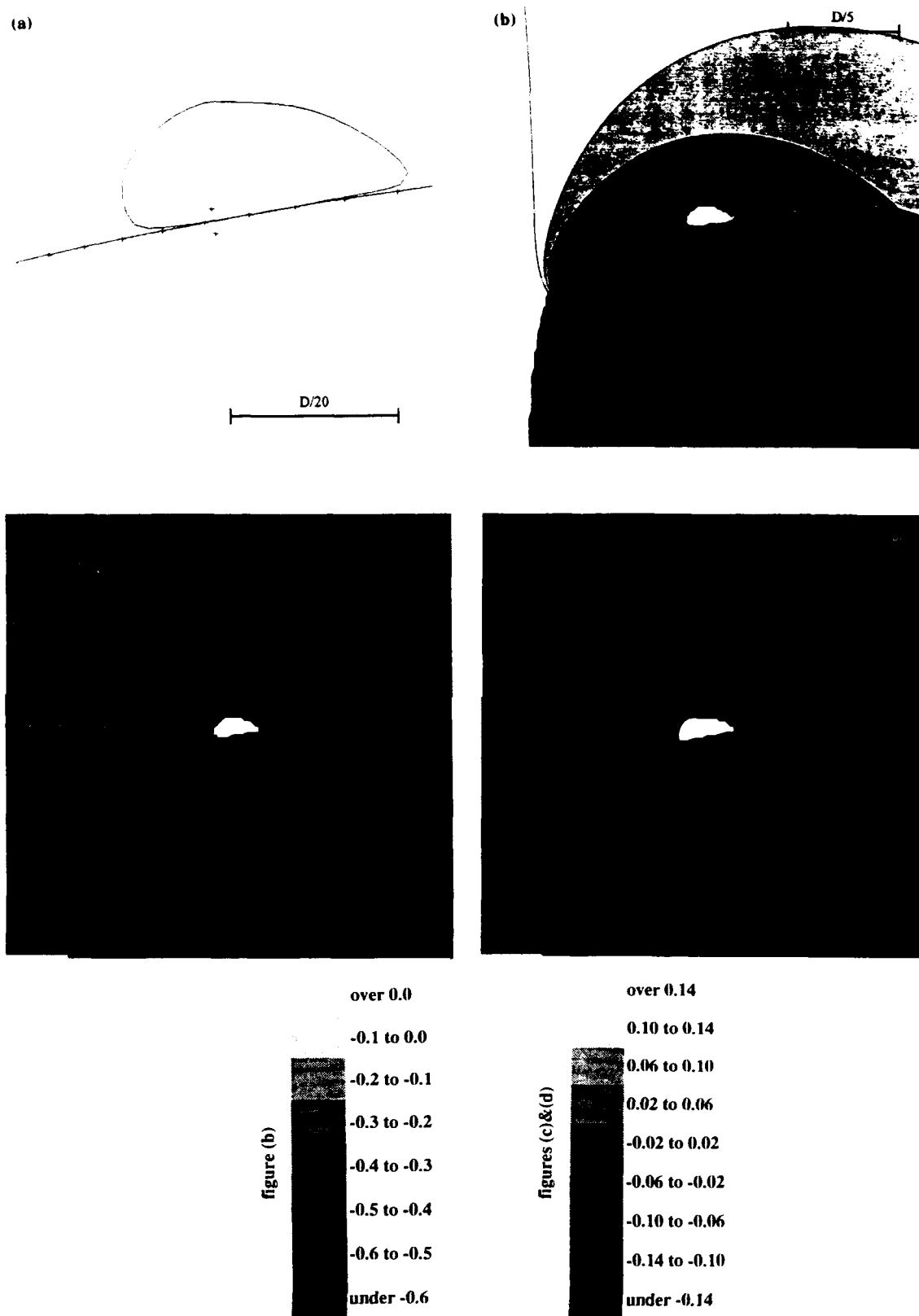


Figure D.12.13, Time,  $\tau=3.048$ . (a) bubble shape, (b)  $C_p$ , (c)  $\Delta C_p$ , (d)  $\Delta C_{p\phi}$   
 $Q=5.02 \times 10^{-5}$ ,  $x_q=0.284$ ,  $r_q=0.444$ ,  $C_{p_q}=-0.39$ ,  $r_{circ}=3.22 \times 10^{-2}$ ,  $v_{surf}=0.0482$

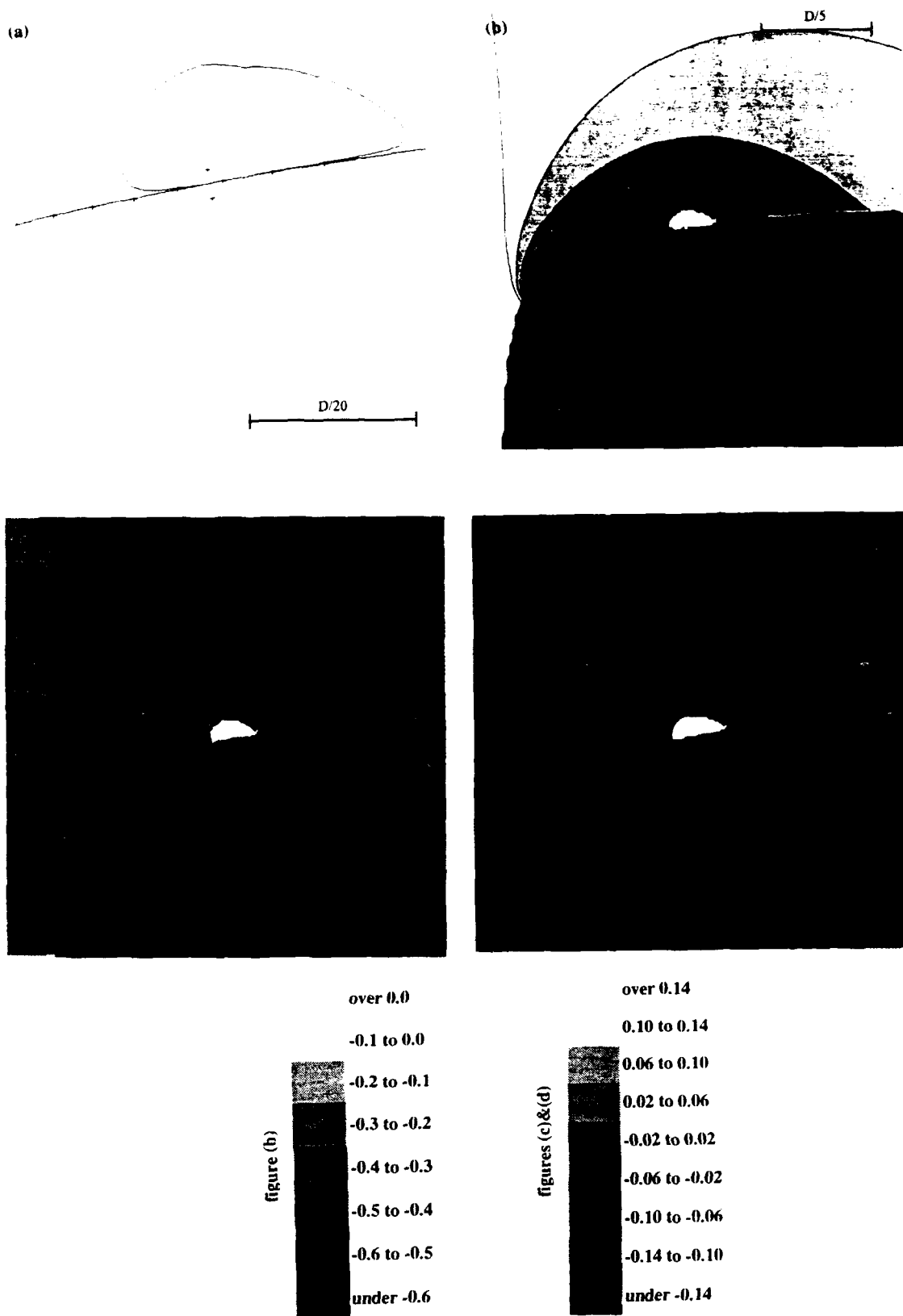


Figure D.12.14, Time,  $\tau=3.068$ . (a) bubble shape, (b)  $C_p$ , (c)  $\Delta C_p$ , (d)  $\Delta C_{p\phi}$   
 $Q=2.68 \times 10^{-5}$ ,  $x_q=0.305$ ,  $r_q=0.448$ ,  $Cp_q=-0.37$ ,  $r_{circ}=3.28 \times 10^{-2}$ ,  $v_{surf}=0.0248$

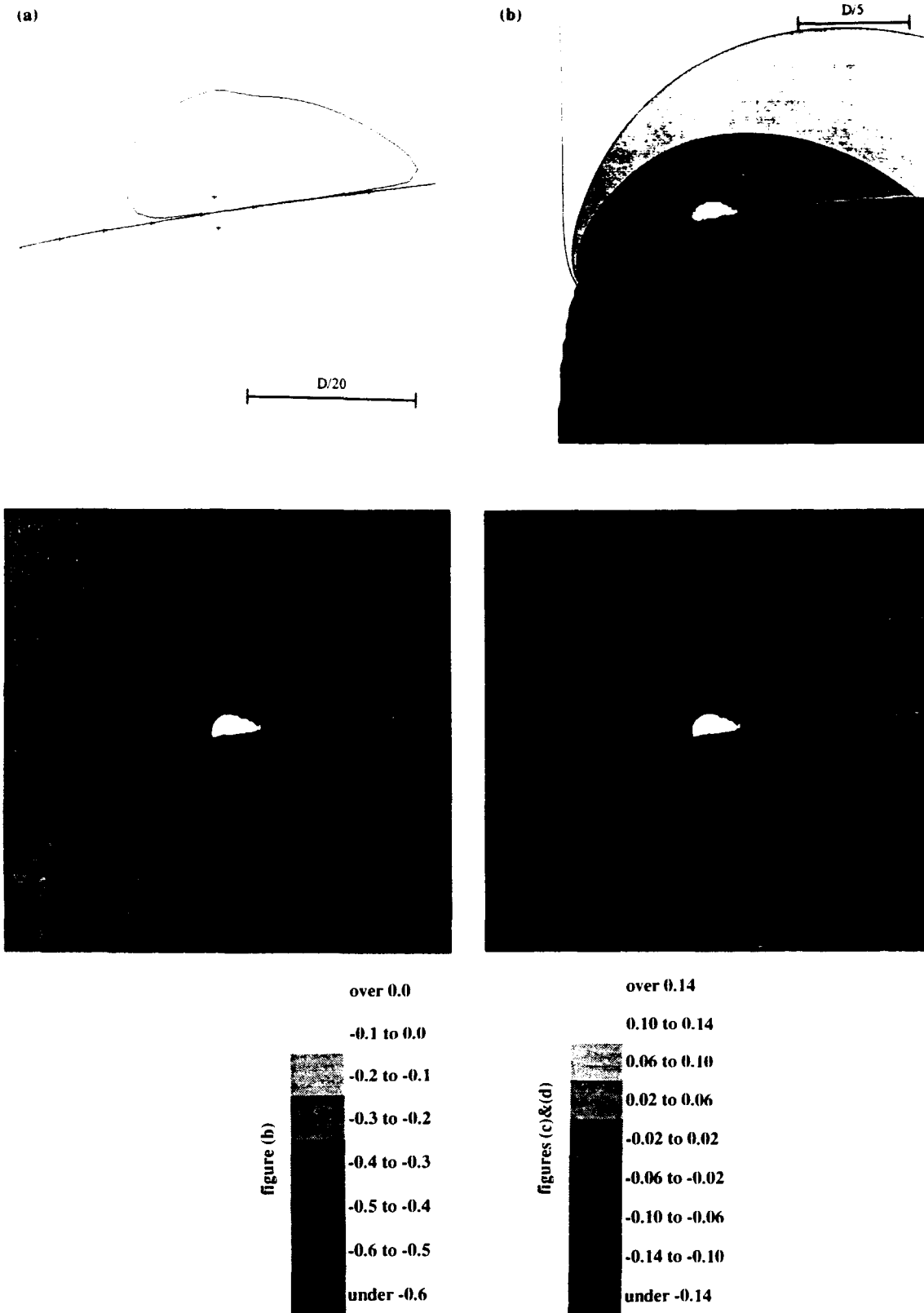


Figure D.12.15, Time,  $\tau=3.089$ . (a) bubble shape, (b)  $C_p$ , (c)  $\Delta C_p$ , (d)  $\Delta C_{p\phi}$   
 $Q=-2.52 \times 10^{-6}$ ,  $x_q=0.328$ ,  $r_q=0.453$ ,  $C_{p_q}=-0.35$ ,  $r_{circ}=3.29 \times 10^{-2}$ ,  $v_{surf}=-0.0023$



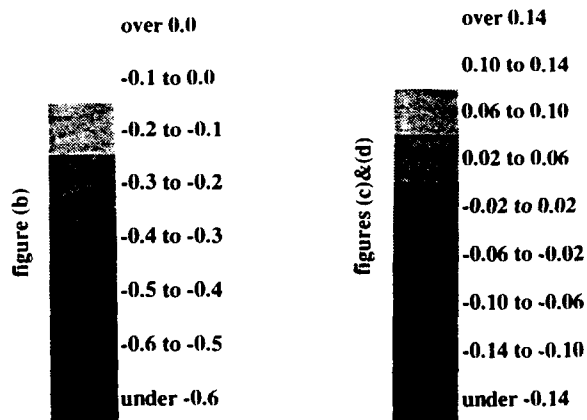
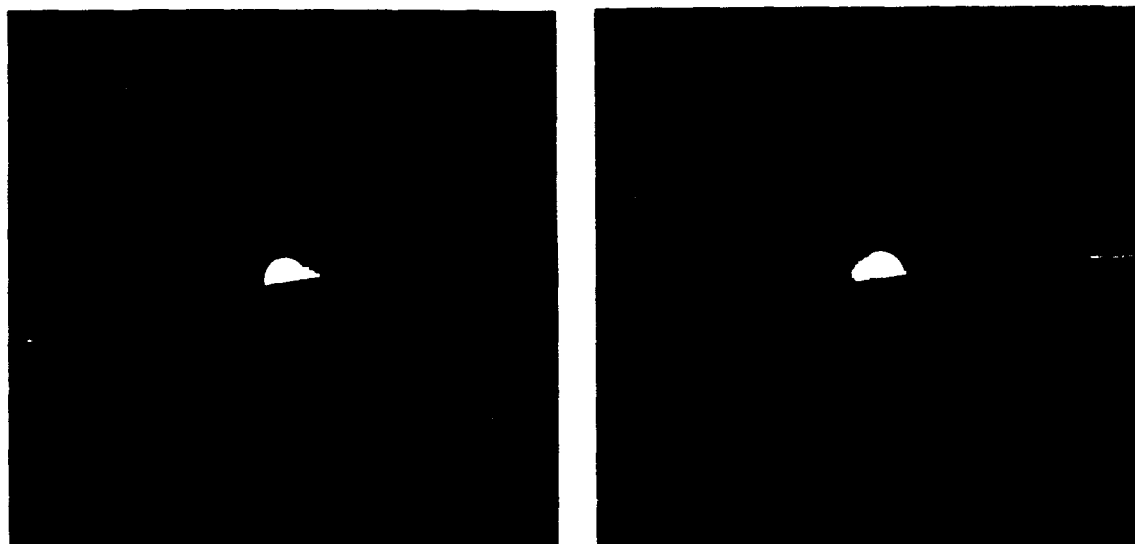
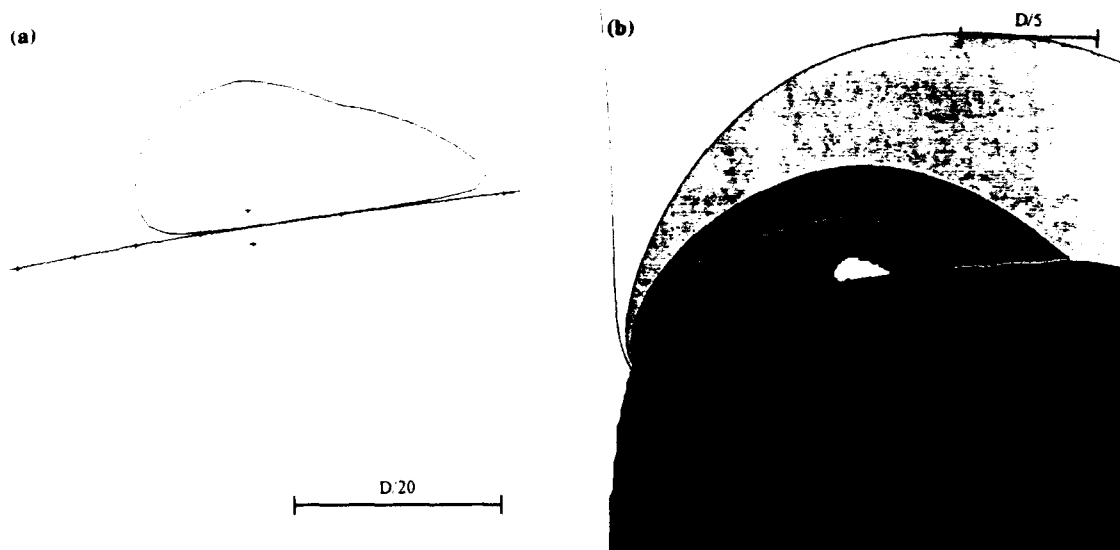


Figure D.12.16, Time,  $\tau=3.109$ . (a) bubble shape, (b)  $C_p$ , (c)  $\Delta C_p$ , (d)  $\Delta C_{p\phi}$   
 $Q=-3.15 \times 10^{-5}$ ,  $x_q=0.352$ ,  $r_q=0.455$ ,  $C_{p_q}=-0.33$ ,  $r_{circ}=3.21 \times 10^{-2}$ ,  $v_{surf}=-0.0306$

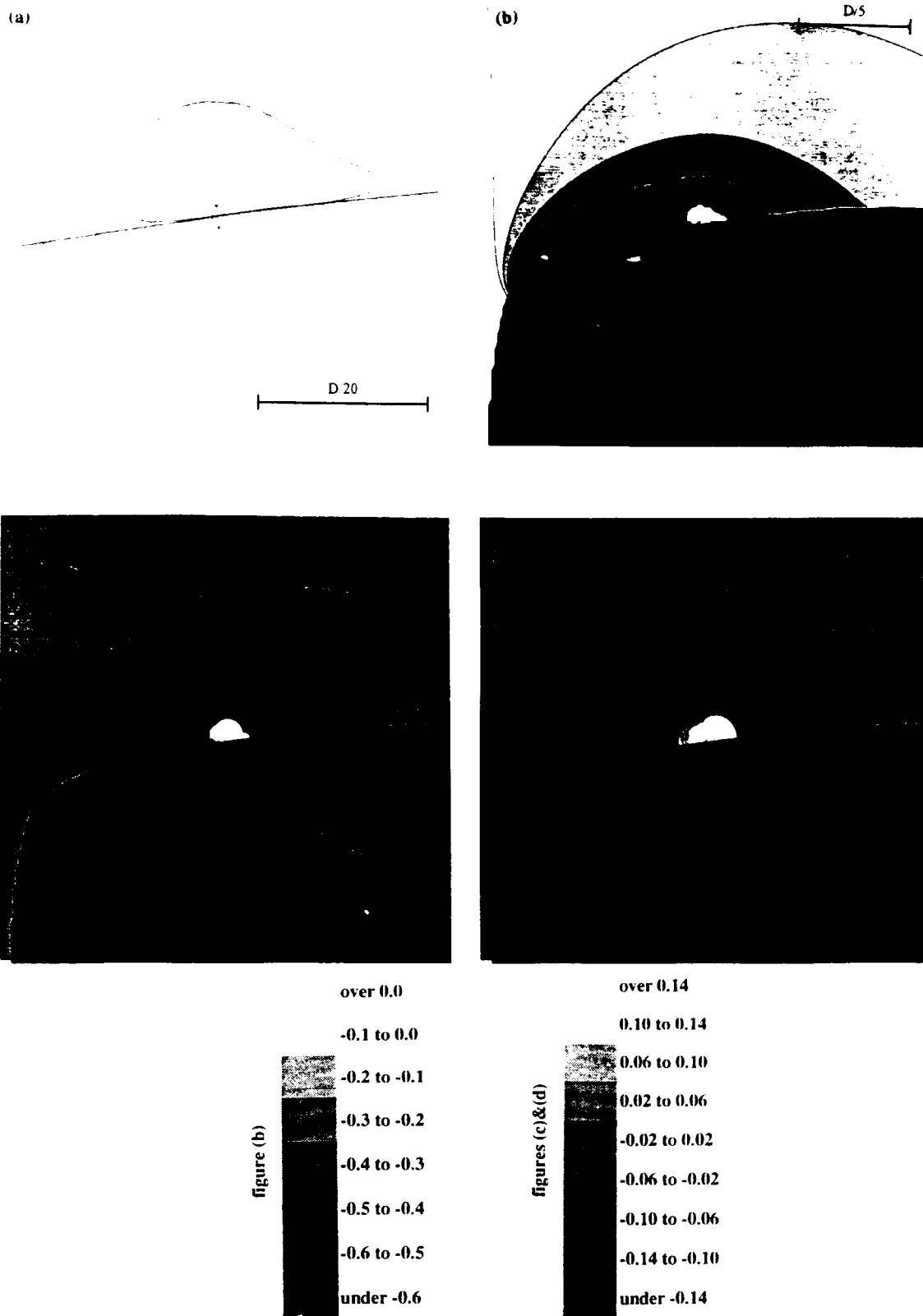


Figure D.12.17, Time,  $\tau=3.128$ . (a) bubble shape, (b)  $C_p$ , (c)  $\Delta C_p$ , (d)  $\Delta C_{p_\phi}$   
 $Q=-5.80 \times 10^{-5}$ ,  $x_q=0.376$ ,  $r_q=0.459$ ,  $C_{p_q}=-0.32$ ,  $r_{circ}=2.97 \times 10^{-2}$ ,  $v_{surf}=-0.0655$

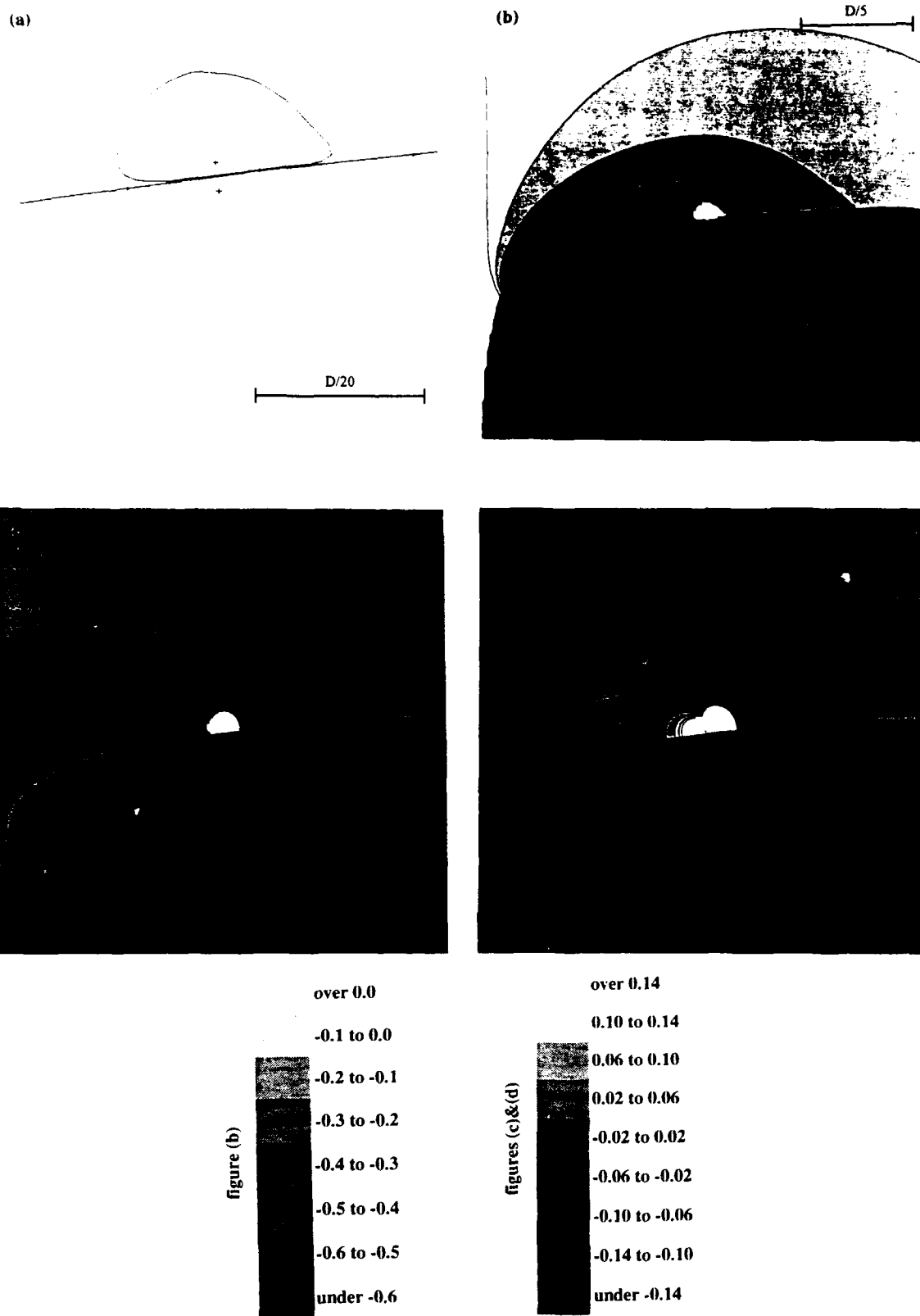


Figure D.12.18, Time,  $\tau=3.148$ . (a) bubble shape, (b)  $C_p$ , (c)  $\Delta C_p$ , (d)  $\Delta C_{p\phi}$   
 $Q=-8.27 \times 10^{-5}$ ,  $x_q=0.401$ ,  $r_q=0.462$ ,  $C_{p_q}=-0.30$ ,  $r_{circ}=2.50 \times 10^{-2}$ ,  $v_{surf}=-0.132$

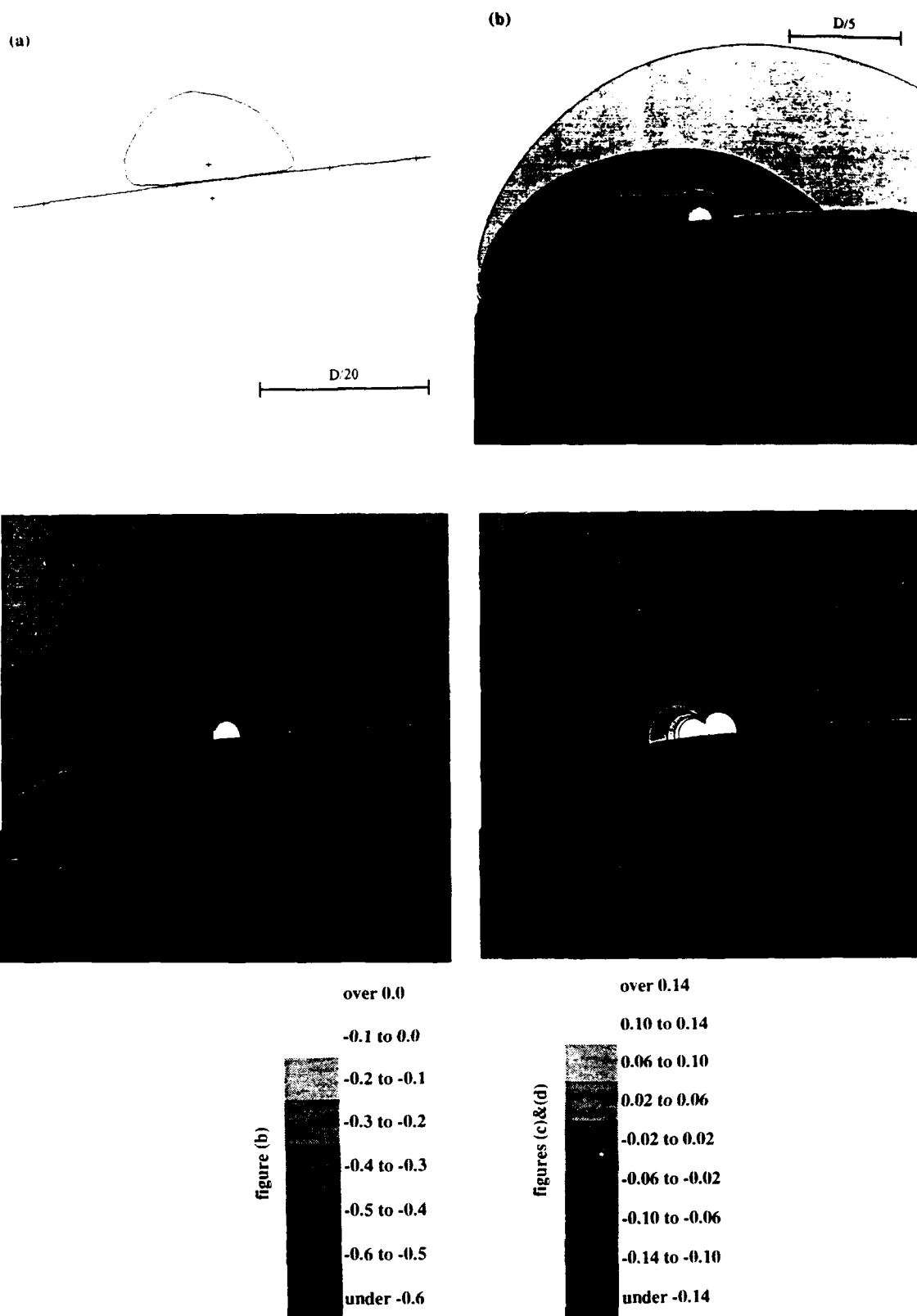


Figure D.12.19, Time,  $\tau=3.168$ . (a) bubble shape, (b)  $C_p$ , (c)  $\Delta C_p$ , (d)  $\Delta C_{p_\phi}$   
 $Q=-9.95 \times 10^{-5}$ ,  $x_q=0.424$ ,  $r_q=0.466$ ,  $C_{p_q}=-0.28$ ,  $r_{circ}=2.04 \times 10^{-2}$ ,  $v_{surf}=-0.237$

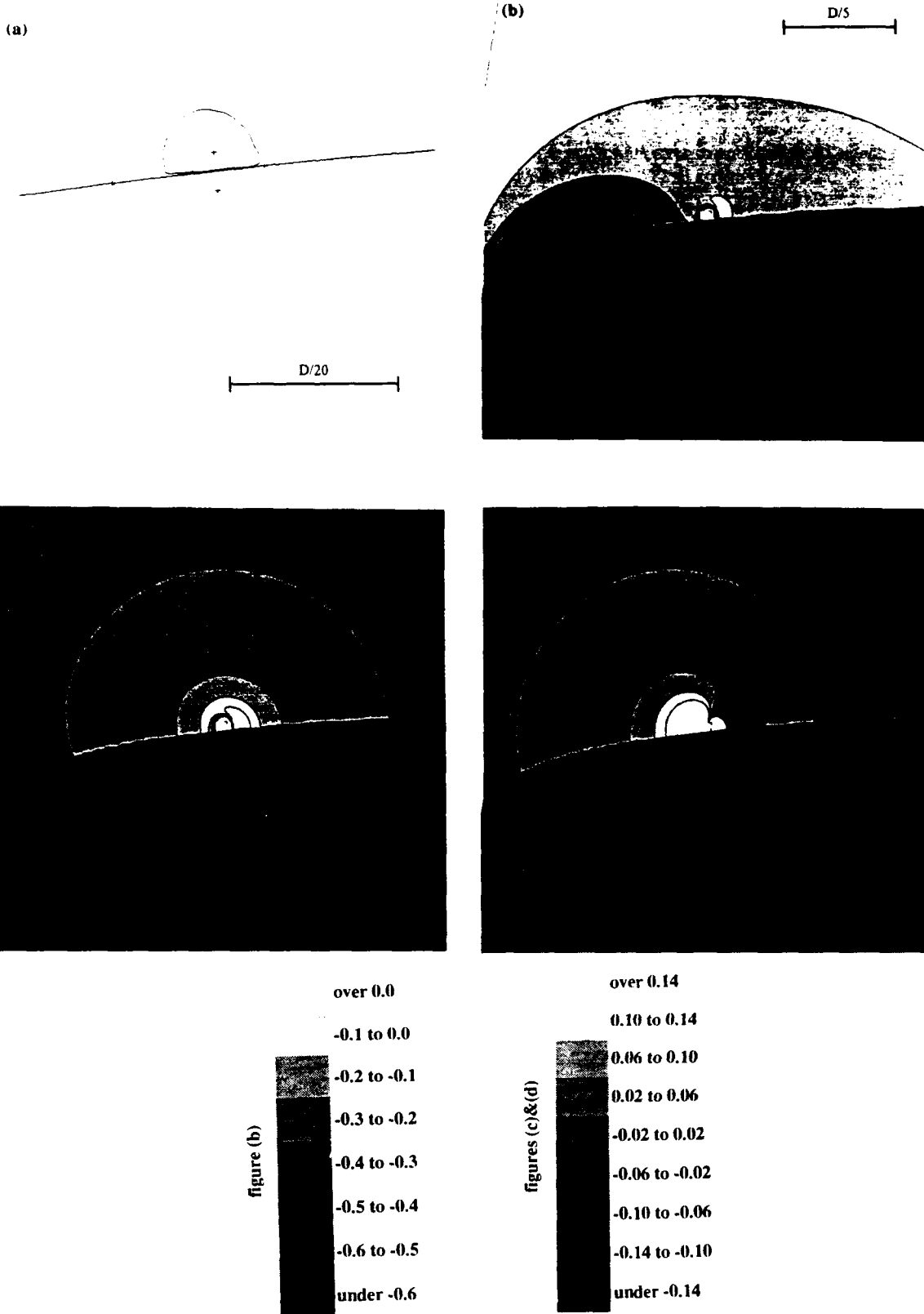
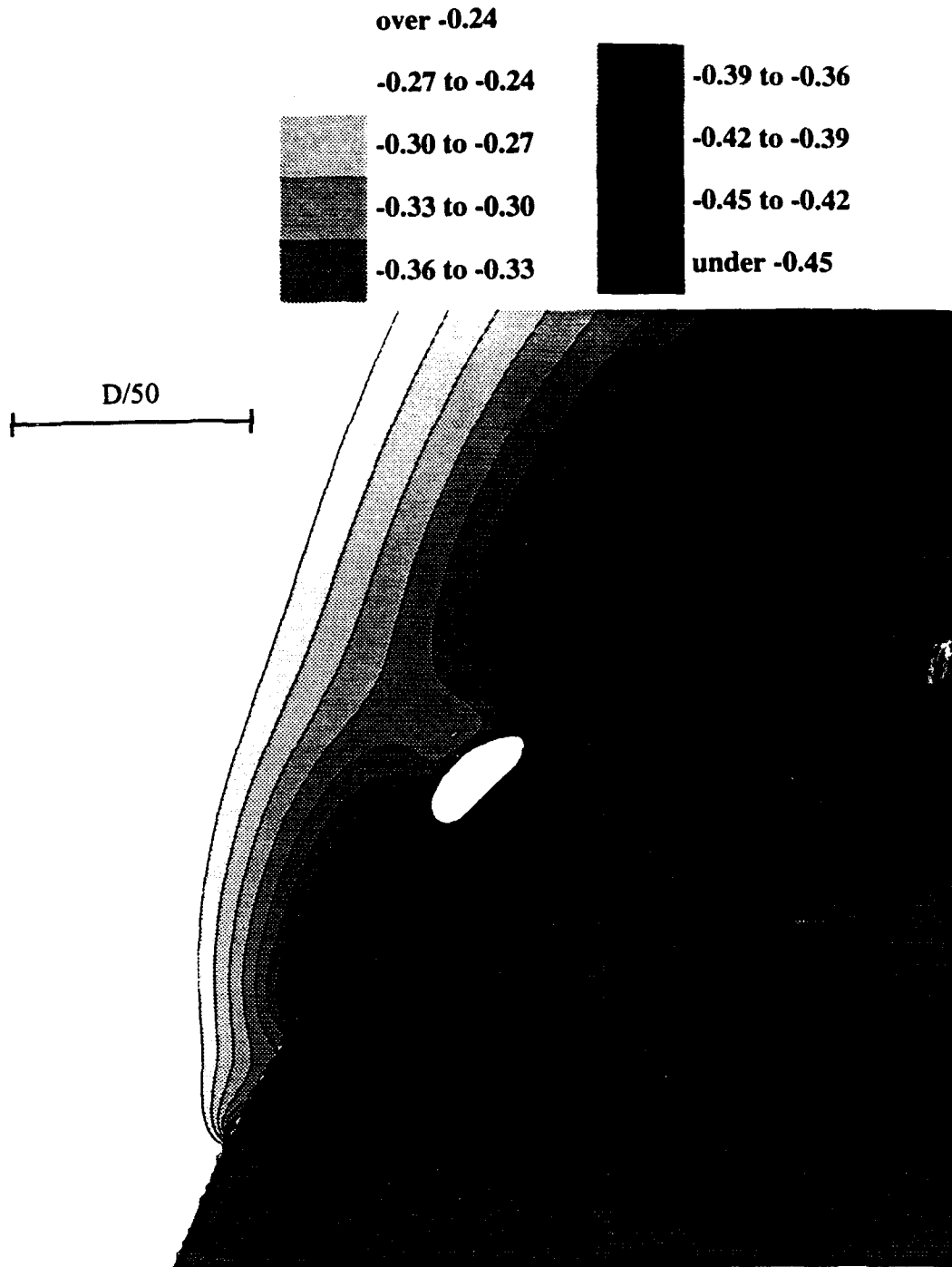


Figure D.12.20, Time,  $\tau=3.188$ . (a) bubble shape, (b)  $C_p$ , (c)  $\Delta C_p$ , (d)  $\Delta C_{p_\phi}$   
 $Q=-9.55 \times 10^{-5}$ ,  $x_q=0.445$ ,  $r_q=0.469$ ,  $C_{p_q}=-0.27$ ,  $r_{circ}=1.29 \times 10^{-2}$ ,  $v_{surf}=-0.575$



**Figure D.13 Pressure distribution,  $C_p$ , close to the bubble**

The conditions shown here are identical to those of figure D.12.2.b:  $\sigma=0.45$ ,  $\tau=2.828$ ,  $Q=4.24 \times 10^{-6}$ ,  $x_q=0.059$ ,  $r_q=0.355$ ,  $C_{p_q}=-0.78$ ,  $r_{\text{circ}}=3.93 \times 10^{-3}$ ,  $v_{\text{surf}}=0.274$ . This figure illustrates the way the isobars curve around the surface of the bubble indicating the  $C_p \approx -\sigma$  condition on the surface. Also shown is the local over-pressure on the exterior of the bubble induced during this early growth phase.

The source and image source locations are also shown in Figure D.12, as represented by the crosses in figures (a). A number of different phases in the life of the bubble may be identified from these figures.

**Figure D.12.1:**

After the nucleus encounters a low enough pressure to cause it to become unstable it first grows very rapidly towards the headform surface, where the pressure is lowest. If the nucleus is a few radii from the surface of the headform when it becomes unstable, the bubble is strongly deformed and becomes elongated as it grows in the direction of the headform. The source location relative to the center of the bubble is also displaced towards the headform.

**Figure D.12.2:**

As the growing bubble interacts with the headform its interior surface next to the headform begins to flatten. The positive pressure perturbations generated in both the (c) and (d) figures appear quite spherical and equal in intensity at this time, indicating that the velocity induced pressure perturbation,  $\Delta C_{p_v}$ , is small. The rate of increase of the source strength  $Q$  is greater than the effect of the source displacement per time step, explaining the quasi-isotropic nature of the  $\Delta C_{p_\phi}$  pressure perturbation. This pressure perturbation translates into a local over-pressure,  $C_p$ , above the exterior surface of the bubble as can be seen in figure (b). Figure D.13 includes a close-up view of the  $C_p$  pressure distribution around the bubble.

**Figures D.12.2-7:**

The local over-pressure on the exterior surface of the bubble observed in figure D.12.2.b remains until figure D.12.7.b at time  $\tau \approx 2.93$  and causes the bubble to be locally depressed. This local "crushing" of the bubble exterior surface is quite violent and might be the source of the dimple depression observed in the LCC experiments. This phenomenon can also be observed in the error estimation figures D.8 and D.9, where the exterior nodes on the surface of the bubble present adverse conditions between the times

2.82 and 2.95 and require corrective displacements that brings them closer to the source. It appears as if, after having been forced toward the headform during the early phase, the growing bubble "rebounds." The position of the source is shifted towards the headform surface during this time. This source location also contributes to produce a flatter and more elongated bubble shape in the directions parallel to the headform surface.

We can see from the (c) figures, that the bubble generates an over-pressure perturbation  $\Delta C_p$  in its surroundings during this time. We may refer to this time as the driving growth phase. Examining the unperturbed pressure field over the headform (figure D.12.1.b) and noting the values of  $C_{p_q}$  in the figure captions, we can see that this phase corresponds to a time when the bubble is traveling through the region where it encounters pressures lower than the cavitation number. Looking at the absolute pressure field,  $C_p$ , in the (b) figures, the intensity of the high pressure perturbation,  $\Delta C_p$ , counteracts the prevailing low pressure field so that the boundary condition on the bubble surface ( $C_p = -\sigma$ ) is met. We note that the large pressure perturbation in both the (c) and (d) figures increases in intensity and reaches its maximum in figure D.12.4 at  $\tau = 2.87$ . This maximum pressure perturbation occurs at a time when the source is already downstream of the minimum pressure coefficient point. After this time the over-pressure intensity decays. We can observe though, that this decay occurs in a non-isotropic manner. This non-sphericity can be explained by analyzing each of the  $\Delta C_{p_\phi}$  and  $\Delta C_{p_v}$  pressure perturbations separately. Looking at the high pressure,  $\Delta C_{p_\phi}$ , in the (d) figures, we observe a low pressure wave perturbation propagating clockwise during this entire growth phase. The positive  $\Delta C_{p_\phi}$  values are located downstream of the source which corresponds to the direction of the source displacement and thus to the direction of maximum momentum increase. As the downstream displacement velocity of the source increases, the momentum change upstream of the source decreases to the point that it eventually produces negative inertial pressure perturbations,  $\Delta C_{p_\phi}$ . On the other hand, the velocity-related pressure perturbation,  $\Delta C_{p_v}$ , exhibits the opposite behavior. Upstream of the



source the velocity induced by the sources is opposite to the flow over the headform and thus produces higher  $\Delta C_{p_v}$  pressure values. Downstream of the source both of these velocities add up producing lower  $\Delta C_{p_v}$  pressure values. The sum of both pressure perturbations  $\Delta C_{p_\phi}$  and  $\Delta C_{p_v}$  in the (b) figures shows that the high velocity-induced pressure,  $\Delta C_{p_v}$ , is the dominant term upstream of the source, whereas the high momentum-induced pressure,  $\Delta C_{p_\phi}$ , is the dominant term downstream. Thus  $\Delta C_p$  shows a fairly uniform high pressure distribution in all directions from the source. From the (c) figures we see that this high pressure perturbation becomes elongated in the upstream direction as the bubble travels downstream. It appears as though the high pressure field upstream of the bubble does not move as fast as the source, causing this elongated pressure shape.

The overall intensity of this high pressure perturbation does decay with time after figure D.12.5 and is almost null by figure D.12.9. The inertial-pressure,  $\Delta C_{p_\phi}$ , decays faster than the velocity-pressure,  $\Delta C_{p_v}$ . The result on the pressure perturbation  $\Delta C_p$  is seen in the form of an expanding counter-clockwise low pressure wave. It is quite remarkable to observe that, while a low  $\Delta C_{p_\phi}$  pressure wave is propagating in the clockwise direction, a low  $\Delta C_p$  pressure wave propagating in the opposite (counter-clockwise) direction.

**Figures D.12.8-10:**

The bubble has just passed through the low pressure region where the pressure coefficient is lower than the cavitation number and has reached the point where  $C_{p_q} = -\sigma$ . The  $\Delta C_p$  pressure perturbation field in the (c) figures is close to zero at this point. We note that the pressure perturbation  $\Delta C_{p_\phi}$  is symmetrical about the source location, generating an over-pressure downstream of the source and an under-pressure upstream. The perturbation  $\Delta C_{p_\phi}$  is thus almost exactly balanced by the perturbation  $\Delta C_{p_v}$  which has the opposite shape distribution.

**Figures D.12.10-15:**

The bubble continues to grow during this phase which may be referred to as the inertial growth phase. The bubble is now traveling through the region where it encounters unperturbed pressures higher than the cavitation number, as is shown by the values of  $Cp_q$ . It still continues to grow due to the fluid inertial terms. The bubble growth is decelerating as is shown by the decay in the source strength,  $Q$ , and of the surface growth velocity,  $v_{surf}$ . The source location remains very close to the headform surface but also shifts in the upstream direction relative to the center of the bubble. Since the source strength is still positive this produces the wedge bubble shape that can be seen in the (a) figures (with the thicker side upstream). As discussed in the previous section, this shape is similar to that observed in the experiments.

During this phase the bubble generates negative pressure perturbations  $\Delta Cp$  in its vicinity (in the (c) figures), which can be explained as follows. In the (d) figures, we continue to observe the same  $\Delta Cp_q$  clockwise low-pressure wave propagation as we did during the driving growth phase. The deceleration of the bubble growth eventually yields large negative values of  $\Delta Cp_q$  even downstream of the source. As the source strength  $Q$  decreases, the influence of the velocity-related pressure perturbation  $\Delta Cp_v$  is reduced. The low pressure perturbation field,  $\Delta Cp$ , becomes almost identical to the momentum-related pressure field  $\Delta Cp_q$ . As in the previous phase, this negative  $\Delta Cp$  pressure distribution is generated by a clockwise low pressure wave expansion.

**Figures D.12.15-16:**

These figures correspond to the time when the source strength  $Q$  is approaching zero at  $\tau=3.09$ . The bubble has reached its maximum size and is now about to start collapsing. Notice that by this time the bubble is quite far downstream (by more than a tenth of the headform diameter) of the unperturbed ending of the low pressure region ( $Cp < -\sigma$ ) and is modifying the pressure field in the high pressure recovery region. As we stated before, the pressure perturbations  $\Delta Cp$  and  $\Delta Cp_q$  are roughly equal in intensity at

this time, indicating that the velocity pressure perturbation,  $\Delta C_{p_v}$ , is almost zero. We notice that this is also the moment when the pressure perturbations  $\Delta C_p$  and  $\Delta C_{p_\phi}$  have reached their minimum negative values. This minimum in  $\Delta C_{p_\phi}$  indicates that this is also the time when the source strength  $Q$  is decreasing most rapidly. The almost spherical pressure perturbation distribution observed is due to the fact that the source displacement effect is small compared to the source intensity decay.

**Figures D.12.16-19:**

The bubble is now collapsing ( $Q < 0$ ). We observe the displacement of the source in the downstream direction relative to the bubble center, which causes the tip of the wedge shaped bubble to disappear gradually. The low pressure perturbation generated by the sources continues to modify the pressure coefficient,  $C_p$ , such that boundary condition on the surface of the bubble remains satisfied. Even though the rate of decrease of the source intensity  $Q$  is not as high as in figure D.12.15, the bubble collapse velocity increases rapidly, as indicated by the values of  $v_{surf}$ , since the bubble radius,  $r_{circ}$  is smaller.

The low pressure field perturbation in the (c) figures has an almost spherical shape and is slightly elongated in the upstream direction, with a shape similar to that of figures D.12.2-8. The overall low pressure perturbation  $\Delta C_p$  decays in intensity with time. This is understandable since the bubble becomes smaller and does not need to generate such a extensive low pressure perturbation to meet the boundary condition on its surface. A high pressure wave perturbation in the (d) figures is now propagating in a clockwise direction indicating an increase in the time derivative of the source strength,  $\partial Q / \partial \tau$ , and the acceleration of the source in the downstream direction. On the other hand, the negative value of the source  $Q$  results in a low pressure perturbation  $\Delta C_{p_v}$  upstream of the source and a high pressure perturbation downstream. The decrease of the positive  $\Delta C_{p_\phi}$  pressure field by a low clockwise pressure propagation in the (d) figures, balances well the appearance of a negative  $\Delta C_{p_v}$  pressure field by a low counter-clockwise pressure

propagation, so that the overall negative  $\Delta C_p$  pressure field in the (c) figures decreases in an almost isotropic manner.

**Figure D.12.20:**

This figure corresponds to the final stage of the collapse. The drastic increase in rate of change of the source strength  $Q$ , produces the large over-pressures in the momentum-related pressure perturbation,  $\Delta C_{p_\phi}$ , as seen in the (d) figure. The source strength  $Q$  is still negative and the bubble surface velocity  $v_{surf}$  continues to increase as the radius of the bubble decreases. The pressure perturbations  $\Delta C_p$  and  $\Delta C_{p_\phi}$  have quite similar values far from the bubble. The term  $\Delta C_{p_v}$  is negligible far from the bubble, which confirms the derivation of equation B.16 indicating that the pressure perturbation in the far field of a collapsing source is simply proportional to the second derivative of the bubble volume (i.e., the rate of change of the source strength). The pressure perturbation at this time extends far from the bubble. However, close to the bubble surface the velocity-related pressure perturbation  $\Delta C_{p_v}$  still influences the  $\Delta C_p$  perturbation. In the immediate neighborhood of the bubble the perturbations  $\Delta C_{p_\phi}$  and  $\Delta C_{p_v}$  have opposite distributions. In this region the high pressure perturbation  $\Delta C_{p_v}$  downstream of the source dominates the low pressure  $\Delta C_{p_\phi}$ . We have therefore a positive  $\Delta C_p$  perturbation downstream of the source which eventually causes the wedge shape of the bubble to disappear. We note from the (b) figure that, at this stage, the dynamic boundary condition is still roughly  $C_p = -\sigma$ . The dissolved gas content and surface tension terms are still small effects at this time. Indeed the bubble collapse velocity is still increasing and is not yet slowed by the non-condensable gas. The over-pressure perturbations  $\Delta C_{p_\phi}$  and  $\Delta C_p$  continue to increase very rapidly and are eventually responsible for the collapse noise impulse. This time frame sequence ends at figure D.12.20 since the bubble has already rebounded by the next time step,  $\tau=3.208$ .

### D.5.3 Pressure distribution over headform

The pressure in the vicinity of the bubble has been computed for times ranging from initial growth to collapse. The purpose of this paragraph is to identify the influence of the bubble on the surrounding flow field. By quantifying the distance below which the influence of the traveling bubble is substantial, we can predict to what extent multiple bubbles may interact with one another. The pressure perturbation of individual bubbles has been computed just above the headform surface, at a distance equal to  $1/100^{\text{th}}$  of the headform diameter,  $D$ . Presented in figures D.14 and D.15, as a function of time and for three different cavitation numbers, is the absolute pressure coefficient,  $C_p$ , and perturbation pressure distribution,  $\Delta C_p$ , parallel to the headform surface. The dimensionless curvilinear abscissa,  $s$ , starts at the nose of the headform ( $x = r = 0$ ). Presented in figure D.16 is the perturbation pressure,  $\Delta C_p$ , in the direction normal to the surface of the headform, as we travel with the source (at the same axial location as the source). For all figures three different cavitation numbers  $\sigma=0.35$ ,  $\sigma=0.45$  and  $\sigma=0.55$  are shown. Note that the time scale on the figure is different for each cavitation number.

The white areas in the figures D.14 and D.15 represent the leading and trailing edge extremes of the bubble. Note that the time scale is different for the three different cavitation numbers. For all three cavitation numbers in figures D.14 we observe that the initial pressure distributions,  $C_p$ , at time  $\tau=2.8$  are identical. The minimum pressure coefficient  $C_{p_{\min}}=-0.78$  is located at about  $s=0.42$ . We observe that the influence of the source counters the initial pressure variations of the flow over the headform (from an under-pressure  $C_p=-0.78$  to the downstream over-pressure  $C_p=0$ ), such that it results in a rather steady pressure value  $C_p=-\sigma$  on the surface of the bubble. We clearly see by observing figures D.14 and D.15 that the source first induces higher pressures in order to counter the original low pressure, then induces low pressure perturbations in higher original pressure fields. The very top part of each graphs shows the final high pressure

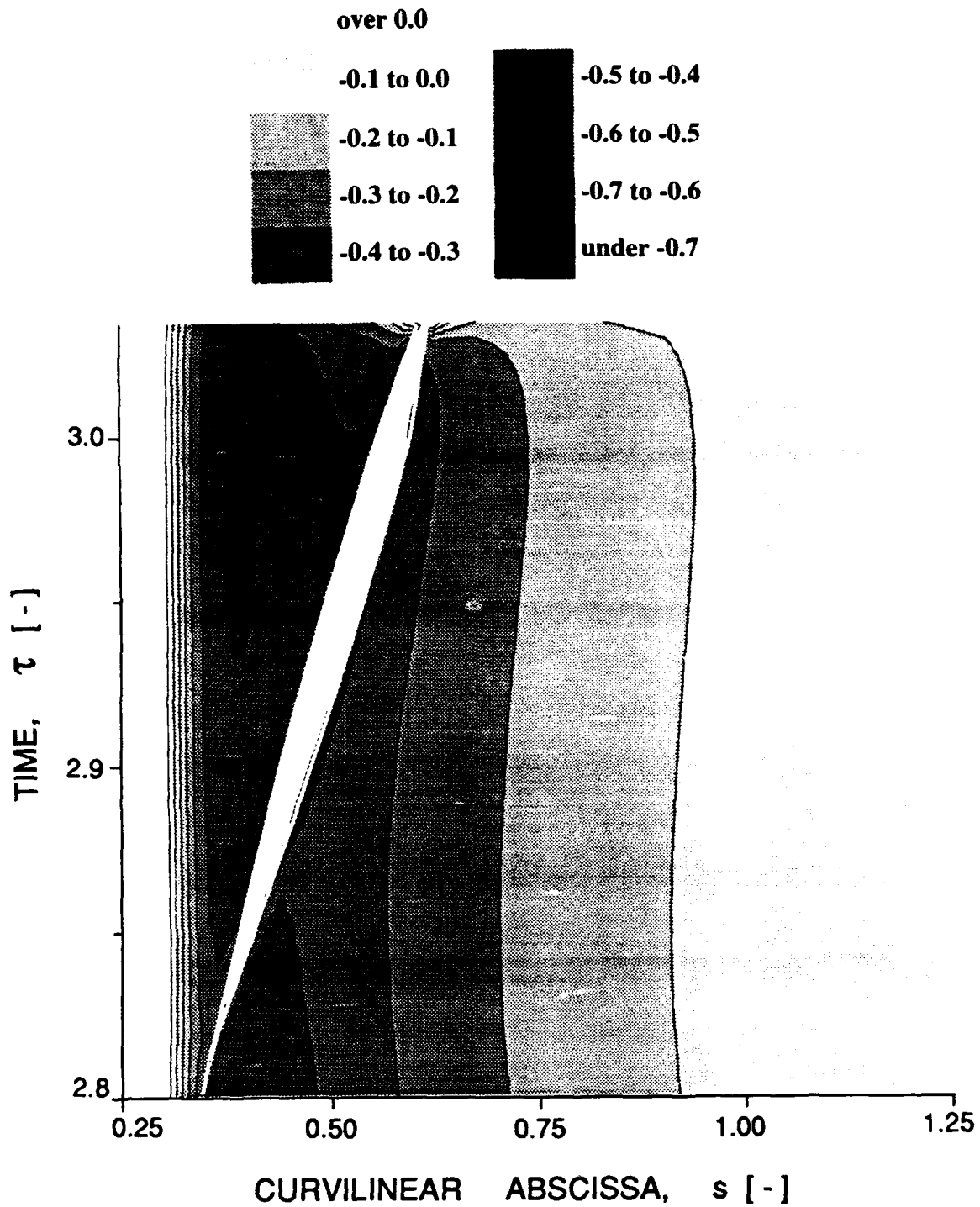


**Figure D.14.1 Pressure coefficient,  $C_p$ , in the direction parallel to the headform,  $\sigma=0.55$**

*The pressure coefficient distribution,  $C_p$ , in the direction parallel to the headform surface is presented as a function of time. The white area represents the bubble width.*

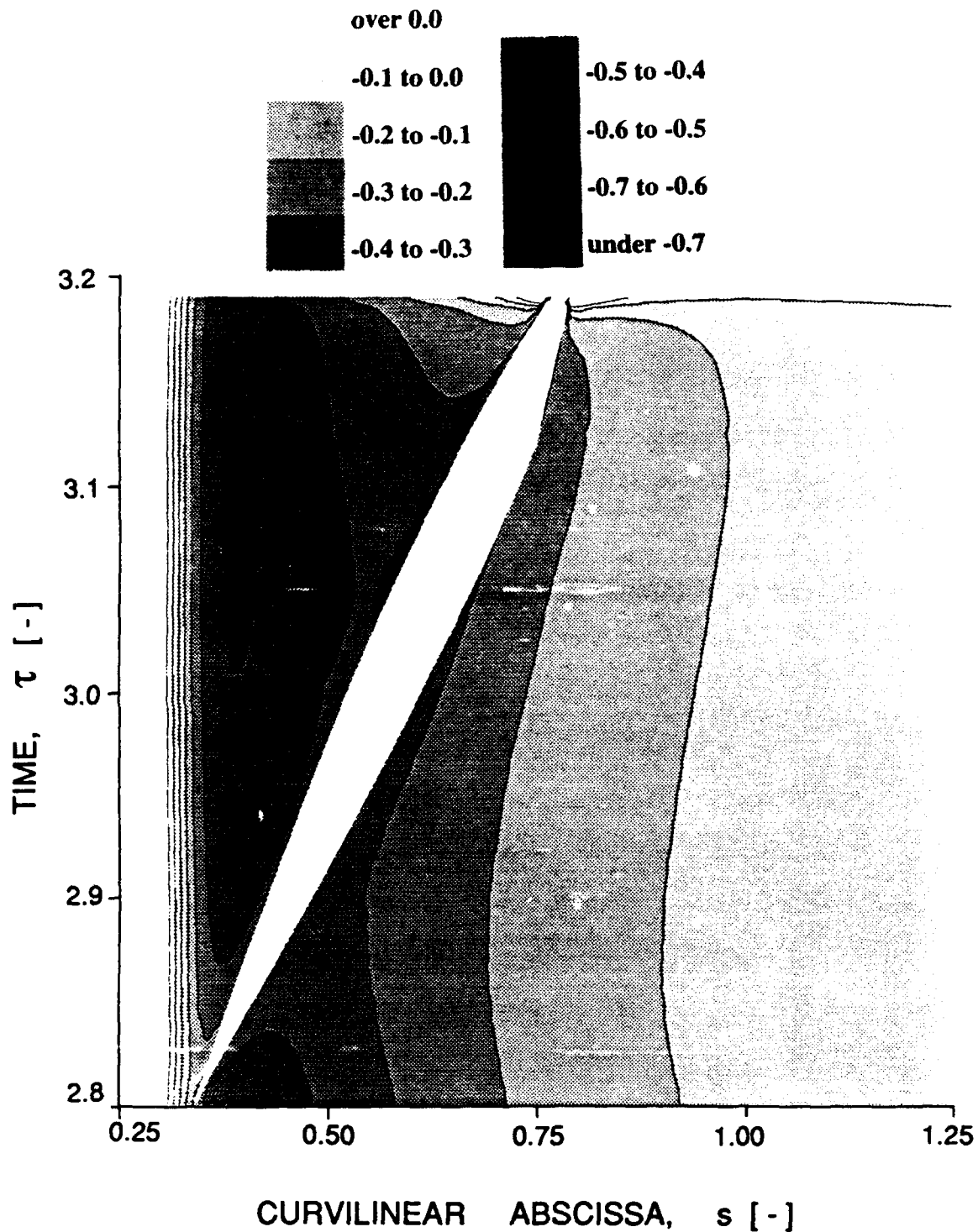


**Figure D.14.2 Pressure coefficient,  $C_p$ , in the direction parallel to the headform,  $\sigma=0.45$**

*The pressure coefficient distribution,  $C_p$ , in the direction parallel to the headform surface is presented as a function of time. The white area represents the bubble width.*

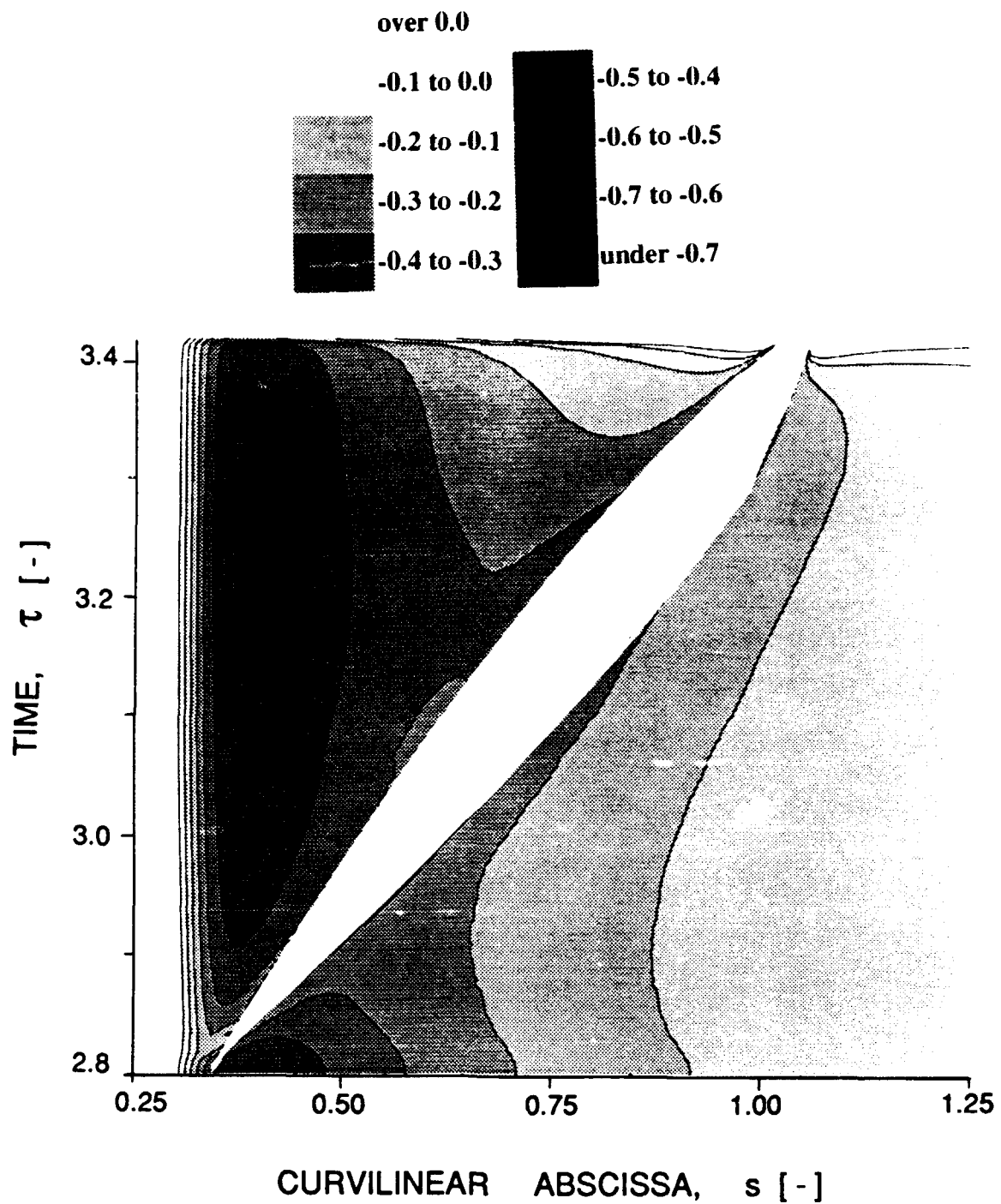


**Figure D.14.3 Pressure coefficient,  $C_p$ , in the direction parallel to the headform,  $\sigma=0.35$**

*The pressure coefficient distribution,  $C_p$ , in the direction parallel to the headform surface is presented as a function of time. The white area represents the bubble width.*



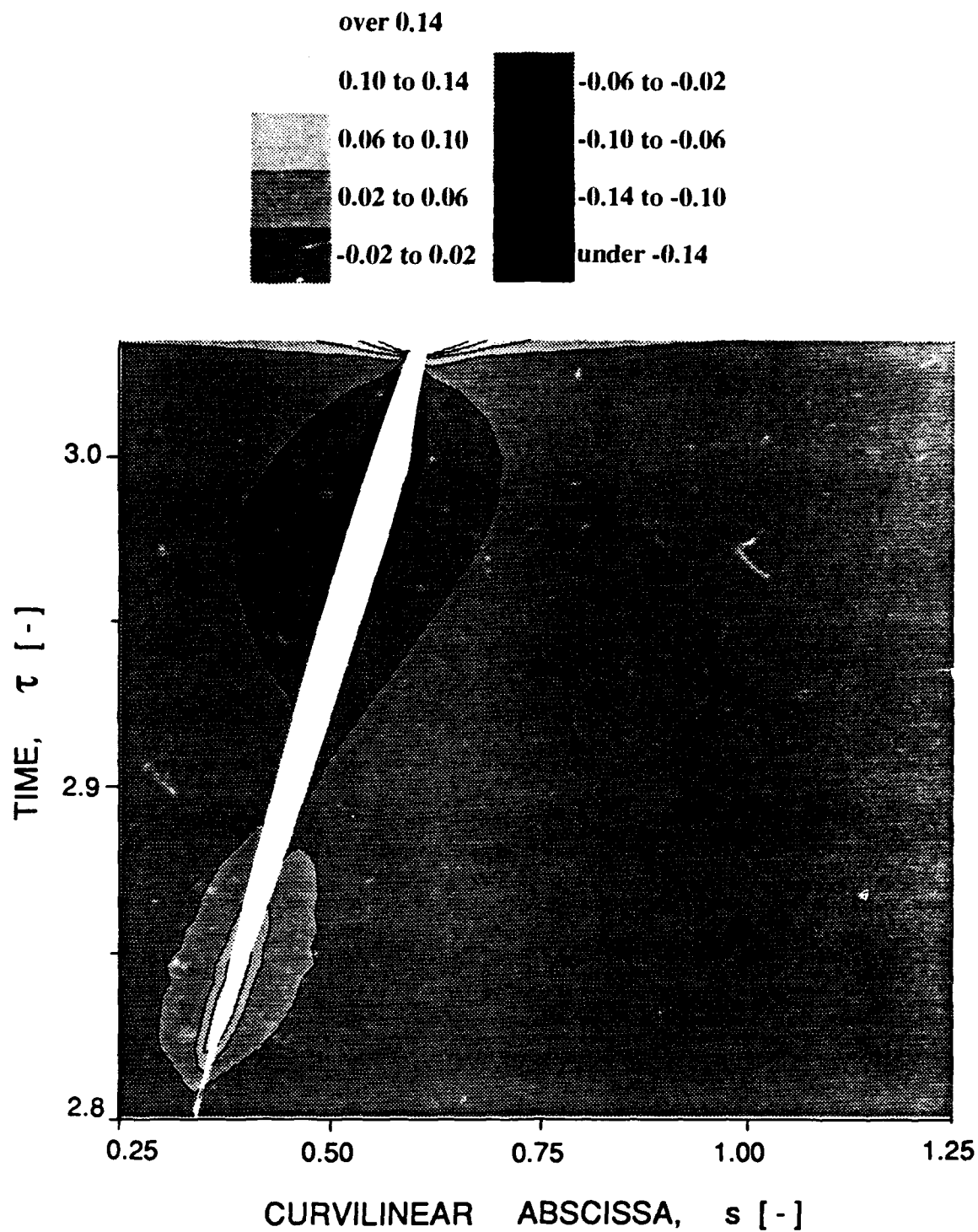


**Figure D.15.1** Pressure perturbation,  $\Delta C_p$ , in the direction parallel to the headform,  $\sigma=0.55$

*The perturbation pressure coefficient distribution,  $\Delta C_p$ , in the direction parallel to the headform surface is presented as a function of time. The white area represents the bubble width.*

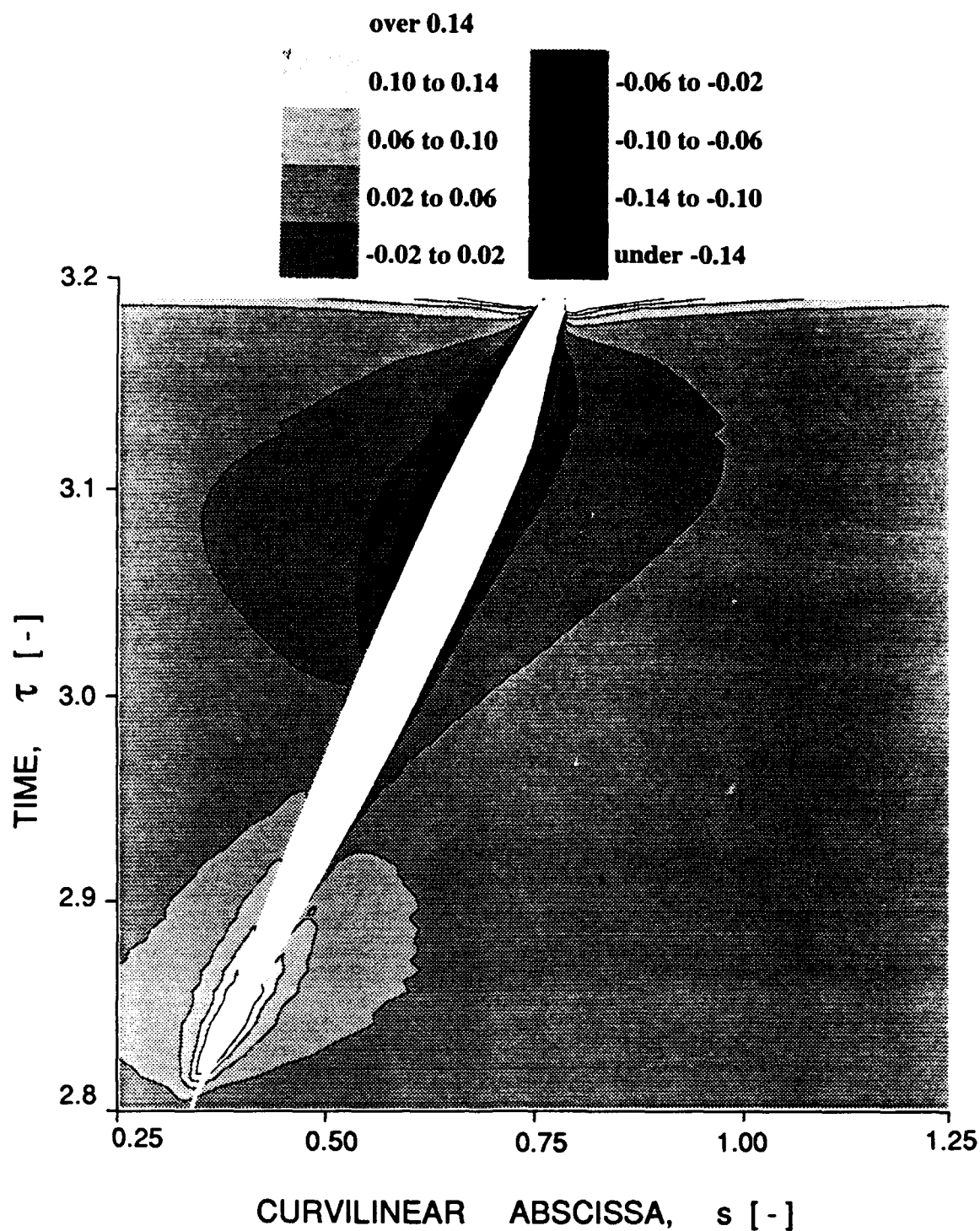


**Figure D.15.2 Pressure perturbation,  $\Delta C_p$ , in the direction parallel to the headform,  $\sigma=0.45$**

*The perturbation pressure coefficient distribution,  $\Delta C_p$ , in the direction parallel to the headform surface is presented as a function of time. The white area represents the bubble width.*

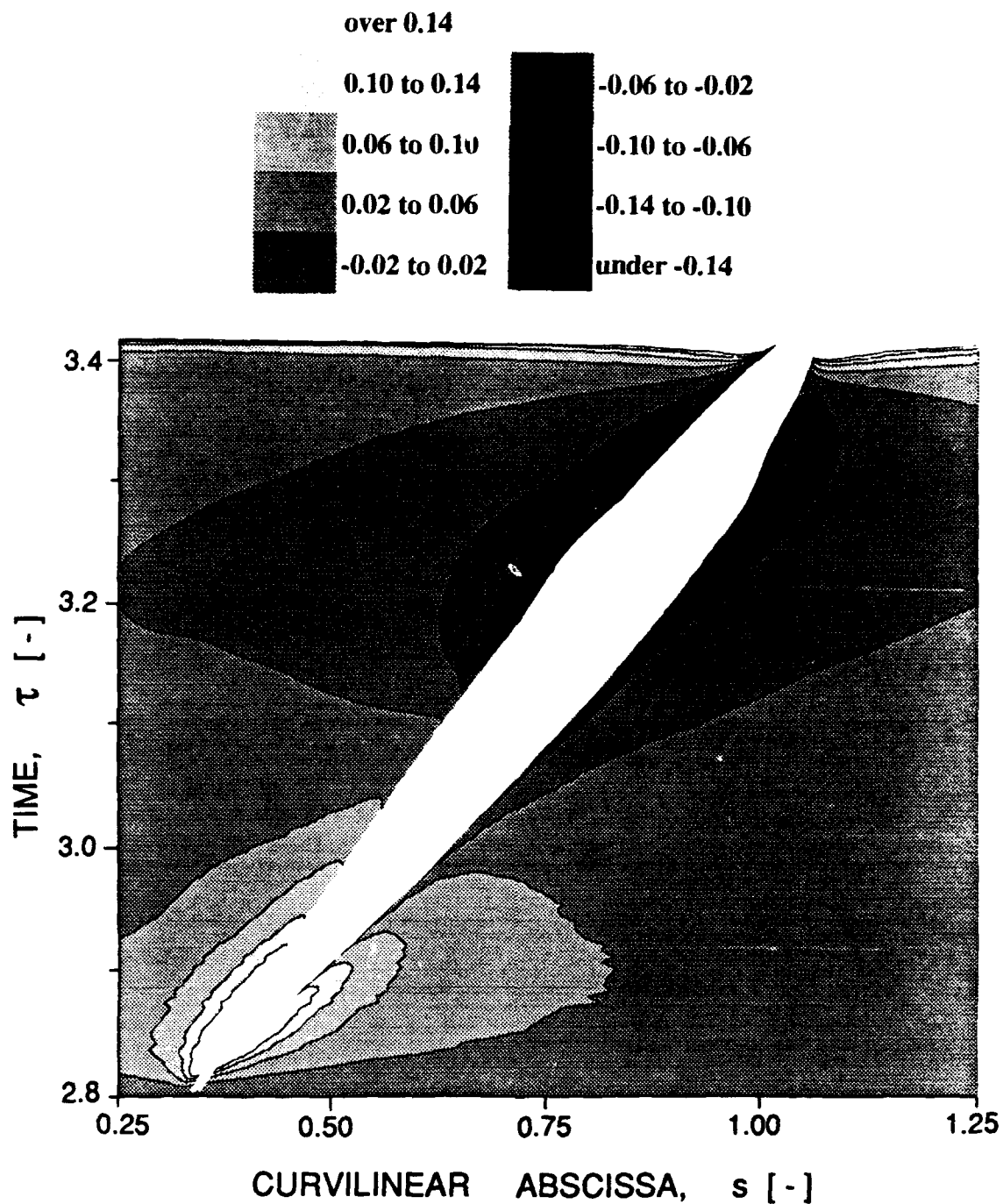


**Figure D.15.3 Pressure perturbation,  $\Delta C_p$ , in the direction parallel to the headform,  $\sigma=0.35$**

*The perturbation pressure coefficient distribution,  $\Delta C_p$ , in the direction parallel to the headform surface is presented as a function of time. The white area represents the bubble width.*

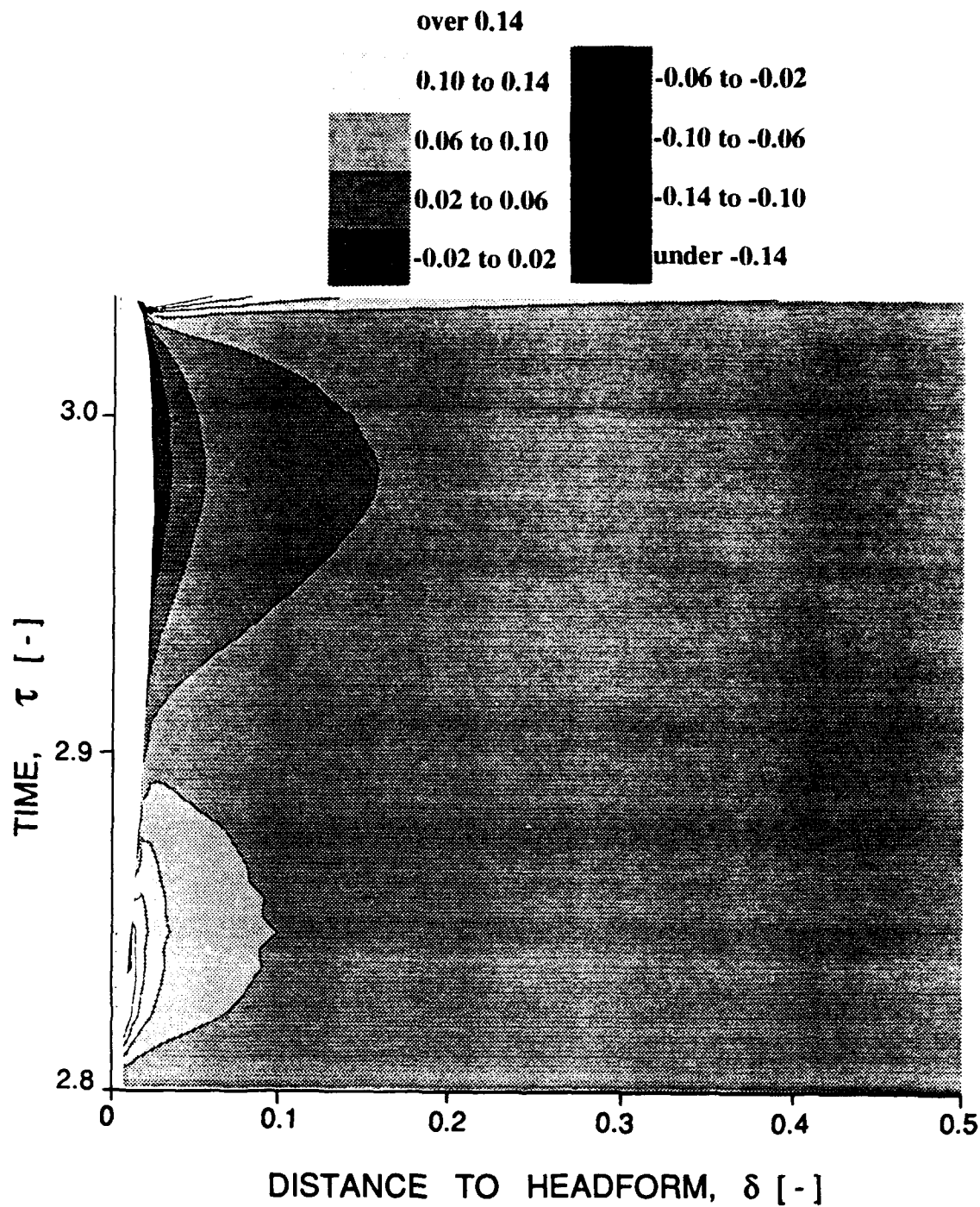


**Figure D.16.1 Pressure perturbation,  $\Delta C_p$ , in the direction normal to the headform,  $\sigma=0.55$**

*The perturbation pressure coefficient distribution,  $\Delta C_p$ , in the direction normal to the headform surface is presented as a function of time. The white area represents the bubble height.*

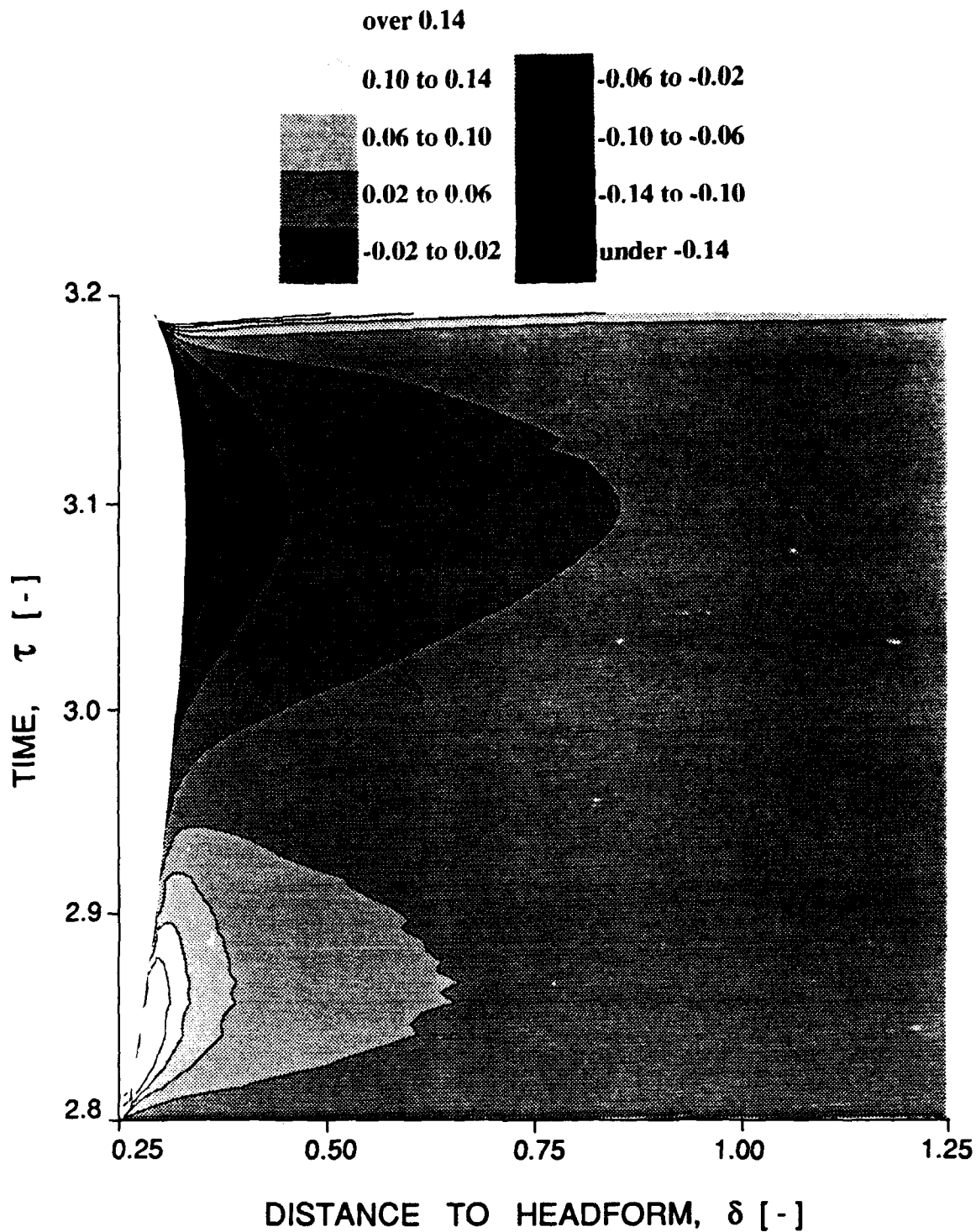


**Figure D.16.2 Pressure perturbation,  $\Delta C_p$ , in the direction normal to the headform,  $\sigma=0.45$**

*The perturbation pressure coefficient distribution,  $\Delta C_p$ , in the direction normal to the headform surface is presented as a function of time. The white area represents the bubble height.*

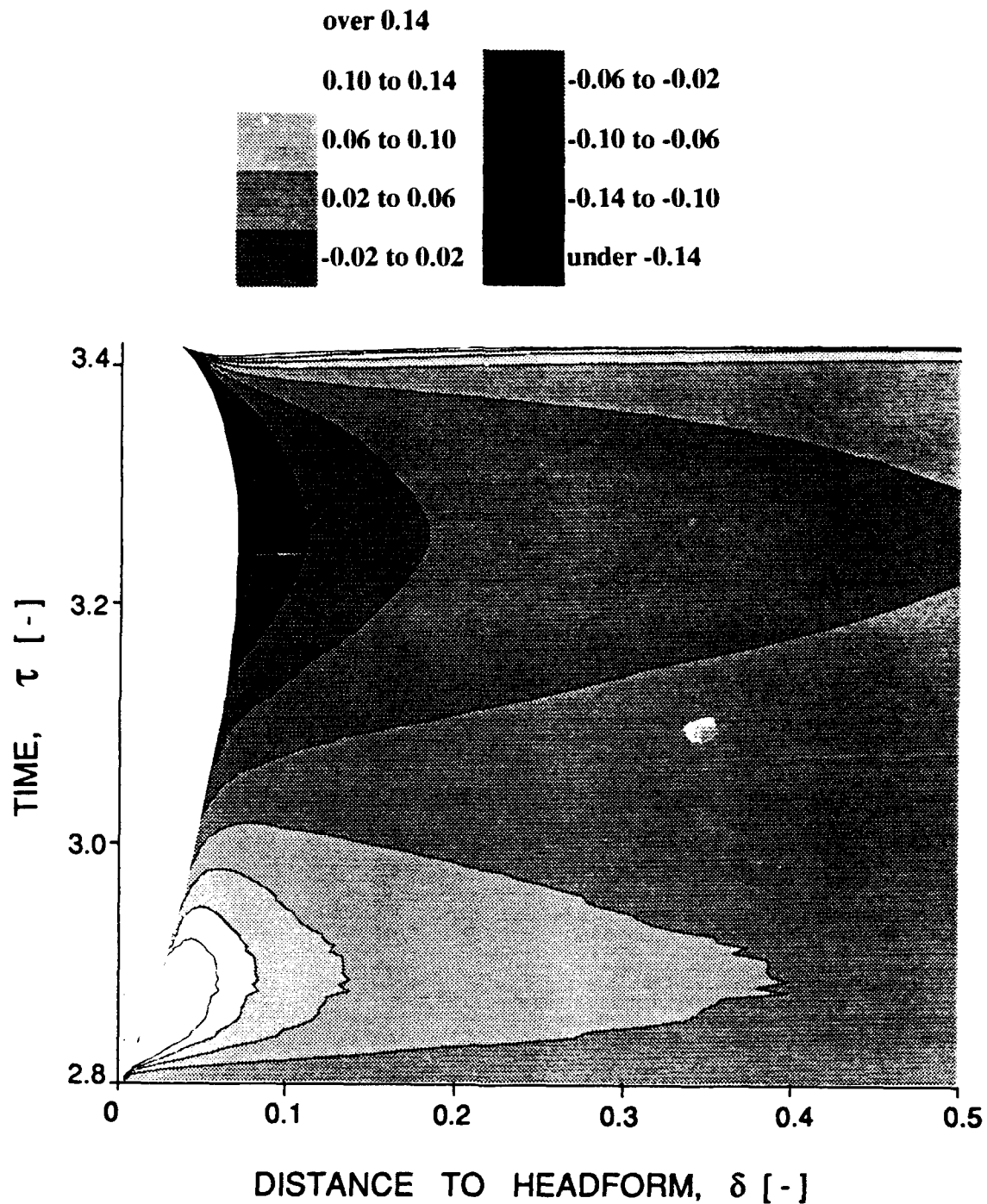


**Figure D.16.3 Pressure perturbation,  $\Delta C_p$ , in the direction normal to the headform,  $\sigma=0.35$**

*The perturbation pressure coefficient distribution,  $\Delta C_p$ , in the direction normal to the headform surface is presented as a function of time. The white area represents the bubble height.*

collapse perturbation in the form of a high pressure wave expansion. From these figures we can also observe some features of the asymmetry of the pressure perturbation upstream and downstream of the source. Figures D.15 clearly shows the increasing influence of the bubble as the cavitation number is reduced. The ratio of the distance of influence to the bubble size is observed to increase as the bubble gets larger. The high pressure perturbation generated during the early growth of the bubble increases the low pressures. One can therefore speculate that this might have an effect on the cavitation event rates, since the nuclei close to a growing bubble will not experience the low pressures which would cause them to become unstable. By observing figures D.16 we see that the pressure perturbation extends as far in the direction normal to the headform as it does in the parallel direction. Again we can measure the increase in the "zone of influence" of a bubble as the cavitation number is decreased.

#### **D.5.4 Program main parameters as a function of time**

In this section we present some of the main parameters as a function of time for a series of cavitation numbers. Among the variables presented here are the average source strength,  $Q$ , in figure D.17; the bubble cap base radius,  $r$ , in figure D.18; the bubble sphericity,  $\epsilon$ , as a function of time in figure D.19; and three different bubble dimensions in figure D.20. As in the previous section, all these bubbles were computed with the following conditions:  $R_0=100\mu\text{m}$ ,  $D=50.8\text{cm}$ ,  $U_\infty=11.5\text{m/s}$  and an initial nucleus position  $x_{q0}=-1.0$ ,  $r_{q0}=0.01$ .

At first look, the average source strength curves as a function of time in figure D.17 appear similar in shape for all cavitation numbers. However a scaling analysis of all these curves does show some differences, indicating that the computed bubble dynamics does not simply scale with cavitation number. It is possible though to estimate crudely the decay law of source strength versus the cavitation number as  $Q \propto \sigma^{-6.5}$ . As discussed in the

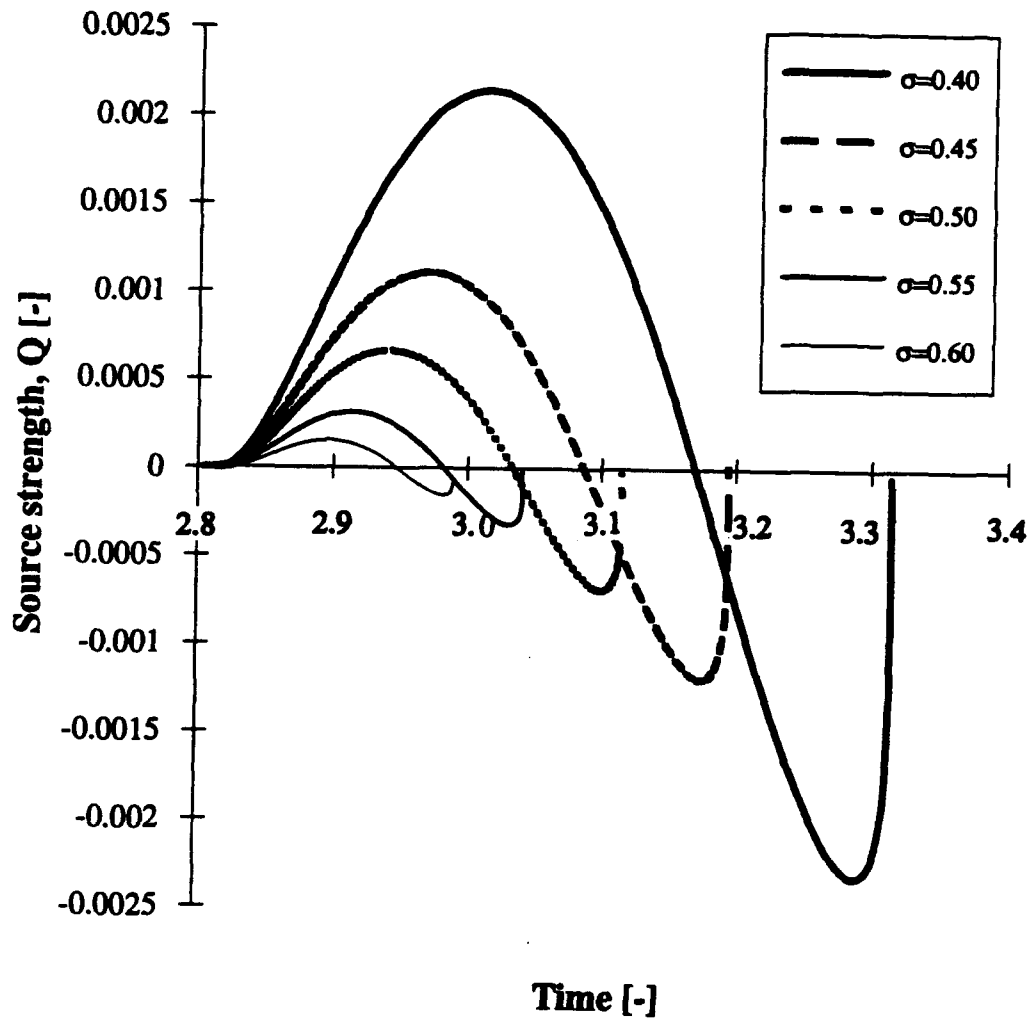


**Figure D.17** Average source strength,  $Q$ , as a function of time  
*The computed average source strength,  $Q$ , is shown as a function of time for different cavitation numbers ranging from  $\sigma=0.40$  to  $\sigma=0.60$ .*



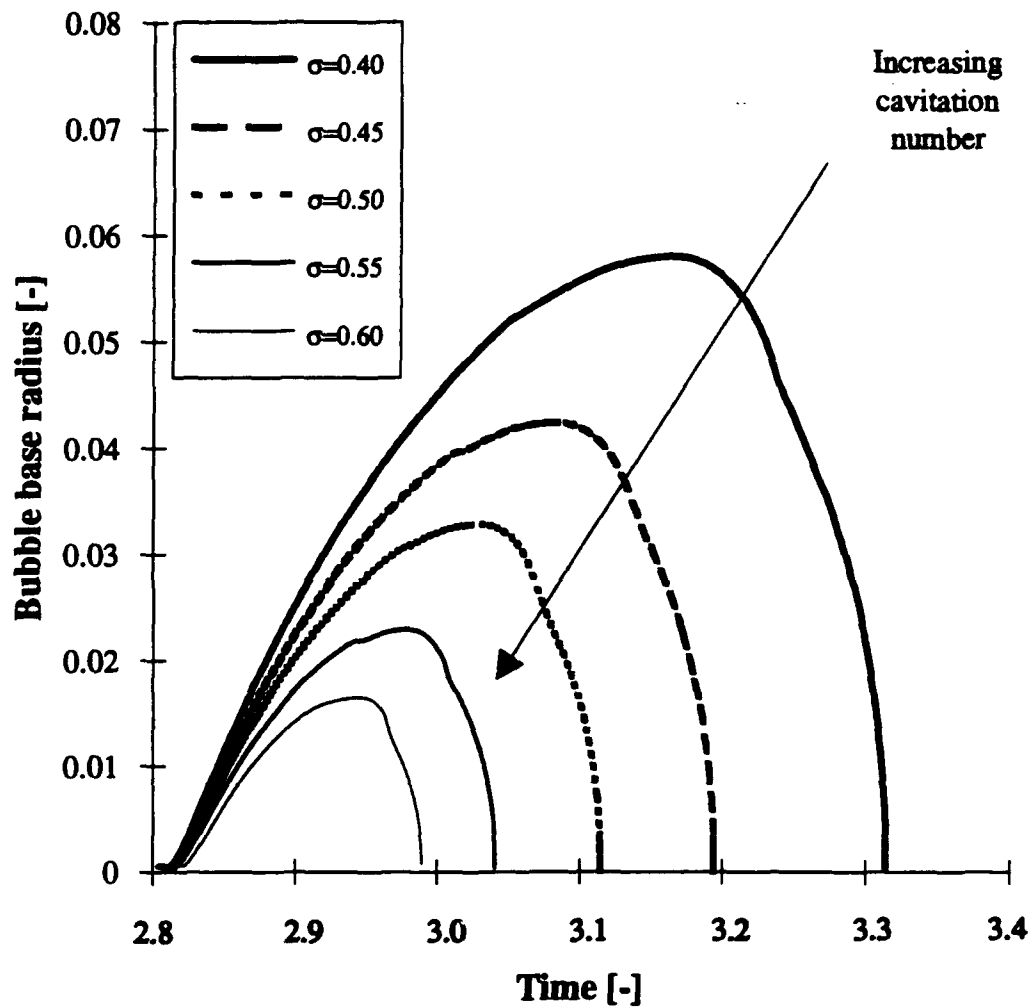


**Figure D.18** Computed bubble base radius as a function of time  
*The computed bubble base radius is shown as a function of time for different cavitation numbers ranging from  $\sigma=0.40$  to  $\sigma=0.60$ . Notice the difference with the radii from the solution of the Rayleigh-Plesset equation shown in figure B.1.*

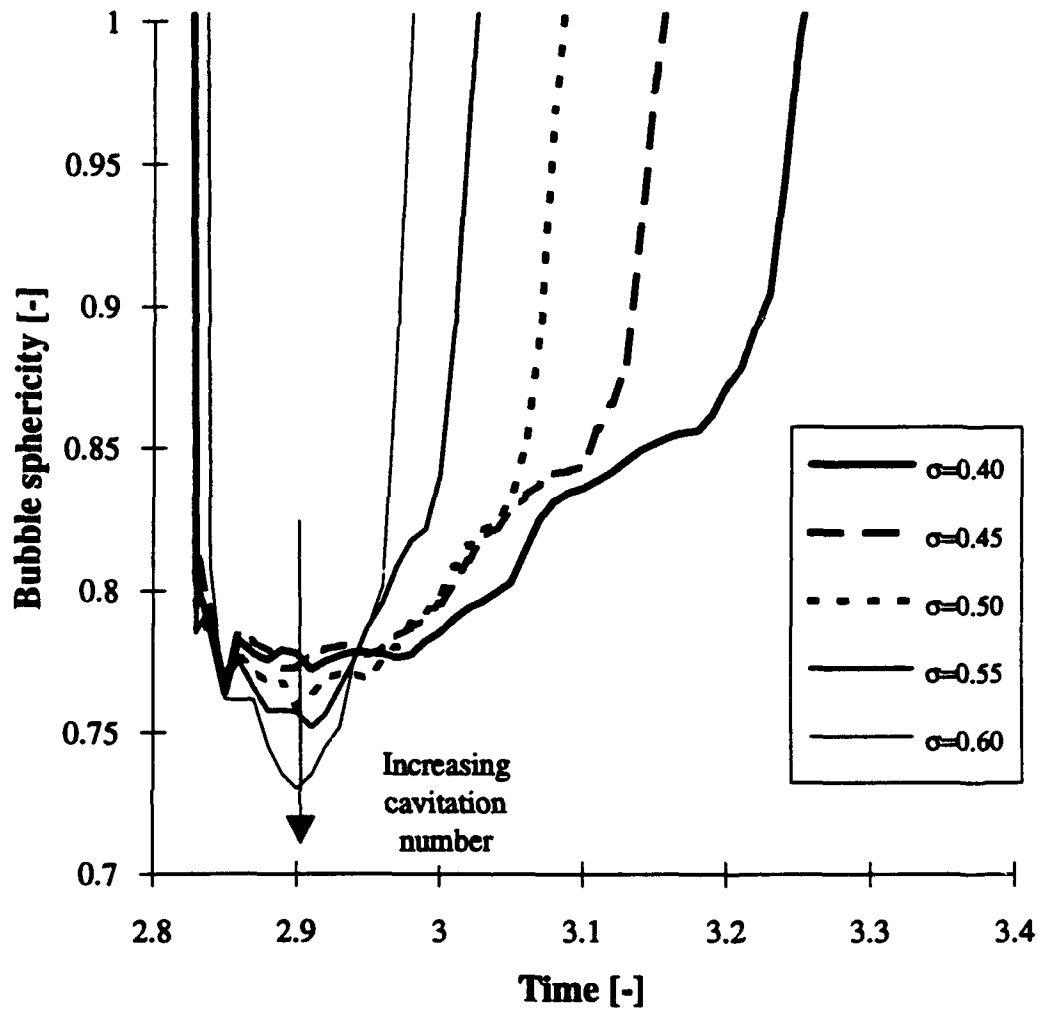


**Figure D.19 Bubble sphericity as a function of time**

*The computed bubble sphericity,  $\epsilon$ , is shown as a function of time for different cavitation numbers ranging from  $\sigma=0.40$  to  $\sigma=0.60$ . Notice the Rayleigh-Plesset solution at  $\epsilon=1$ .*

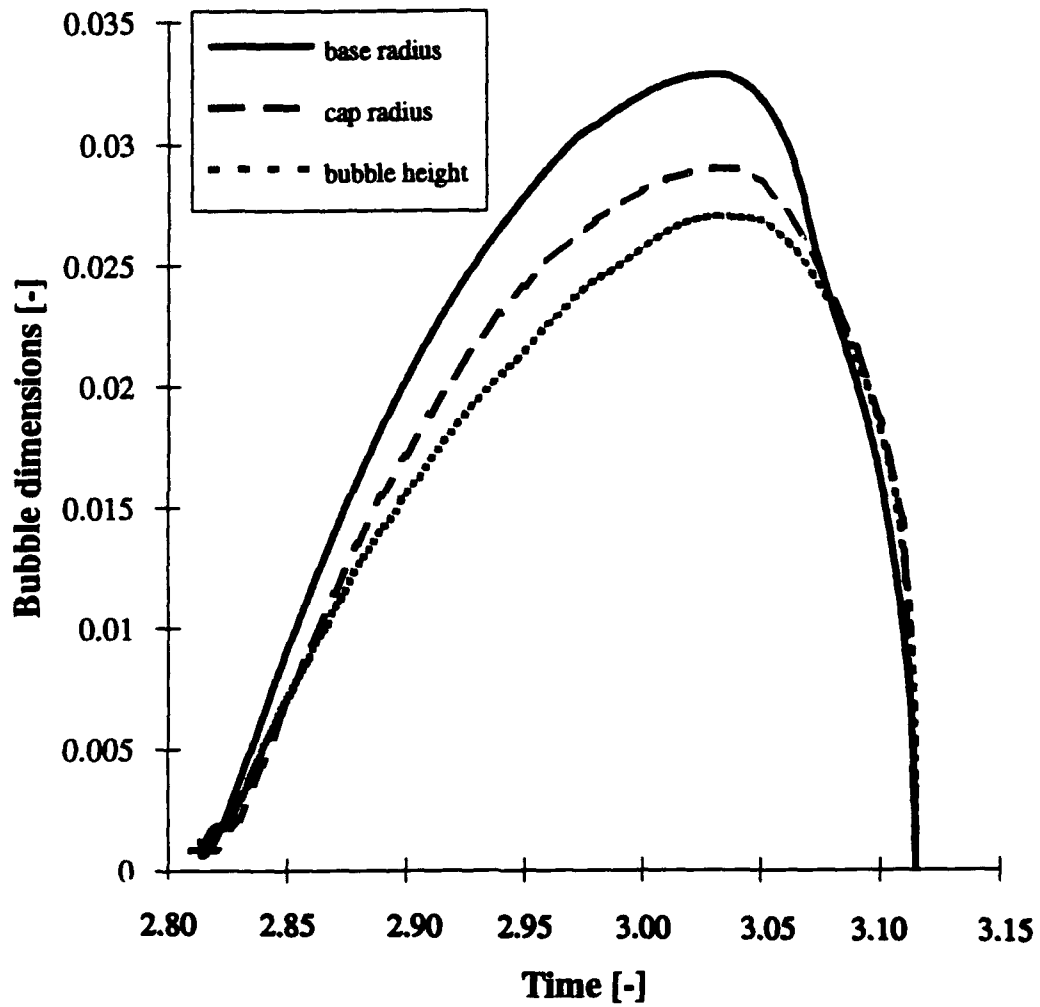


**Figure D.20 Bubble dimensions as a function of time**  
*Different bubble dimensions are shown for a cavitation number  $\sigma=0.50$ , indicating the three dimensional shape of the bubble.*

previous section, the value of the source strength is an important parameter for computing the value of the velocity-related pressure perturbation  $\Delta C_{p_v}$ . On the other hand, the variation of the source strength in time,  $\partial Q/\partial \tau$ , will dictate the value of the momentum-related pressure perturbation,  $\Delta C_{p_\phi}$ . Considering the direction downstream of the source, we can therefore see from figure D.17 why the  $\Delta C_{p_v}$  perturbation is first positive, then negative as  $Q$  becomes negative. Similarly, we see why  $\Delta C_{p_\phi}$  first exhibits positive values up to the point where the source strength,  $Q$ , reaches its maximum value, then negative values up to the point where  $Q$  is minimum, then positive again during the final collapse phase. We also observe that the minimum value of  $\partial Q/\partial \tau$  occurs when  $Q$  just crosses the zero value, generating the lowest  $\Delta C_{p_\phi}$  perturbation pressures at that time. The maximum value of  $\partial Q/\partial \tau$  generating the largest  $\Delta C_{p_\phi}$  pressures occurs during the final collapse of the bubble.

The computed bubble base radius,  $r$ , is presented as a function of time in figure D.18. It is interesting to compare this set of curves with the spherical Rayleigh-Plesset radius solution shown in figure B.1. We see that the traveling source model solution yields smaller bubble sizes than the Rayleigh-Plesset model. Furthermore the bubbles collapse much sooner in figure D.18 than in figure B.1. The main difference in the shape of these curves occurs at the time when the bubble has reached its maximum size and starts to collapse. The collapse phase happens much faster in the traveling source model than in the spherical model where the bubble takes a long time to increase its momentum inwards.

The bubble sphericity,  $\epsilon$ , as a function of time in figure D.19 shows that bubbles tend to become more elongated with increasing cavitation numbers. For all cavitation numbers, the minimum sphericity value of the bubble is found during the growth phase. After this time the increase in sphericity is not due to the fact that the bubble height,  $\delta$ , increases during the collapse phase, but to the fact that the thin leading edge of the wedge-like bubble disappears, thus leading to a smaller bubble base radius. The single source

model is not able to model the thinning of this wedge shape in the manner observed in the experiments. Figure D.20 gives another representation of the three-dimensional shape of the bubble as a function of time, for the cavitation number  $\sigma=0.50$ . In this figure are shown the bubble height,  $\delta$ , normal to the headform surface, the bubble base radius,  $r$ , (radius of the bubble at the base of the cap) and an estimated bubble cap radius,  $r_{cap}$ , based on the area of the bubble in the plane of symmetry,  $S$ , and defined by  $r_{cap} = \sqrt{2S/\pi}$ . We see from this figure that the base radius is larger than the two other dimensions indicating the non-sphericity of the bubble. However, towards the end of the collapse the evanescence of the leading edge of the bubble reduces this dimension. The bubble height  $\delta$  is the smallest of these three dimensions, indicating the flattened-elongated shape of the bubble. As the bubble collapses, though, we see that  $r_{cap}$  is almost equal to  $\delta$ , indicating that the bubble has almost a hemispherical cap shape ( $\epsilon=1$ ).

#### D.5.5 Comparison with the LCC experiments

Using the figures D.17 through D.20 we are able to compare the computed bubble size, collapse location and sphericity with the experimental data. The computed maximum bubble base radius is shown in figure C.18 along with the experimental data points and the solution of the Rayleigh-Plesset model. We see that the base radius computed using the traveling source model has values well within the envelope of the experimental data. The spherical Rayleigh-Plesset model overshoots the experimental data particularly at the lower cavitation numbers.

The same trend can be seen for the collapse location,  $x_c$ , in figure C.20. Again we see that the traveling source model is able to predict the location of collapse very well. The Rayleigh-Plesset model solution yields larger values of  $x_c$  which were not observed in the experiments.

Finally the bubble sphericity,  $\epsilon$ , is presented in figure C.19. As noted earlier, the computed sphericity using the traveling source model is larger than the experimental

values. This model causes the bubble exterior surface to be flattened during the growth phase, but is not able to elongate the bubble enough in the direction parallel to the headform surface. Note that the computed and experimental sphericity values presented here are measured at the time when the bubble reaches its maximum size and that the numerical program does allow lower sphericity values (down to  $\epsilon=0.73$ ) at earlier times as can be seen in figure D.19. We do observe a decrease in sphericity with increasing cavitation numbers as seen in the experimental data. Note that the Rayleigh-Plesset spherical model yields sphericity values  $\epsilon=1$  for all conditions.

Analysis of cavitation scaling effects was performed using this numerical method but is not presented here in great detail since varying of the Weber number,  $We$ , Reynolds number,  $Re$ , or ratio of initial radius to headform diameter,  $r_o=R_o/D$ , did not significantly affect the results of the computation. All the computational results presented here therefore used identical stream velocities,  $U_\infty=11.5\text{m/s}$ , headform diameter,  $D=50.8\text{cm}$ , and initial nucleus radius,  $R_o=100\mu\text{m}$ . In some cases though, for certain values of  $r_o$  and  $r_{qo}$ , important variations were observed during the initial nucleus growth. As stated in section B.2 some nuclei start to interact with the headform surface before they even reach pressures sufficiently low to cause them to become unstable. We noticed that these headform interactions occur mostly in the case of large nucleus to headform size ratios,  $r_o$ , and are almost always present in the case of the 5.08cm headform. These nuclei are sheared and compressed on the headform surface before they become unstable and the time at which they actually start to grow is thus modified. A critical parameter in this case appears to be the initial off-axis location,  $r_{qo}$ , of the source. Further studies are needed in order to understand the significance of each of these parameters influencing both the initial nucleus stability criteria and the bubble dynamics.

## E. CONCLUSIONS

In this thesis we have presented some of the results from a series of experiments carried out in the Large Cavitation Channel (LCC) to investigate the scaling of the dynamics and acoustics of individual cavitation bubbles in flows around headforms. Many of the phenomena observed by Ceccio and Brennen (1989, 1991) in experiments on 5.08cm headforms were seen again in the present experiments. Such micro-fluid mechanical phenomena included the hemispherical shape of individual cavitation bubbles, the thin film separating them from the surface, the destabilization of that film, the occasional production of attached streaks in the wake of the bubbles and the complex processes during the bubble collapse including bubble fission and roll-up into vortices.

Among some of the phenomena that were observed for the first time using such large headforms were the following. The present experiments yielded substantially lower cavitation inception numbers for the larger headforms. One result of this was that for the same air content, velocity and cavitation number, we observed bubble inception on the smallest headform and fully developed attached cavitation on the largest. Some of the differences in the appearance of individual bubbles on the three headforms could be attributed to this large difference in inception numbers since it implied quite different locations for the critical  $C_p = -\sigma$  isobars. The most noticeable effect of scale on the appearance of cavitation was the increase in bubble-generated attached streaks and patches for the larger headforms. On the 5.08cm headform a traveling bubble would occasionally generate two attached streaks or tails at the lateral extremes of the bubble. These would disappear almost immediately after the bubble collapsed. On the larger headforms at higher speeds (larger Reynolds numbers) and low cavitation numbers the streaks began to occur more frequently and extend behind the entire width of the bubble. The streaks would tend to produce a transient patch of attached cavitation which would disappear shortly after the bubble collapsed. For low enough cavitation numbers however,

the patches would persist almost indefinitely and create larger attached cavitation structures. It is possible that this is the mechanism of formation for most patch and attached cavitation. Also the simultaneous coexistence and interaction of all the forms of cavitation structures over the large headforms is remarkable.

Another new observation during the present experiments was the appearance of a remarkably repeatable "dimple" on the exterior surface of the traveling bubbles on the two larger headforms. These seem to be more pronounced when the bubble (or headform) is sufficiently large which suggests that the dimples are influenced by surface tension effects.

Cavitation event rates were also evaluated from the photographs and videotapes and this data clearly complements the observations of cavitation inception since inception was based on a chosen event rate. The event rates increase with increasing headform size and with decreasing cavitation number in the expected fashion if one assumes a fixed nuclei concentration. It is also demonstrated that the event rates appear to correspond to a nuclei population of the order of  $0.1 \text{ nuclei/cm}^3$  which is at least an order of magnitude lower than the expected nuclei population. We are continuing to investigate possible explanations for this discrepancy including the bubble screening effect first suggested by Johnson and Hsieh (1966).

The noise generated by individual events and the variations in the noise with the type of event were also investigated. We first demonstrate that the acoustic impulse generated by individual traveling bubbles scales quite well with headform size and tunnel velocity and that this scaling is in accord with that expected from the Rayleigh-Plesset or Fitzpatrick-Strasberg analysis. As expected, lower cavitation numbers lead to larger bubbles and larger impulses as long as the bubbles do not interfere with one another or with larger patch cavities.

As in the previous study by Ceccio and Brennen (1989, 1991) the impulses generated are substantially less than the magnitude predicted by the Rayleigh-Plesset analysis. It seems likely that the shearing and fission the bubble experiences prior to



collapse lead to a less highly focused and less "efficient" noise-producing event. The present study has added to this information. We have shown that the events which generate attached "streaks" or "tails" and which represent a greater fraction of the events at higher Reynolds numbers also produce significantly smaller acoustic impulses. This correlation was observed by a special cross-correlation of the surface electrode signals and the hydrophone output. The above observation has clear implications for the scaling of cavitation noise.

Some additional observations were made for those conditions at which the cavitation number was small enough for persistent attached patches to form and at which the void fraction of bubbles in the cavitation region became significant. First it was clear that when a traveling bubble encountered (or rode over) a patch its dynamics were altered and its acoustic output substantially diminished. Secondly like Arakeri and Shanmuganathan (1985) we also observed a significant decrease in the noise when the void fraction was sufficiently large so that the bubbles covered about 20% of the area in the cavitation region.

This significant decrease led us to develop a new numerical method which would allow us to study the interactions between the traveling bubble and the surrounding flow field. The single source method has proven to be quite adequate to capture many of the dynamics involved. Because the bubble is only deformed by the combined effect of the two sources and the headform ring panels, the kinematic conditions on the bubble surface and on the entire headform surface are quite accurately satisfied. The method developed here is valid in the sense that it does not induce significant errors on the zero normal velocity condition on the entire headform. The dynamic condition on the bubble surface though can only be satisfied on the average around the circumference of the bubble. The single source algorithm therefore does require some corrective effects in order for the evolution of the bubble shape to remain stable in time. We have seen that these corrections add up to less than 30% of the bubble volume.

Comparisons with the LCC experiments showed that the bubble shape, size and collapse location were remarkably accurate. Furthermore it reproduces a number of the features in the dynamics of the bubble such as the compression of the exterior surface during the growth phase and the evolution from a cap shape to a wedge shape. We have observed the dynamics with which the growing nuclei first interacts with the surface of the headform and generates an over-pressure above its exterior surface. This phenomena is assumed to be responsible for the appearance of the dimples observed on the photographs taken in the LCC. Perhaps the most significant value of this method is that it allows to compute the unsteady pressure field surrounding the bubble as it travels above the headform surface, and thus allows evaluation of bubble interactions. We have thus been able to quantify, for different cavitation numbers, the distance below which the bubble significantly alters the pressure field. The analysis of the pressure perturbation induced by the source showed us that it is caused by the combined effect of both a velocity-induced pressure perturbation and a momentum-change-induced pressure perturbation, both of which are three dimensional. By modeling these perturbations for different cavitation numbers we were able to predict the distance below which the source has a significant influence and thus to predict some bubble interactions. Computations also showed that the bubble first generates a high pressure perturbation, followed by low pressure and finally by a very strong over pressure during the final collapse phase. It also showed that the low pressure generated after the first over-pressure extended farther from the bubble than the latter and lasted for a longer period of time. As a result, the bubble lifetime is able to extend much farther downstream than the original low pressure region ( $C_p < -\sigma$ ), as has been observed by Favre *et al.* (1987).

Further interesting development of this method would include the study of nucleus stability as it travels along different streamlines and starts to interact with the headform surface. The way these dynamics influence the event rate prediction still needs to be addressed. This numerical model can also be extended to include interaction between

several bubbles. Because of the simplicity inherent in this single source model (as compared to the boundary element method), the addition of several sources should be very straightforward. Finally the simple source model could also be improved by adding higher order terms to the simple source, such as a dipole.

The experiments performed in the LCC proved very useful and allowed for the first time experiments on large headforms. A number of scaling effect trends have been observed that are presented here. It would be extremely interesting to perform additional measurements to accurately study some the trends, particularly the decreasing noise impulse as the cavitation number is reduced below a certain value. In order to fully analyze the dynamics of the deformation of the bubble surface, some very high-speed film (at a rate of at least 10kHz) would be extremely useful. This would also allow comparison in time of the experimental bubble shape with the numerical solution of the single source method. It might be possible to refine the sensitivity of the electrode sensing device close to the location of the bubble collapse in order to trigger such camera.

## REFERENCES

- [1] Albers, V.M. *"Underwater acoustics handbook."* Penn State Univ. Press, 1902.
- [2] Arakeri, V.H. and Acosta, A.J. 1973. *"Viscous effects in the inception of cavitation on axisymmetric bodies."* ASME Journal of Fluids Engineering, Vol. 95, pp. 519-527.
- [3] Arakeri, V.H. and Shanmuganathan, V. 1985. *"On the evidence for the effect of bubble interference on cavitation noise."* J. Fluid Mech., Vol. 159, pp. 131-150.
- [4] Baiter, H.J. 1986. *"On different notions of cavitation noise and what they imply."* Proc. ASME Intl. Symp. on Cavitation and multi-phase flow noise, FED-Vol. 45, pp. 107-118.
- [5] Benjamin, T.B. and Ellis, A.T. 1966. *"The collapse of cavitation bubbles and the pressures thereby produced against solid boundaries."* Phil. Trans. Roy. Soc., London, Ser. A, Vol. 260, pp. 221-240.
- [6] Billet, M.L. 1985. *"Cavitation nuclei measurement - A review."* ASME Cavitation and Multiphase flow Forum, Booklet, pp. 31-38.
- [7] Billet, M.L. and Holl, J.W. 1979. *"Scale effects on various types of limited cavitation"* ASME International Symposium on Cavitation Inception, pp. 11-24.
- [8] Blake, F.G. 1949. *"The onset of cavitation in liquids: I."* Acoustic Res. Lab, Harvard Univ., Tech. Memo. No. 12.
- [9] Blake, W.K., Wolpert, M.J. and Geib, F.E. 1977. *"Cavitation noise and inception as influenced by boundary layer development on a hydrofoil."* J. Fluid Mech., Vol. 80, pp. 617-640.
- [10] Brennen, C.E. and Ceccio, S.L. 1989. *"Recent observations on cavitation and cavitation noise."* Proc. ASME Third Int. Symp. on Cavitation Noise and Erosion in Fluid Systems, San Francisco, FED-Vol. 88, pp. 67-78.

- [11] Briançon-Marjollet, L. Franc, J.P. and Michel, J.M. 1990. *"Transient bubbles interacting with an attached cavity and the boundary layer."* J. Fluid Mech., Vol. 218, pp. 355-376.
- [12] Ceccio, S.L. 1989. *"Observations of the dynamics and acoustics of traveling bubble cavitation."* Ph.D. Thesis, California Institute of Technology.
- [13] Ceccio, S.L. and Brennen, C.E. 1991. *"The dynamics and acoustics of traveling bubble cavitation."* J. Fluid Mech., Vol. 233, pp. 633-660.
- [14] Chahine, G.L. 1977. *"Interaction between an oscillating bubble and a free surface."* ASME J. Fluids Eng., Vol. 114, pp. 680-686.
- [15] Chahine, G.L., Delepoule E., and Hauwaert, P. 1993. *"Study of the interaction between a bubble and a vortical structure."* Proc. ASME Cavitation and Multiphase Flow Forum, Washington D.C., FED-Vol. 153, pp. 39-43.
- [16] Coates, R.F. *"Underwater acoustic systems"*. Halsted press, John Wiley & Sons Inc., New York, 1889.
- [17] D'Agostino, L., Brennen, C.E. and Acosta, A.J. 1988. *"Linearized dynamics of two-dimensional bubbles and cavitating flows over slender surfaces."* J. Fluid Mech., Vol. 199, pp. 155-176.
- [18] Duncan, J.H. and Zhang, S. 1991. *"On the interaction of a collapsing cavity and a compliant wall."* J. Fluid Mech, Vol. 226, pp. 401-423.
- [19] Epstein, P.S. and Plesset, M.S. 1959. *"On the stability of gas bubbles in liquid-gas solutions."* Journal of chemical physics, Vol. 18, pp. 1505-1509..
- [20] Favre, J.N., Avellan, F., Ryhming, I.L. 1987. *"Cavitation performance improvement using a 2-D inverse method of hydraulic runner design."* Proc. Int. Conf. on Inverse Design Concepts and Optimization in Engineering Science-II., Penn. State University.
- [21] Fitzpatrick, H.M. and Strasberg, M. 1956. *"Hydrodynamic sources of sound."* First Symp. on Naval Hydrodynamics, Washington D.C., pp. 241-280.

- [22] Gates, E.M., Billet, M.L., Katz, J., Ooi, K.K., Holl, W. and Acosta A.J. 1979. *"Cavitation inception and nuclei distribution. Joint ARL-CIT experiments."* Rep. E244-1, Calif. Inst. of Tech., Div. of Eng. and Appl. Sciences, Pasadena, CA 91125.
- [23] Hamilton, M.F., Thompson, D.E. and Billet, M.L. 1982. *"An experimental study of traveling bubble cavitation and noise."* Proc. ASME Int. Symp. on Cavitation Noise, pp. 25-33.
- [24] Johnson, V.E. and Hsieh, T. 1966. *"The influence of gas nuclei on cavitation inception."* Proc. Sixth Symposium on Naval Hydrodynamics, Washington D. C.
- [25] Kellog, O.D. *"Foundations of potential theory."* New York, Dover Publications Inc., 1953.
- [26] Knapp, R.T., Daily, J.W. and Hammitt, F.G. *"Cavitation."* McGraw-Hill publishing co., 1970.
- [27] Kuethe A.M. and Chow C.Y. 1986. *"Foundations of aerodynamics."* Fourth Edition. John Wiley & Sons publishing Inc.
- [28] Kuhn de Chizelle, Y.P., Brennen, C.E. 1993. *"Cavitation scaling experiments with headforms: Bubble dynamics."* Proc. IUTAM Symp. on Bubble Dynamics and Interface Phenomena, Birmingham, U.K.
- [29] Kuhn de Chizelle, Y.P., Ceccio, S.L., Brennen, C.E. and Shen, Y. 1992. *"Cavitation scaling experiments with headforms: Bubble dynamics."* Proc. Second International Symposium on Propeller and Cavitation, Hangzhou, China, pp. 272-279.
- [30] Kuhn De Chizelle, Y.P., Ceccio, S.L., Brennen, C.E. and Shen, Y. 1992, *"Cavitation scaling experiments with headforms: bubble acoustics."* Proc. Nineteenth Symposium on Naval Hydrodynamics, Seoul, Korea.
- [31] Kuhn de Chizelle, Y.P., Ceccio, S.L., Brennen, C.E. and Shen, Y. 1992. *"Scaling experiments on the dynamics and acoustics of traveling bubble cavitation."* Proc. Institution of Mechanical Engineers, Cambridge, UK, pp. 165-170.

- [32] Kumar, S. and Brennen, C.E. 1991. *"Statistics of noise generated by traveling bubble cavitation."* Proc. ASME Cavitation and Multiphase Flow Forum, Portland, FED Vol. 109, pp. 55-62.
- [33] Kumar, S. and Brennen, C.E. 1992. *"An acoustical study of traveling bubble cavitation."* J. of Fluid Mech, Vol. 255, pp. 541-564.
- [34] Lauterborn, W. and Bolle, H. 1975. *"Experimental investigation of cavitation bubble collapse in the neighborhood of a solid boundary."* J. Fluid Mech., Vol. 72, pp. 391-399
- [35] Lezzi, A. and Prosperetti, A. 1986. *"Bubble dynamics in a compressible liquid, part 1: First order theory."* J. Fluid Mech., Vol. 168, pp. 457-478.
- [36] Lezzi, A. and Prosperetti, A. 1987. *"Bubble dynamics in a compressible liquid, part 2: Second order theory."* J. Fluid Mech., Vol. 185, pp. 289-321.
- [37] Lindgren, H. and Johnsson, C.A. 1966. *"Cavitation inception on headforms. ITTC comparative experiments."* Proc. 11th Int. Towing Tank Conf., pp. 219-232.
- [38] Liu, Z., Kuhn de Chizelle, Y.P. and Brennen, C.E. 1993. *"Cavitation event rates and nuclei distribution"* Proc. ASME Cavitation and Multiphase Flow, New Orleans, to appear.
- [39] Marboe, M.L., Billet, M.L. and Thompson, D.E. 1986. *"Some aspects of traveling bubble cavitation and noise."* Proc. ASME Int. Symp. on Cavitation and Multiphase Flow Noise, FED-Vol. 45, pp. 119-126.
- [40] Meyer, R.S., Billet, M.L. and Holl, J.W. 1989. *"Free-stream nuclei and cavitation."* Proc. ASME Third Int. Symp. on Cavitation Noise and Erosion in Fluid Systems, San Francisco, FED-Vol. 88, pp. 52-62.
- [41] Morgan, W.B. 1990. *"David Taylor Research Center's Large Cavitation Channel."* Proc. Int. Towing Tank Conference, Madrid, Spain, pp. 1-9.
- [42] Plesset, M.S. 1949. *"The dynamics of cavitation bubbles."* ASME Journal of applied Mechanics, Vol. 16, pp. 228-231.

- [43] Plesset, M.S. and Chapman, R.B. 1971. *"Collapse of an initially spherical vapor cavity in the neighborhood of a solid boundary."* J. Fluid Mech., Vol. 47, pp. 283-290.
- [44] Plesset, M.S. and Prosperetti, A. 1977. *"Bubble dynamics and cavitation."* Annual Review of Fluid Mechanics, Vol. 9, pp. 145-185.
- [45] O'Hern, T., D'Agostino, L. and Acosta, A.J. 1988. *"Comparison of holographic and coulter measurements of cavitation nuclei in the ocean."* ASME J. Fluids Eng., Vol. 110, pp. 200-207.
- [46] O'Hern, T., Katz, J. and Acosta, A.J. 1985. *"Holographic measurements of cavitation nuclei in the sea."* ASME Cavitation and Multiphase Flow Forum Booklet, FED Vol. 23, pp. 39-42.
- [47] Rood, E.P. 1989. *"Mechanisms of cavitation inception."* Proc. ASME Intl. Symp. on Cavitation Inception, FED-Vol. 89, pp. 1-22.
- [48] Schiebe, F.R. 1972. *"Measurements of the cavitation susceptibility of water using standard bodies."* St. Anthony Falls Hydraulic Lab., Univ. of Minnesota, Rep. No. 118.
- [49] Shen, Y.T., Gowing, S. and Pierce, R.D. 1984. *"Cavitation susceptibility measurements by a venturi."* Proc. ASME, Int. Symp. on cavitation inception, New Orleans, Winter annual meeting.
- [50] Van der Meulen, J.H. and Van Renesse, R.L. 1989. *"The collapse of bubbles in a flow near a boundary."* Seventeenth Symp. on Naval Hydrodynamics, The Hague.
- [51] Vogel, A., Lauterborn, W. and Timm, R. 1989. *"Optical and acoustic investigations of dynamics of the Laser-produced cavitation bubbles near a solid boundary layer."* J. Fluid Mech., Vol. 206, pp. 299-338.



## APPENDIX

### PROGRAM STRUCTURE

The program "3D\_SOURCE" presented in chapter D is written in C language. It includes 2100 lines of code and can be run in different modes: either calculating bubble deformations in time, given an initial nuclei position, or using already existing bubble calculations to compute pressure field over the headform at a given time (as presented in figure D.12 for example). The run time to compute a complete bubble from an initial nuclei to the final collapse is about 5 hours on a Sun SparcStation 10. In order to run, the program requires two files. The first file, "SCHIEBE.DAT," includes all information regarding the headform geometry. The second file, "BUBBLE.YKC," includes information about the flow and initial conditions. In addition the programs asks the user for output file names which will include the bubble shape, source position and strength, and pressure distribution on the surface of the bubble. The gray-level pressure distribution contour plots (as the ones presented in figures D.12 for example) have been post-processed from data files generated by the program 3D\_SOURCE. These plots have been created using various commercial software such as Mathematica, PvWave or XImage. In the following section we present examples of the two files required to run the program 3D\_SOURCE. The program VISU.C runs on IBM-PC compatible machines with vga screen capability and produces a graphical animation of the bubble shape from files created by the 3D\_SOURCE program.

#### FILE "SCHIEBE.DAT"

This file consists of the headform name, number of headforms, number of panels on headform,  $N_p$ , and the list of dimensionless coordinates,  $x_i$ ,  $r_i$ , for each panel:

*Schiebe Headform*

1

93

0.000000	0.000000
0.000000	0.003640
0.000000	0.007270
0.000000	0.010920
0.000000	0.014650
0.000000	0.018190
0.000050	0.027600
0.000190	0.037500
0.000470	0.050000
0.000840	0.062500
0.001280	0.075190
0.001740	0.087500
0.002280	0.100000
0.002890	0.112500
0.003820	0.128440
0.004400	0.137500
0.005080	0.147300
0.006360	0.163540
0.007370	0.175000
0.008570	0.187500
0.009900	0.200000
0.011360	0.212500
0.012720	0.223060
0.014780	0.237500
0.016780	0.250000
0.019080	0.262800
0.021560	0.275000
0.025440	0.291100
0.027950	0.300000
0.031800	0.311480
0.038160	0.326120
0.044510	0.336880
0.050870	0.345220
0.055200	0.350000
0.060270	0.355000
0.066010	0.360000
0.072380	0.365000
0.079420	0.370000
0.087160	0.375000
0.095660	0.380000
0.104930	0.385000
0.115050	0.390000
0.126050	0.395000
0.138020	0.400000
0.144380	0.402500
0.151020	0.405000
0.157980	0.407500
0.165180	0.410000
0.172720	0.412500
0.180600	0.415000
0.188820	0.417500
0.197420	0.420000

0.206400	0.422500
0.215800	0.425000
0.225620	0.427500
0.235930	0.430000
0.246750	0.432500
0.258120	0.435000
0.270080	0.437500
0.282680	0.440000
0.295980	0.442500
0.310000	0.445000
0.324840	0.447500
0.340580	0.450000
0.375120	0.455000
0.414610	0.460000
0.460340	0.465000
0.486080	0.467500
0.514180	0.470000
0.545060	0.472500
0.579100	0.475000
0.616940	0.477500
0.659710	0.480000
0.708620	0.482500
0.764850	0.485000
0.830180	0.487500
0.909730	0.490000
1.009820	0.492500
1.138260	0.495000
1.379760	0.498240
1.582220	0.500000
1.800000	0.500000
2.050000	0.500000
2.350000	0.500000
2.699990	0.500000
3.100000	0.500000
3.500000	0.500000
4.000000	0.500000
4.500000	0.500000
5.000000	0.500000
10.000000	0.500000
50.000000	0.500000
100.000000	0.500000

# **FILE "BUBBLE.YKC"**

This file is structured in the following way:

```

Mode   PrintCpFile
Stop_time
a_S_incr_print   Time_incr_print
 $x_{q0}$        $r_{q0}$ 
D            $U_{\infty}$        $R_0$        $\sigma$ 

```

where the Mode variable is defined as follows:

Mode= 0	calculate normal bubble growth.
Mode= 1	calculate bubble at time Stop_time.
Mode= 2	calculate bubble at all time increments Time_incr_print.
Mode= 3	calculate bubble at all bubble radius increments a_S_incr_print.

The PrintCpFile variable is defined as follows:

PrintCpFile=0	do not create Cp files for the pressure field above the headform.
PrintCpFile=1	create Cp file with size scaled the bubble radius.
PrintCpFile=2	create Cp file with a standard fixed scale.
PrintCpFile=3	create files for both cases 1 and 2.
PrintCpFile=4	create file which includes Cp, normal and tangential velocities on the headform surface.

An example of the file is shown as follows:

```

2      2
10     .01   .02
-1.    0.01
0.508  11.5  100e-6  0.45

```

## PROGRAM "3D\_SOURCE"

Because of the length of the source code file "3D\_SOURCE.C", we do not include a listing in this thesis but rather just present a list of the main array variables used in the program, which should help the user to understand the structure of the program. The program itself is written in a number of subroutines which should be fairly easy to comprehend. It also includes a number of comments.

Coord[0][i]=x <sub>pi</sub>	panel points (on body geometry).
Coord[1][i]=r <sub>pi</sub>	
Coord[2][i]=x <sub>ci</sub>	control points(normal velocity = 0).
Coord[3][i]=r <sub>ci</sub>	

Coord[4][i]=sin <sub>ci</sub>	sine of angle of panel with U <sub>∞</sub> (i.e. normal to control point).
Coord[5][i]=cos <sub>ci</sub>	
Coord[6][i]=Δs <sub>i</sub>	length of panel.
Coord[7][i]=x <sub>ai</sub>	center of rotation of the panels (used to locate the image source).
Coord[8][i]=r <sub>ai</sub>	
Coord[9][i]=x <sub>li</sub>	panel for larger headform (at D=1/100 from the headform surface).
Coord[10][i]=r <sub>li</sub>	
Result[0][i]=μ <sub>i</sub>	panel source strength.
Result[1][i]=Cp <sub>ci</sub>	pressure coefficient on control point i.
Result[2][i]=v <sub>Ni</sub>	normal velocity on control point i.
Result[3][i]=phi <sub>ci</sub>	potential on control point i.
Result[4][i]=v <sub>Ti</sub>	tangent velocity on control point i.
Result[5][i]=θ <sub>ci</sub>	boundary layer thickness at control point i.
Result[6][i]=k + 0.09	shape parameter(if k less than -0.09 we have detachment of the Boundary Layer).
Result[7][i]=γ	transition to turbulence parameter
Result[8][i]=μ <sub>i</sub>	panel source strength from previous time step "p"
Bubble[0][i]=x <sub>i</sub>	bubble node coordinate.
Bubble[1][i]=r <sub>i</sub>	bubble point node coordinate.